PhD Dissertation

Subwavelength Light Confinement in Metal and Metal-Oxide Nano-Hybrids for the Applications in Energy Conversion and Sensing

Dao Duy Thang

Nara Institute of Science and Technology

March 2015

Subwavelength Light Confinement in Metal and Metal-Oxide Nano-Hybrids for the Applications in Energy Conversion and Sensing

A Dissertation

Submitted to the Graduate School of Materials Science

Nara Institute of Science and Technology

In partial fulfilment of the requirements for the

degree of Doctor of Philosophy

by

Dao Duy Thang

March 2015

Date:_____

Approved by:

_____ Chair, Doctoral Dissertation Committee
Professor **Hiroshi Daimon**

_____ Members, Doctoral Dissertation Committee
Professor **Hisao Yanagi**

_____
Professor **Katsunori Yogo**

_____
Professor **Ken Hattori**

ACKNOWLEDGMENTS

I would like to express my sincere thanks, gratitude and appreciation to those who have helped and inspired me during my doctoral study. My dissertation would not have been succeeded without those supports from many people.

To be a PhD student at NAIST, I have received strong support from Prof. Hiroshi Daimon, who gave me an opportunity to apply for the PhD program at NAIST. I would like to express my sincere gratitude to him, for offering me a chance to become a PhD student in his group, for his support and all the advices on my PhD research content. I also would like to thank Prof. Hisao Yanagi, Prof. Katsunori Yogo and Prof. Ken Hattori, for the fruitful scientific discussions, and for their approval and advices on my PhD research content. I am very thankful to Mrs. M. Nagata, Dr. S. N. Takeda, and all students in Daimon's Lab for their helps during the time I have been there.

Being a PhD student at NAIST, I have been working in Nano-System Photonics Group (MANA-NIMS) of Dr. Tadaaki Nagao, where I have grown from being an outsider to being a researcher in materials science, nano-fabrications, design and simulation of plasmonic nanostructures. I would like to express my sincere gratitude to Dr. Tadaaki Nagao, for offering me a chance to work with him, for providing me equipment, training and guidance, for sharing me his knowledge, experience and sense, and for devoting his precious time to teach me and construct my research work. Without his understanding, encouragement and patience, full support and scientific advice, I could not have been carried out any research outputs and would not be able to apply for the PhD course at NAIST.

All of this work would not have been carried out without the effort and guidance of many people in Nano-System Photonics Group. I am very thankful to Dr. C.V. Hoang, Dr. H. Gui, Dr. S. Ishii, Dr. K. Chen, Dr. R. P. Sugavaneshwar, Dr. H. L. Nghiem, Prof. M. Kitajima,

Mrs. T. C. Dang, Mrs. N. Arai, Mr. T. Yazawa, for sharing me the experience and knowledge, for advising me in scientific research as well as giving me many useful discussions. I also would like to thank Dr. T. Nabatame, Dr. A. Ohi, and all MANA staff members, for advising me in the fabrication and characterization of nanostructures. It is also essential to recognize the contributions from them and other collaborators, Mr. Z. Li, Dr. L. Q. Liu, Dr. Minami in all my contributed works. I would like to extend my sincerest thanks to Prof. Nguyen Dai Hung and Prof. Dinh Van Trung (IOP-VAST) who helped me become a scientist, and always encourage me. I also would like to give my very warm thanks to all my dear friends for their cordiality and unique support.

Finally, I would like to say that nothing would have been possible without the support of my family. My heartiest and genuine gratitude is extended to my wife and my son for their patience, love and tolerant support. I would like to express my most cordial gratitude to my father and all my family members, for their great supports and thoughtfulness to me in my life. This dissertation is especially dedicated to my mother.

CONTENTS

ACKNOWLEDGMENTS ii

CONTENTS iv

ABSTRACT viii

LIST OF FIGURES ix

1. INTRODUCTION 1

1.1. Motivation and objective 1

1.2. An overview of the dissertation 3

2. PLASMONICS AND NEAR-FIELD ENHANCEMENT IN PLASMONIC NANO-HYBRIDS 5

2.1. Plasmonics 5

2.1.1. Plasma oscillation in metal and dielectric function the free electron gas 5

2.1.2. Surface plasmon wave 9

2.1.2.1. Surface plasmon-polariton propagation at metal-dielectric interface 9

2.1.2.2. Kretschmann configuration for optical excitation of SPPs 16

2.1.2.3. Localized surface plasmon resonance 18

2.1.3. Electromagnetic simulations of plasmonic nanostructures 20

2.1.3.1. Rigorous coupled-wave analysis (RCWA) 21

2.1.3.2. Finite-difference time-domain (FDTD) 21

2.2. Plasmonic nanostructures for sensing and energy conversion applications 24

2.2.1. Optical properties of percolated gold film and nonlinear electrons dynamic induced by intense THz pulse 25

2.2.2. Gold nano-sandwich hybrid arrays based plasmonics metamaterial 27

2.2.3. Gold nanocages (AuNCs) and AuNCs-TiO_2 hybrids 31

2.3. Summary of Chapter 2 33

3. PLASMONIC NANOGAPS FOR SERS AND SEIRA 34

3.1. Surface-enhanced vibrational spectroscopy: SERS and SEIRA 34

3.2. Floating aluminum nanobowtie based plasmonic antenna for SERS 35

3.2.1. Optical properties of plasmonic bowtie nanoantenna 36

3.2.2. Floating aluminum nanobowtie: optical properties and SERS application 38

3.2.2.1. Optical properties of floating aluminum bowtie antenna 39

3.2.2.2. SERS study on plasmonic Al bowtie antenna 44

3.2.3. Conclusion of plasmonic aluminum nanoantennas 48

3.3. *In situ* chemical synthesis of random gold nano-islands and patchy gold nano-shell for in situ SEIRA spectroscopy 48

3.3.1. *In situ* FTIR-controlled growth of gold nano-islands for SEIRA 50

3.3.2. *In situ* chemical synthesis of plasmonic Au-patchy nanoshells for SEIRA 53

3.3.2.1. *In situ* synthesis of plasmonic Au-patchy SiO_2 core-shell particles 54

3.3.2.2. *In situ* SEIRA using Au-patchy nanoshells array 58

3.3.2.3. SERS study on Au-patchy SiO_2 core-shell 61

3.3.3. Conclusion of plasmonic Au-patchy SiO_2 for SEIRA 63

3.4. Summary of Chapter 3 64

4. METAL OXIDE SEMICONDUCTORS FOR PHOTOELECTRIC CONVERSION AND PLASMONIC NANO-HYBRID FOR EFFICIENT PHOTOCATALYSTS 65

4.1. ZnO NWs and TiO_2 film: Chemical synthesis and characterizations 65

4.1.1. Metal-oxide ZnO and TiO_2 nanostructures 65

4.1.2. Chemical synthesis of ZnO NWs and TiO_2 thin film 66

4.1.2.1. Hydrothermal growth and characterizations of ZnO NWs 66

4.1.2.2. Cr –doped TiO_2 thin film prepared by sol-gel method 71

4.2. Cr-doped TiO_2-ZnO core-shell p-n junction array for high sensitivity ultraviolet photodetector 74

4.2.1. ZnO NWs based UV photodetector 74

4.2.2. Cr-doped TiO_2-ZnO core-shell nanowires array 76

4.2.3. Ideality factor of the Cr-doped TiO_2-ZnO core-shell p-n junction 78

4.2.4. Spectral response of Cr-doped TiO_2-ZnO NWs photodiode 81

4.2.5. High internal gain in Cr-doped TiO_2-ZnO UV photodiode 83

4.2.6. Conclusion of Cr-doped TiO_2-ZnO p-n junction UV photodiode 86

4.3. Plasmonic NPs-ZnO NWs hybrids for efficient solar-driven photocatalysis 86

4.3.1. Plasmon-enhanced photocatalysis 87

4.3.2. Preparation and characterization of metal NPs-ZnO NWs hybrid arrays 89

4.3.3. Photodegradation of MB in water using metal NPs-NWs hybrid catalyst 94

4.3.4. Electric field enhancement and discussion on the mechanism of plasmon-enhanced photocatalysis in plasmonic NPs-ZnO hybrid 98

4.3.5. Conclusion of plasmonic NPs-ZnO NW hybrids for efficient photocatalyst .. 102

4.4. Summary of Chapter 4 103

5. METAL-INSULATOR-METAL PLASMONIC PERFECT ABSORBER 105

5.1. Plasmonic metamaterial perfect absorber 105

5.2. Design, simulation and fabrication of the metal disk-insulator-metal film perfect absorber ranging from VIS to IR 108

5.2.1. Proposed structure and its optical properties 108

5.2.2. Fabrication of Al-PAs using conventional colloidal lithography 114

5.3. Al-PAs based selective thermal emitters 119

5.4. Al-PAs based surface-enhanced infrared spectroscopy 121

5.5. Al-PAs on Cu plate 124

5.6. MIM holes Al-PAs based dual-band perfect absorber 126

5.7. Broadband perfect absorber based on random gold nano-islands 130

5.8. Summary of Chapter 5 131

6. SUMMARY 133

PUBLICATIONS 135

REFERENCES 138

ABSTRACT

In this dissertation, we present a variety of the plasmonic nanogaps of metal and metal-oxide hybrids in which their resonance are ranged from VIS to IR regions for the suitable applications in molecular sensing, photoelectric and thermal energy conversion materials. In the first two chapters, we introduce the introductory overview of plasmonics, from fundamental concept to numerical simulations and applications in the field of nanophotonics as well as nanomaterials science. The light confinement in plasmonic nano-hybrids is also briefly indicated in the last part of Chapter 2. Then, the designs, fabrications and applications of some plasmonic metal and metal-oxide hybrids are presented in Chapter 3, 4, and 5. A floating plasmonic nanoantenna array using earth-abundant aluminum is designed for surface-enhanced Raman scattering (SERS) at 532 nm excitation with a demonstration on the sensing of Nile blue molecules. Beside the use of plasmonic hybrid in VIS for sensing based on SERS, we also demonstrate the *in situ* FTIR sensing of bio-molecules and detection of mercury ions in water based on SEIRA using multiple nanogaps on the random gold nano-islands and gold-patchy SiO_2 core-shell particles, that are synthesized by *in situ* chemical growth technique. A part of this work presents the combination of metal-oxide ZnO nanowire and TiO_2 thin film for realizing high sensitivity ultra violet photodetector. In addition, by using metallic nanoparticles as plasmonic antenna, where the electric fields are confined in a small volume of nanometer scale and extremely enhanced at nanometal surfaces, we carried out plasmonic nanoparticles-ZnO nanowire hybrids for efficient photocatalyst. Finally, we show the design and fabrication of the metal-insulator-metal infrared plasmonic perfect absorber using aluminum with top metallic layer consisting of Al disks or Al holes array. Our developed techniques using colloidal lithography and variety of aluminum plasmonic perfect absorbers can be useful in wide-range applications such as selective thermal emitters and SEIRA that we have introduced in this thesis.

LIST OF FIGURES

Figure 1.1. Electromagnetic field confinement in plasmonic nano-hybrids and their applications. (a) Applications of UV-VIS plasmonic materials. Background presents enhanced near-field in a UV-VIS plasmonic metal-ZnO nano-hybrid. (b) Applications of NIR-IR plasmonic materials. Background presnts enhanced near-field in an IR aluminum plasmonic perfect absorber composed of metal and metal-oxide. Arrows indicate our works on plasmonic metal/metal-oxide hybrids based: UV-VIS plasmonic hybrids for SERS, photocatalyst, and IR plasmonic hybrids for selective thermal emitter and SEIRA. 1

Figure 2.1. Plasma oscillation in metal 5

Figure 2.2. (a) Dielectric functions of Au and Ag[31]. (b) Comparison between Drude model ($\varepsilon_\infty = 6.9$, $\omega_p = 8.9$, $\gamma = 0.07$)[32], [33] and experiment data[31] of dielectric function of Au with interband transitions region. 8

Figure 2.3. (a) Geometry for SPP propagation at metal-dielectric interface. (b) Dispersion relation of the fundamental coupled SPPs at different interfaces of Ag and dielectrics of air, glass, and Si. 14

Figure 2.4. (a) Kretschmann configuration for optical excitation of SPP propagation at metal-dielectric interface. (b) Simulated electric field of SPP propagated along Ag-air interface at resonant excitation of 600 nm under incident angle of 46.2°. (c) Simulated SPP resonant spectra of Ag-air interface under different wavelength excitations. (d) Dispersion relation of the coupled SPP mode at Ag-air interface plotted using Kretschmann configuration and a comparison with the fundamental coupled SPP. 16

Figure 2.5. (a) Schematic of localized surface plasmon excitation of metallic nanoparticle. (b) Near-field distribution of localized surface plasmon of Au nanoparticle under resonance excitation at 520 nm. Extinction cross-section spectra of metal nanoparticles in different surrounding medium of air and water: (a) Ag nanoparticles and (b) Au nanoparticles. 18

Figure 2.6. In a Yee cell of dimension Δx, Δy, Δz. The E field components are in the middle of the edges, the H field components are in the centre of the faces.[40] 22

Figure 2.7. Electromagnetic simulation of Au-dimer on glass substrate with Au diameter of 15 nm, gap size of 5 nm, and domain size (periodicity) of 60×40 nm. (a) Simulated extinction of Au-dimer using RCWA with polarization along the dimer axis ($E_{//}$, red), and perpendicular to the dimer axis ($E_{\perp}$, black). (b) Simulated electric field distribution of Au-dimer excited at resonance (546 nm) under

parallel polarization (parallel-mode). Insets in (b) show schematic of the charge profile of Au-dimer, parallel dipole (bright-mode) and anti-parallel dipole (dark-mode). 23

Figure 2.8. (a) SEM image of a percolated Au film with multiple Au-islands. (b) Strong electric field confinement in the gaps between nano-islands 25

Figure 2.9. (a-c) SEM images of Au films: (a) agglomerated Au nano-islands (S1), (b) Coalesced Au nano-islands (S2), and (c) Connected Au-islands with gaps (S3). (d) Simulated transmittances of Au films (S1, S2, S3) from IR - THz region. (e) Illustration of nonlinear dynamic of electrons in Au film induced by electron-electron collision or tunnelling effect at the gaps of Au-islands. 26

Figure 2.10. (a) Proposed Au nano-sandwich hybrid arrays, and SEM image of a fabricated sample. (c) Measured and (d) Simulated transmittance spectra of variety of gold nano-sandwich hybrids show two resonances related to electric-dipole (short-wavelength) and magnetic-dipole (long-wavelength) modes. 28

Figure 2.11. Simulated electrical field (Ex) and magnetic field (Hy) gold nano-sandwich (10 nm etching) arrays. (a) Ex and (b) Hy fields distributions under excitation at electric dipole mode of 675 nm. (c) Ex and (d) Hy fields distributions under excitation at magnetic dipole mode of 1040 nm. 29

Figure 2.12. AuNCs-TiO_2 photocatalyst. (a) AuNCs, from top to bottom: Au cubic (without hole), with small holes, and with big holes. (b) Simulated and measured extinction spectra of AuNCs without TiO_2 and with different holes sizes. (c) Simulated and measured extinction spectra of AuNCs-TiO_2 hybrids. (d) TEM image of AuNCs-TiO_2 hybrid. (e) Simulated electric field distribution of AuNC-TiO_2 hybrid excited at 700 nm shows multiple hot-spots at Au-TiO_2 interface with strong electric field enhancement of 40 folds. 31

Figure 3.1. (a) Schematic of non-floating bowtie array. (b) Schematic of the charge profile of triangle, parallel and anti-parallel modes[48]. (c) Simulated extinction spectra of non-floating Au bowtie on a glass substrate excited at different polarizations. (d) Simulated field distribution of bowtie antennas at resonance of 785 nm. The scale bar is 100 nm. 36

Figure 3.2. (a) Schematic of floating bowtie array. (b) Simulated extinction spectra of floating Au bowtie supported by SiO_2 pillars on a glass substrate at different polarized excitations. (c) Simulated electric field distribution of floating Au bowtie under excitation paralleled to bowtie axis. 37

Figure 3.3. (a) Top-view and (b) Tilted-view SEM images of floating bowtie aluminum fabricated on Si substrate. 40

Figure 3.4. Dark-field spectroscopy of Al bowtie antenna. (a) Dark-field optical image. (b) Dark-field scattering spectra of single bowtie (black curve) and on an area (10×10 μm^2) bowtie (red curve). (c)

Dark-field spectral mapping image integrated at around resonance wavelength of single antenna (530 - 600 nm) showing the scattering responded at centre of bowtie. (d) Dark-field spectral mapping image integrated at around 650 nm indicating the interaction between bowties. 42

Figure 3.5. (a) Dark-field scattering spectra of Al bowtie with 105 nm width, 840 nm periodicity, 1120 nm spacing and 20 nm gap and (b) Its dark-field spectral mapping image integrated at around resonance wavelength of single antenna (530 - 600 nm). (c) Dark-field scattering spectra of Al bowties with 1400 nm periodicity, 1120 nm spacing and different gaps of 10 and 20 nm. (d) Dark-field spectral mapping image integrated around 560 nm peak of 10 nm gap bowtie. 43

Figure 3.6. Demonstration of electric field enhancement of freestanding bowtie antenna by means of surface enhanced Raman spectroscopy (SERS). (a) Bright-field optical image (seen under confocal microscope). (b) Raman mapping. (c) Dark-field spectral image indicating the plasmonic mapping of the antenna arrays. (d) SERS measurements of NB molecules on Al bowtie antenna. The black curve and red curve show Raman signals OFF and ON the objects. The small inset indicates the Raman signals under different excitation conditions, parallel to the gap and perpendicular to the gap, respectively. 44

Figure 3.7. (a) Simulated extinction of Al bowtie with parallel excitation mode (different gaps size of 10, 20, 30 nm) or perpendicular excitations (10 nm gap). The electric field enhancement is well known as the primary mechanism of SERS. In addition to demonstrate the SERS effect on the Al bowtie nanoantenna, the electric field distribution around Al bowtie at 532 nm excitation was simulated with two polarized excitations. (b) Perpendicular polarization. (c) and (d) Parallel polarization with size-view and top-view, respectively. The scale bar is 50 nm. 46

Figure 3.8. *In situ* growth of random gold nano-islands with multiple gaps (hot-spots) for SEIRA application. (a) Schematic illustration of a SEIRA substrate using Au-islands with multiples hot-spots on Si crystal under ATR configuration. (b) Evolution of vibrational signals from water during the growth of Au-islands indicating the plasmon resonance responded to IR range when the size of AuNPs increased. (c) SEM images show the evolution of Au-islands corresponded to the enhancement of vibrational signals of water. The scale bar is 200 nm. 51

Figure 3.9. (a) Vibrational signals of BSA molecules adsorbed on Au-islands show high sensitivity of the Au nano-islands based SEIRA substrate (sub pico-molar). (b) SEM image of Au-islands with multiples gaps. (c) Corresponding multiple near-field hot-spot located at the gaps under IR excitation (2000 cm^{-1}). (d) A cross-section view of electric field distribution of Au-islands. 53

Figure 3.10. *In situ* growth of Au-patchy SiO_2 core-shell particles on Si-ATR substrate for SEIRA. (a)-(c) Schematic illustrates the growing process. (d) Evolution of vibrational signals from water corresponded to the evolution of Au-islands on SiO_2 particle. 55

Figure 3.11. SEM image of Au-patchy SiO_2 core-shell particles. (a) Before growth. (b) After growth for 60 second. (c) Final growth (200 second). 56

Figure 3.12. (a) Relative reflectance signal at 3200 cm^{-1} of water vibration (combination of symmetric stretch mode and overtone of bending mode) by growth time of Au-patchy shell layer. (b) Simulated the enhancement of water vibrations induced by near-field plasmon enhancement of Au-patchy SiO_2 core-shell particles. 57

Figure 3.13. (a) *In situ* FTIR sensing of glutathione (GSH) molecules using Au-patchy SiO_2 core-shell particles as SEIRA substrate. (b) *In situ* FTIR detection of mercury ions in water using GSH-functioned Au-patchy SiO_2 core-shell by monitoring the relevant conformational changes of GSH vibrations when mercury ions adsorbed into GSH molecules. 59

Figure 3.14. (a) Evolution of relevant conformal changes of GSH vibrations induced by adsorption of mercury ions into GHS molecules. (b) Model for mercury ions adsorb into GSH molecules. 60

Figure 3.15. (a) SEM image of Au-patchy SiO_2 core-shell particles. (b) Dark-field scattering spectrum of Au-patchy shells with resonance peak located at around 780 nm. SERS study of MB adsorbed on Au-patchy shells (c) SERS mapping image (integrated at 1618 cm^{-1}, excited by 785 nm laser) and (d) Comparison between SERS spectra excited by 785 nm (red) and 532 nm (blue) lasers. 61

Figure 3.16. Electric field distributions of Au-patchy SiO_2 core-shells. (a) Au-SiO_2 core-shells with completed Au shells layer (without gaps) under IR excitation (5 μm or 2000 cm^{-1}). Au-patchy SiO_2 particles: (b) Under IR excitation (5 μm or 2000 cm^{-1}), (c) Under VIS excitation (532 nm). (d) Under NIR excitation (785 nm). The scale bar is 50 nm. 62

Figure 4.1. Schematic of the hydrothermal growth of ZnO NWs 66

Figure 4.2. Structure and morphology characterization of ZnO NWs fabricated by hydrothermal method. (a) SEM image of ZnO nanoseeds formed by spin-coating and annealing processes. (b) Top-view, (c) Tiled-view and (d) Cross-sectional SEM images of typical ZnO NWs with averaged diameter of 50 nm and length of about 0.8 – 1 μm. (c) HR-TEM image of a single ZnO NW with [0001] growth orientation. Inset shows SAED of the ZnO NWs. (f) XRD patterns of single crystal ZnO NWs on ITO-glass substrate and bare ITO-glass. 68

Figure 4.3. FTIR (a) and Raman (b) spectra of ZnO NWs. 69

Figure 4.4. (a) Absorption and (b) Photoluminescence spectra of ZnO NWs. 69

Figure 4.5. (a) SEM and TEM (insets) images of ZnO nanowires and nanosheets and (b) Their photoluminescence properties. 70

Figure 4.6. (a) XRD patterns and (b) FTIR spectra of Cr-doped TiO_2 thin films 72

Figure 4.7. (a) Top view and cross-sectional (inset) SEM images of TiO_2 thin film fabricated on ITO-glass substrate. (b) Transmittance spectra of undoped and Cr-doped TiO_2 thin films. 73

Figure 4.8. Morphology characterization of Cr-doped TiO_2/ZnO NWs core-shell. (a) Tilted-view SEM image of ZnO NWs array. (b) Cross-sectional SEM image of the Cr-doped TiO_2/ZnO NWs. (c) TEM image and (d) High-angle annular dark-field scanning TEM and EDS elemental mapping of Zn, O, Ti and Cr of a single Cr-doped TiO_2/ZnO NW. 76

Figure 4.9. (a) Photoluminescence spectra of pristine ZnO NWs (blue curve) and the ZnO NWs covered by the Cr-doped TiO_2 laminate (red curve). (b) Absorbance spectra of the ZnO NWs without (blue curve) and with (red curve) TiO_2 shell layer. 77

Figure 4.10. (a) Schematic illustration of the Cr-doped TiO_2-ZnO NWs p-n heterojunction device. (b) I-V response and ideality factor of p-n heterojunction device. 79

Figure 4.11. (a) Spectral response of the device taken under the UV, VIS, IR illumination with the same power (104 μW). The inset shows the transmission characteristics of the filters used in this measurement. (b) Power-dependent photocurrent of device. (c) Photocurrent response as function of incident power and reverse applied bias. (d) Dependence of rectification ratio and reverse current on incident power under 373 nm illumination and 5 V reverse applied bias. 82

Figure 4.12. (a) Oxygen adsorbed on TiO_2 shell surface, in the dark (top) and in the light illumination (bottom). (b) Time dependence of the photocurrent with switching on/off the 373 nm UV illumination at 5 V reverse-biased. 84

Figure 4.13. (a) Cross-sectional SEM image of a ZnO NWs array and a HR-TEM image (inset) of a single ZnO NW with [0001] growth orientation. (b) Tilted-view SEM image of a AuNPs-ZnO NWs array. (c) HR-TEM image of a AuNP on the ZnO NW surface. (d) XRD patterns of a AuNPs coated and a non-coated ZnO NWs array. 90

Figure 4.14. (a) Simulated and (b) Measured transmission spectra of bare ZnO NWs array (black curve), AgNPs-ZnO NWS hybrid (blue curve), and AuNPs- ZnO NWs hybrid (red curve). The insets in (a) shows simulation model for a unit cell, including NPs on ZnO surface with tilted angle of 30° with respect to the incident light direction. The photo luminescence spectra of the ZnO nanowires

before and after annealing at 400 °C. Inset in (b) shows the experimental transmission spectra of the original AgNPs and AuNPs suspensions in water. 92

Figure 4.15. Photodegradation of methylene blue (MB) molecules in water under solar light illumination. (a) Experimental setup. (b) Photodegradation evolution as increasing the transparency of MB in presence of catalyst by the time irradiation. (c) Reductions of the concentration of MB are shown: without catalyst (gray curve), in the presence of bare ZnO NWs array (red curve), AuNPs-ZnO NWs array (green curve) and AgNPs-ZnO NWs array (blue curve). (d) The MB photodegradation rate constants in the presence of the different catalysts are shown. The inset shows a TEM image of a thin TiO_2 layer-coated ZnO NW catalyst..... 94

Figure 4.16. Photocurrent density of ZnO NWs and NPs-ZnO NWs hybrid photoanodes of the PEC cell under photovoltaic configuration. (a) Under solar light illumination with power density of 100 $mWcm^{-2}$ (standard AM 1.5G filter) and (b) Under visible light illumination (wavelength in the range of 400 – 900 nm with power density of 33 $mW\text{-}cm^{-2}$). (c) Schematic of the photoelectrochemical cell under photovoltaic configuration. (d) Schematic illustration of the mechanism for VIS photocatalytic activity by plasmon-induced hot-electron of plasmonic NPs-ZnO NWs hybrid. 97

Figure 4.17. Simulated transmittance (red curves) of (a) AgNPs-ZnO NWs hybrid and (d) AuNPs-ZnO NWs hybrid in real working-condition medium of water. Simulated electric field distribution around plasmonic NPs-ZnO hybrids shows strong E-field enhancement and the hot-spots located at the interface of the metal and semiconductor would provide smart potential to hot-electrons: For AgNPs-ZnO NWs - (b) Under UV excitation of 365 nm with E-field enhancement of 4 and (c) under visible of plasmon resonance at 450 nm with strong E-field enhancement of 20. For AuNPs-ZnO NWs - (e) Under UV excitation of 365 nm with E-field enhancement of 3 and (f) Under visible of plasmon resonance at 560 nm with strong E-field enhancement of 18..... 99

Figure 4.18. Electromagnetic simulations for the incident angle-dependent absorption of plasmonic NPs–ZnO NWs hybrids show the efficient absorption of the nanowire morphology with tiled-angle: (a) AgNP-ZnO NWs and (b) AuNP-ZnO NWs. 102

Figure 5.1. (a) Schematic design of the Al-PA with definition of a unit cell and parameters: periodicity (lattice constant) *p*, diameter of Al disk resonator *d* and insulator thickness *t*. The incident electromagnetic fields propagate along the z axis and the electric field is parallel to the x axis. (b) Simulated spectra of a typical Al-PA with p = 4.4 μm, d = 3.3 μm, and t = 0.2 μm, show the absorption efficiencies of the two resonance peaks at 4.16 μm and 8.65 μm with their absorption efficiencies were 97 % and 100 %, respectively..... 108

Figure 5.2. (a) Dielectric functions of common plasmonic materials (Au and Ag) and lossy metallic Al and W and (b) Their perfect absorption properties. 110

Figure 5.3. Simulated optical properties of the designed Al-PA. (a) The size-dependent resonance frequencies of resonator of the Al-PA. The periodicity of the Al-PA was fixed at 4.4 μm. (b) The periodicity-dependent resonance frequencies of the Al-PA. The resonator of Al-PA was fixed at 3.3 μm. (c) The polarization-independent resonance frequencies of the Al-PA. (d) Slightly red-shift of Al-PAs spectra by increasing the thickness of Al resonator. The periodicity, diameter and the thickness of insulator layer were 4.4 μm, 3.3 μm and 0.2 μm, respectively for the both (c) and (d). 111

Figure 5.4. (a-c) and (d-f) Electromagnetic field distributions in Al-PA structure under polarized excitation at magnetic resonance at SP-photonic coupling mode (4.26 μm) and magnetic mode (8.65 μm), respectively. The electric fields propagate along *Z* axis and oscillate in *X* direction. The electromagnetic incident fields were normalized to 1..... 112

Figure 5.5. Wide-range tunability of the Al-PAs. (a) Simulated the dependence of the absorption efficiency on the isolator thickness in the case where p = 4.4 μm, r = 3.3 μm. The dashed oval shows highest absorption efficiency corresponding to the insulator thickness of about 200 nm. (b) Simulated the tunable resonance frequencies at magnetic mode ranging from 0.5 – 9 μm by tuning the size of Al disk with the suitable periodicity - p (or suitable PS spheres with variable diameters ranging from 0.2 μm to 4.4 μm,) and isolator thickness t..... 113

Figure 5.6. Illustration of the fabrication process. (a) Sputtered Al-Al_2O_3-Al film on a Si (100) substrate. (b) Self-assembled monolayer of PS spheres in close-packed hexagonal arrays. (c) Shrank PS mask after the RIE process with oxygen. (d) Final structure of the device after RIE of Al top layer and removal of the PS mask..... 114

Figure 5.7. (a-c) SEM images of PS at different etching time. The scale bar is 5 μm for each image. (d) Size of PS mask as a function of etching time with the etching rate of about 3.1 nm/ second. 115

Figure 5.8. SEM images of three typical fabricated Al-PAs with their resonances as designed: (a) S1 (p = 1.1 μm, d = 0.7 μm, t = 0.05 μm) at 2.85 μm, (b) S2 (p = 3.0 μm, d = 1.7 μm, t = 0.15 μm) at 5.67 μm and (c) S3 (p = 4.4 μm, d = 3.3 μm, t = 0.2 μm) at 8.65 μm. The scale bar is 5 μm for each image. (d) Typical defects of the fabricated samples. The inset in (b) is a photograph of a fabricated Al-PA of 2×3 cm^2. 116

Figure 5.9. (a) Simulated and (b) Measured reflectance spectra of samples S1, S2 and S3 shown in Fig. 5.8. 117

Figure 5.10. Incident angle-dependent resonance spectra of Al-PA. (a) Simulated and (b) Measured results for the case of S3 (p = 4.4 μm, d = 3.3 μm, t = 0.2 μm, magnetic resonance at 8.65 μm)..... 118

Figure 5.11. Al-PA based thermal emitter. (a) Photo and (b) Schematic of an Al-PAs thermal emitter device. (c) Simulated and measured reflectance spectra of an Al-PA designed at magnetic resonance of 7.26 μm (p = 4.4 μm, d = 2.3 μm, t = 0.2 μm). (d) Emission from Al-PA thermal emitter at different temperatures ranging from 75 – 300 °C. 119

Figure 5.12. (a) Simulated and (b) Measured reflectance spectra of the samples S3a-d. (c) Emission spectra of samples S3a-d heated at 250^{o}C. The peak positions of the emissions match to the dips in reflectance spectra. (d-g) SEM images of the fabricated samples S3a-d, respectively. The scale bar is 5 μm for each SEM image. 120

Figure 5.13. Vibrational sensing of BSA molecule adsorbed on Al surface using Al-PAs as a SEIRA substrate. (a) Simulated resonance spectra of Al-PAs with different resonator (p = 3 μm, t = 0.15 μm) in which Al-PAs resonance covered vibrations of molecules. (b) Simulated reflectance of an Al-PA (p = 3 μm, d = 1.9, t = 0.15 μm) with resonance of 6.46 μm for sensing amide-II band of BSA molecule. (c) Reflectance measurement of BSA-adsorbed Al-PA. (d) Vibrational signals of BSA molecules adsorbed on Al planar film with ATR (blue), or on Al planar film (dash red) and Al-PA (sloid red) with normal reflection configurations. 122

Figure 5.14. (a) SEM image of BSA adsorbed on Al-PA shows that BSA molecules are adsorbed on Al-PA surface. There is no molecule at the center of Al disk where Al-Al_2O_3 surface was modified during etching process. (b) Simulated electric field distribution on Al-PA under resonance excitation at magnetic mode -1548 cm^{-1}. 123

Figure 5.15. (a) Schematic of Al-PA using Cu plate. (b) Simulated absorption spectra of Al-PA on Cu plate with different Al resonator for the 3 μm periodicity and 0.15 μm thick Al_2O_3 insulator. 125

Figure 5.16. (a) SEM image of Al-PA on Cu plate, the inset shows a photo of fabricated sample. (b) Reflectance spectra of three fabricated Al-PAs on 0.2 μm Cu plate. 125

Figure 5.17. (a) Schematic of Al holes-Al_2O_3-Al MIM perfect absorber. (b) Simulated spectra of MIM holes Al-PAs with two perfect absorption bands at 3.5 μm and 4.7 μm in case 3 μm periodicity, 1.8 μm Al hole size, 0.7 μm thick insulator, and 0.1 μm thick top and bottom Al layers. 126

Figure 5.18. (a) Simulated absorption spectra of MIM holes Al-PAs with variable of periodicity p and Al holes sizes (d = 0.6p). Thicknesses of top and bottom Al layers were 0.1 μm, and thickness of insulator was 0.7 μm. (b) Simulated reflectance spectra of three MIM holes Al-PAs with resonances ranging from VIS to MIR regions. Parameters of these three Al-PAs are: PA1 p = 0.5 μm, d = 0.38

μm, t = 0.11 μm; PA2 p = 1.1 μm, d = 0.77 μm, t = 0.3 μm; and PA3 p = 3 μm, d = 1.8 μm, t = 0.7 μm. 127

Figure 5.19. Illustration of fabrication process of MIM holes Al-PAs. (a) SAM of PS sphere on layered Al_2O_3-Al films. (b) RIE process to reduce PS mask size. (c) E-beam or thermal deposition of top Al layer. (d) Forming of MIM holes Al-PAs by removing PS mask. 128

Figure 5.20. SEM images of four fabricated MIM holes Al-PAs. (a) S1: p = 3 μm, d = 2.5 μm, t = 0.7 μm. (b) S2: p = 3 μm, d = 2.2 μm, t = 0.7 μm. (c) S3: p = 3 μm, d = 1.9 μm, t = 0.7 μm. (d) S4: p = 3 μm, d = 1.65 μm, t = 0.7 μm. (e) and (f) Typical defects in fabricated MIM holes Al-PAs. 129

Figure 5.21. (a) Simulated and (b) Measured reflectance of four Al-PAs holes MIM devices. S1: p = 3 μm, d = 2.5 μm, t = 0.7 μm; S2: p = 3 μm, d = 2.2 μm, t = 0.7 μm; S3: p = 3 μm, d = 1.9 μm, t = 0.7 μm; S4: p = 3 μm, d = 1.65 μm, t = 0.7 μm. 130

Figure 5.22. Proposed broadband perfect absorber for the efficient photocatalysis 130

1. INTRODUCTION

1.1. Motivation and objective

Wide variety of nanomaterials have been developed in the past decades ranging from graphene[1], carbon nanotube[2], fullerene derivatives[3], semiconductor quantum dots[4] to oxide nanowires (NWs)[5], [6] as well as metallic nanoparticles[7]–[10]. Among many applications of these classes of nanomaterials, the central topics related to nanophotonics are nano-bio spectroscopy and solar energy conversion. The interaction between electromagnetic field and the free electrons at metallic interfaces or in sub-wavelength metallic structure leads to an enhanced electromagnetic near-field in a small volume near metal surfaces, forming a new branch of photonics so-called plasmonics.

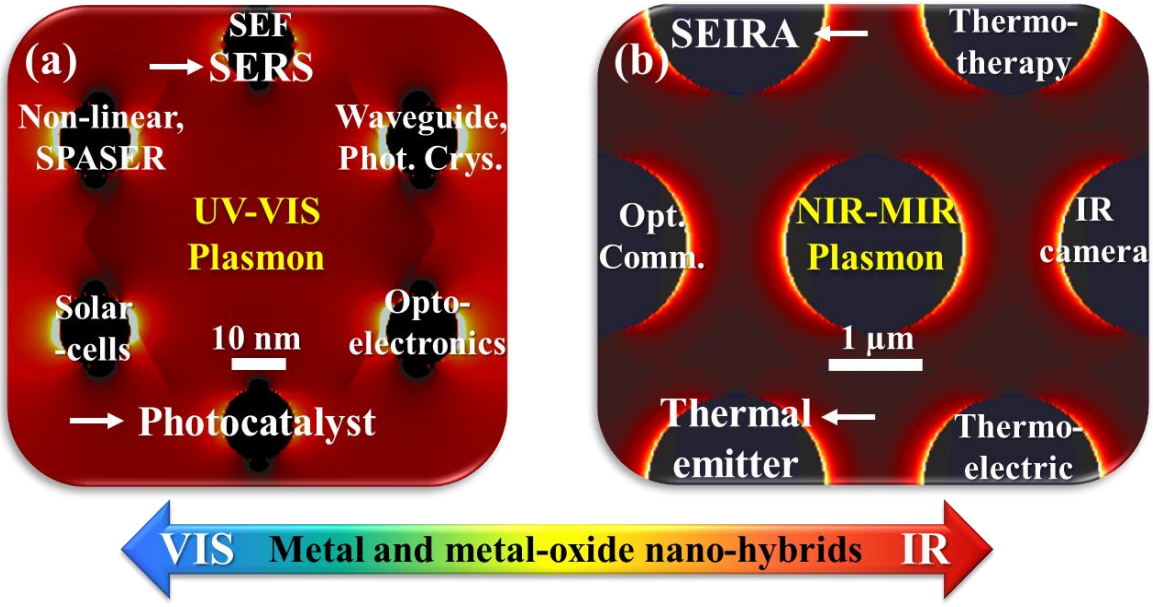

Figure 1.1. Electromagnetic field confinement in plasmonic nano-hybrids and their applications. (a) Applications of UV-VIS plasmonic materials. Background presents enhanced near-field in a UV-VIS plasmonic metal-ZnO nano-hybrid. (b) Applications of NIR-IR plasmonic materials. Background presnts enhanced near-field in an IR aluminum plasmonic perfect absorber composed of metal and metal-oxide. Arrows indicate our works on plasmonic metal/metal-oxide hybrids based: UV-VIS plasmonic hybrids for SERS, photocatalyst, and IR plasmonic hybrids for selective thermal emitter and SEIRA.

Plasmonics creates a major part of the fascinating field of nanophotonics, which explores how electromagnetic fields can be confined in a small volume of subwavelength scale[11]. Because of its unique optical properties in which the optical resonance wavelength of plasmonic structures strongly depends on size, shape and dielectric functions of the metallic materials as well as surrounding medium, plasmonics covers a wide range application from UV-VIS to IR regions. For example, figure 1.1 shows near-field enhancement and their suitable applications of two plasmonic structures which are designed for UV-VIS and IR range. An UV-VIS plasmonic structure can be designed for application in nano-bio spectroscopy such as surface plasmon resonance (SPR) sensing[12], [13], surface-enhanced fluorescence (SEF)[14], surface-enhanced Raman scattering (SERS[15]–[17] or for photoelectric conversion application such as plasmonic solar-cell[18] and plasmonic photocatalysis[19], [20]. While an IR plasmonic structure can be designed for the application in surface-enhanced infrared absorption spectroscopy (SEIRA)[21]–[25] or photothermal and selective thermal emitters devices[26].

This dissertation is aimed to study the effect of light confinements in plasmonic metal and metal-oxide hybrids that can promote strong light-matter interaction and thus lead to the high near-field intensity and high optical density in plasmonic hybrid structures. The suitable plasmonic hybrids for applications in high-sensitivity molecular sensing, efficient photoelectric devices as well as the selective thermal emitters are investigated using electromagnetic simulation and spectroscopic measurement. This study is also devoted to investigate the combination of plasmonic nano-structures and metal-oxide semiconductors or dielectrics where the synergy effects can be gained in photoelectric transfer and thermal energy conversion.

1.2. An overview of the dissertation

The structure in this dissertation is organized as follows:

In Chapter 2, first basic aspects of nanophotonics and plasmonics will be described such as propagation properties of surface plasmon polaritons on the surfaces of planar metallic thin films and localized-surface plasmons in the nano-hybrids. Some technical aspects of numerical simulations to study the interaction of electromagnetic fields to metallic nanostructures as well as metal-dielectric nano-hybrids are explained. Some examples from the preceding works in the field of nano-bio sensing and energy conversion are included in this part.

In Chapter 3, we demonstrate the plasmon-enhanced spectroscopic sensing. The SERS and SEIRA spectroscopic studies were performed and numerically verified. In the SERS study, suspended bow-tie antenna supported on dielectric pillars were designed to improve the field enhancement by reducing the dielectric screening from the substrate, and the plasmonic responses in UV-VIS region were demonstrated by choosing aluminum (Al) as plasmonic metal. Al is an inexpensive base metal and in our study, it showed that Al performs similar to noble metals. In the SEIRA study, *in situ* experiments were used to control the nanogaps between random gold nano-islands and gold-patchy SiO_2 core-shell particles to engineer multiple hot-spots in IR region for enhancing the vibrational absorption of molecules. In the experiment, the *in situ* infrared sensing using these structures showed detection limit in the nanomolar (10^{-9} M) region for bio molecules and sub-nanomolar detection limit for mercury ions in water.

In Chapter 4, we present the chemical fabrications and characterizations of ZnO NWs and TiO_2 thin films, and demonstrate the composites of n-type ZnO NWs and p-type TiO_2 forming p-n core-shell heterojunction structures. The nano-hybrid structure exhibited highest photocurrent ever reported for ultraviolet illumination due to enhanced light scattering and

charge separations at the ultrathin core shell p-n junctions. To further investigate the synergy effect of oxide nanowires and plasmonic structures, we studied the coupling between the ZnO NWs and Ag or Au nanoparticles under electromagnetic field excitation to promote efficient electronic excitations in the vicinity of the metal-ZnO interfaces. It was found that, the electric field was extremely enhanced at the ZnO-particle interface, and this concentrated plasmonic electric field can act as efficient source of plasmonic hot-electrons injecting into the conduction band of the ZnO catalyst. Photodegradation and photoelectrochemical cell experiments performed on these structures verified the enhancement of the catalytic activity in visible region which formed a promising basis for the applications in solar energy conversion.

Finally, Chapter 5 presents our development on the plasmonic metamaterial perfect absorbers (PAs) based on metal-dielectric-metal (MIM) structures with top layer being disks or holes arrays using Al. Our original fabrication approach combined scalable colloidal lithography and reactive ion etching, which enabled easy large-area fabrication and offered wide-range tunability of the absorption wavelengths from VIS to mid-infrared (MIR) regions. The fabricated PAs have narrowband absorption (bandwidth ~ 0.5 - 0.75 μm) with efficiency as high as 98 %. Our demonstration of using Al for MIR PAs indicated that Al can be used as a cost-effective alternative plasmonic material even for other IR plasmonic devices. As an extension of this study, we also demonstrated the broadband PAs in visible range and possible applications include plasmonic photocatalytic activities by adopting a metal oxide semiconductor film between the top and bottom metallic layers.

Finally, in Chapter 6, we conclude with the brief summary of work presented in the dissertation.

2. PLASMONICS AND NEAR-FIELD ENHANCEMENT IN PLASMONIC NANO-HYBRIDS

This chapter introduces the fundamental concepts of plasmonics[11] and exemplifies the near-field enhancement in various plasmonic nanostructures. The first section presents optical properties of metal, including plasmon and dielectric function of the free electron gas, the excitations of the surface plasmon polaritons (SPPs) at metal-dielectric interfaces and the localized-surface plasmons (LSPs) in metallic nanostrutures. The electromagnetic simulations of plasmonic nanostructures, including the rigorous coupled-wave analysis (RCWA) and the finite-difference time-domain (FDTD) methods, are described in this section. In the second section, we demonstrate optical properties and near-field enhancement of several plasmonic nano-hybrids[27]–[30], which have been applied for enhancing vibrational spectroscopy and photocatalysis.

2.1. Plasmonics

2.1.1. Plasma oscillation in metal and dielectric function the free electron gas

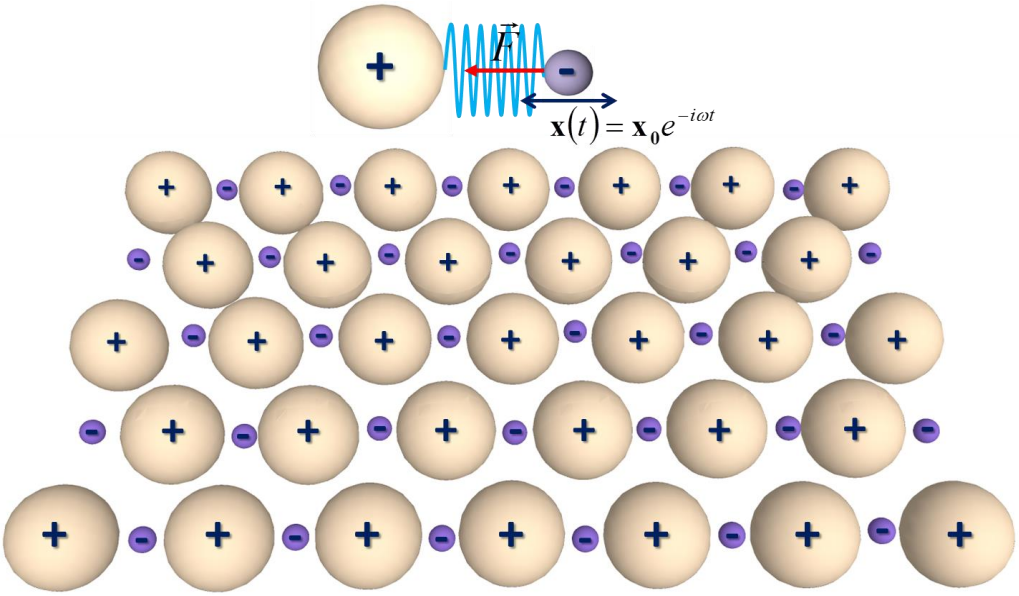

Figure 2.1. Plasma oscillation in metal

I begin this chapter by reviewing the optical properties of metals based on plasma model (Drude model). In this model, valence electrons are assumed to be completely detached from their ions to form an electron gas. The free electrons gas with the number density *n* moves against a fixed background of positive ion cores (Fig. 2.1). In the plasma model, details of the lattice potential and electron-electron interactions are not taken into account.[11] One can write a simple equation of motion for an electron for the displacement **x** of the plasma sea subjected to an external electric field **E** polarized along x-axis[11]:

$$m\ddot{\mathbf{x}} + m\gamma\dot{\mathbf{x}} = -q\mathbf{E}(t) = -q\mathbf{E_0}e^{-i\omega t} \tag{2.1}$$

where m is effective optical mass of each electron, γ is a characteristic collision frequency known as the coefficient of friction damping force of the medium, q is the element charge of electron, ω is the frequency of electromagnetic field, and $\mathbf{E_0}$ is amplitude of the driven electric field. The solution of this equation describes the oscillation of electron:

$$\mathbf{x}(t) = \mathbf{x_0}e^{-i\omega t} \tag{2.2}$$

then Eq. 2.1 can be written:

$$\mathbf{x}(t) = \frac{q}{m(\omega^2 + i\gamma\omega)}\mathbf{x_0}e^{-i\omega t} \tag{2.3}$$

Therefore, the displaced electrons gas contribute to the polarization $\mathbf{P} = -nq\mathbf{x}$, where n is the number of electron per volume (electron density), is given by:

$$\mathbf{P} = -\frac{nq^2}{m(\omega^2 + i\gamma\omega)}\mathbf{E} \tag{2.4}$$

The dielectric displacement **D** can be written by:

$$\mathbf{D} = \varepsilon_0 \mathbf{E} + \mathbf{P} = -\varepsilon_0 \left(1 - \frac{nq^2}{\varepsilon_0 m} \frac{1}{(\omega^2 + i\gamma\omega)} \right) \mathbf{E} \tag{2.5}$$

or:

$$\mathbf{D} = \varepsilon_0 \left(1 - \frac{\omega_p^2}{\omega^2 + i\gamma\omega} \right) \mathbf{E} \tag{2.6}$$

Where $\omega_p = \left(\frac{nq^2}{\varepsilon_0 m} \right)^{1/2}$ is the plasma frequency of the free electron gas, or quantization of plasma oscillation energy which is so-called "plasmon", and ε_0 is the permittivity of vacuum. Thus the dielectric function at different electromagnetic frequencies can be written as the:

$$\varepsilon(\omega) = 1 - \frac{\omega_p^2}{\omega^2 + i\gamma\omega} \tag{2.7}$$

The real and imaginary components of this complex dielectric function $\varepsilon(\omega) = \varepsilon_1(\omega) + i\varepsilon_2(\omega)$ are given by:

$$\varepsilon_1(\omega) = 1 - \frac{\omega_p^2}{(\omega^2 + \gamma^2)} \tag{2.8a}$$

$$\varepsilon_2(\omega) = 1 - \frac{\omega_p^2 \gamma}{\omega(\omega^2 + \gamma^2)} \tag{2.8b}$$

It is noted that the collision frequency is inversed to the relaxation time τ of the free electron gas ($\gamma = \frac{1}{\tau}$). At high frequencies close to ω_p, the product $\omega\tau >> 1$, the dielectric function is predominantly real:

$$\varepsilon_1(\omega) = 1 - \frac{\omega_p^2}{\omega^2} \tag{2.9}$$

can be taken as the dielectric function of the undamped free electron gas. As seen from Eq. 2.9, when $\omega < \omega_p$, dielectric function of metals is negative and the metals become reflection as a metallic property. In a contrast, when $\omega > \omega_p$, dielectric function of metals is positive and the metals become transparent as dielectrics.

It should be noted that the description above has assumed an ideal free-electron metal, now we consider to expand the model to the real metals like Au, Ag, Al, which are often used in plasmonics. For these coinage metals, in the region $\omega > \omega_p$ (where the response is dominated by free s electrons), the d band closed to the Fermi surface causes a highly polarized environment. It is due to the positive background of the ion cores can be described by adding $\mathbf{P}_\infty = \varepsilon_0(\varepsilon_\infty - 1)\mathbf{E}$ (where $1 < \varepsilon_\infty < 10$) to the right of Eq. 2.5, then the dielectric function of metals can be written as:

$$\varepsilon(\omega) = \varepsilon_\infty - \frac{\omega_p^2}{\omega^2 + i\gamma\omega} \tag{2.10}$$

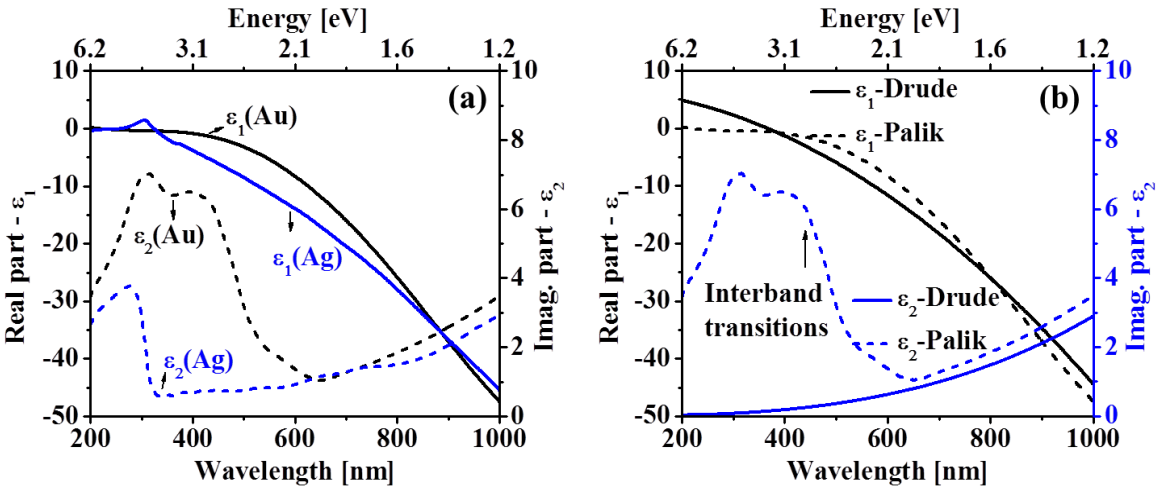

Figure 2.2. (a) Dielectric functions of Au and Ag[31]. (b) Comparison between Drude model ($\varepsilon_\infty = 6.9$, $\omega_p = 8.9$, $\gamma = 0.07$)[32], [33] and experiment data[31] of dielectric function of Au with interband transitions region.

However, this expanded dielectric function of metals cannot express the interband transitions, which can be fully described by the extended Lorentz-Drude model. Figures 2.2a plots the measured dielectric functions of Au and Ag taken from literature [31]. As seen that, both Au and Ag have the interband transitions (see imaginary parts, dash curves in Fig. 2.2a) at short-wavelength region (high energy). As a comparison shown in Fig. 2.2b, a plotted Durde modal for free electrons in Au with $\varepsilon_\infty = 6.9$, $\omega_p = 8.9$, $\gamma = 0.07$ does not express the interband transition of Au.

2.1.2. Surface plasmon wave

2.1.2.1. Surface plasmon-polariton propagation at metal-dielectric interface

We start from Maxwell's equation of macroscopic electromagnetism:

$$\nabla \cdot \mathbf{D} = \rho_{ext} \tag{2.11}$$

$$\nabla \cdot \mathbf{B} = 0 \tag{2.12}$$

$$\nabla \times \mathbf{E} = -\frac{\partial \mathbf{B}}{\partial t} \tag{2.13}$$

$$\nabla \times \mathbf{H} = \mathbf{J}_{ext} + \frac{\partial \mathbf{D}}{\partial t} \tag{2.14}$$

where **D** is the dielectric displacement, **B** is the magnetic induction or magnetic flux density, **E** is the electric field, **H** is the magnetic field, and with the external charge ρ_{ext} and current densities $\mathbf{J}_{ext}$. In isotropy, linear and nonmagnetic media, the constitutive relations can be written:

$$\mathbf{D} = \varepsilon_0 \varepsilon \mathbf{E} \tag{2.15}$$

$$\mathbf{B} = \mu_0 \mu \mathbf{H} \tag{2.16}$$

where ε_0 and μ_0 are the permittivity and permeability of vacuum, respectively. In the absence of external charge and current densities, by combining of Eq. 2.13 and Eq. 2.14 we can write:

$$\nabla \times \nabla \times \mathbf{E} = -\mu_0 \frac{\partial^2 \mathbf{D}}{\partial t^2} \tag{2.17}$$

or can be simplified as:

$$\nabla^2 \mathbf{E} - \frac{\varepsilon}{c^2} \frac{\partial^2 \mathbf{E}}{\partial t^2} = 0 \tag{2.18}$$

We assume in all generality a harmonic time dependence of the electric field $\mathbf{E}(\mathbf{r},t) = \mathbf{E}(\mathbf{r})e^{-i\omega t}$, then the Eq. 2.18 yields the Helmholtz equation:

$$\nabla^2 \mathbf{E} + k_0^2 \varepsilon \mathbf{E} = 0 \tag{2.19}$$

where $k_0 = \frac{\omega}{c}$ is the wave vector of the propagating wave in vacuum. Then, we consider to the propagation geometry of the electromagnetic waves propagating at the interface between two different materials. We assume for simplicity the propagation is only along x-direction of a Cartesian coordinate system and there is no spatial variation in the perpendicular, in-plane y-direction. Thus, this is a one dimensional problem and the dielectric constant ε depends only on one spatial coordinate z, $\varepsilon = \varepsilon(z)$. Applying to electromagnetic surface problems, the plane $z = 0$ coincides with the interface sustaining the propagating surface waves, which can described as $\mathbf{E}(x,y,z) = \mathbf{E}(z)e^{i\beta x}$. The complex parameter $\beta = k_x$ is called the propagation constant of the traveling surface waves and corresponds to the component of the wave vector in the direction of propagation. Inserting this expression into Eq. 2.19 yields the desired form of the wave equation:

$$\frac{\partial^2 \mathbf{E}(z)}{\partial z^2} + \left(k_0^2 \varepsilon - \beta^2\right)\mathbf{E} = 0 \tag{2.20}$$

For harmonic time dependence ($\frac{\partial}{\partial t} = -i\omega$), and for propagation along the x-direction ($\frac{\partial}{\partial x} = i\beta$), homogeneity in the y-direction ($\frac{\partial}{\partial y} = 0$), we can get the following set of coupled equations:

$$\frac{\partial E_y}{\partial z} = -i\omega\mu_0 H_x \tag{2.21a}$$

$$\frac{\partial E_x}{\partial z} - i\beta E_z = i\omega\mu_0 H_y \tag{2.21b}$$

$$i\beta E_y = i\omega\mu_0 H_z \tag{2.21c}$$

$$\frac{\partial H_y}{\partial z} = i\omega\varepsilon_0\varepsilon E_x \tag{2.21d}$$

$$\frac{\partial H_x}{\partial z} - i\beta H_z = -i\omega\varepsilon_0\varepsilon E_y \tag{2.21e}$$

$$i\beta H_y = -i\omega\varepsilon_0\varepsilon E_z \tag{2.21f}$$

These six equations allow two sets of self-consistent solutions with different polarization properties of the propagating waves. The first set are the transverse magnetic (TM) modes, where only the field components E_x, E_z and H_y are nonzero, and the second set is the transverse electric (TE) modes, with only H_x, H_z and E_y being nonzero.

For TM modes, the system of governing Eq. 2.21 reduces to:

$$E_x = -i\frac{1}{\omega\varepsilon_0\varepsilon}\frac{\partial H_y}{\partial z} \tag{2.22a}$$

$$E_z = -\frac{\beta}{\omega\varepsilon_0\varepsilon}H_y \tag{2.22b}$$

And the wave equation for TM modes is:

$$\frac{\partial^2 H_y}{\partial z^2} + \left(k_0^2\varepsilon - \beta^2\right)H_y = 0 \tag{2.22c}$$

For TE modes the analogous set is

$$H_x = i\frac{1}{\omega\mu_0}\frac{\partial E_y}{\partial z} \tag{2.23a}$$

$$H_z = \frac{\beta}{\omega\mu_0}E_y \tag{2.23b}$$

with the TE wave equation:

$$\frac{\partial^2 E_y}{\partial z^2} + \left(k_0^2\varepsilon - \beta^2\right)E_y = 0 \tag{2.23c}$$

Based on these equations, we can find the solutions of propagating wave of the surface plasmon polaritons confined to the $z = 0$ interface. The most simple geometry sustaining surface plasmon polaritons (SPPs) is the materials of upper half space ($z > 0$, illustration Fig. 2.3a) should be dielectric and non-absorbing with positive real dielectric constant ε_d, while the materials of lower half space ($z < 0$, illustration Fig. 2.3a) is required to be a metallic character with negative real part of the dielectric constant ε_m ($\mathrm{Re}[\varepsilon_m] < 0$). For metals, this condition is fulfilled at frequencies below the bulk plasmon frequency ω_p. We want to consider the propagating wave solutions confined to the interface, i.e. with evanescent decay in the perpendicular *z*-direction.

We first look at TM mode solutions. Using the equation set (2.22) in both half spaces yields, for $z > 0$:

$$H_y(z) = A_d e^{i\beta x} e^{-k_d z} \tag{2.24a}$$

$$E_x(z) = iA_d \frac{1}{\omega\varepsilon_0\varepsilon_d} k_d e^{i\beta x} e^{-k_d z} \tag{2.24b}$$

$$E_z(z) = -A_d \frac{\beta}{\omega\varepsilon_0\varepsilon_d} e^{i\beta x} e^{-k_d z} \tag{2.24c}$$

and for $z < 0$:

$$H_y(z) = A_m e^{i\beta x} e^{-k_m z} \tag{2.25a}$$

$$E_x(z) = iA_m \frac{1}{\omega\varepsilon_0\varepsilon_m} k_m e^{i\beta x} e^{-k_m z} \tag{2.25b}$$

$$E_z(z) = -A_m \frac{\beta}{\omega\varepsilon_0\varepsilon_m} e^{i\beta x} e^{-k_m z} \tag{2.25c}$$

Here, k_m and k_d are the components of the wave vectors perpendicular to the interface in the metal and dielectric media, respectively. Its reciprocal value, $\hat{z} = 1/|k_z|$, defines the evanescent decay length of the fields perpendicular to the interface which quantifies the confinement of the wave. By applying the boundary conditions at $z = 0$ interface, continuity of H_y and $\varepsilon_{m,d} E_z$ requires that $A_m = A_d$ and:

$$\frac{k_d}{k_m} = -\frac{\varepsilon_d}{\varepsilon_m} \tag{2.26}$$

It should be noted that with our convention of the signs in the exponents in equation set 2.24 and 2.25, confinement to the surface demands $\mathrm{Re}[\varepsilon_m] < 0$ if $\varepsilon_d > 0$, the surface waves exist only at interfaces between materials with opposite signs of the real part of their permittivities, i.e. between a conductor and an insulator, the expression for H_y further has to fulfil the wave Eq.2.22c, yielding:

$$k_m^2 = \beta^2 - k_0^2 \varepsilon_m \tag{2.27a}$$

$$k_d^2 = \beta^2 - k_0^2 \varepsilon_d \tag{2.27b}$$

Based on Eq.2.26 and equation set 2.27, we obtain the dispersion relation of SPPs propagating at the interface between the two half spaces:

$$k_x = \beta = \frac{\omega}{c} \sqrt{\frac{\varepsilon_m \varepsilon_d}{\varepsilon_m + \varepsilon_d}} \tag{2.28}$$

Now we briefly analyse the possibility of TE surface modes, the respective expressions for the field components are:

$$E_y(z) = A_d e^{i\beta x} e^{-k_d z} \tag{2.29a}$$

$$H_x(z) = -iA_d \frac{1}{\omega\mu_0} k_d e^{i\beta x} e^{-k_d z} \tag{2.29b}$$

$$H_z(z) = A_d \frac{\beta}{\omega\mu_0} e^{i\beta x} e^{-k_d z} \tag{2.29c}$$

for $z > 0$, and:

$$E_y(z) = A_m e^{i\beta x} e^{-k_m z} \tag{2.30a}$$

$$H_x(z) = iA_m \frac{1}{\omega\mu_0} k_m e^{i\beta x} e^{-k_m z} \tag{2.30b}$$

$$H_z(z) = A_m \frac{\beta}{\omega\mu_0} e^{i\beta x} e^{-k_m z} \tag{2.30c}$$

for $z < 0$. Continuity of E_y and H_x at the interface requires the condition to be satisfied:

$$A_m(k_m + k_d) = 0 \tag{2.31}$$

Since confinement to the surface requires $\mathrm{Re}[k_m] > 0$ and $\mathrm{Re}[k_d] > 0$, this condition is only fulfilled if $A_m = 0$, so that also $A_d = A_m = 0$. Thus, no surface modes exist for TE polarization. Surface plasmon polaritons only exist for TM polarization.

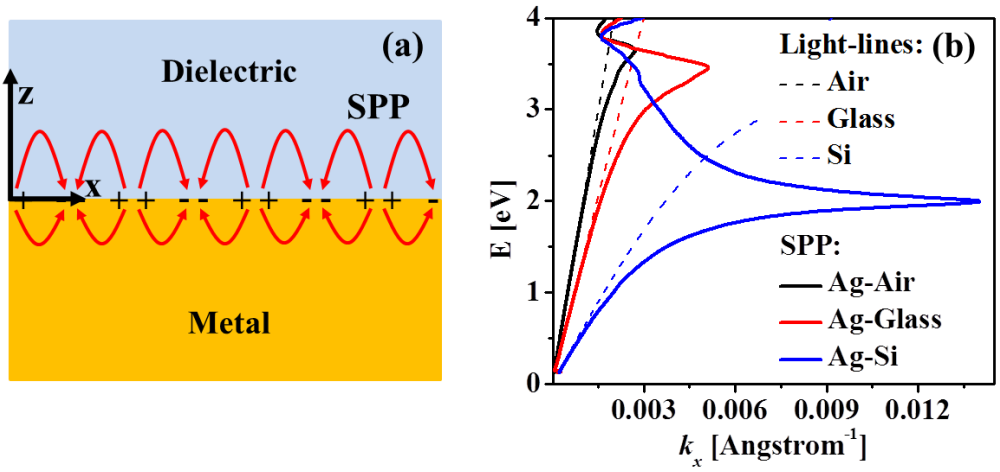

Figure 2.3. (a) Geometry for SPP propagation at metal-dielectric interface. (b) Dispersion relation of the fundamental coupled SPPs at different interfaces of Ag and dielectrics of air, glass, and Si.

Now we can examine the properties of SPPs by using Eq.2.28. Figure 2.3a shows the schematic for surface plasmon polaritons propagation at an interface between metal and dielectric materials. Figure 2.3b plots the dispersion relation of SPPs at the interfaces between an Ag film with several dielectrics, including air, glass and Si. The dielectric functions of the materials were taken from literature[31]. For small wave vectors corresponding to low (mid-infrared or lower) frequencies, the SPP propagation constant is close to k_0 at the light line (has slope equal to $c/\sqrt{\varepsilon_d}$). In this regime, SPPs acquire the nature of a grazing-incidence light field, also known as Sommerfeld-Zenneck wave. However, for the large wave vectors, the frequency of the SPPs approaches the characteristic surface plasmon frequency (when $\varepsilon_m = -\varepsilon_d$):

$$\omega_{sp} = \frac{\omega_p}{\sqrt{1+\varepsilon_d}} \tag{2.32}$$

Surface plasmon polaritons can be excited by the electron or optical beams. However optical excitation of the SPPs on a flat metal-dielectric interface cannot be excited directly by light beams since the SPPs dispersion curve lies entirely below that of free space light in the dielectric, such that $k_{sp} = k_x = \beta > k$, where k is the wave vector of light on the dielectric side of the interface. It requires the conservation of momentum (wave vector) parallel to the surface (phase-matching). To satisfy this phase-matching, several special techniques are employed such as grating coupling or prims coupling configurations. In the prims coupling configuration, also known as attenuated total internal reflection, involves the coupling of the SPPs to the evanescent electromagnetic field that is formed upon total internal reflection of a light beam on an interface. There are three different configurations for prism coupling, including Otto configuration, Kretschmann (or Kretschmann-Raether) configuration, and the mixed hybrid arrangement of these two prisms coupling configurations[34], [35], [11].

2.1.2.2. Kretschmann configuration for optical excitation of SPPs

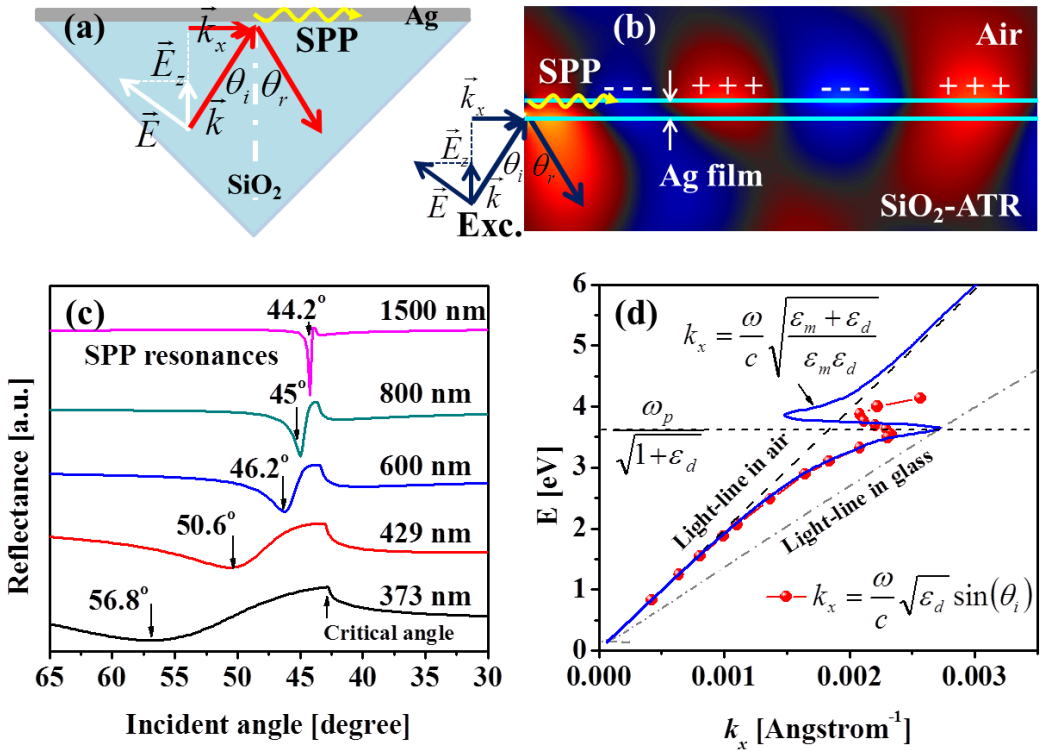

Figure 2.4. (a) Kretschmann configuration for optical excitation of SPP propagation at metal-dielectric interface. (b) Simulated electric field of SPP propagated along Ag-air interface at resonant excitation of 600 nm under incident angle of 46.2°. (c) Simulated SPP resonant spectra of Ag-air interface under different wavelength excitations. (d) Dispersion relation of the coupled SPP mode at Ag-air interface plotted using Kretschmann configuration and a comparison with the fundamental coupled SPP.

The in-plane momentum $k_x = k\sin\theta$ of the excited photon with incident angle of θ to the interface normal is always smaller than the SPPs propagation constant β, even at grazing incidence, prohibiting phase-matching. This mismatch can be overcome by using a well-known prims coupling named Kretschmann configuration (Fig. 2.4a). This configuration consists of a metallic thin film deposited on top of a prism with dielectric function ε_d, and the film is illuminated from the dielectric prism at an incident angle θ_i greater than the angle of total internal reflection. For simplicity, we assume that the dielectric medium on top of metal is air with dielectric function of $\varepsilon = 1$. At a certain incident angle θ_i, the in-plane momentum

along *x*-direction of the excited photon coincides with momentum k_{sp} of SPPs (or SPPs propagation constant β) at metal-air interface, resonance tunnelling of the fields of the excitation beam to the metal-air occurs and light is coupled to the surface polaritons:

$$\beta = k_x = \frac{\omega}{c}\sqrt{\varepsilon_d}\sin\theta \tag{2.33}$$

Under these resonant conditions, a sharp minimum is observed in the reflectivity from the metal-prism interface as light can be coupled to SPPs. The efficiency of the SPPs excitation can be almost 100% of the excited light, and it decreases as the tunnelling distance increases with the increase in metal film thickness. It should be noted that, the SPPs at Ag-glass interface cannot be excited by Kretschmann configuration as the momentum of SPPs at this interface is greater than the momentum of excited light in the prism at all angles of incidence.

For further understanding the surface plasmon polaritions propagating at a metal-air interface, the electromagnetic simulations of SPPs at an Ag-air interface excited via Kretschmann configuration were performed using a commercial software (Rsoft-Synopsys) consisted of two packages, the DiffractMOD based on the RCWA method for calculating diffraction efficiencies, and the FullWAVE based on the FDTD method for simulating the time-dependent field distributions. These simulation methods will be introduced in the subsection 2.1.3. The thickness of Ag film was chosen to 30 nm, it is thin enough for the incident energy to be able to penetrate to the Ag-air interface and excite surface plasmons[36]. The dielectric functions of Ag, glass were taken from literature[31]. As shown in Fig. 2.4c, the SPPs resonances of Ag-air interface were archived at the certain excitations, which satisfy the energy ($\omega = \omega_{sp}$) and momentum ($k_x = k_{sp}$) conservations, resulting in the minimum of the reflectivity from Ag-air interface. As a demonstration, the simulated electric field distribution of the SPPs excited at 2.067 eV (600 nm of wavelength) under the incident angle of 46.2° was carried out as shown

in Fig. 2.4b. It is clearly seen that, by using Kretschmann configuration and under resonance excitation, the SPPs is excited and propagated along Ag-air interface. By plotting the energy-momentum relation using Eq. 2.33 at certain resonant excitations, the SPPs dispersion relations at an Ag-air interface was obtained and in good agreement with the SPPs curve plotted by using Eq. 2.28 as shown in Fig. 2.4d.

2.1.2.3. Localized surface plasmon resonance

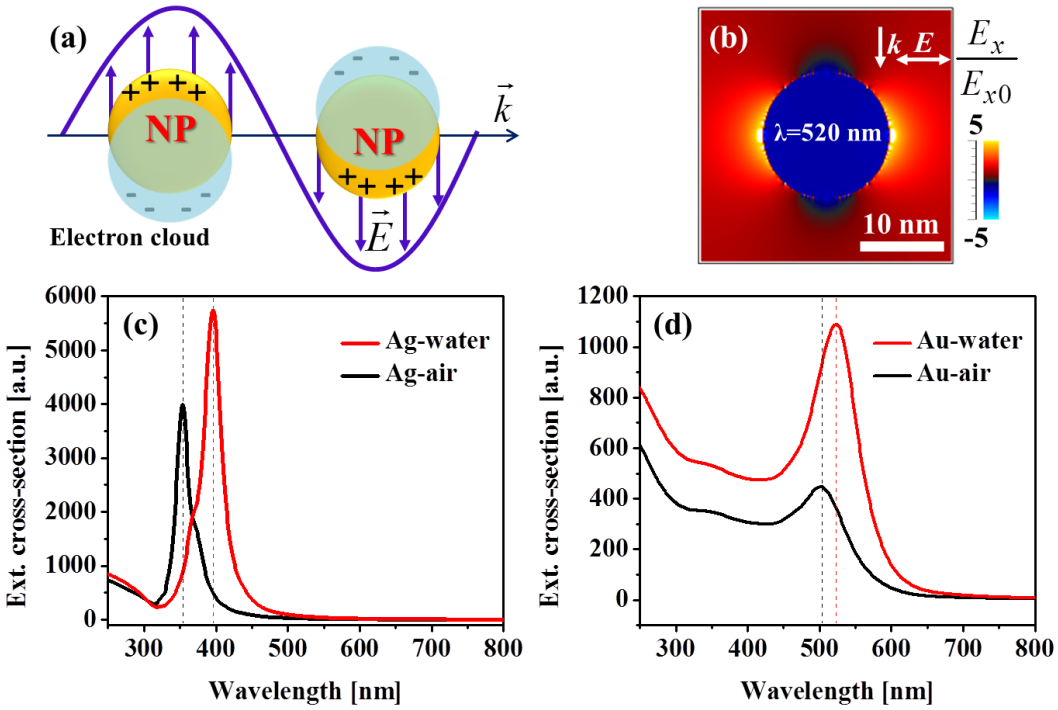

Figure 2.5. (a) Schematic of localized surface plasmon excitation of metallic nanoparticle. (b) Near-field distribution of localized surface plasmon of Au nanoparticle under resonance excitation at 520 nm. Extinction cross-section spectra of metal nanoparticles in different surrounding medium of air and water: (a) Ag nanoparticles and (b) Au nanoparticles.

In the previous section, we have seen the SPPs are propagating wave. Here, in contrast, we introduce the second fundamental excitation of plasmons, the localized surface plasmons (LSPs). The LSPs are non-propagating excitations of the free electrons in in a closed metallic nanostructure coupled to the electromagnetic field. The LSPs arise naturally from the scatter-

ing problem of a small, sub-wavelength conductive nanoparticle in an oscillating electromagnetic field. The roughness and the curved shape of particle surface exerts an effective restoring force on driven electrons (Fig. 2.5a), giving rise to a resonance that amplifies the field both inside and in the near-field zone outside the particle. As an example shown in Fig. 2.5b, the electric field is enhanced by 5 times and confined in a nanometer scale on surface of Au particle excited by an external field (at resonance, 520 nm). Furthermore, the LSPs can be directly excited by light illumination, in contrast to propagating SPPs, where the excitation requires the phase-matching. In addition, the LSPs properties, including absorption, scattering and field enhancement are dependent on the size, shape, and dielectric function of the nanometal and surrounding medium.

The physics of localized surface plasmons in the simple cases such as nanoparticle can be explained by analytical solutions based on Mie theory or quasi-static approximation, etc. For example, the extinction cross-section of metal nanosphere can be given by the dipole absorption:

$$\sigma_{ext}(\omega) = 9\frac{\omega}{c}\varepsilon_d^{3/2}V_0\frac{\varepsilon_2(\omega)}{[\varepsilon_1(\omega)+2\varepsilon_d(\omega)]^2+\varepsilon_2^2(\omega)} \tag{2.34}$$

where V_0 is the sphere particle volume, $\varepsilon_d(\omega)$ and $\varepsilon_m = \varepsilon_1(\omega)+i\varepsilon_2(\omega)$ denote the dielectric functions of the surrounding medium and of the metal nanoparticle, respectively. It is clearly seen that this formula can explain the effect of the surrounding medium. Figures 2.5c-d plot the extinction cross-section spectra of Ag (Fig. 2.5c) and Au (Fig. 2.5d) nanoparticles with diameter of 15 nm in different surrounding mediums of air and water. As seen in Fig. 2.5c, the resonance of Ag nanosphere can be red-sifted from 355 nm to 385 nm when the surrounding medium changes from air (lower dielectric constant) to water (higher dielectric constant). While the resonance of Au nanosphere is located at longer wavelength of 510 nm in air, and

it is also red-shifted to 520 nm in water. This property of nanometal can be used for refractive index sensing so-called SPR sensing.[10], [12], [13], [37]

Because of the unique optical properties, including the extremely near-field enhancement, absorption and scattering (extinction) enhancement, directly excited by light illumination, size and shape dependence, the LSPs plasmonic nanostructures can provide great variety of applications in many fields in optics and photonics. However, many plasmonic applications required complicated plasmonic structures and they cannot be explained by simple analytical solutions. Thus the numerical simulations are required, and several methods have been developed and imported in the commercial software as we will describe in the next subsection.

2.1.3. Electromagnetic simulations of plasmonic nanostructures

The solution of Maxwell's equations for a problem of the plasmonic structure lets us know the interaction between plasmonic structure with electromagnetic field as well as plasmonic properties of metal nanostructure. However, most of plasmnonic nanostructures are complicated and we cannot find analytical solution in the entire problem (structure) domain. Therefore, numerical simulation methods are the only choices when they can split the problem (plasmonic structure) into smaller domains or pieces (discretization). There are many numerical methods for solving Maxwell's equations such as the discrete dipole approximation (DDA), the finite element method (FEM), the method of moments (MoM), the rigorous coupled-wave analysis (RCWA), and the finite-difference time-domain (FDTD). In general, they can be classified into two classes: frequency-domain methods and time-domain methods. In this section, we briefly introduce the RCWA (frequency-domain) and FDTD (time-domain) methods, which are used for simulating the plasmonic structures in this dissertation. The electromagnetic simulations are performed using a commercial software (Rsoft-Synopsys)[38]

with two packages, including the DiffractMOD and the FullWAVE, which are based on the RCWA and the FDTD methods, respectively.

2.1.3.1. Rigorous coupled-wave analysis (RCWA)

Rigorous coupled-wave analysis (RCWA) is a numerical method in electromagnetic simulations that is mostly applied to solve scattering from periodic structures through rigorously solving Maxwell's equations. The DiffractMOD package based on the RCWA method has been enhanced with modal transmission line (MTL) theory and fast Fourier factorization (FFF), making it as a powerful software, easy to use tool (incorporated with a CAD layout) for design and analysis 2D or 3D periodic structure such as photonic bandgap crystal, grating-assisted or plasmon-assisted devices [38], [39].

RCWA represents the electromagnetic fields as a sum over coupled waves. A periodic permittivity function is represented using Fourier harmonics. Each coupled wave is related to a Fourier harmonic, allowing the full vectorial Maxwell's equations to be solved in the Fourier domain (frequency domain). In this frequency domain, by factoring out an assumed time harmonic factor $e^{-i\omega t}$, the time dependence in Maxwell's equations can be easily eliminated and the fields are functions solely of space coordinates. The diffraction efficiencies are then calculated at the end of simulation. The spatial field distributions are derived from the Fourier harmonics. In our work, the RCWA was used for calculation of the diffraction efficiencies of the plasmonic structures, including the transmission, reflection and absorption.

2.1.3.2. Finite-difference time-domain (FDTD)

While the RCWA is based on the frequency domain method, the finite-difference time-domain (FDTD) is a numerical method based on the time-dependent Maxwell's equations. The FullWAVE package based on the FDTD method is a highly sophisticated simulation tool

for studying the propagation of light in a wide variety of photonic structures, especially for producing the time-dependent results of the field in the nanophotonic structures as well as plasmonic devices. The FDTD method is time-tested and stable, and can efficiently handle material dispersion and nonlinearities. Also, because it is based in the time-domain, it can cover a wide frequency range with a single simulation run. Furthermore, FDTD lends itself to cluster computing. This allows the computational demand for a single problem to be shared among several computers on a network, and permits us to simulate problems otherwise impossible on a single computer.

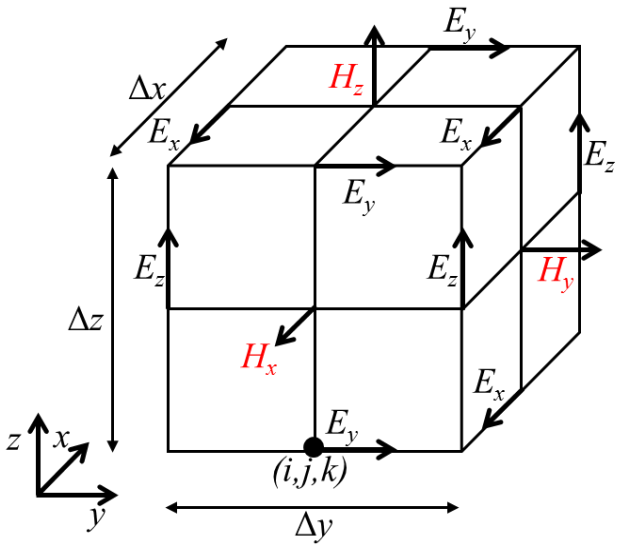

Figure 2.6**.** In a Yee cell of dimension Δx, Δy, Δz. The **E** field components are in the middle of the edges, the **H** field components are in the centre of the faces.[40]

The FDTD method solves Maxwell's equations by first discretizing the equations via central differences in time and space and then numerically solving these equations in software. The most common method to solve these equations is based on Yee's mesh[40] and computes the **E** and **H** field components at points on a grid with grid points spaced Δx, Δy, and Δz apart. The **E** and the **H** field components are then interlaced in all three spatial dimensions as shown in Fig. 2.6. Furthermore, time is divided up into discrete steps of Δt. The **E** field components are then computed at times $t = n\Delta t$ and the **H** fields at times $t = (n+1/2)\Delta t$, where n is an

integer representing the computing steps. For example, the **E** field at a time $t = nt$ is equal to the **E** field at $t = (n-1)\Delta t$ plus an additional term computed from the spatial variation, or curl, of the **H** field at time *t*.[38]

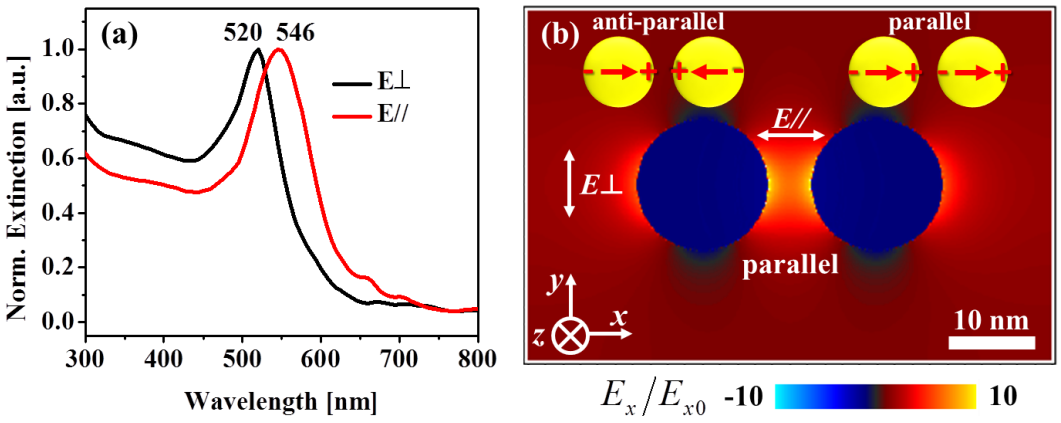

Figure 2.7. Electromagnetic simulation of Au-dimer on glass substrate with Au diameter of 15 nm, gap size of 5 nm, and domain size (periodicity) of 60×40 nm. (a) Simulated extinction of Au-dimer using RCWA with polarization along the dimer axis ($E_{//}$, red), and perpendicular to the dimer axis ($E_{\perp}$, black). (b) Simulated electric field distribution of Au-dimer excited at resonance (546 nm) under parallel polarization (parallel-mode). Insets in (b) show schematic of the charge profile of Au-dimer, parallel dipole (bright-mode) and anti-parallel dipole (dark-mode).

For most periodic structures, the RCWA method implanting in DiffractMOD is faster than FDTD method implanting in FullWAVE. The diffraction efficiencies calculated by RCWA method from DiffractMOD can be combined with the time-dependent results of the field calculated by FDTD (FullWAVE) to fully investigate plasmonic properties of the metal nanostructures. For example, by using RCWA and FDTD, we have numerically stimulated optical properties of gold periodic nano-dimer (Au-dimer), which can act as a plamonic nanogap where the near-field is confined at the gap of Au spheres. The Au-dimer parameters were chosen to be 15 nm for Au sphere diameter, 5 nm for the gap between two Au spheres and 60×40 nm of domain size (periodicity), and sitting on top of a glass substrate. The dielectric function of Au and glass were taken from literature[31]. The simulated results are shown

in Fig. 2.7. As seen in Fig. 2.7a, the extinction spectra of Au-dimer show the polarization dependence, the resonant peak at 520 nm (black) is corresponded to the polarization perpendicular to the dimer axis, it is almost similar to the extinction spectrum of the individual Au sphere particle. In contrast, when the polarization is along the dimer axis, the Au-dimer supports both parallel and anti-parallel dipole modes due to hybridization between dipole modes of the two identical plasmonic nanoparticles[41]–[48] . The schematic of the charge profile of Au-dimer indicating two dipole modes are shown in the insets of Fig. 2.7b. It would be noted that the anti-parallel mode cannot be excited by a plane wave, this is so-called dark-mode, while the parallel mode (bright-mode) shows resonant extinction at 546 nm, and it is red-shifted compared to the perpendicular polarization case. In particular, due to the coupling between two Au particles, the bright-mode gives rise to a highly near-field enhancement in the gap of Au-dimer. Figure 2.7b shows the electric field distribution of Au-dimer under excitation of bright mode. The electric field enhancement was found to be 10 time, it is far higher compared to the single AuNP as shown in Fig. 2.5b. Thus, this simple plasmonic nanogap Au-dimer with strong hot-spot has extensive application such as surface-enhanced spectroscopy[49] or plasmon-enhanced nonlinear process[50]. We will discuss in more detail this plasmonic nanogap in another dimer structure composed of two triangles in Chapter 3.

2.2. Plasmonic nanostructures for sensing and energy conversion applications

Plasmonic nanostructures have found broad promising applications from biosensing, photocatalysis, metamaterials, to light harvesting devices due to their unique plasmonic properties. In this section, we describe three examples of plasmonic strutures in which their optical properties can be applied for molecular sensing (SERS)[28] and the efficient photocatalysts[29], [30]. The first example introduces optical properties of gold percolated film. The nonlinear dynamic of free electrons in this gold percolate film induced by intense THz electromagnetic

field are also discussed[27]. The second example presents one of the well-known structure so called MIM plasmonic metamaterial, which is composed of two gold nano-disks isolated by an oxide insulator. The third example describes the gold nanocages (AuNCs)-TiO_2 hybrids with multiple hot-spots for the plasmon-enhanced photocatalysis application.

2.2.1. Optical properties of percolated gold film and nonlinear electrons dynamic induced by intense THz pulse

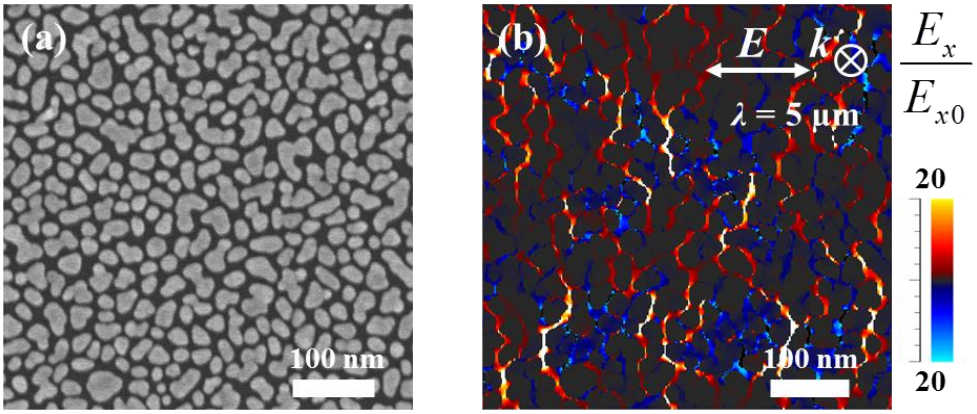

Figure 2.8. (a) SEM image of a percolated Au film with multiple Au-islands. (b) Strong electric field confinement in the gaps between nano-islands

Gold has been extensively studied in the fields of microelectronics and bio-sensing because of its high conductivity and stability. Plasmonic Au nanostructures have been extensively studied over past decades due to their unique plasmonic property. A simple plasmonic nanostructure can provide strong near-field enhancement that is Au nanoparticle as shown in previous section. Depending on the size and shape, the resonance of AuNPs can be tuned from VIS to NIR regions. Here we introduce AuNPs with random size and shape so-called Au-islands which are formed on Au percolated film. As we can see in Fig. 2.8a, an SEM image of Au film composes of random Au-islands is deposited by wet-chemical method. As their size and shape are random, the resonance of Au-islands can be ranged from VIS to MIR with strong field confinement at the gaps between Au-islands. As an example, under excitation at 5 μm, multiple hot-spots at the gaps in Au film can be achieved (Fig 2.8b). This plas-

monic Au film with multiple gaps can be applied for surface-enhanced spectroscopy such as *in situ* SEIRA, which will be introduced in Chapter 4.

The optical properties of plasmonic nanostructures are dependent on the dynamics of free electrons in metals, i.e. they are affected by the intense electromagnetic fields. For example, free electron in Au NPs or Au film can be accelerated by intense THz pulse, resulting in non-linear dynamic response of free electrons, and therefore, the plasma frequency and damping constant of metals can be changed. Recently, nonlinear dynamics of free electrons in Au films and percolated films were observed[27], [51]. It was found that, by applying an intense THz pulse (maximum of 284 kV/cm), the plasma frequency of electrons is slight increased and the damping constant is significantly decreased, resulted in a the nonlinear decrease of the transmittance of Au film.[27]

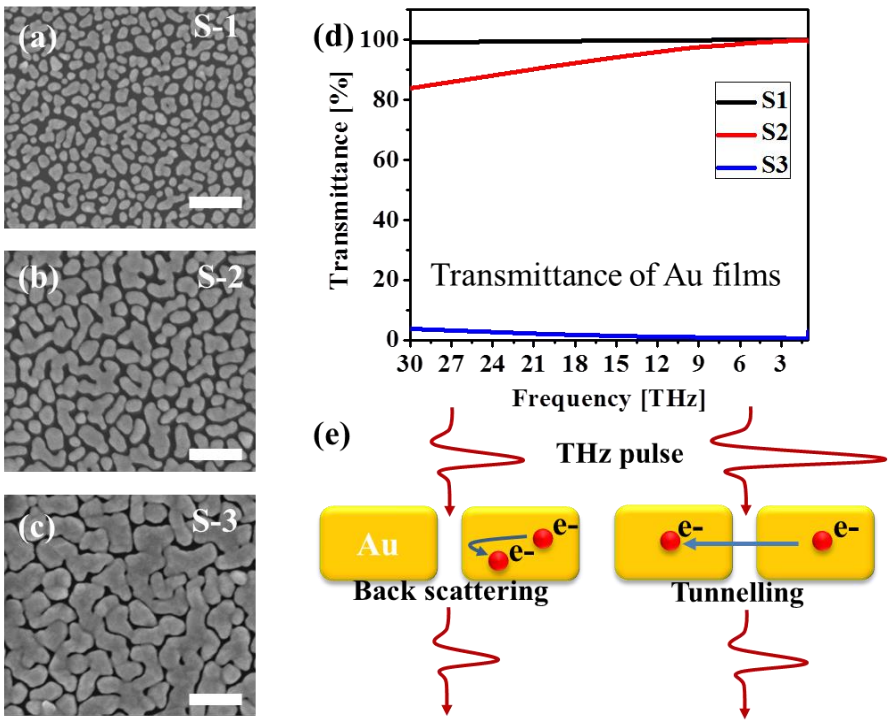

Figure 2.9. (a-c) SEM images of Au films: (a) agglomerated Au nano-islands (S1), (b) Coalesced Au nano-islands (S2), and (c) Connected Au-islands with gaps (S3). (d) Simulated transmittances of Au films (S1, S2, S3) from IR - THz region. (e) Illustration of nonlinear dynamic of electrons in Au film induced by electron-electron collision or tunnelling effect at the gaps of Au-islands.

The nonlinear dynamics of electrons induced by intense THz pulse can be explained as shown in Fig. 2.9. Au films with nanogaps (percolated film, Fig. 2.9a-c) have linearity transmittance as shown in Fig. 2.9d. When an intense THz field is applied, the free electrons in Au-islands are accelerated and scattered at the boundaries of Au-islands (Fig. 2.9e, back scattering). When increasing the THz field intensity, the free electrons are accelerated at a high speed and they can tunnel over boundaries between Au-islands, resulted in the decrease of the transmittance (Fig. 2.9e, tunnelling).[51]

2.2.2. Gold nano-sandwich hybrid arrays based plasmonics metamaterial

We have discussed the hybridization between two plasmonic nanometals such as Au-dimer across plasmonic nanogaps, which can give rise to high electric field enhancement in the gaps when excited by an optical plane waves. In contrast, the coupling between plasmonic nanometals that are vertically stacked by a thin dielectric layer can give rise not only electric field enhancement at metal surfaces but also can induce magnetic field enhancement in the gap between nanometals. For example, a pair of gold nanodisks stacked in a sandwich-like structure gives a large enhancement of the magnetic field when excited by a plane optical wave[52], [53]. In this subsection, we demonstrate optical properties of the metal-insulator-metal (MIM) gold nano-sandwich arrays fabricated by nanoplastic forming combined with thermal dewetting process[28].

The proposed Au nano-sandwich hybrid array is shown in Fig. 2.10a. Firstly, a layered Au-SiO_2-Au film was deposited using sputtering, and then nano-sandwich structure was formed using nanoplastic forming combined with thermal dewetting process[28]. By controlling the experimental conditions, 3D internal structure with tandem plate-dot architecture by Au-SiO_2-Au stacking is successfully fabricated as shown in SEM image (Fig. 2.10a). Reactive ion etching was employed to study the effects of the selective etching of the SiO_2 layer on the

optical properties of the Au nano-sandwiches. Electromagnetic simulations using RCWA and FDTD were also performed to further study plasmonic properties of the Au nano-sandwich hybrid.

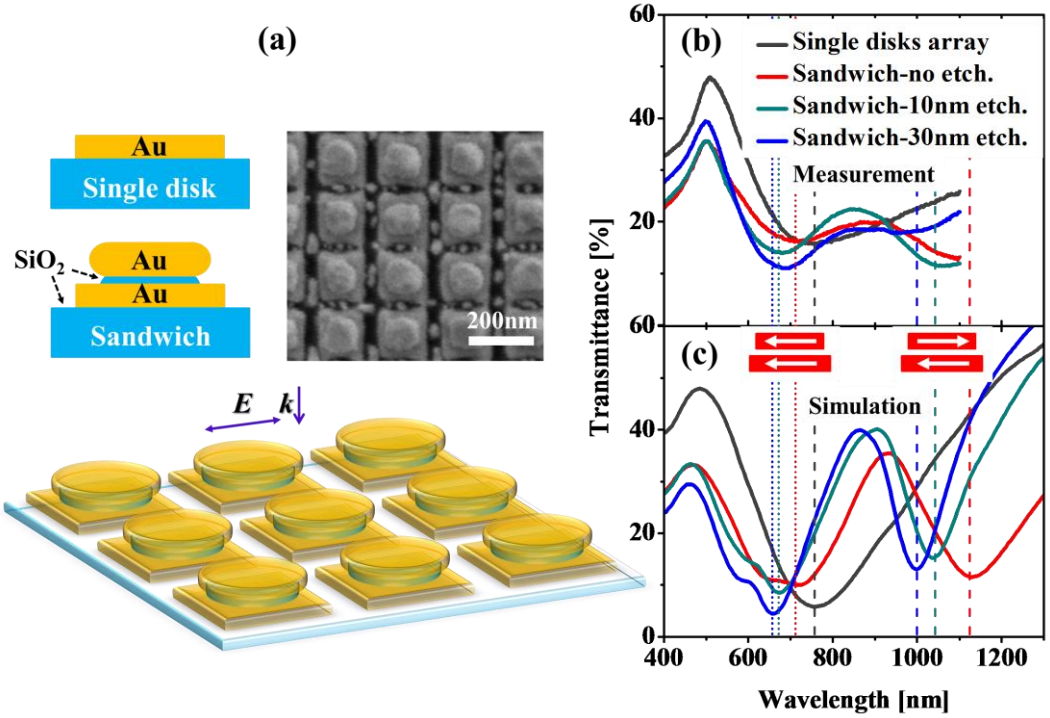

Figure 2.10. (a) Proposed Au nano-sandwich hybrid arrays, and SEM image of a fabricated sample. (c) Measured and (d) Simulated transmittance spectra of variety of gold nano-sandwich hybrids show two resonances related to electric-dipole (short-wavelength) and magnetic-dipole (long-wavelength) modes.

Figure 2.10b presents the measured transmittance spectra of the Au nano-sandwich hybrid with different etching thickness. Double peaks are observed representing the surface plasmon resonance in the Au nano-sandwiches. The two distinctive features are considered as a high-energy resonance that peaks at around 670 nm and a low-energy resonance with a maximum at about 1000 nm. For comparison, the spectrum from single purely metallic nano-plate array shows a peak at around 760 nm. It is considered that the resonance features of the double layer nanodot array cannot be identified as elementary contributions from its individual layer nanodot. In contrast, the double resonance peaks is due to dynamic coupling between the two

layer components. When the sample was etched 10 nm, the peaks blue-shift indicating the SiO_2 layer was etched out, and the environmental media of the first layer nano-plate changes to air. When etching 30 nm, the size and thickness of second layer Au dot became smaller due to over-etching and the second peak reduced a lot.

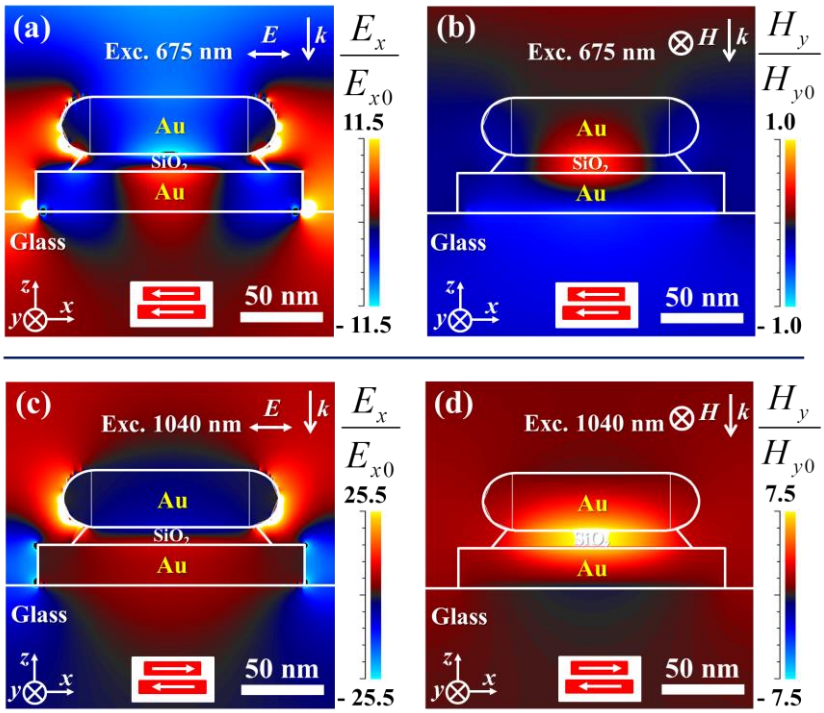

Figure 2.11. Simulated electrical field (Ex) and magnetic field (Hy) gold nano-sandwich (10 nm etching) arrays. (a) Ex and (b) Hy fields distributions under excitation at electric dipole mode of 675 nm. (c) Ex and (d) Hy fields distributions under excitation at magnetic dipole mode of 1040 nm.

Numerical simulations were conducted to study the origin spectral characteristics. The experimental transmittance spectra are compared with the spectra simulated based on RCWA method. Figure 2.10c shows simulated transmittance spectra of monolayer disks arrays and Au nano-sandwich hybrids in their evolution changing of SiO_2 layer by etching process. The agreement between experiment and theory is good in terms of the peak positions. In the case of single layer nano-plate array (gray curve), there is a broaden peak around 750-760 nm due to the plasmon resonance of the squared Au disk array. Nevertheless, in the case of double layer nanostructure, there are two resonance peaks corresponding to the electric dipolar (par-

allel, high-energy mode at wavelength of about 650 – 700 nm) and magnetic-dipolar (antiparallel, low-energy mode at wavelength of about 1000 – 1150 nm). As shown in Fig. 2.10b, the peak positions in both electric dipolar and magnetic dipolar modes are slightly blue-shifted by etching processes. These blue-shifts were confirmed by simulated results as shown in Fig. 2.10c due to the change of the dielectric function around bottom layer surface from SiO_2 to air and the size reduction of the metal objects during etching process. Some quantitative variations between the experimental results and numerical results are expected because the numerical structure does not precisely represent the real structure (e.g., including metal and dielectric permittivity, the shape, etc). It is thus likely that the large experimental peak widths are a result of inhomogeneous broadening, due to a distribution of nanostructure morphology for the measured samples.

To clarify the optical properties of the gold nano-sandwich hybrids, the electric and magnetic fields distribution around structure were simulated as shown in Fig 2.11 for the case of 10 nm SiO_2 etching. Figures 2.11a-b show the simulated electric and magnetic fields distribution around Au nano-sandwich structure under high-energy mode excitation at 675 nm. The regions of intense electromagnetic field indicate the "hot spot". The electric field enhancement was found to be 11.5 at the hot spots and placed at the sides of top and bottom objects with the same phase (positive electric field) of electric dipoles oscillation, while there was no enhancement of magnetic field, indicating the symmetric and parallel nature of the electric dipoles. In contrast, Figures 2.11c-d show that clear enhancements in both electric and magnetic fields were found in the vicinity of the structure under low-energy mode excitation at 1040 nm, to be 25.5 and 7.5, respectively. Furthermore, in this case, the electric dipoles at the sides of top and bottom objects are oscillated in opposite phases (electric field at top object is positive, while electric field at bottom object is negative), resulting in a loop-like charge motion which generates a strong magnetic field in between top and bottom objects at the center of the

object. This indicates that our present plasmonic hybrid can be applied as plasmonic metal-materials as well as surface-enhanced Raman scattering since the strong electric field enhancement was found on Au surface[28].

2.2.3. Gold nanocages (AuNCs) and AuNCs-TiO_2 hybrids

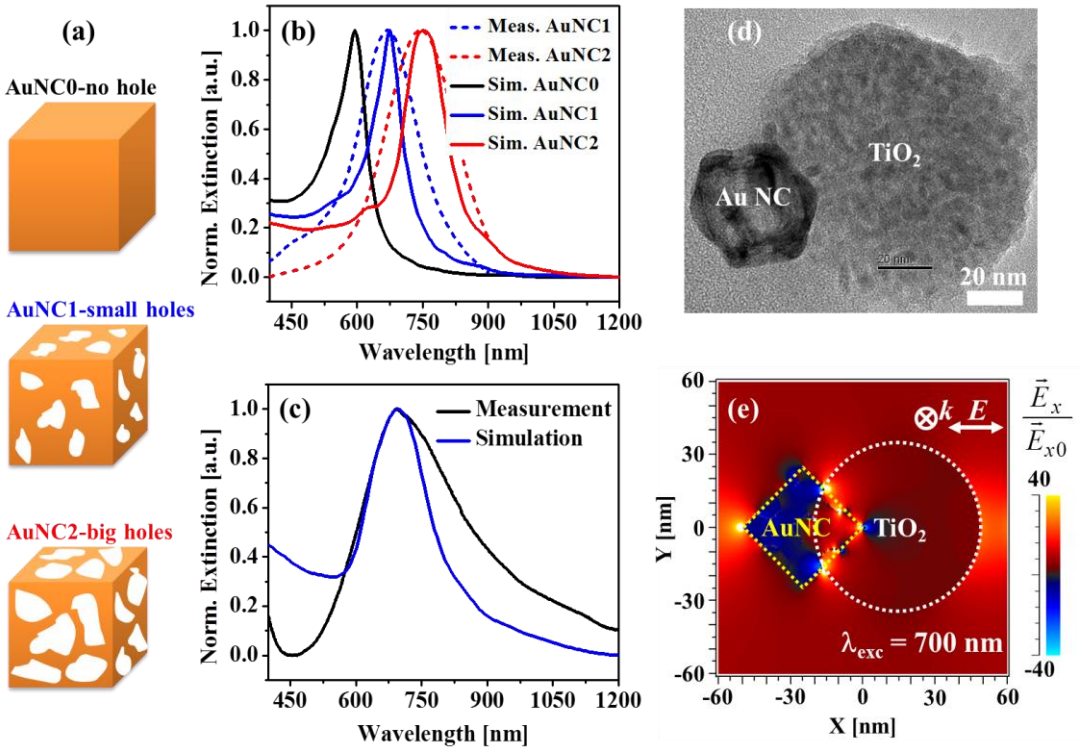

Figure 2.12. AuNCs-TiO_2 photocatalyst. (a) AuNCs, from top to bottom: Au cubic (without hole), with small holes, and with big holes. (b) Simulated and measured extinction spectra of AuNCs without TiO_2 and with different holes sizes. (c) Simulated and measured extinction spectra of AuNCs-TiO_2 hybrids. (d) TEM image of AuNCs-TiO_2 hybrid. (e) Simulated electric field distribution of AuNC-TiO_2 hybrid excited at 700 nm shows multiple hot-spots at Au-TiO_2 interface with strong electric field enhancement of 40 folds.

Recently, incorporating plasmonic coinage metal nanoparticles (Au, Ag, Cu NPs) with strong electromagnetic fields enhancement has emerged as a promising new strategy for the plasmon-assisted light harvesting applications such as efficient-sunlight photocatalysis[25]. Taking into account of the critical roles played by AuNPs, i.e., photon harvesting and energy transfer, asymmetric AuNCs nano-hybrid is particularly attractive. Moreover, the non-

centrosymmetric coupling of the metal and semiconductors nanoparticles at their small, inter-connecting junction has been found to potentially generate extremely strong local electric near-fields through interparticle coupling. Though a few attempts have been made to prepare AuNCs hybrids that can be applied to long-wavelength visible light harvesting still remains a great challenge. In this subsection, we numerically investigate the optical properties of AuNCs and AuNCs-TiO_2 hybrids in which their resonance can be tuned in a wide range from VIS to NIR with multiple hot-spots providing potential application in solar-assisted photo-catalysts[29], [30].

The AuNCs used in this work were synthesized using an Ag nanocube template with edge length of about 35 nm, which was first synthesized via a polyol method as described else-where. The optical properties of the plasmonic AuNCs, including resonance spectra as well as near-field enhancement, can be engineered by changing the size of AuNCs and nanoholes. Figure 2.12a shows a three AuNCs without and with different holes sizes named AuNC0, AuNC1 and AuNC2. The resonance of AuNCs were carried out and confirmed by electro-magnetic simulation using the RCWA as shown in Fig. 2.12a. As seen that, the resonance wavelength of AuNCs increases when increase the holes sizes. In addition, an AuNCs-TiO_2 hybrid was synthesized and its resonance was also investigated by both measurement and simulation with a maximum peak located at around 700 nm as shown in Fig. 2.12c. The simulation model is based on geometries of Janus AuNCs-TiO_2 hybrid from TEM images (Fig. 2.12d) with excited plane wave propagated along the -z axis and oscillated in the xz plane, which is parallel to the cross-section of Janus AuNCs-TiO_2. The simulated extinction of Janus AuNCs-TiO_2 is similar to its UV-vis spectrum from experiment, indicating the simu-lation model is well established. The electric field distribution of this Janus AuNCs-TiO_2 hy-brid was performed using FDTD method as result shown in Fig. 2.12e. The electric fields around AuNCs and AuNCs-TiO_2 interface are extremely enhanced as the “hot spots”, which

should provide the enhancement of the efficiency of the photocatalyst. The electric field enhancements at the AuNCs surface and AuNCs-TiO_2 hybrids interface are reached 38 times that of the incident electric field. That is, the field intensity ($|E|^2$) is about 1400 times higher than that of incident one, which means the photon absorption rate as well as electron-hole pair generation rate in TiO_2 catalyst, are largely enhanced. In addition, the strong near-field hot-spot located at metal-TiO_2 interface can provide sufficient energy for electrons to overcome Schottky barrier between metal-semiconductor, inducing hot-electrons injection from AuNCs to conduction band of TiO_2, resulted in the photocatalytic activity of TiO_2 under long-wavelength (VIS - NIR) excitation[29], [30].

2.3. Summary of Chapter 2

We have introduced the fundamental of plasmonics, the optical property of metallic materials. Two plasmonic waves, including the SPPs at metal-dielectric interface and the LSPs of metallic nanostructures were investigated through classical theory as well as numerical simulations. Two numerical methods included RCWA and FDTD (Rsoft-Synopsys) were briefly introduced, and applied to examine the optical properties of the Au-dimer. The electric field confinement in plasmonic nanogaps, and nonlinear electrons dynamic induced by intense THz pulse in Au percolated film were also discussed. We have further numerically demonstrated optical properties of two plasmonic hybrids composed of metal and metal-oxide, which have been used for SERS[28] and efficient photocatalyst[29], [30]. The Au nano-sandwich hybrid presented double resonances, which were assigned to electric-dipole mode (short-wavelength) and magnetic-dipole mode (long-wavelength) when the electric dipoles in top and bottom metallic nanoplates and are oscillated in the same phases and in the inversed phases, respectively. The metal-insulator-metal plasmonic hybrid will be discussed in more detail when we introduce the MIM plasmonic perfect absorber in Chapter 5.

3. PLASMONIC NANOGAPS FOR SERS AND SEIRA

In previous chapter, we have introduced the fundamental of plasmonic, especially the optical property of plasmonic nanostructure, which can provide huge near-field enhancement and light-confinement in nanometer scale at surface of nanometals. As one example of Au nano-sandwich with strong electric field enhancement at the gaps between Au plates on top layer, and this has been used for SERS application[28]. In this chapter, we demonstrate the uses of plasmonic hybrids composed of nanogaps as the multiple hot-spots for SERS and SEIRA application. I begin this chapter by reviewing the SERS and SEIRA. Then in the second section, the dark-field scattering and SERS spectroscopies are studied on a floating aluminum antenna structure designed for 532 nm resonance. In the third section, the *in situ* chemical synthesis of plasmonic nano-hybrids with multiple hot-spots for SEIRA and their applications for *in situ* sensing of biomolecules and mercury ions in water will be shown.

3.1. Surface-enhanced vibrational spectroscopy: SERS and SEIRA

Localized surface plasmons (LSPs) spectroscopy of metallic micro- and nanostructures is a powerful technique for chemical and biological sensing experiments[13]. Moreover, the LSPs is responsible for the electromagnetic field enhancement that leads to surface-enhanced Raman scattering (SERS)[15], [17], surface-enhanced infrared absorption spectroscopy (SEIRA)[21]–[23], [25], [24], [54], and other surface-enhanced spectroscopies.

SERS is a spectroscopic technique, which combines laser spectroscopy with the excited near-field of the plasmonic nanostructures, the induced near-field so-called hot-spot located at metal surface can also excite the molecules attached on metal surface, resulting in strongly increased Raman signals[55], [56]. Because Raman intensity is proportional to λ^{-4}, where λ is the laser wavelength, the SERS enhancement factor therefore is also a function of $(E/E_0)^4$,

where E and E_0 are the amplitudes of the induced and incident electric field, respectively. Depending on the structure and the matching between laser wavelength and resonance wavelength of plasmonic structure, the SERS enhancement factor can be ranged from several to more than 10 orders[56]. The plasmonic structure with small gaps such as Au-dimer[57] or Au-bowtie antenna[58] can produce very high SERS enhancement factor (exceeding 10^{11}), which have been used to detect single molecule.

The discovery of SERS[15], [17] opened the field of surface-enhanced spectroscopy, including surface-enhance fluorescence (SEF)[14], linear and nonlinear optical phenomena. In particular, the realization of SEIRA[21]–[24] permitted one to speak of a unified field of surface-enhanced vibrational spectroscopy, supported by the enhanced Raman and infrared techniques[54]. Unlike the enhancement of $\left(E/E_0\right)^4$ for SERS, the enhancement factor for the SEIRA is proportional to $\left(E/E_0\right)^2$. The plasmonic structure is SEIRA active where the near-field enhancement in infrared region is matched to the molecular vibrations, and therefore, this IR near-field can also enhance the vibrational absorption of molecules. In addition, if the plasmonic resonance frequency is well-matched to the vibrations of the molecules, the strong coupling between them can occur, giving rise to the Fano-type behaviour of the spectral signal[24]. SERS and SEIRA are two sensitive vibrational spectroscopic techniques supported by plasmonic structures. In the next sections, we will demonstrate our study on these spectroscopies using plasmonic metal and metal-oxide nano-hybrids.

3.2. Floating aluminum nanobowtie based plasmonic antenna for SERS

In this section, we present the design, simulation and experimental study of optical properties and the SERS application of the floating aluminum bowtie based plamonic antenna. Before starting the Al bowtie antenna, we firstly investigate optical properties of plasmonic Au bow-

tie antenna[58]–[60], which have been extensively studied in recent years since this structure can provide a strong field confinement in the gaps of the bowtie antennas.

3.2.1. Optical properties of plasmonic bowtie nanoantenna

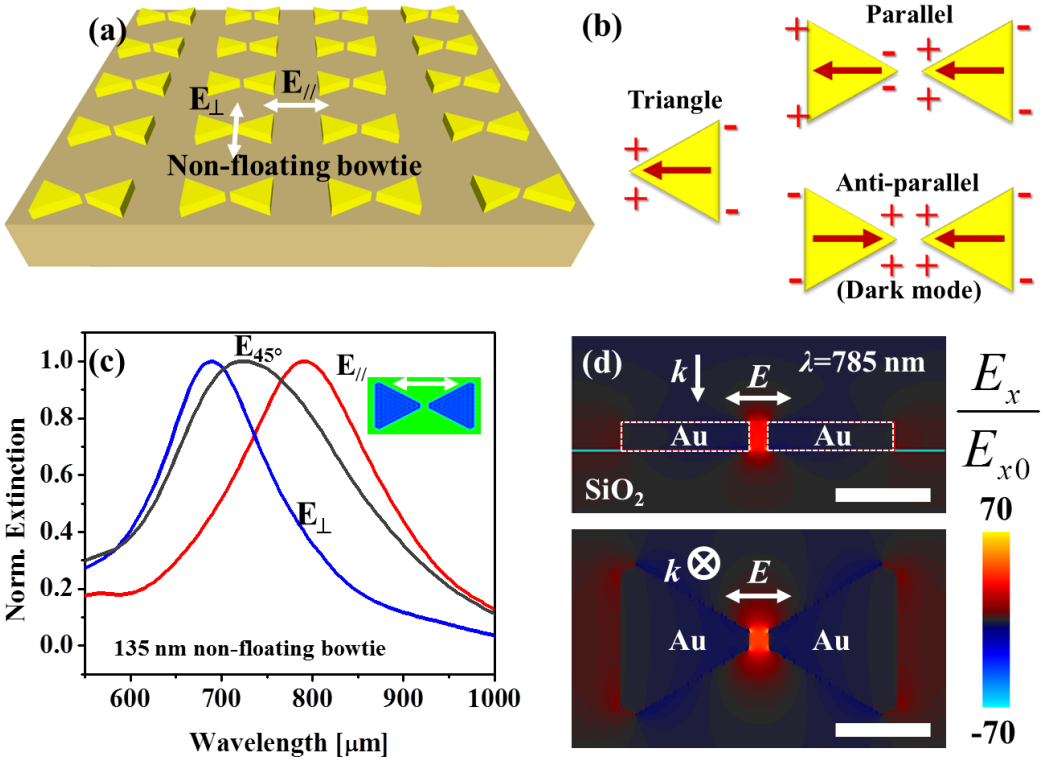

Figure 3.1. (a) Schematic of non-floating bowtie array. (b) Schematic of the charge profile of triangle, parallel and anti-parallel modes[48]. (c) Simulated extinction spectra of non-floating Au bowtie on a glass substrate excited at different polarizations. (d) Simulated field distribution of bowtie antennas at resonance of 785 nm. The scale bar is 100 nm.

Plasmonic bowtie nanoantennas can provide huge enhanced electric fields that are confined to spatial scales far below the diffraction limit at the gaps of bowties[59]. Fig. 3.1a shows a schematic of an Au non-floating bowtie antenna arrays designed to 785 nm resonance. The Au triangle in each bowtie sitting on top of a glass (SiO_2) substrate has the size of 135 nm. As shown in Fig. 3.1b, the simulated extinction spectra of Au bowtie have a resonance at 785 nm when excited polarization is parallel to the bowtie axis (red curve), which is so-called parallel-mode[48] as discussed in Chapter 2. Likewise, the perpendicular polarized excitation is

similar to the excitation of the individual triangles (triangle-mode), and the resonance spectrum is blue-shifted compared to parallel excitation as shown in Fig. 3.1 c (peak at 680, blue curve). It would be noted that, the anti-parallel mode cannot be excited by a plane wave so-called dark-mode[48]. It can be excited by electron beam, and detected by cathodoluminescence spectroscopy. Figure 3.1c shows electric field distribution (side view and top view) of the non-floating Au bowtie antennas excited at 785 nm (parallel-mode). It was found that, the electric field is confined at the gap of the bowtie with an enhancement factor as high as 70.

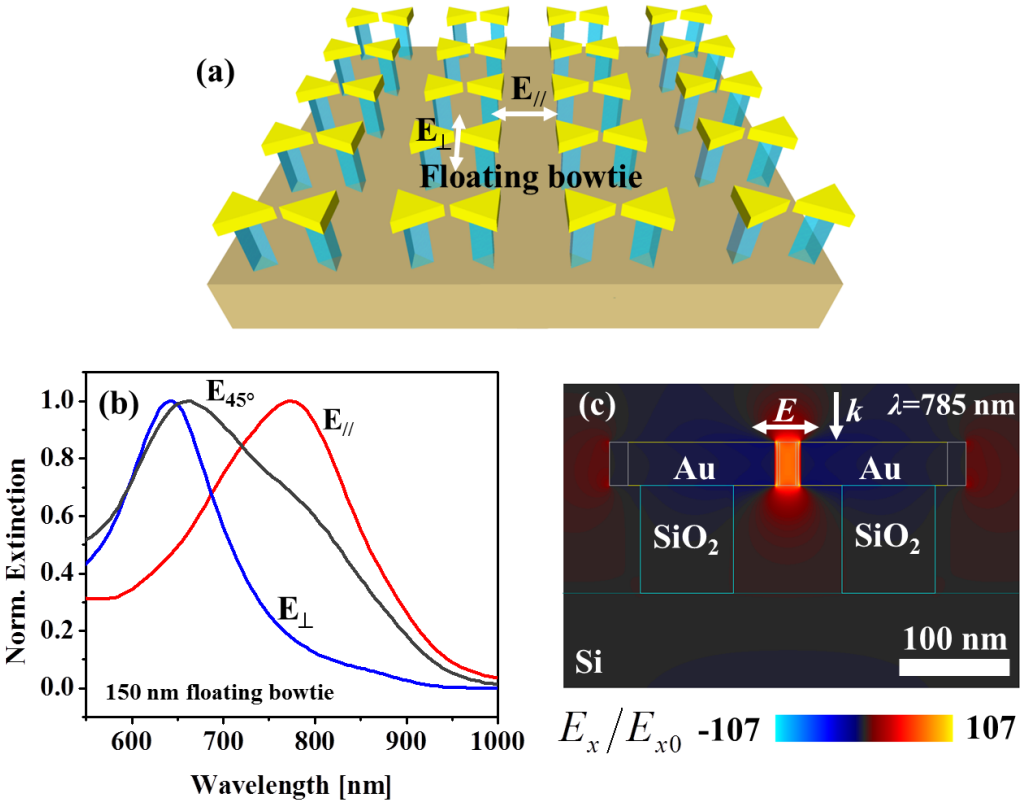

Figure 3.2. (a) Schematic of floating bowtie array. (b) Simulated extinction spectra of floating Au bowtie supported by SiO_2 pillars on a glass substrate at different polarized excitations. (c) Simulated electric field distribution of floating Au bowtie under excitation paralleled to bowtie axis.

To reduce the screening of the substrate with high permittivity and high optical quenching, the bowtie can be floated by low-permittivity pillar as the schematic shown in Fig. 3.2a. Because the free surrounding medium like air has smaller permittivity than that of any dielectric

substrates, the floating bowtie antenna therefore has a larger size compared to non-floating bowtie antenna designed at the same resonance. For example, a floating Au bowtie antenna array supported by SiO_2 pillars has the size of 150 nm designed to 785 nm resonance wavelength at parallel-mode, while non-floating Au bowtie requires smaller size of 130 nm at the same 785 nm resonance. This is importance since the size and shape of plasmonic nanostructures are not easy to be controlled at nanometer scale, while their optical properties are strongly depended on these parameters. In addition, the enhancement factor as wells as the total volume of the enhanced electric field on free metal surface can be improved compared to non-floating bowtie. As seen in Fig. 3.2c, the electric field enhancement factor is as high as 107, this value is far higher than that of non-floating Au antenna designed at the same resonance wavelength of 758 nm. This evaluation expected the advantage of floating bowtie compared to non-floating bowtie antenna in the application related to near-field enhancement such as surface-enhanced spectroscopy. In the next study, we will describe the use of floating bowtie antenna made by Aluminum for SERS application.

3.2.2. Floating aluminum nanobowtie: optical properties and SERS application

Being the third most abundant element in the earth, after silicon and oxygen, aluminum has been used widely in industry. Recently, it attracts tremendous interest in the plasmonics research as it is promising as an alternative replacement for noble metals such as gold and silver[61]–[65], [33]. Despite of displaying a drawback of the native oxide Al_2O_3 layer (2 - 4 nm) which induce a red-shift in resonance, plasmonic aluminum nanostructure is an emergent in the field of plasmonic sensing as the detection mechanism is based on the electromagnetic field enhancement rather than the charge transfer effect[66], [67]. Compared to gold and silver whose interband transitions are at ~500 nm and ~330 nm[32], relatively, aluminum has lower interband transition energy of about ~800 nm. In addition to that, with plasma fre-

quency of 12.7 eV and real part of the dielectric constant is negative even below 200 nm while imaginary part is still lower than that of absolute value of relatively real part, making Al a perfect Drude metal from visible (VIS) to the ultra-violet (UV) range[68]–[70], especially in UV range. Therefore, plasmonic resonance of aluminum nanoantenna can be tuned over the UV-VIS to the near-IR band-edge of aluminum, just by adopting suitable architectures on the objects[71]–[73].

UV plasmonic study is not widely investigated though it is promising for the study on the photo-induced chemical reactions as well as molecular sensing. The latter case holds a great interest since Raman cross section of molecules is increased in the short-wavelength region λ^{-4}. Group velocity of the "slow light" formed by the coupling of plasmon and light is screened by the dielectric property of the surrounding media. Thus, having an equality of the group velocity (by having homogeneously surrounded dielectric medium) between the upper and lower metal/dielectric interfaces would give a better homogeneity of the distribution of electromagnetic field[58]. The induced field enhancement at the nanogaps located between two plasmonics structures are therefore could be increased and occupy a larger total volume. In this study, we investigate the plasmonic mapping of the scattering spectra of the freestanding aluminum bowtie antenna, correlated the obtained resonance with their sensing capability by SERS study. Supported by the numerical simulations, we show a demonstration of the floated Al antenna as the Raman active objects for SERS. Our result figures out the possible applications of the oxide-coated Al bowtie antenna for the SERS research.

3.2.2.1. Optical properties of floating aluminum bowtie antenna

The freestanding Al bowtie nanoantennas were fabricated by the standard procedure using electron beam lithography, lift-off and reactive ion etching. Prior to the fabrication, a 200 nm thick layer of SiO_2 was prepared by thermal oxidation on the Si wafer. A 4 nm Cr layer was

used as an adhesive layer stack for the Al on SiO_2 posts. Morphology of the Al bowtie arrays was characterized by using a field-emission scanning electron microscope (FE-SEM, Hitachi SU8000). Figure 3.3 presents the top-view (Fig. 3.3a) and tilted-view (Fig. 3.3b) SEM image of an Al bowtie antenna array with parameters of 105 nm width, 20 nm gap, 1400 nm periodicity (the distance between two bowties) and 1120 nm spacing (the distance between two bowties lines). The inset in Fig. 3.3a-b shows a bowtie antenna standing freely on the SiO_2 posts with triangular shape.

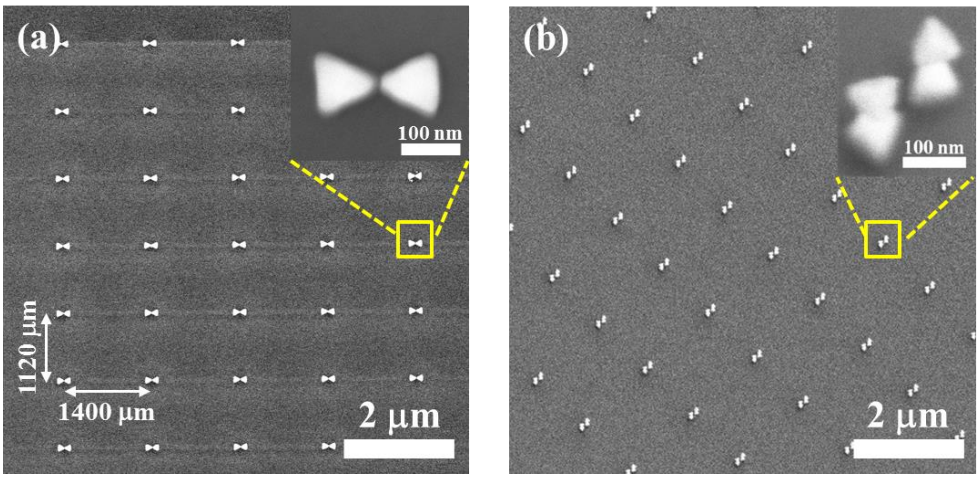

Figure 3.3. (a) Top-view and (b) Tilted-view SEM images of floating bowtie aluminum fabricated on Si substrate.

A con-focal Raman microscope (WITec Alpha 300S) combined with a halogen lamp (Lucir-LAHL100) in UV-NIR range and a 50x (Zeiss) dark-field lenswas used for the investigation of the plasmonic scattering property (dark-field geometry). The spectroscopic measurements of the Al bowtie antenna are presented in Fig. 3.4 and Fig. 3.5. As the obtained spectra are achieved by normalization the dark-field scattering on the area with the presence of bowtie antenna to the reference area of the bare SiO_2 sample, it is hence inferred that our measurement reflects the plasmonic characteristics in the far-field of the antenna resonances. In the near-field measurement regime, in the particular case of bowtie antenna, the resonance spectrum depends on the position of excitation of single object. For example, the bowtie gap-

mode (bright mode) and dark-mode are seen under the excitation at the point near the gap, and at the point located far from the gap, respectively[48]. For the far-field measurement, the resonance spectrum is a superimposition of the scattering, emission and interaction from the objects. The difference between the near-field and far-field resonance in the Au nanorod- and nanotube-array and their impacts on SERS have been discussed[74]: the far-field measurements imply the resonant nature (with longitudinal-mode and transverse-mode) of the plasmonic nanoantenna and does not influence much on the SERS effect; in contrast, the near-field resonance (or cavity mode) does effect on the SERS signals.

Figure 3.4 shows a spectroscopy study on a floating Al bowtie array with 105 nm width, 1400 nm periodicity and 1120 nm spacing and 20 nm gap. A dark-field optical image (Fig. 3.4a) shows a highly contrast of an Al antenna array indicating the dark-field scattering of the individual bowtie, while their scattering spectra (Fig. 3.4b) shows a broad band resonance with two main peaks featured at 565 nm and 650 nm. In addition, the scattering spectrum on each individual bowtie (black curve in Fig. 3.4b) is slightly different compared to the averaged spectrum (red curve in Fig. 3.4b) taken on a $10\times10\ \mu m^2$ scanning area. While both the single and averaged area shows the broad spectra, the resonance spectrum of single bowtie is dominant and featuring at the short-wavelength peak (565 nm). It is clearly seen in Fig. 3.4c, by integrating scattering spectra around 565 nm, the dark-field spectral image shows clearly scattering signal responded at bowtie position. In contrast, the dark-field spectra image integrated at around long-wavelength peak (650 nm) is show the scattering responded at centre position between bowties, indicating the interaction between bowties in the periodic structure. However, due to the limitation of the spatial resolution, the scattering spectra taken on individual bowtie and between bowties are influenced by each other spectrum.

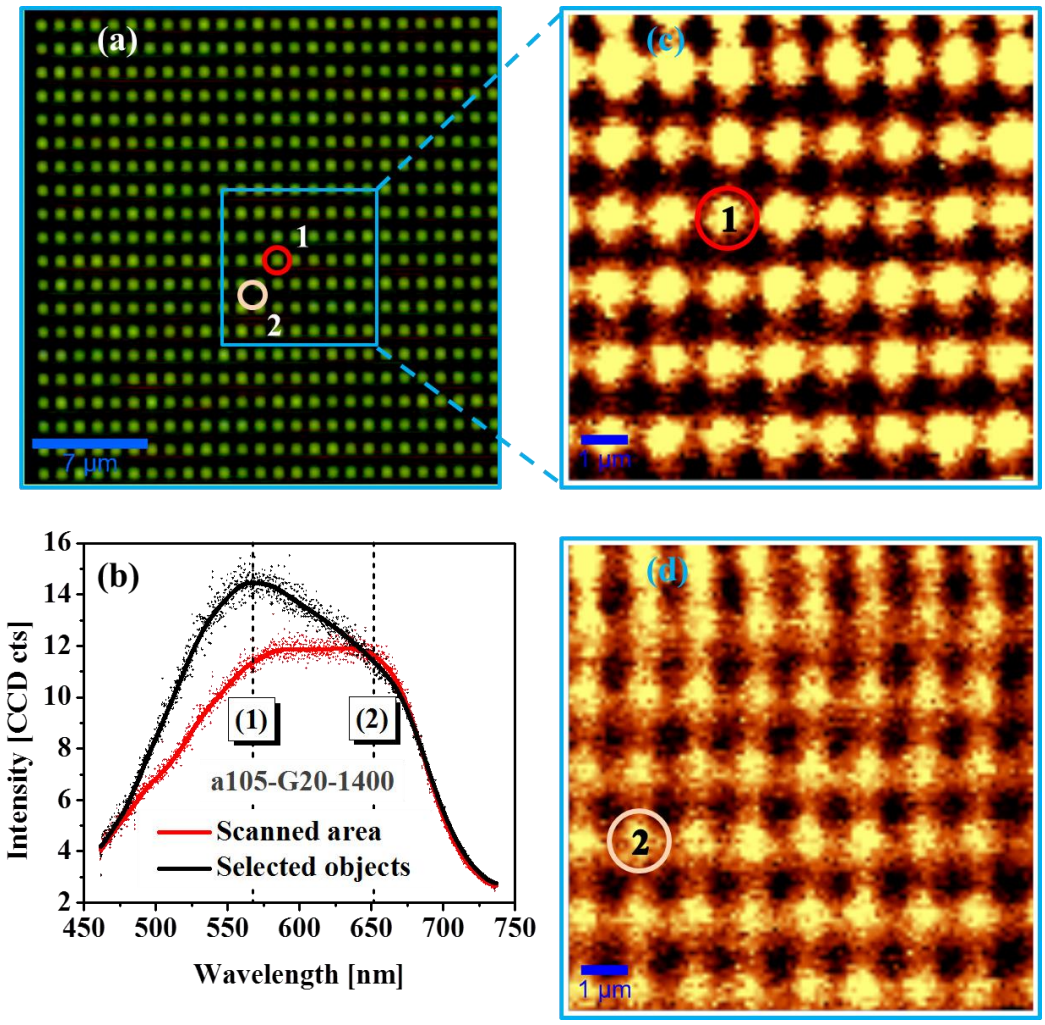

Figure 3.4. Dark-field spectroscopy of Al bowtie antenna. (a) Dark-field optical image. (b) Dark-field scattering spectra of single bowtie (black curve) and on an area (10×10 μm^2) bowtie (red curve). (c) Dark-field spectral mapping image integrated at around resonance wavelength of single antenna (530 - 600 nm) showing the scattering responded at centre of bowtie. (d) Dark-field spectral mapping image integrated at around 650 nm indicating the interaction between bowties.

We further investigated the dark-field scattering spectroscopy on different bowties as shown in Fig. 3.5. As seen in Fig. 3.5a, the scattering spectra taken from the individual bowtie and a 10x10 μm^2 scanning area of a floating Al bowtie array with 105 nm width, 840 nm periodicity, 1120 nm spacing and 20 nm gap show the broadband features similar to 1400 nm periodicity Al bowtie. A little blue-shift was found on the averaged spectra of the 840 nm periodicity bowtie compared to the 1400 nm bowtie, which is caused by a shorten periodicity of

this 840 nm bowtie compared to 1400 nm bowtie. The dark-field spectral image integrated around short-wavelength peak of this 840 nm periodicity Al bowtie is shown in Fig. 3.5b, indicating the scattering signal on each individual bowties. Figure 3.5c shows the dependence of resonance spectra on the gap of Al bowties. These two spectra are taken on the individual bowties with 105 nm width, 1400 nm periodicity and different gaps of 10 nm (black curve) and 20 nm (red curve). As clearly seen that, the resonance spectra of Al bowtie is blue-shifted when the gaps increased. Figure 3.5d shows a dark-field spectral image integrated around 560 nm of 10 nm gap Al bowtie, indicating strong scattering from single Al bowtie objects.

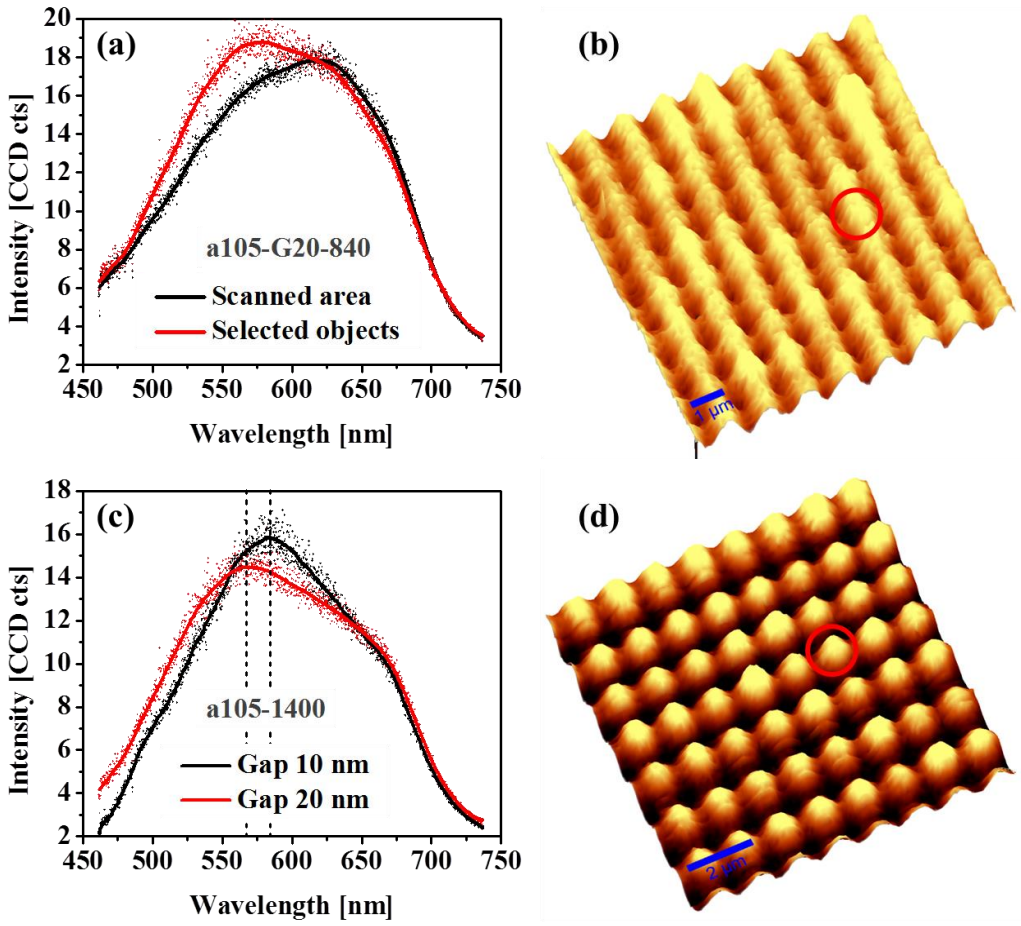

Figure 3.5. (a) Dark-field scattering spectra of Al bowtie with 105 nm width, 840 nm periodicity, 1120 nm spacing and 20 nm gap and (b) Its dark-field spectral mapping image integrated at around resonance wavelength of single antenna (530 - 600 nm). (c) Dark-field scattering spectra of Al bowties with 1400 nm periodicity, 1120 nm spacing and different gaps of 10 and 20 nm. (d) Dark-field spectral mapping image integrated around 560 nm peak of 10 nm gap bowtie.

3.2.2.2. SERS study on plasmonic Al bowtie antenna

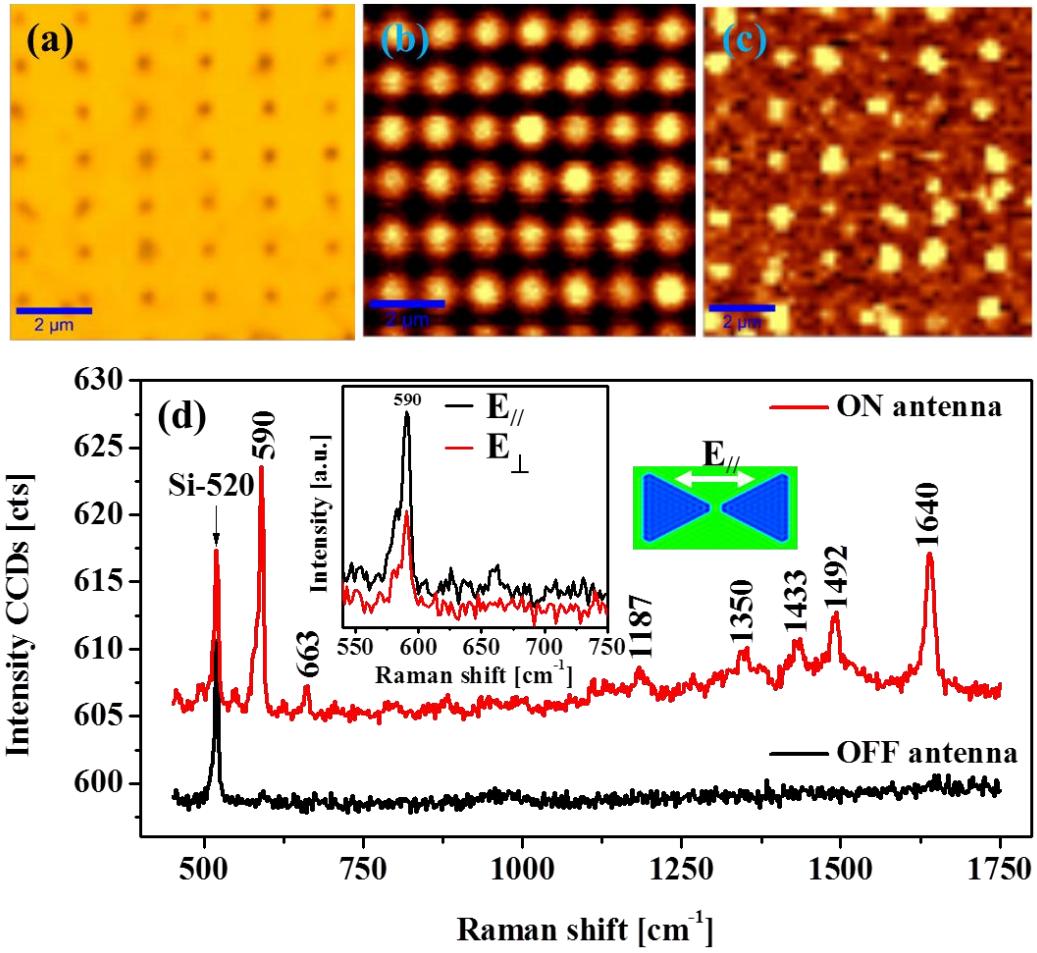

Figure 3.6. Demonstration of electric field enhancement of freestanding bowtie antenna by means of surface enhanced Raman spectroscopy (SERS). (a) Bright-field optical image (seen under confocal microscope). (b) Raman mapping. (c) Dark-field spectral image indicating the plasmonic mapping of the antenna arrays. (d) SERS measurements of NB molecules on Al bowtie antenna. The black curve and red curve show Raman signals OFF and ON the objects. The small inset indicates the Raman signals under different excitation conditions, parallel to the gap and perpendicular to the gap, respectively.

As for the demonstration of SERS effect, a 10 μl droplet of Nile blue solution (NB, concentration 3μM) was spread over entire the Al bowtie arrays on 1×1 cm^2 Si substrate and then dried in ambient condition. The mapping of SERS measurements were performed on an area of 10×10 μm^2, spatial resolution of 40 pixels (250 nm/ pixel), integration time 0.2 s/pixel. A 100x lens was used to focus a 532 nm laser (500 μW) on NB treated Al bowtie antenna for

SERS excitation. Figure 3.6 shows our demonstration on the field enhancement of Al free-standing bowtie antenna by means of SERS measurements on NB molecules. Very different from Au and Ag nanoparticles surfaces which allow for a well-defined absorption of a single layer of probe molecules (ODT, for instance), giving a precise estimation of the enhancement factor of the nano-objects[24]; the Al antenna are naturally coated by a few nm thick Al_2O_3 that protects the Al surface from contacting directly to the probe molecules. However, the Al_2O_3 is a fairly inert and reusable surface making it a promising SERS template for practical applications. The use of the Al_2O_3-Al configuration for the SERS measurements is also a demonstration of the electromagnetic field enhancement effect on the SERS effect as the charge transfer (also known as chemical effect) between the plasmonic antenna and the Nile blue molecules is completely eliminated. The SERS effect on the Al bowtie arrays was investigated by evaluating the enhancement of the Raman spectrum of NB molecules.

Figure 3.6a-c show an optical image (seen by con-focal microscope), a dark-field scattering mapping image of the corresponding area, and a reconstructed Raman mapping image (integrated at 590 cm^{-1} band), respectively. Fig. 3.6d shows the SERS spectra of Nile blue molecules at the position "ON" the Al bowtie (red spectrum) and at the position "OFF" the Al bowtie (black spectrum). It is noted that the peak located at 520 cm^{-1} is originated from phonon vibration in Si substrate, and two main Raman peak of NB at 590 cm^{-1} and 1640 cm^{-1} are attributed to a collective 'ring-breathing mode' and a NH_2 deformation mode of the molecule structure, respectively[75]. It is obvious that the Raman signals of NB fingerprints are strongly enhanced if the molecules are located at the position of Al bowties, giving a clear evidence of SERS effect due to the near-field enhancement at the gaps of the Al bowties antenna. Additionally, the measurement of the polarization-dependent on the SERS effect was performed by using a half-wave plate to change polarization of the excitation laser. The inset in Fig. 3.6d shows that the relative intensity of Raman signals at 590 cm^{-1} peak in case of polariza-

tion laser in parallel (to the bowties axis, black curve) is significantly higher than that of perpendicular excitation regime (red curve). As the NB molecules cover entirely the bowtie antenna, the overwhelming of Raman signals in the parallel excitation to the perpendicular mode reflects that the gap-mode of plasmonic antenna (known as parallel-mode) gives a larger enhancement than the quadrupole mode (triangle-mode) which is typically smaller (in term of energy) and higher energy (or in term of frequency), compared to the gap-mode.

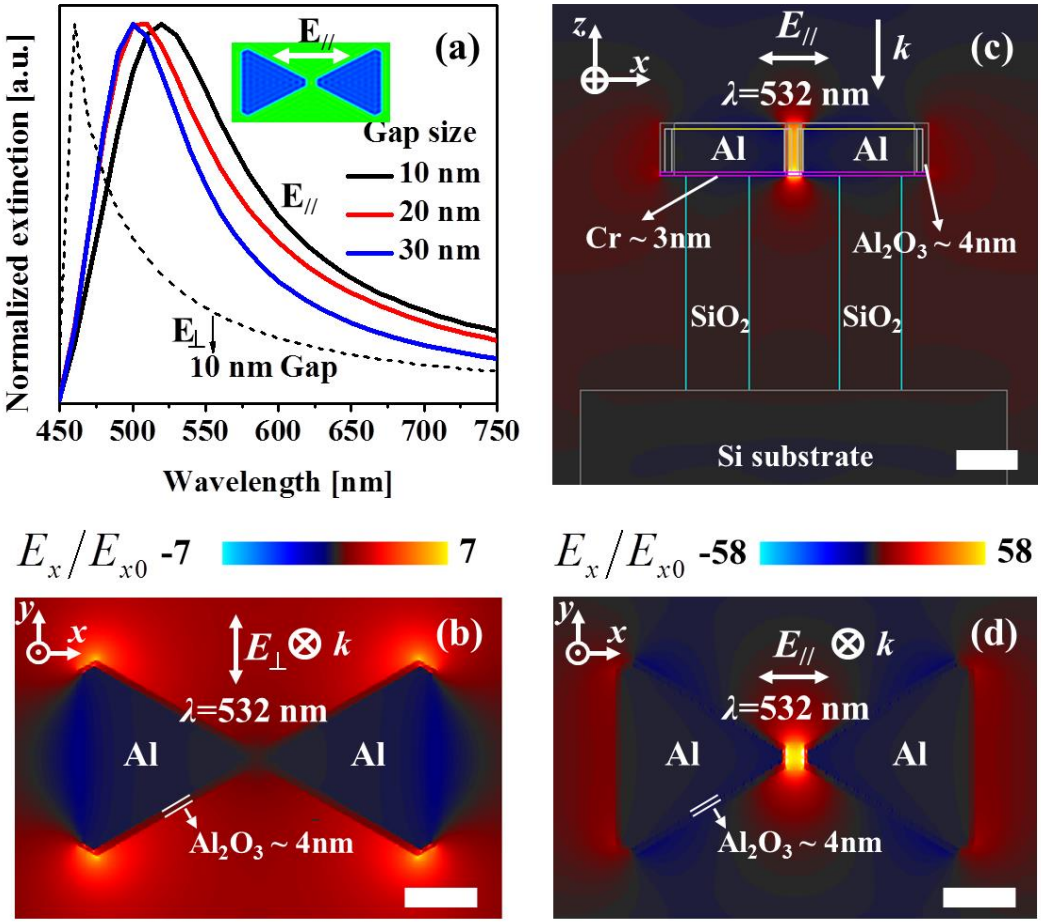

Figure 3.7. (a) Simulated extinction of Al bowtie with parallel excitation mode (different gaps size of 10, 20, 30 nm) or perpendicular excitations (10 nm gap). The electric field enhancement is well known as the primary mechanism of SERS. In addition to demonstrate the SERS effect on the Al bowtie nanoantenna, the electric field distribution around Al bowtie at 532 nm excitation was simulated with two polarized excitations. (b) Perpendicular polarization. (c) and (d) Parallel polarization with size-view and top-view, respectively. The scale bar is 50 nm.

The plasmonic property of the floating Al bowtie antenna arrays is further investigated by means of electromagnetic simulation. The RCWA and FDTD numerical simulations were employed to get further understanding of the optical property of the Al bowties as well as the enhancement nature of the electromagnetic field at their gaps and surfaces. Dielectric functions of Al, Cr, Si and SiO_2 were referred from [31], [76]. Each floating bowtie antenna composed of a SiO_2 substrate and two SiO_2 posts (height of 180 nm) and Al bowties. The Al bowties have the triangle shapes (width of 105 nm, thickness of 40 nm) and composed of a 4 nm thick native Al_2O_3 oxide layer on top and 4 nm thick Cr adhesive stack layer underneath. To mimic the real structures, the triangular truncations were placed at the corners of the triangles. The periodic boundary and grid size conditions were optimized to simulate for a structure with an infinite geometry and capability of resolving the dielectric property of the ultrathin material layers.

Figure 3.7a shows the simulated extinction spectra of Al bowtie with parallel excitation mode (for different gaps size of 10, 20, 30 nm) or perpendicular excitations (for 10 nm gap). The parallel (to the bowtie axis) shows that the resonance of Al bowtie is located at around 520 nm and it is blue-shifted when the gap size increased. The perpendicular spectrum shows a tail of a possible resonance from the UV-range towards visible wavelength. In comparison to the scattering spectrum measured on a single bowtie, presented in Fig. 3.4b, the simulated spectrum indicated a single peak, located closely to the main measured peak (565 nm). However, the simulation could not retrieve the second - shadow like - peak at 650 nm. This discrepancy could be assigned to the fact the freestanding architecture of the bowtie antenna results in a relatively strong far-field interaction that could be seen only by far-field scattering experiments as shown in Fig. 3.4b-c and Fig. 3.4d, not the near-field simulations[74]. Figure 3.7b shows the electric field distribution of Al bowtie under excitation at 532 nm with perpendicular polarization. In this case, the excited hot-spot is located at the corners of each tri-

angles and the field enhancement was found to be about $E_x/E_{x0} = 7$ where E_x and E_{x0} are the amplitudes of the enhanced and incident electric fields, respectively. Figures 3.7c-d show the electric field distribution under the excitation at 532 nm with parallel polarization, side-view (Fig. 3.7c) and top-view (Fig. 3.7d). The electromagnetic field is mainly comfined at the nanogap of the bowtie antenna. The enhanced area is homogeneously distributed over the gap and the enhancement factor is calculated to be about $E_x/E_{x0} = 58$, is much more stronger compared to perpendicular excitation. It is consistent with the SERS results as discussed above where the SERS signal intensity under parallel excitation is stronger than that of perpendicular excitation.

3.2.3. Conclusion of plasmonic aluminum nanoantennas

In summary, we have investigated optical properties of plasmonic bowtie antenna. The floating and non-floating gold bowtie antennas designed for 785 nm resonance were studied using RCWR and FDTD simulations. A design for 532 nm resonance of floating Al bowtie antenna were carried out and carefully characterized by dark-field and SERS spectroscopies. Despite of having a natural oxide Al_2O_3 layer, the floating Al bowties showed the SERS effect owing to the enhancement of Raman signals in the strongly confined electromagnetic field locating inside the nanogaps. This work puts another step towards the application of aluminum bowtie antenna in plasmonic sensing.

3.3. *In situ* chemical synthesis of random gold nano-islands and patchy gold nano-shell for in situ SEIRA spectroscopy

The discovery SEIRA as the analogue of SERS has gained much interest in the field of the surface-enhanced vibrational spectroscopy in the past decades[21], [22]. The vibrational signals of the individual molecules substrate are proportionally related to amount of molecules

supported by SEIRA substrate [25]. This means the suitability of SEIRA spectroscopy for quantitative analysis in order to detect trace amount of the molecules as well as detailed molecular structural information in a label-free fashion. Especially the *in situ* monitoring of molecule in the presence of water, SEIRA can directly targets the molecules adsorbed on plasmonic surface, resulting in a highly enhancement of the signal to noise ratio (molecules signals to background signal of liquid water).

Among the *in situ* SEIRA techniques, the ATR configuration supported by IR plasmonic structures can support very high sensitivity in real time of the evolution and interaction of the bio-molecules network. An IR plasmonic antennas with resonance frequency matching to the molecular vibrations can be fabricated using nanolithography techniques[24]. However, this is expensive and time-consuming. Recently, Au-islands film fabricated by *in situ* chemical deposition is a simple, cost-effective and less time consuming technique[25], [77], [54].

In this study we investigated the optical properties of Au nano-island films and gold patchy nanospheres at various stages of morphological development by both *in situ* IR spectroscopy and *ex situ* scanning electron microscopy (SEM) to clarify their applicability for high-sensitivity SEIRA analysis. The optical properties as the broadband background development and that of certain vibrational lines are discussed in detail based on IR spectra measured during the wet-chemical deposition of Au films onto Si or SiO_2 spheres. The strong correlation between SEIRA activity and Au nano-islands and Au-patchy nanoshells morphology are proven for vibrational spectra of self-assembled monolayers (SAMs) of bovine serum albumin (BSA) or glutathione (GSH) probe molecules on the Au surface of Au-island or Au-patchy nanoshells, respectively.

3.3.1. *In situ* FTIR-controlled growth of gold nano-islands for SEIRA

Au films on the Si ATR crystal were prepared by wet-chemical deposition using surface-deposited spherical Au nanoparticles as seeds[77]. In detail, we firstly prepared spherical AuNPs with diameter of 15 ± 1 nm using the citrate reduction method introduced by Turkevitch and Stevenson and further developed by Frens[25], [77]. The Si-ATR crystal was also treated with an SAM layer of (aminopropyl) triethoxysilane (APTES)/methanol solution (10% APTES/methanol solution for 1 hour). Then AuNPs was deposited at the center of the planar probe surface of Si-ATR by placing a 150ml droplet of AuNPs suspension (at room temperature). After 1 hour, the suspension was removed by decanting the droplet and rinsing the surface with water to remove unbound AuNPs. This treatment was previously shown to ensure sub monolayer coverage of AuNPs on the surface of ATR crystal. The AuNPs sub-monolayer was exposed to Au^{3+}/NH_2OH solution [0.3 mM HAuCl4 (Aldrich) and 0.4 mM NH_2OH in water at room temperature] at a constant flow of 3 ml/min using a micro pump. This condition allows the film to grow and become percolated at around 240 s. During the film preparation in situ ATR-IR spectra were measured (see discussion of spectra below). The Au deposition was stopped by replacing the Au^{3+}/NH_2OH solution with pure water as soon as a certain stage of the reflectance spectrum was reached. The growth of each film was stopped at a different stage of the ATR spectrum (i.e. after different deposition times), resulting in different morphological states for each film. Except a few minor deviations, these different states (1) to (4) (as deposited AuNPs, agglomerated Au nano-islands, coalesced Au nano-islands with plasmonic gaps, and connected islands with gaps, nearly closed film) could be prepared in a reproducible way with desired optical characteristics with this method and using our custom-made ATR liquid flow cell (polytetrafluoroethylene - PTFE) flow cell, which we tested several times.

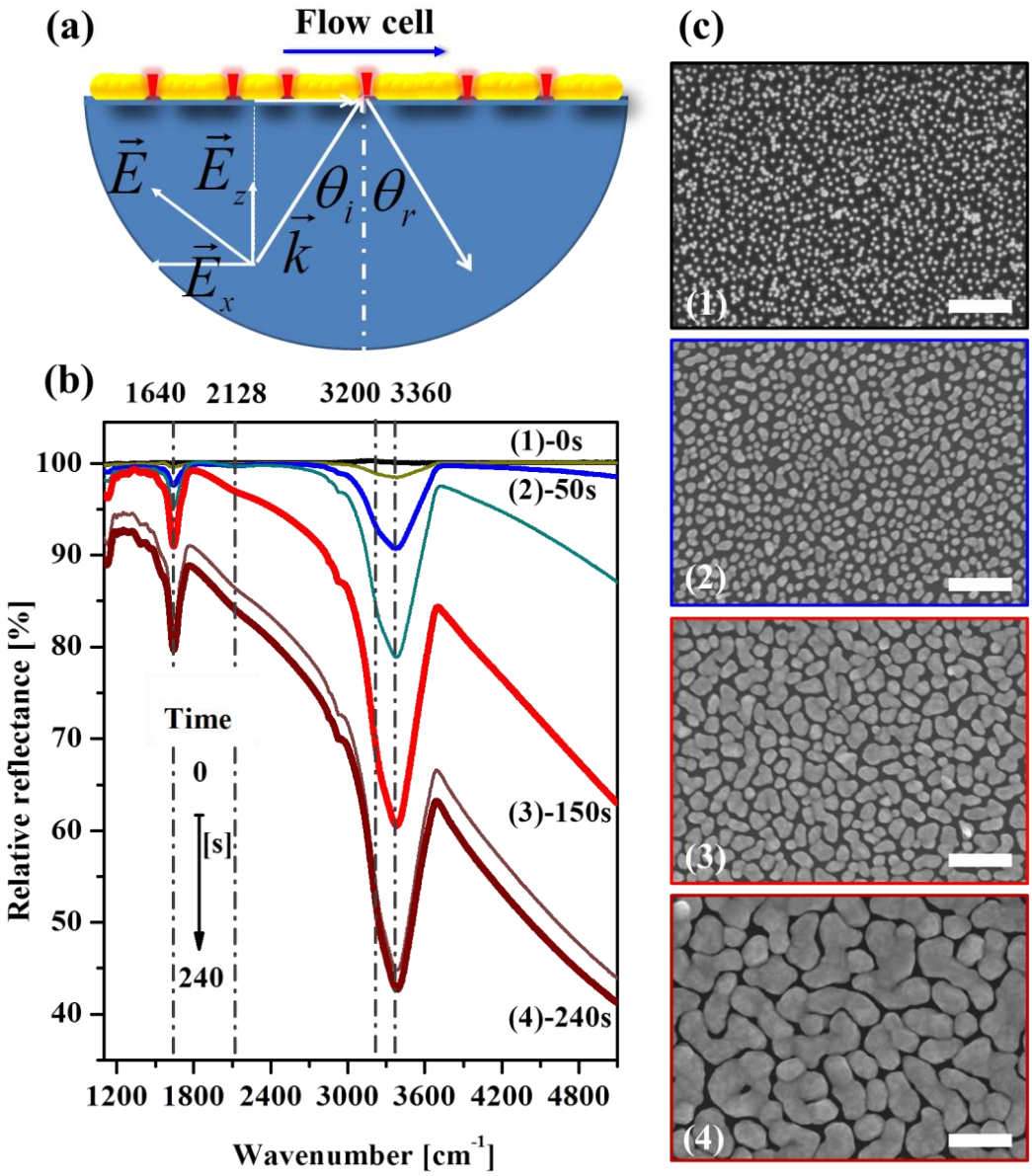

Figure 3.8. *In situ* growth of random gold nano-islands with multiple gaps (hot-spots) for SEIRA application. (a) Schematic illustration of a SEIRA substrate using Au-islands with multiples hot-spots on Si crystal under ATR configuration. (b) Evolution of vibrational signals from water during the growth of Au-islands indicating the plasmon resonance responded to IR range when the size of AuNPs increased. (c) SEM images show the evolution of Au-islands corresponded to the enhancement of vibrational signals of water. The scale bar is 200 nm.

During the process of deposition of Au on the pre-adsorbed AuNPs on the ATR crystal, the Au-nanoparticle distribution, the size and shape of the nanoparticles, and their interaction (electromagnetic coupling) change. This morphological development causes drastic changes of the electromagnetic field at the gaps of Au nano-islands on the ATR active surface. Figure

3.8a describes the experiment setup of the *in situ* SEIRA spectroscopy. Figure 3.8b schematically illustrates four different stages of the forming of plasmonic nanogaps corresponded to their enhancements on the vibrational signals of water, where stage (1) is the virgin AuNPs (as deposited of AuNPs) with the IR spectrum was taken as the background. The enhancent of vibrational signals of water by forming of Au nano-islands from states (2)-(4) are shown in Fig. 3.8b, and the coressponded Au nano-islands were confirm by SEM as shown in Fig. 3.8c. It was found that, by increasing the size of Au inslands, the vibrational signals of water, including a bending mode located at 1640 cm^{-1}, a combination of bending and libration mode located at 2128 cm^{-1}, and a combination of symmetric stretch mode and overtone of bending mode located at around 3360 cm^{-1}, were increased due to the plasmon-enhanced near field responded to IR range. The vibration signals of water are maximum when the Au-islands are grown after 140 second at state (3), where the Au film are formed as coalesced Au nano-islands with plasmonic nanogaps. However, the vibration signals were then sligtly dicreased when increase the deposition time up to 240 second as state (4). In this state, Au-islands are formed like percolated film, reducing the localized suface plasmon density. The Au-islands can be connected completely to form Au planar film with no localized surface plasmon resonance. Therefore, the Au nano-islands were optimized to sate (3), where the enhancement is maximum.

The Au nano-islands based IR plasmonic nanogaps were used as a SEIRA substrate for *in situ* molecular sensing. A sensing of bovine serum albumin (BSA) molecule dissolved in water was systematically evaluated with different concentrations ranged from 3 pM to 300 nM. As results shown in Fig. 3.9a, the vibrational signals of BSA with two highest bands named amide-I at 1648 cm^{-1} and amide-II at 1536 cm^{-1} are detected even at very low concentration. The sensitivity of the Au nano-island with multiple plasmonic nanogaps based SEIRA is down to sub picomolar. To elucidate the field enhancement of the SEIRA substrate, the elec-

tric field distribution of Au nano-island formed plasmonic nanogaps was performed using FDTD simulation with simulation model imported from corresponded SEM images (Fig. 3.9 b). As shown in Fig. 3.9c-d, the hot-spots are located at the gaps of Au-island arrays with strong near-field enhancement of 20 folds under IR (2000 cm^{-1}) excitation, making the potential application in the *in situ* molecular sensing.

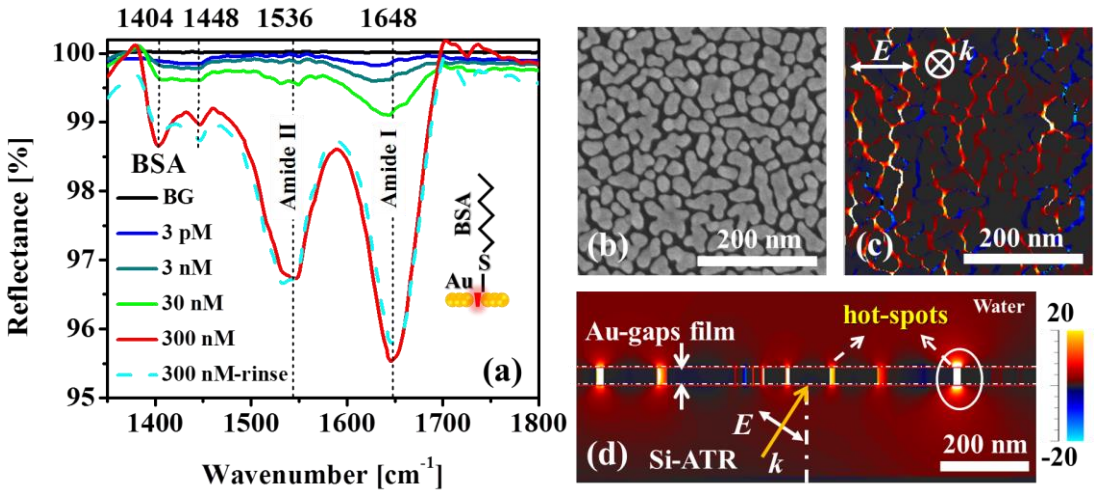

Figure 3.9. (a) Vibrational signals of BSA molecules adsorbed on Au-islands show high sensitivity of the Au nano-islands based SEIRA substrate (sub pico-molar). (b) SEM image of Au-islands with multiples gaps. (c) Corresponding multiple near-field hot-spot located at the gaps under IR excitation (2000 cm^{-1}). (d) A cross-section view of electric field distribution of Au-islands.

3.3.2. *In situ* chemical synthesis of plasmonic Au-patchy nanoshells for SEIRA

Au-nanoshell, a plasmonic nanoshell structure, is consisting of a dielectric core which is covered by an Au shell with nanometer thickness[78]. By varying the relative dimensions of the core and shell, the optical resonance of these plasmonic particles can cover a wide-range wavelength from VIS to IR regions. Because of its unique plasmonic properties, Au-nanoshell has been used in many nano-bio spectroscopic applications such as SERS[79], surface-enhanced fluorescence (SEF) [80], SEIRA[81]. However, the use of Au-nanoshell for near-field enhancement is mostly devoted to the near-field enhancement on the surfaces or in

the gaps between nanoshells. By contrast, we focus not only on the gaps between Au-nanoshells but also on the gaps between Au-islands of the Au-patchy shell layer, which can produce a large number of the internal hot-spots.

In previous subsection, the *in situ* chemical synthesis of random Au-islands based plasmonic nanogaps for SEIRA application was introduced. Here, we demonstrate another plasmonic nanogaps structure composed of Au-patchy on SiO_2 nanospheres, which also can provide a three dimensional multiple plasmonic nanogaps for *in situ* SEIRA spectroscopy application. Each individual nanoparticle contains multiple nanogaps where the electric field is highly concentrated and amplified under broadband excitation from near to middle infrared (IR). These IR-active plasmonic structures show high sensitivity in sensing the vibrations of bio-molecules. Furthermore, we demonstrate our *in situ* SEIRA study on the detection of trace amount of mercury ion down to nM level in water by studying the relevant conformational changes of glutathione (GSH) molecules, which is induced by the adsorption of mercury ions. In addition, this structure also showed large SERS enhancement on methylene blue molecules under NIR laser excitation of 785 nm. Hence, we propose that the ensemble of plasmonic Au-patchy nanoparticles with multiple hot-spots and facile synthesis method can be another promising candidate for plasmonic biosensor applications.

3.3.2.1. *In situ* synthesis of plasmonic Au-patchy SiO_2 core-shell particles

We approached the present method on the *in situ* controlled growth of plasmonic Au-patchy SiO_2 core-shell particles on Si-ATR crystal for SEIRA application. Firstly, we prepared AuNPs-SiO_2 particles as the seeds for growing plasmonic Au-patchy SiO_2 core-shell array. The seeds particles were prepared by “seeds and growth” method using silica core with diameter of 180 nm synthesized by Stober route[82]. Silica particles suspended in water with diameter of 180 nm synthesized by Stober route were functioned with amine groups by reaction

with APTES. A 1 ml of APTES-functionalized silica NPs were then added to 3 ml of AuNPs (1-2 nm) solution, which is prepared by modified Duff method as a shell layer on SiO_2 core[82]. Gold NPs adsorb to the amine groups on the silica NPs surface, resulting in a APTES functionalized silica NP decorated with discrete of small gold NPs, called the 'seeds' particles. A 5-10 nm AuNPs shell layer was then grown on these 'seeds' via the electroless gold plating process by using gold plating solution in the presence of formaldehyde.

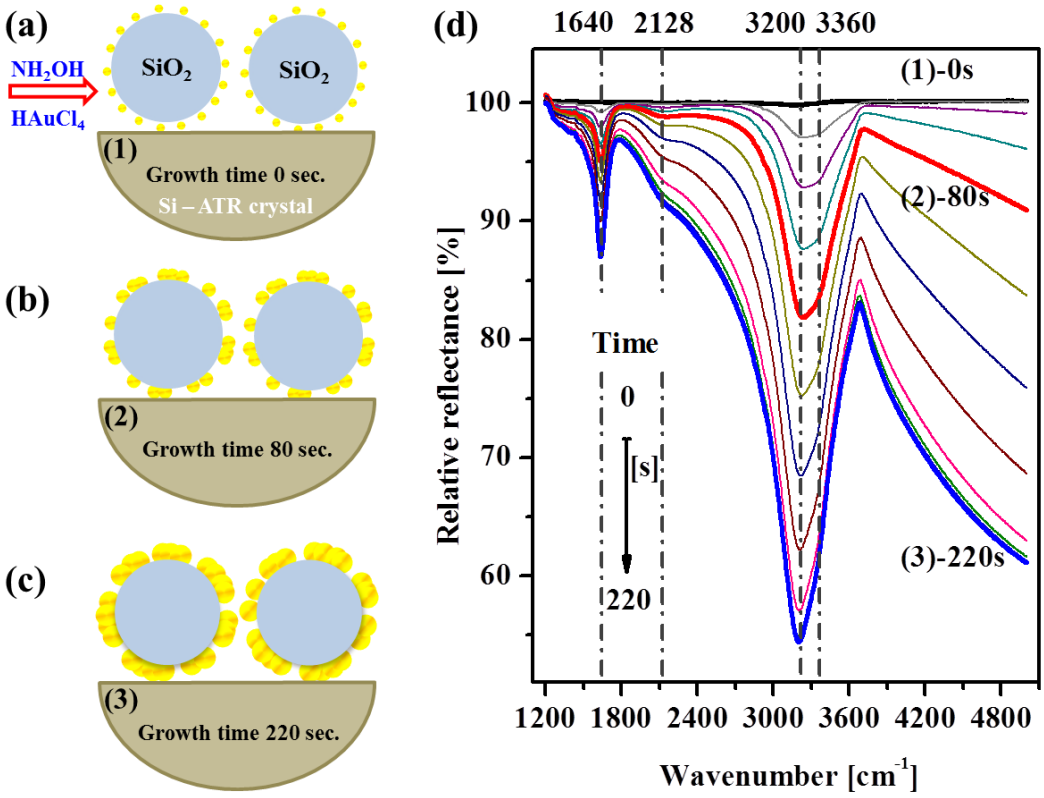

Figure 3.10. *In situ* growth of Au-patchy SiO_2 core-shell particles on Si-ATR substrate for SEIRA. (a)-(c) Schematic illustrates the growing process. (d) Evolution of vibrational signals from water corresponded to the evolution of Au-islands on SiO_2 particle.

The AuNPs-SiO_2 seeds were then formed a sub monolayer on Si-ATR crystal. Firstly, a SAM of APTES was formed on Si-ATR crystal by immersing the cleaned Si-ATR in 10% APTES-methanol solution for 1 hour. The APTES-functionalized Si-ATR was then cleaned in methanol under a pulse sonication for 5 min to remove any exceed molecules. A 200μl droplet of AuNPs-SiO_2 seeds suspension was then deposited at centre of the planar probe surface of the

APTES-functionalized Si-ATR crystal. After one hour, the AuNPs-SiO_2 seeds adsorbed on Si-ATR crystal was rinse 3 times by distilled water to remove the exceed nanoseeds, and a sub monolayer AuNPs-SiO_2 seeds was finally formed on Si-ATR crystal surface.

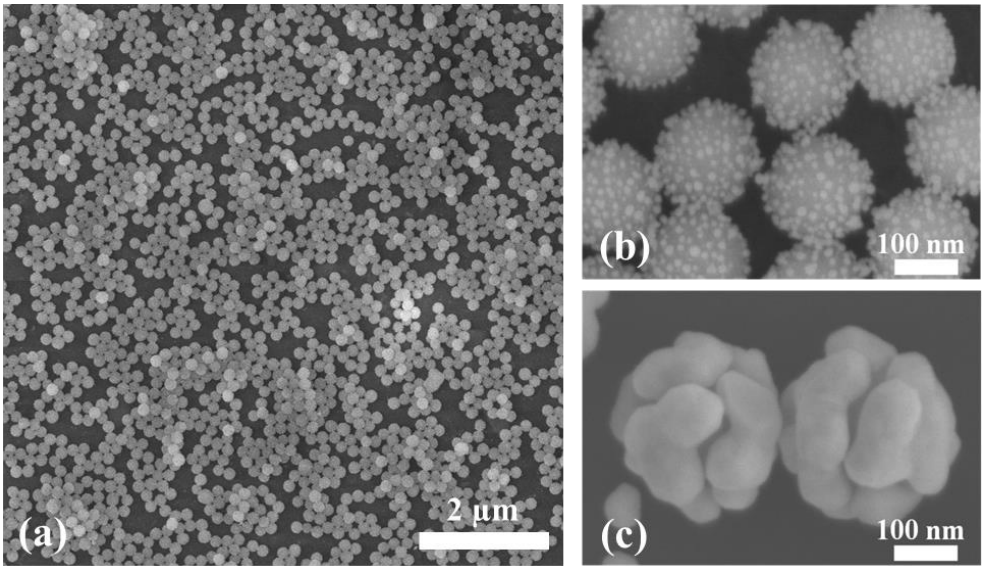

Figure 3.11. SEM image of Au-patchy SiO_2 core-shell particles. (a) Before growth. (b) After growth for 60 second. (c) Final growth (200 second).

The *in situ* FTIR controlled growth of the plasmonic Au-patchy SiO_2 core-shell particles are demonstrated in Fig. 3.10, including the growth process (Fig. 3.10a-c) and the monitoring of water vibrations as evolution of Au-patchy shells (Fig. 3.10d). Firstly, the AuNPs-SiO_2/Si-ATR crystal was set into a custom made PTFE flow-cell in a FTIR spectrometer (Thermo Nicolet Nexus 670 FT-IR spectrometer, KBr beam splitter, MCT detector). Distilled water was pumped into flow-cell for 2 min to remove any contaminations using a micro-pump with a constant flow rate of 3 ml/min. The reflectance signal from water was set as the background for *in situ* growth process as shown in state (1) (Fig. 3.10a). A mixed tetrachloroauric acid trihydrate ($HAuCl_4.3H_2O$, 99.9 %) (0.3 mM) and NH_2OH (0.4 mM) solution was then pumped into flow-cell as the precursor solution for growing the Au-patchy shell layer via electroless gold plating process. Similar to the *in situ* growth process of random Au nano-

islands, the vibrational signals from water were enhanced during the evolution of Au shell layer on SiO_2 core particles as shown in states (2) (Fig. 3.10b) and (3) (Fig. 3.10c), which is due to the near-field enhancement induced by hot-spots between gold nano-islands on SiO_2 spheres surface. Similar to the growth of random Au nano-islands, the Au-patchy nanoshells are optimized to state (3) (Fig. 3.10c) at growth time of 200 second with a highest enhancement. Beside the *in situ* controlled growth of Au-patchy nanoshells by *in situ* FTIR spectroscopy, the *ex situ* SEM was also employed to confirm the morphology of Au-patchy nanoshells as shown in Fig. 3.11. The SEM images of the functioned SiO_2 particles with Au seeds mono-dispersed on Si-ATR crystal, after growth for 60 second, and after growth for 200 second are shown in Fig. 3.11a-c, respectively. It was found that, after growth for 200 seconds, the Au-patchy shell layer has a thick ness of about 20 - 30 nm, and the gaps between Au-islands were 5-10 nm.

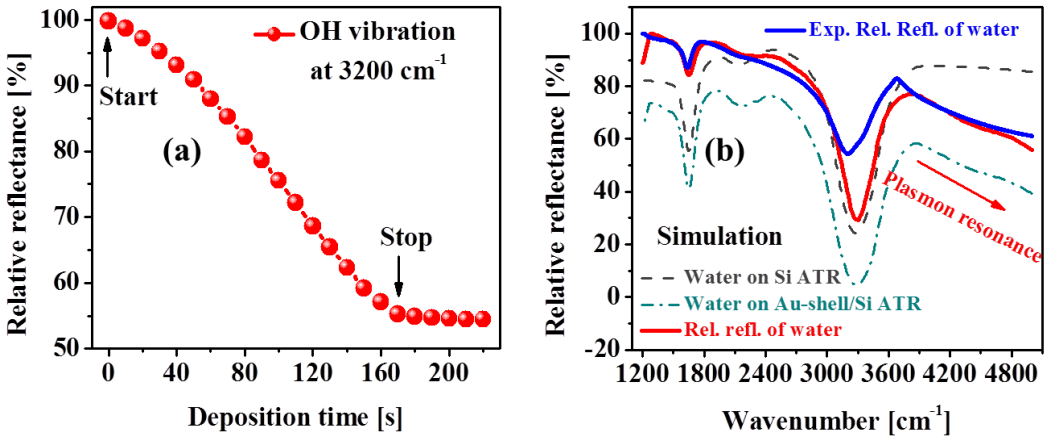

Figure 3.12. (a) Relative reflectance signal at 3200 cm^{-1} of water vibration (combination of symmetric stretch mode and overtone of bending mode) by growth time of Au-patchy shell layer. (b) Simulated the enhancement of water vibrations induced by near-field plasmon enhancement of Au-patchy SiO_2 core-shell particles.

The evolution of Au-patchy shells is summarized by taking the reflectance of vibrational signal at 3200 cm^{-1} (combination of the symmetric stretch mode and overtone of bending mode) as shown in Fig. 3.12a. As seen that the intensity of the vibration signal is saturated when the

Au-patchy shells grown after 170 second. We further performed RCWA numerical simulation to investigate the enhancement effect of the Au-patchy SiO_2 hybrid. As shown in Fig. 3.12b, by normalizing the vibrational signals of water using Au-patchy shells to bare Si-ATR crystal, the enhancement is clearly seen in the Au-patchy shells compared to bare Si-ATR substrate.

The Au-shells were then applied for *in situ* vibrational sensing. The sensing of glutathione molecule and the detection of toxic mercury ions at low concentration will be present in the next parts.

3.3.2.2. *In situ* SEIRA using Au-patchy nanoshells array

The L-glutathione reduced (γ-Glu-Cys-Gly, GSH) (Sigma–Aldrich) molecule was first dissolved in distilled water with variety of concentrations. A 5 ml of GSH molecule solution was then inserted into PTFE flow-cell of Au-patchy nanoshells/ATR at a slow rate of 0.5 ml/second. Due to the binding of thiols group (-S-, deprotonated state) on Au with negative surface charges, the GSH molecules were then adsorbed on Au surface as well as at the Au gaps, which can be excited as the extreme hot-spots to enhance vibrations of GSH. As seen in Fig. 3.13a, the vibrational signals of GSH, beside two strong bands related to amide-I band (1640 cm^{-1}) and amide-II band (1536 cm^{-1}), the carboxylic acid vibrations ν(-COOH) (1724 cm^{-1}) and the symmetric ν_s(-COO-) (1404 cm^{-1}) and asymmetric ν_{as}(-COO-) (1593 cm^{-1}) stretching vibrations related deprotonated states of carboxylic acid are also observed. The vibrational signals are gradually increased when increase concentration of the GSH molecule. It was found that, the sensitivity detection of GSH molecule using Au-patchy nanoshells can be down at low concentration of 0.1 μM.

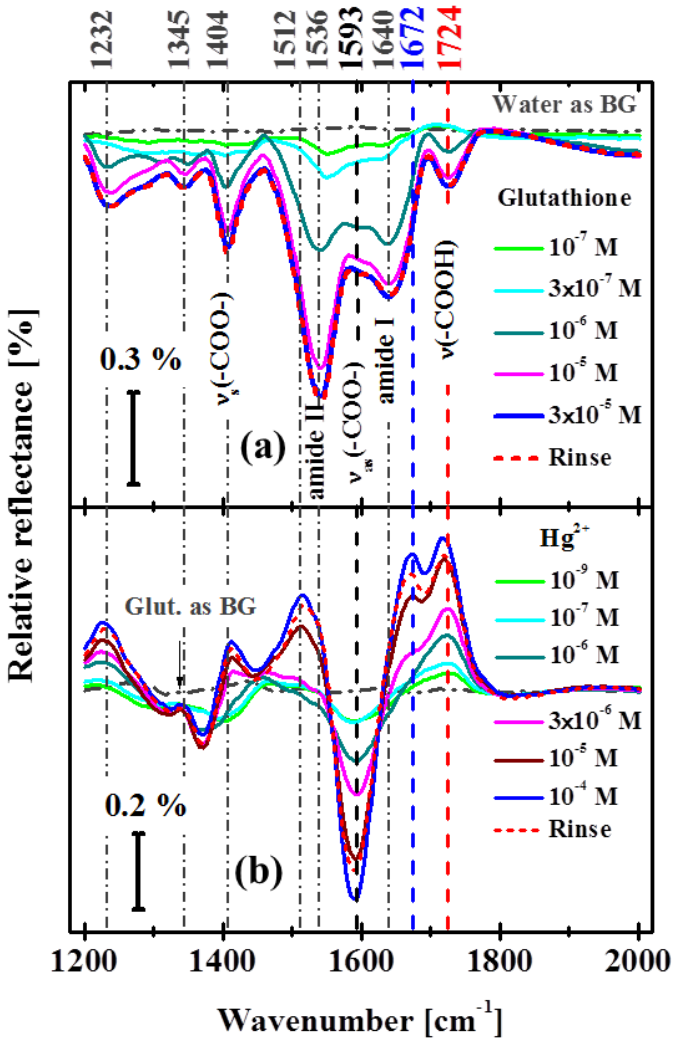

Figure 3.13. (a) *In situ* FTIR sensing of glutathione (GSH) molecules using Au-patchy SiO_2 core-shell particles as SEIRA substrate. (b) *In situ* FTIR detection of mercury ions in water using GSH-functioned Au-patchy SiO_2 core-shell by monitoring the relevant conformational changes of GSH vibrations when mercury ions adsorbed into GSH molecules.

The GSH molecule is well-known as a treatment molecule of mercuric toxicity[83]. As a result of the specific binding of mercury ion to GSH by (–COO–Hg–OOC–) bridge, the GSH molecule can also be used as a linker molecule in the detection of Hg ions[83]–[86]. In this study, the *in situ* detection of mercury ions in water was performed using Au-patchy SiO_2 plasmonic hybrid as SEIRA substrate and GSH as linker molecule. The sensing mechanism is described as following. The GSH molecules adsorbed on Au nano-islands on Au-patchy nanoshells/Si-ATR after rinsed by distilled water to remove any unbounded molecules was

then taken as a back ground spectra. Now any conformal and intensity changes of the vibrational signals of GSH can be detected by monitoring the IR spectra. A 5 ml of diluted Hg^{2+} ions ($HgCl_2$) in water with variety concentrations were inserted in to GSH treated Au-patchy shells/Si-ATR at a rate of 0.5ml/second, and keep until the adsorption of toxic ions is saturate. It was found that, the Hg^{2+} ions are immediately captured by GSH molecules within few seconds, it make the fast response in the detection of Hg^{2+} ions. The conformal and intensity changes of GSH vibrations were detected due to the adsorption of Hg^{2+} ions to GSH by (–COO–Hg–OOC–) binding as shown in Fig. 3.13 b. As seen that, due to the binding of Hg^{2+} ions with GSH molecules, the relative reflectance peaks of GSH at 1724 cm^{-1}, 1672 cm^{-1}, 1512 cm^{-1}, 1404 cm^{-1} and 1232 cm^{-1} are systematically decreased depending on the concentration of Hg^{2+} ions, while the peak at 1593 cm^{-1} is increased. These changes were not observed from the water without Hg^{2+} ions.

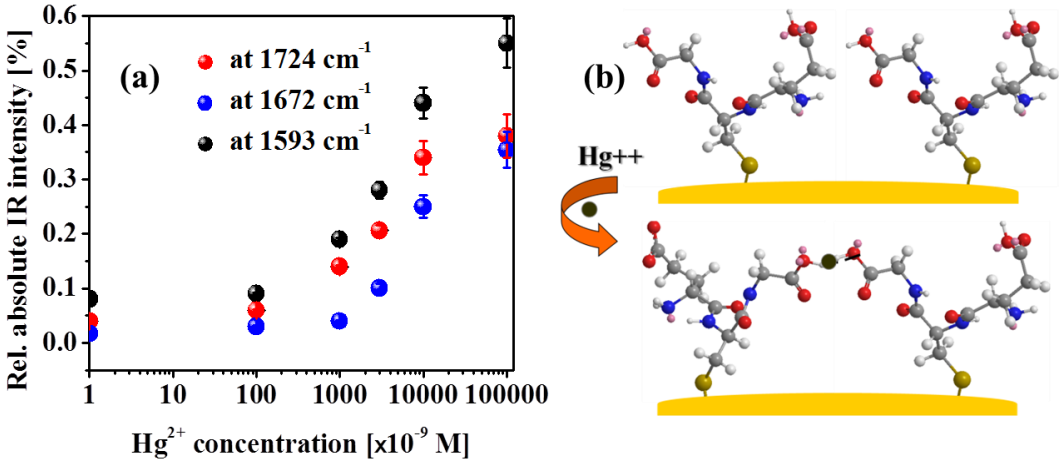

Figure 3.14. (a) Evolution of relevant conformal changes of GSH vibrations induced by adsorption of mercury ions into GHS molecules. (b) Model for mercury ions adsorb into GSH molecules.

Figure 3.14a plots the relation absolute intensity of the conformal change of GSH molecules adsorbed Hg^{2+} ions for three peaks at 1724 cm^{-1}, 1672 cm^{-1}, and 1593 cm^{-1}. Figure 3.14 illustrates the binding mechanism between GSH molecules with Hg^{2+} ions. Using this Au-patchy

SiO_2 hybrid with multiple gaps for *in situ* SEIRA, the sensitivity in the detection of mercury ions in water was found to be 1 nM.

3.3.2.3. SERS study on Au-patchy SiO_2 core-shell

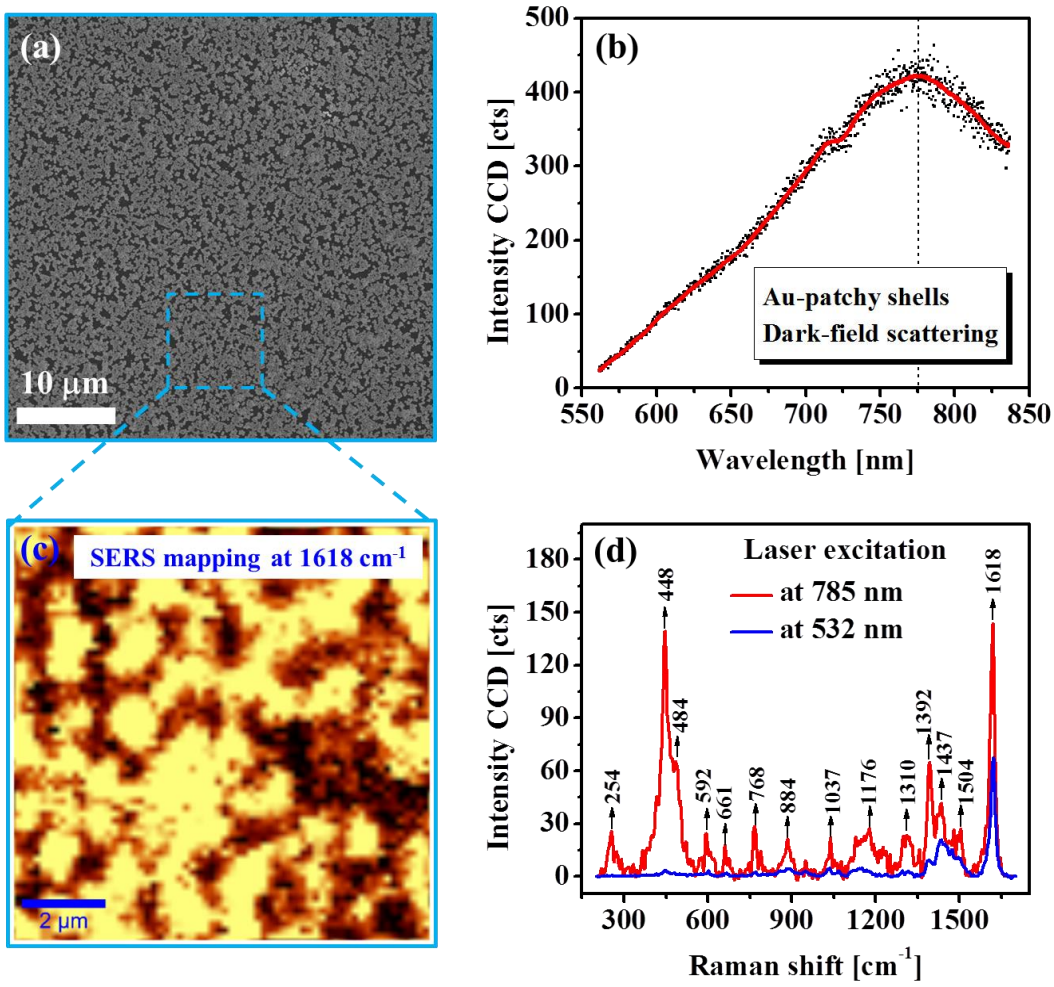

Figure 3.15. (a) SEM image of Au-patchy SiO_2 core-shell particles. (b) Dark-field scattering spectrum of Au-patchy shells with resonance peak located at around 780 nm. SERS study of MB adsorbed on Au-patchy shells (c) SERS mapping image (integrated at 1618 cm^{-1}, excited by 785 nm laser) and (d) Comparison between SERS spectra excited by 785 nm (red) and 532 nm (blue) lasers.

Because the nano-islands have random size ranging from few tens to several hundred nanometers, the Au-patchy SiO_2 hybrid can provide a broad resonance from NIR to IR ranges. Therefore, Au-patchy nanoshells with multiple gaps can act as multiple hot-spots are expected to be a good candidate for SERS application. The Au-patchy nanoshells arrays grown

by *in situ* chemical method were then applied for SERS experiment. Firstly, the dark-field scattering spectrum of Au-patchy nanoshells were carried out using an optical microscope (Raman microscope WITec alpha 300S, dark-field lens 50x, 0.55 NA, Zeiss) combined with a white light source (halogen lamp, Lucir-LAHL100). Figure 3.15a shows an SEM image of Au-patchy nanoshells arrays in which its dark-field spectrum has a broad resonance in NIR as shown in Fig. 3.16b. The Au-patchy SiO_2 hybrid was then treated with methylene blue (MB) molecule by shocking in a MB solution (0.5×10^{-5} M in water) for 10 hour, and rinsed with distilled water to remove any unbounded MB molecules. The SERS on the MB treated Au-patchy shells was studied using two different continuous lasers, 532 nm and 785 nm at the same power of 0.1 mW as results shown in Fig. 3.15d. As seen that, the SERS signal intensity of MB adsorbed on Au-patchy shells in case excited by 785 nm laser is stronger than that of the case excited by 532 nm laser, indicating the SERS active at 785 nm and it is consistent with dark-field spectrum with resonance in NIR range.

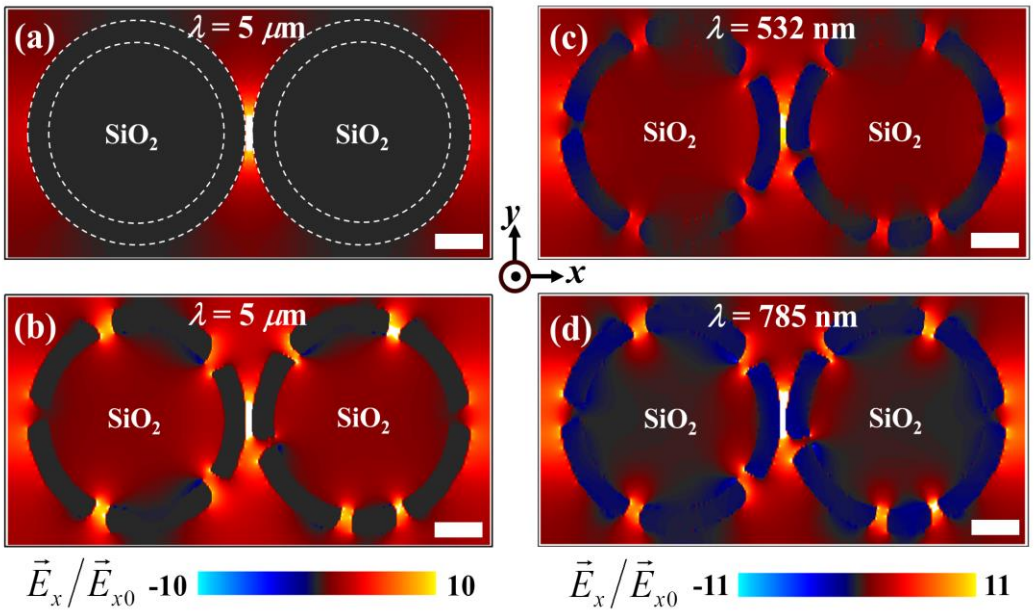

Figure 3.16. Electric field distributions of Au-patchy SiO_2 core-shells. (a) Au-SiO_2 core-shells with completed Au shells layer (without gaps) under IR excitation (5 μm or 2000 cm^{-1}). Au-patchy SiO_2 particles: (b) Under IR excitation (5 μm or 2000 cm^{-1}), (c) Under VIS excitation (532 nm). (d) Under NIR excitation (785 nm). The scale bar is 50 nm.

The simulated electric field distribution of Au-patchy nanoshells arrays were carried out for both IR and NIR regions using FDTD simulation as results shown in Fig. 3.16. A comparison of the electric field distributions between Au-shell (completed shell, Fig. 3.16a) and Au-patchy shells (Fig. 3.16b) were performed under excitation at 5 μm (2000 cm^{-1}). It is clearly seen that, the Au-patchy shells show multiple hot-spots located between Au-islands on the shell layer and between Au-patchy shells, while Au-completed shells show the hot-spot at only the gaps between Au-shells. It makes an advantage of the Au-patchy shells compared to Au-completed shells in SEIRA application. The field distribution of Au-patchy shells under excitation at 532 nm and 785 nm were also simulated as results shown in Fig. 3.16c and Fig. 3.16d, respectively. As seen that, the hot-spots of enhanced electric near-field of Au-patchy shells in case excited by 785 nm laser are stronger than that of 532 nm excitation.

3.3.3. Conclusion of plasmonic Au-patchy SiO_2 for SEIRA

The *in situ* chemical synthesis of Au nano-islands and their application for *in situ* SEIRA spectroscopy were investigated. The method was applied for Au-patchy nanoshells, which can provide three dimensional plasmonic nanogaps as the multiple hot-spots for vibrational sensing application. The Au-patchy SiO_2 nanoshells hybrid with random Au-islands on shell layer showed dual SEIRA and SERS active substrate due to its broad resonance. The *in situ* sensing of GSH molecule as well as the *in situ* detection of mercury ions in water were studied on the Au-patchy nanoshells based SEIRA substrate with a high sensitivity of 1 nM. We expect that the developed *in situ* SEIRA on Au-patchy nanoshells arrays can be a good candidate for the *in situ* vibrational sensing application.

3.4. Summary of Chapter 3

We have investigated the use of plasmonic nanogaps hybrids for molecular sensing application, including the SERS and SEIRA. Floating aluminum bowtie antenna array was designed as the SERS active antenna for 532 nm excitation. The optical properties of Al bowtie were studied using both electromagnetic simulation and dark-field scattering spectroscopy. The fabricated Al bowtie antenna showed strong near-field enhancement at the gaps of bowtie antenna under excitation at 532 nm, provided a good candidate for SERS study at 532 nm excitation as well as the SERS imaging spectroscopy in the molecular sensing. An *in situ* SEIRA spectroscopy on Au-patchy nanoshells with multiple plasmonic nanogaps was developed and studied. The Au-patchy nanoshells showed high performance *in situ* molecular sensing and detection of mercury ions at low level of 1 nM. In addition, the Au-patchy nanoshells also can act as a NIR-active SERS substrate, provided a plasmonic substrate for dual SERS and SEIRA spectroscopy.

4. METAL OXIDE SEMICONDUCTORS FOR PHOTOELECTRIC CONVERSION AND PLASMONIC NANO-HYBRID FOR EFFICIENT PHOTOCATALYSTS

We have proposed two plasmonic hybrids with strong near-field confinement at the plasmonic nanogaps for sensing applications, including Al bowties for SERS and Au-patchy nanoshells for SEIRA. The combination of plasmonic materials with metal-oxide semiconductor can also provide an efficient absorption of the light in photoelectric conversion. In this chapter, we demonstrate the application of metal-oxide semiconductor nanostructure and its coupling with localized plasmonic nanoparticle for efficient photocatalyst. The first section introduces the chemical synthesis of metal oxide ZnO nanowires and TiO_2 thin film. The second section presents a combination of ZnO NWs and TiO_2 in a core-shell p-n heterojunction for application in UV photodetector. And in the third section, we investigate the coupling of localized plasmonic NPs with ZnO in NPs-ZnO NWs hybrid for efficient photocatalysts.

4.1. ZnO NWs and TiO_2 film: Chemical synthesis and characterizations

4.1.1. Metal-oxide ZnO and TiO_2 nanostructures

Metal oxide semiconductors have great potential for many applications such as in the field of electronics, optoelectronics, and light-harvesting devices because they are inexpensive compared to silicon and metal nitride. Recently, there have been a great deal of interest in oxide based nanomaterials such as ZnO, TiO_2, CuO_2/Cu_2O and so on because of the availability/possibility of soft chemical synthesis besides tremendous application potential. Among them, ZnO nanostructure has been considered as a promising material for optoelectronic devices. ZnO nanostructure includes highly ordered nanowire arrays, tower-like structures, nanorods, nanobelts, nanosprings, nanocombs, and nanorings[87], [88]. ZnO nanowires (NWs), one-dimensional nanostructures with high surface-volume ratio, have shown an efficient light

absorption and charge separation. With the direct bandgap energy in near ultraviolet (3.37 eV)[87], [89] range and high quantum efficiency make ZnO nanostructure an excellent candidate for many applications such as solar cell[90], UV photodetector[91], [92], UV laser[93], [94], piezoelectric generators[6] and photocatalyst[95], [96]. Similar to ZnO, TiO_2 is a large bandgap semiconductor that is commonly investigated in rutile (bandgap 3.0 eV) and anatase (bandgap 3.2 eV)[97]. In this work, by using wet chemical fabrication process, we aim to fabricate a large-area ZnO NWs array as well as core shell TiO_2/ZnO NWs, and especially, integrating ZnO NWs with plasmonic nanoantenna for the efficient photoelectric conversion devices.

4.1.2. Chemical synthesis of ZnO NWs and TiO_2 thin film

4.1.2.1. Hydrothermal growth and characterizations of ZnO NWs

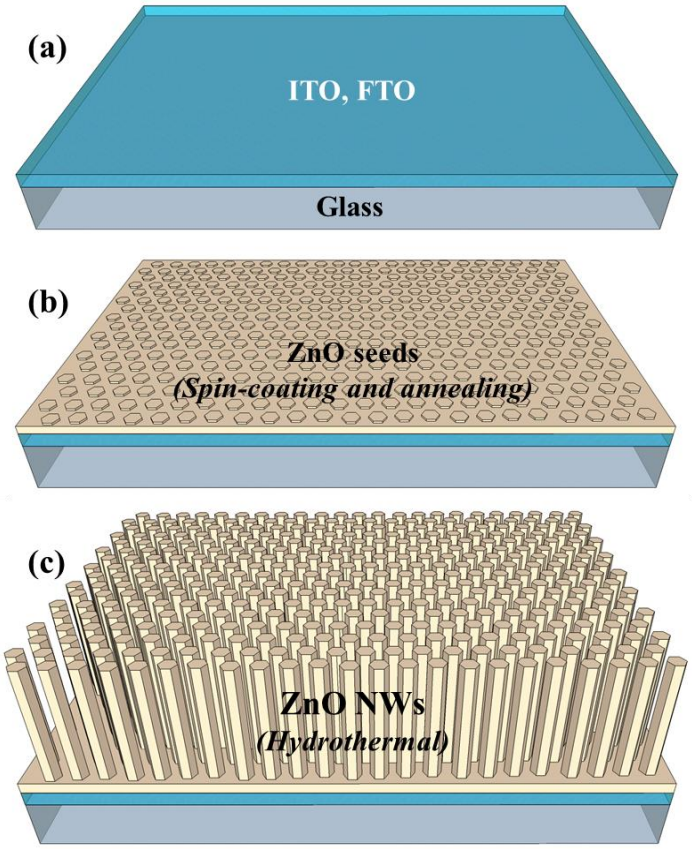

Figure 4.1. Schematic of the hydrothermal growth of ZnO NWs

The ZnO NWs array was synthesized on ITO-glass substrates by hydrothermal method[98], this has been proven to be a simple and efficient method. Figure 4.1 illustrates the fabrication process of ZnO NWs. First, the ITO-glass was cleaned thoroughly one time in acetone, two times in ethanol and one time in de-ionized water (5 min for each time), and subsequently dried with N_2 gas (Fig. 4.1a). A ZnO seeds layer was then prepared on top of the ITO-glass substrate (Fig. 4.1b). The mixed solution of zinc acetate dihydrate [$Zn(C_2H_3O_2)_2.2H_2O$] (0.3 M) and monoethanolamine (MEA) solution (0.3 M) in ethanol was coated onto ITO-glass substrate three times by spin-coating at 3000 rpm for 30s. The ZnO seeds layer was the dried at room temperature and annealed in ambient air at 300 °C for one hour. For the growth of ZnO NWs, a mixed aqueous solution of zinc nitrate hexahydrate [$Zn(NO_3)_2.6H_2O$] (0.03 M), hexamethylenetetramine [$(CH_2)_6N_4$, HMT] (0.03 M) and polyethylenimine (PEI) (0.003 M) was prepared. The ZnO seeds coated substrates was dip into this solution and stirred at 68 $^{\circ}$C for 3 hours. The fabricated ZnO NWs array (Fig. 4.1c) was then washed in de-ionized water, ethanol and then thermally treated (write treating procedure) in ambient air.

Figure 4.2 presents the structure and morphology characterizations of a typical fabricated ZnO NWs. Figure 4.2a shows an SEM image of the ZnO seeds formed onto ITO-glass substrate. Figures 4.2b-c show the top-view, tilted-view, and cross-sectional SEM images of the typical ZnO NWS grown by present hydrothermal method. The ZnO NWs in the array are growing nearly vertically on the ITO glass substrate with an average diameter of 50 nm, average length of 0.8-1μm, and wire density of 2.10^{10} cm^{-2}. A high-resolution TEM image of a single ZnO NW (Fig. 4.1e) shows very high crystalline quality of ZnO NW with [0001] growth orientation. Figure 4.1f shows the XRD patterns (XRD, Rigaku Rint 2000, Cu K_α) of the ZnO NWs on ITO substrate (red curve) and a comparison with bare ITO substrate (black curve), these exhibiting ZnO diffraction peaks are in good agreement with the JCPDS card No. 36-1451 of

bulk ZnO with hexagonal wurtzite structure. In addition, a strong peak at 34.39° of ZnO (002) plane shows that the nanowires are well oriented and high crystalline quality.

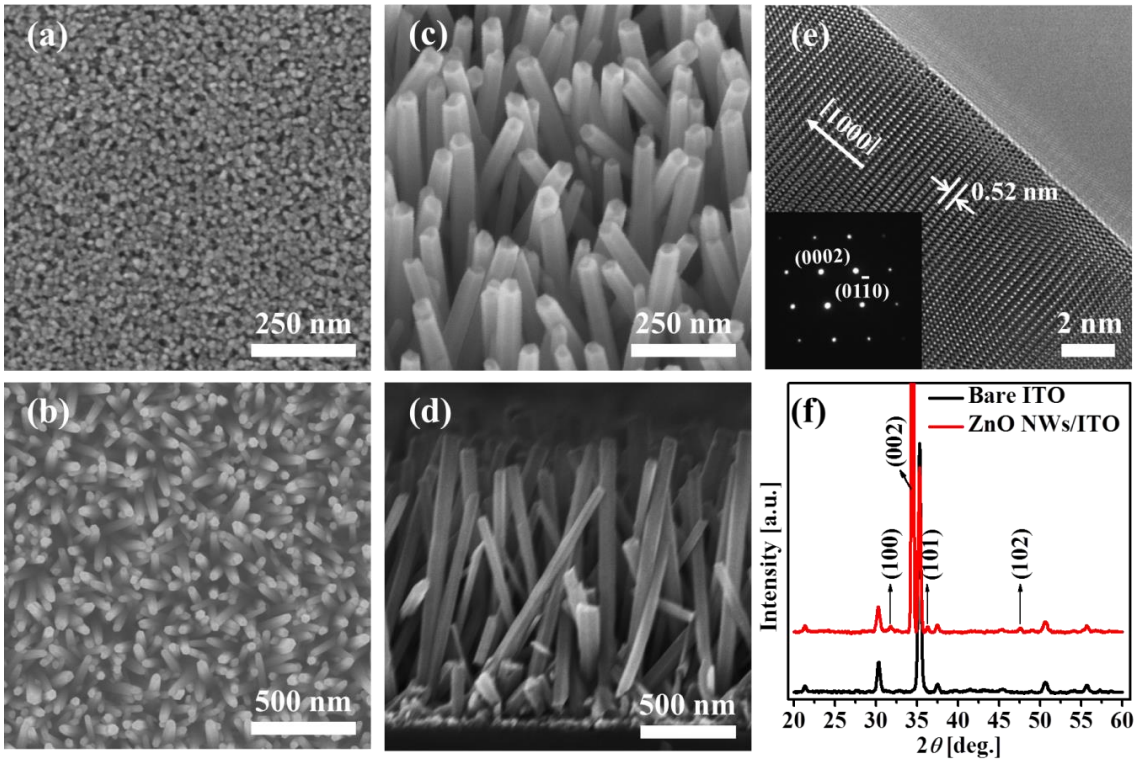

Figure 4.2. Structure and morphology characterization of ZnO NWs fabricated by hydro-thermal method. (a) SEM image of ZnO nanoseeds formed by spin-coating and annealing processes. (b) Top-view, (c) Tiled-view and (d) Cross-sectional SEM images of typical ZnO NWs with averaged diameter of 50 nm and length of about 0.8 – 1 μm. (c) HR-TEM image of a single ZnO NW with [0001] growth orientation. Inset shows SAED of the ZnO NWs. (f) XRD patterns of single crystal ZnO NWs on ITO-glass substrate and bare ITO-glass.

The vibrational spectroscopy of ZnO NWs were carried out using FTIR (Nicolet IS50R-FTIR, DTGS-ATR detector and KBr beam splitter) and Raman (Micro Raman Witec Alpha 300S) spectrometers as shown in Fig. 4.3. The FTIR spectra of ZnO NWs was taken from a ZnO NWs array fabricated on a Si (111) substrate as result shown in Fig. 4.3a with the a strong band of Zn-O stretching vibrational located at 400 cm^{-1}. Figure 4.3b shows Raman spectra of ZnO NWs with strong peaks located at 99 cm^{-1}, 332 cm^{-1}, 437 cm^{-1}, 481 cm^{-1}, and 572 cm^{-1}, which are related to E_{2l}, multiphoton, E_{2h}, 2LA and A_1(LO) modes[99], [100].

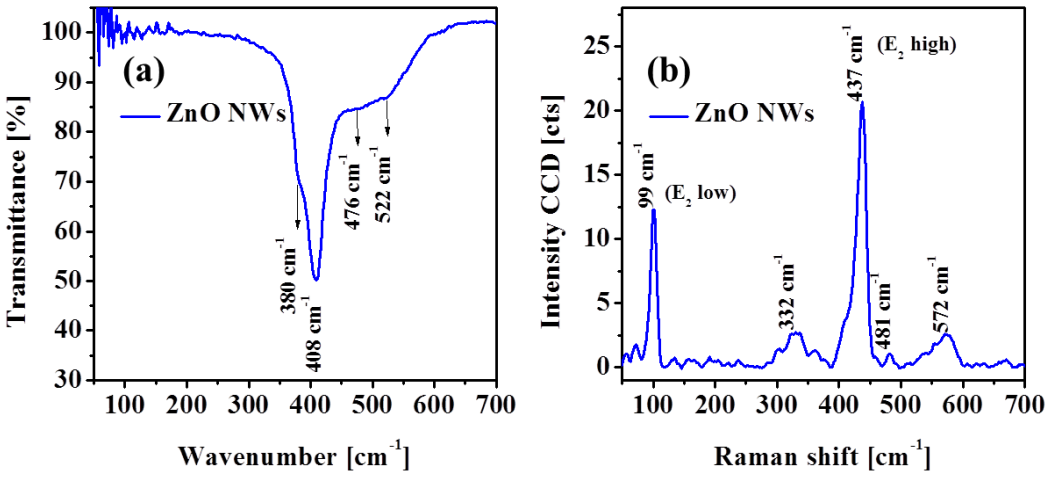

Figure 4.3. FTIR (a) and Raman (b) spectra of ZnO NWs.

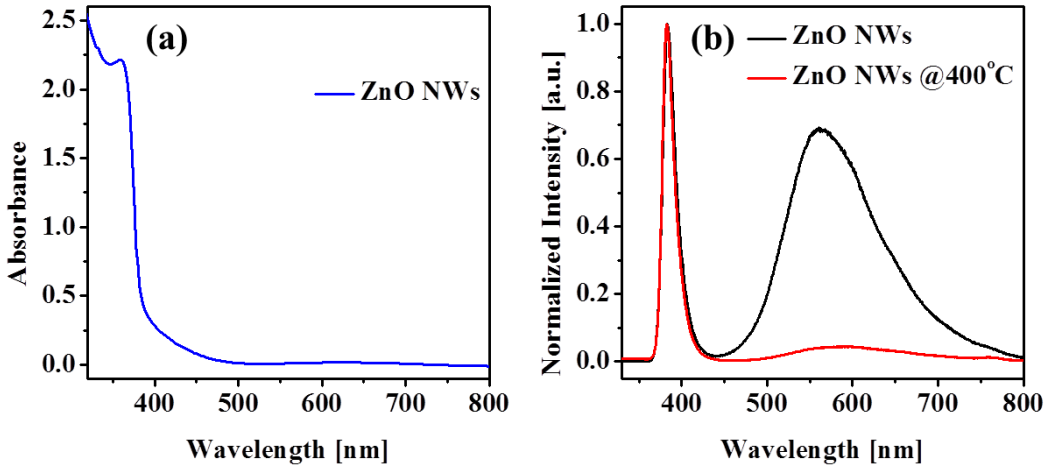

Figure 4.4. (a) Absorption and (b) Photoluminescence spectra of ZnO NWs.

Optical properties of the ZnO NWs were characterized by UV-VIS spectrometer (Jasco V-570) and the fluorescence microscope (Horiba Jobin-yvon, 325 nm He-Cd excitation laser source). Figure 4.4a shows the absorbance of ZnO NWs with strong absorption peak at 365 nm related to band gap absorption of ZnO. Figure 4.4b shows the photoluminescence spectra of ZnO NWs with (red curve) and without (black curve) thermal treatment at 400 °C. Beside the band-edge emission at 384 nm, we observed a broad visible emission around 560nm mainly originated from the surface oxygen vacancies, or from other defect such as oxygen interstitials and zinc vacancies[89], [101]–[104] known as deep donors. However, the visible emission was significantly reduced after the thermal treatment process (red curve in Fig.

4.4b). This reduction can be attributed to the transformation of the ZnO deep levels into shallow donor levels by the thermal annealing process[102], [105].

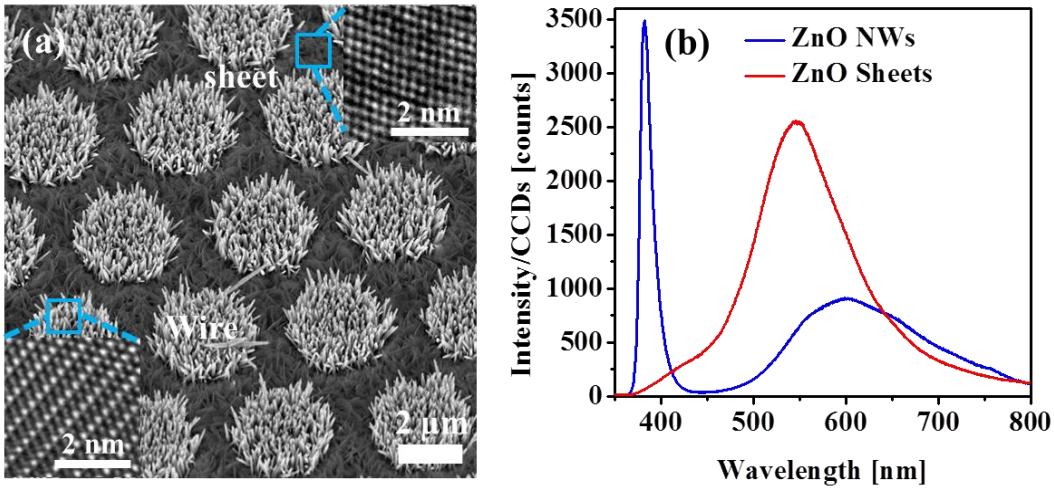

Figure 4.5. (a) SEM and TEM (insets) images of ZnO nanowires and nanosheets and (b) Their photoluminescence properties.

We also further investigate the optical properties of ZnO nanostructures through patterned selective ZnO nanowires- nanosheets (NWs-NShs) array. Figure 4.5a presents an SEM image of the ZnO NWs-NShs grown on an ITO-glass substrate using colloidal lithography method. First, polystyrene spheres (PS, Polybead® Polystyrene Microspheres - Polysciences) with diameter of 4.4 μm were chosen as the original lithography mask to create the patterned Al holes array. A monolayer of PS spheres was prepared on top of the ZnO seeds grown on ITO-glass substrates. The reactive ion etching using O_2 gas (RIE) was employed to shrink the size of PS with an etching rate of 3.1 nm/ second. The designed lithography masks with different sizes were obtained by controlling the etching time. Then an Al film of 50 nm was deposited on the etched PS arrays using electron beam deposition. The patterned ZnO seeds layer was achieved by removing the etched PS arrays. Finally, the partnered ZnO NWs-NShs array was growth using present hydrothermal method where ZnO NWs is grown inside Al holes mask and ZnO Shs is grown on top of Al film (SEM image in Fig. 4.5a). Figure 4.5b shows the different photoluminescence property of the ZnO NWs (blue) and ZnO NShs (red). It could be

originated from the different morphology of these two ZnO nanostructures. ZnO NWs is one dimensional structure with high crystallinity (TEM image in the inset of Fig. 4.5a) showing a strong band-edge emission (384 nm) and a weak defect emission (590 nm), which defect emission is mainly contributed by oxygen vacancies defect[89], [103], [104], [106]. In contrast, the ZnO NShs is two dimensional structure with low crystallinity (TEM image in the inset of Fig. 4.5a) showing a strong broad green band centered at 547 nm, which emission is mainly contributed by zinc vacancies defect[89], [103], [104], [107], while it shows a weak band-edge emission around 400 nm.

4.1.2.2. Cr –doped TiO_2 thin film prepared by sol-gel method

Similar to ZnO, anatase titanium oxide (TiO_2) semiconductor is also active in UV with indirect band gap of 3.2 eV[108] and p-type TiO_2-based materials can be prepared by doping with Fe[109], Mn[110], Cr[111]. This present work demonstrates the fabrication and characterization of the p-type Cr –doped TiO_2 thin film. A sol–gel technique was used to synthesize Cr-doped TiO_2 thin films[112]. To synthesize pristine TiO_2 and Cr-doped TiO_2 thin film, TiO_2 sol was prepared by hydrolysis of tetrabutoxide [$Ti(O(C_4H_9))_4$, Wako] as a precursor, and $Cr(NO_3)_2$ was used as a Cr dopant source. Firstly, a variety solutions of $Cr(NO_3)_2$ x (g) dissolved in 1.71 ml ethanol (99.5 %) were stirred at room temperature for 1 hour, and then 1ml of $Ti[O(C_4H_9)]_4$ was added in to $Cr(NO_3)_2$ solutions. In this work, x (g) values were 0, 0.035, 0.07, 0.14 to obtain Cr:Ti molar ratios of 0 (undoped), 0.03, 0.06 and 0.12. The mixed solutions were diluted by adding a 3 ml of a mixed solution of 24 μl water, 5 ml ethanol and 26 μl HNO_3, and then stirred continuously for 30 min at room temperature. A 70 nm estimated TiO_2 (Cr-doped TiO_2) films was formed by spin-coating (3000 rpm, 30 second) of a 50 μl TiO_2 (mixed Cr:TiO_2) solution onto cleaned ITO-glass or Si substrates, after air-dried, the coated film was then annealed at 450 °C in ambient air for 1 hour. It is noted that the thick-

ness of the TiO_2 thin film can be tuned by changing the viscosity of the TiO_2 solution or spin-coating rate.

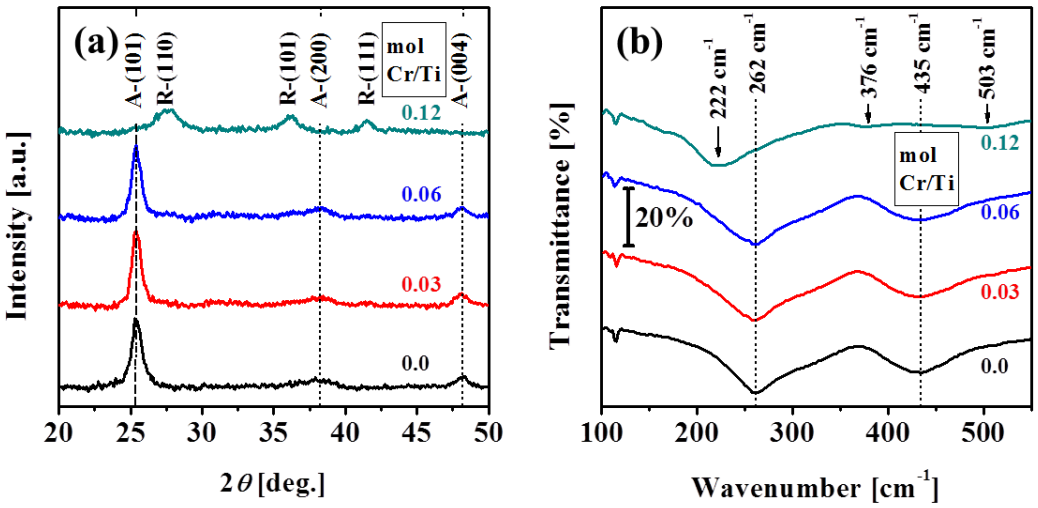

Figure 4.6. (a) XRD patterns and (b) FTIR spectra of Cr-doped TiO_2 thin films

The fabricated Cr-doped TiO_2 thin films were characterized by XRD and transmission FTIR spectroscopies. The films used in these two spectroscopies were fabricated on Si (100) substrates. Figure 4.6a presents the XRD patterns of the undoped and Cr-doped TiO_2 thin films. As seen that, the XRD pattern of the undoped and Cr-doped TiO_2 films in cases of Cr:Ti concentration ratios of 0.03 and 0.06 show a strong diffraction peak at 25.8° and two weak peaks at 36.9° and 48.2° indicating that these films were crystallized into anatase phase (JCPDS card No. 84-1286), while the highest dopant TiO_2 film shows three peaks at 27.5°, 36.2° and 41.6° indicating the features of rultile phase (JCPDS card No. 88-1175). In addition to that, the crystalline phases of the Cr-doped TiO_2 films were further confirmed by FTIR as shown in Fig. 4.6b, while the undoped and two lower dopant Cr-TiO_2 thin films show two transverse optical phonon bands of anatase film at 262 cm^{-1} and 435 cm^{-1}[113], [114], the highest dopant Cr-TiO_2 shows the absorption of rutile film at 222 cm^{-1}, 376 $cm^{-1}$and 503 cm^{-1}.

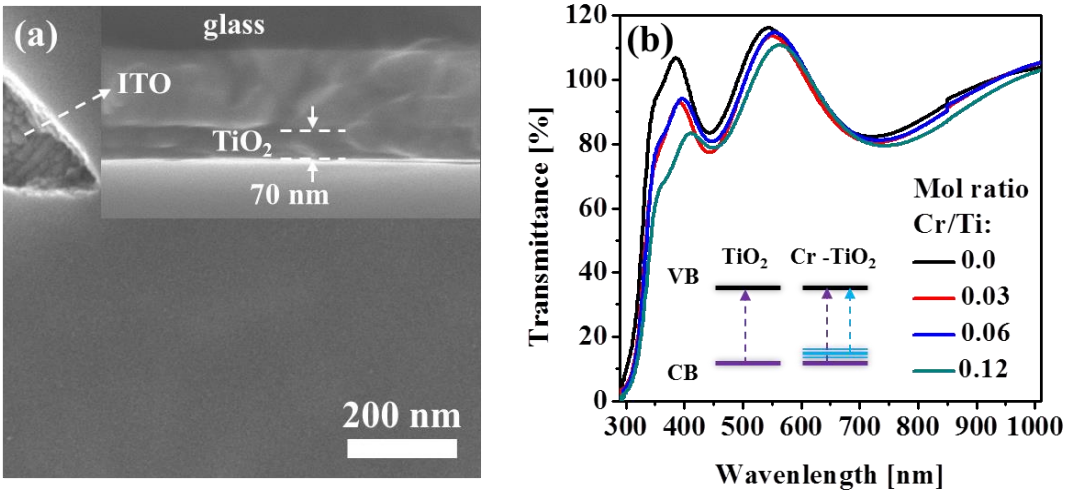

Figure 4.7. (a) Top view and cross-sectional (inset) SEM images of TiO_2 thin film fabricated on ITO-glass substrate. (b) Transmittance spectra of undoped and Cr-doped TiO_2 thin films.

The fabricated thin films were further characterized by SEM and UV-VIS spectroscopy. Figure 4.7a shows top-view and cross-sectional SEM images of TiO_2 thin film fabricated on ITO-glass substrate. It was found that the smooth TiO_2 film was formed on ITO-glass substrate with thickness of 70 nm. The transmittances of the fabricated TiO_2 thin films (Fig. 4.7b) with different Cr dopant concentrations indicate the strong band gap absorption of TiO_2 in UV region. In addition, the slightly absorptions at near band-edges were observe in Cr-doped TiO_2 films, which are induced by deep-acceptor levels related to the Cr doping and other defects in TiO_2 thin film. It is noted that the valleys located at 360 nm, 440 nm and 700 nm are interference peaks induced by ITO film layer. Although Cr-doped TiO_2 is expected to be a p-type semiconductor since the Ti^{4+} ions are replaced by Cr^{3+} ions, but it might also induce the deep-acceptors by heavy doping with Cr due to the excitation of 3d electron of Cr^{3+} to the conduction band of TiO_2[111], [112]. Therefore, a sufficient Cr dopant concentration is considered in the applications required p-type conducting materials.

4.2. Cr-doped TiO_2-ZnO core-shell p-n junction array for high sensitivity ultraviolet photodetector

This section demonstrates the combination of n-type ZnO NWs and p-type Cr-doped TiO2 in order to fabricate p-n junction photodetector[115]. This p-n heterojunction with core-shell structure nanowires array consists of n-type ZnO NWs as a core covered by a Cr-doped p-type TiO_2 shell. ZnO NWs arrays were grown on a transparent indium tin oxide (ITO) coated on glass substrate by hydrothermal method. The Cr-doped p-type TiO_2, was prepared by sol-gel method with optimal condition of Cr-doping concentration[112]. This p-TiO_2/n-ZnO heterojunction device operates as an array of parallel p-n diodes with ideality factor of ~2.45, revealing the excellent quality of the fabricated p-n junction. Towards the photodetector application, this device is proved to be extremely sensitive in UV and blind in the infrared and visible regions, providing a great promise for the UV sensitive photodiode applications. Under UV illumination at 373 nm with incident power of 104 μW, it shows a switch current ratio of 140 and a responsivity as large as 250 A/W at 5V reverse bias.

4.2.1. ZnO NWs based UV photodetector

Zinc oxide (ZnO) has been considered as a promising material for optoelectronic devices. The bandgap energy of 3.37 eV (at room temperature) and high quantum efficiency make this material an excellent candidate for ultra-violet (UV) photodiode since 1980s[116]. ZnO nanowires (NWs), one-dimensional nanostructures with high surface-volume ratio, have shown great potentials in UV sensitive photodiode application. There have previously been reported on two main junction nanostructures of UV photodiode based on ZnO nanowire, including metal-semiconductor (ZnO)-metal (MSM)[91], [92], [117]–[119] and p-n junction[120]–[124]. The MSM-based ZnO nanowire photodiode offers a fast response, but high dark current and requires applied-bias[91]–[93]. Comparing with MSM ZnO NWs photodiode, a p-n

junction ZnO NWs photodiode not only offers a fast response, it has advantages of small dark current and should be working without applied bias. Therefore, the p-n junction ZnO NWs photodiode have been widely investigated in application of the UV photodetector.

ZnO has a n-type natural semiconducting behavior due to the presence of the shallow donor levels[89], [103]–[105], [125], [126]. In order to fabricate p-n junction ZnO nWs photodiode, several attempts have been paid to develop p-type materials such as by incorporating Al-N co-doping (AZO:N) to obtain a large area p-n homojunction[120], or by using p-type polyaniline in hybrid structure of double rod array p-n heterojunction[121]. In addition, the n-ZnO/p-Si heterojunction have also been intensively considered as a promising structure[122]–[124]. However, for a commercially available device, the cost-effectiveness needs to be considered in fabrication method. The simple chemical fabrication routes are attracting much interest because they offer alternative way to fabricate p-n junctions on a complex nanomaterial with perfect wettability and low cost, which should be taken into account in commercially available[120]–[122]. Similar to ZnO, anatase titanium oxide (TiO_2) is also a key and the most interesting optoelectronic material. Otherwise, TiO_2 is also active in UV region with band gap of 3.2 eV[108] and p-type TiO_2-based materials can be prepared by doping with Fe[109][109], Mn[110], Cr[111]. Therefore, p-TiO_2 is promising candidate to combine with n-ZnO in the p-n heterojunction UV detector application. However, to obtain highest sensitivity of an UV photodiode, the improvement of interface density of p-n junction is needed and the devices can be able to work at high applied-bias.

Here we demonstrate on the fabrication of a core-shell p-n heterojunction architecture that is composed of an n-type ZnO nanowire array chemically laminated by an ultrathin layer of p-type Cr-doped TiO_2 shell. This core-shell nanowire architecture realizes a remarkably enhanced heterojunction area and can swiftly transport photoexcited carriers across a nanome-

ter-thick TiO_2 lamination layer and single-crystalline ZnO NWs. The p-type TiO_2 was prepared by a low-cost sol-gel process with small amount of Cr as p-type dopant, which yielded complete coating of the ZnO surface by single-step spin-coating with very small thickness in the range of 5 to 10 nm. This novel TCO heterojunction operates as an array of parallel diodes with large junction area and shows excellent rectifying characteristics. This device exhibited extremely high sensitivity in the UV region larger than 250 A/W and perfectly insensitive in the visible to infrared regions (i.e. IR-VIS blind). Under UV illumination at 373 nm, it shows a switch current ratio of 140 at -5V bias and 104 μW incident power (shed onto the 0.1 cm^2 device), exhibiting a high potential for UV photodiode applications.

4.2.2. Cr-doped TiO_2-ZnO core-shell nanowires array

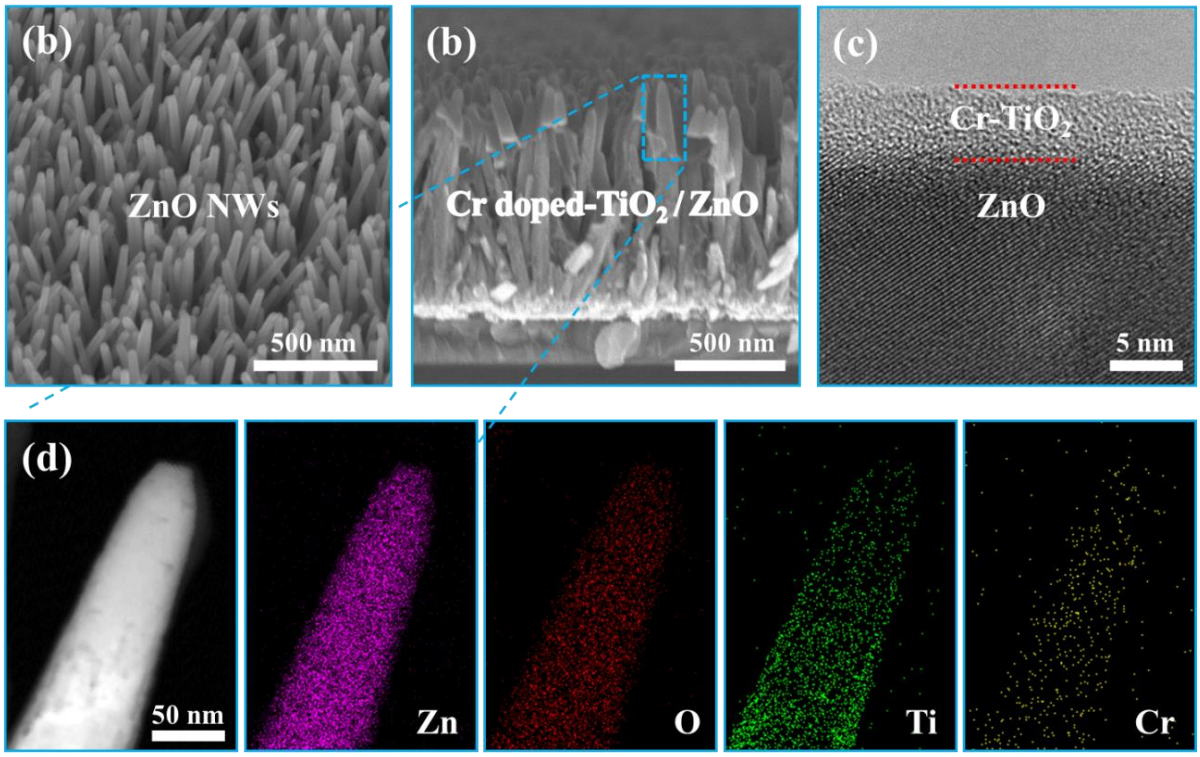

Figure 4.8. Morphology characterization of Cr-doped TiO_2/ZnO NWs core-shell. (a) Tilted-view SEM image of ZnO NWs array. (b) Cross-sectional SEM image of the Cr-doped TiO_2/ZnO NWs. (c) TEM image and (d) High-angle annular dark-field scanning TEM and EDS elemental mapping of Zn, O, Ti and Cr of a single Cr-doped TiO_2/ZnO NW.

Figure 4.8a shows an SEM image of the ZnO NWs array after the hydrothermal growth on indium tin oxide (ITO) coated glass substrate. The ZnO NWs in the array are growing nearly vertically on the ITO glass substrate with an average diameter of 50 nm, average length of 1 μm, and wire density of 2×10^{10} cm^{-2}. Following the synthesis of the ZnO NWs array, Cr-doped TiO_2 laminate was conformally coated onto the NWs array to form core-shell architecture. Figure 4.8b shows the SEM image of the cross-section of the Cr-doped TiO_2-ZnO NWs p-n heterojunction array. It can clearly be seen that NWs array is uniformly coated by a thin layer of TiO_2. The structure was further examined by TEM that evidences a uniform TiO_2 shell layer with a thickness in the range of 5 to 10 nm (Fig. 4.8c). Figure 4.8d presents a high-angle annular dark-field scanning TEM image and EDX elemental mapping of Zn, O, Ti and Cr of a single nanowire heterojucntion. It is clearly seen that the shell layer of TiO_2 is well-formed on core ZnO NW with a uniform Cr doping and smooth morphology.

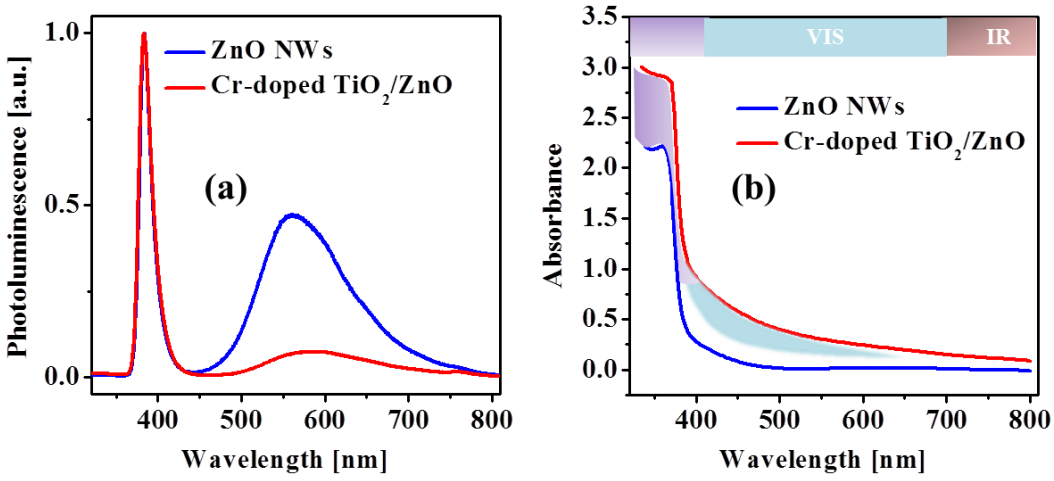

Figure 4.9. (a) Photoluminescence spectra of pristine ZnO NWs (blue curve) and the ZnO NWs covered by the Cr-doped TiO_2 laminate (red curve). (b) Absorbance spectra of the ZnO NWs without (blue curve) and with (red curve) TiO_2 shell layer.

The optical property of the core-shell structure was examined by measuring the device prior to the fabrication of Ag back contact-reflector (Fig. 4.9). Figure 4.9a presents the photoluminescence (PL) spectra of the pure ZnO NWs (blue curve) and core-shell NWs (red curve). In

the case of pure ZnO NWs, in addition to the band-edge emission at 384 nm, we observed a broad visible emission around 560 nm as discussed in the previous section. However, the visible emission was significantly reduced after the lamination by the TiO_2 thin layer. This reduction can be attributed to the transformation of the ZnO deep levels into shallow donor levels by the thermal annealing process[105] during the TiO_2 shell formation. This indicates that the absorption in the visible (VIS) to near infrared (NIR) region of ZnO in our device is efficiently suppressed[101], [105] which also prevents the unwanted photocurrent due to the ZnO defects by the IR and VIS illumination. Figure 4.9b shows the absorbance of the core-shell NWs (red curve) together with that of pure ZnO NWs (blue curve). A dramatic enhancement in the absorbance, a 30% enhancement of absorption in the UV spectral region, is clearly observed for core-shell NWs although the thickness of the TiO_2 shell layer is only around 10 nm, far smaller than the wavelength of the incident light. This would indicate that efficient charge separation is realized owing to the formation of p-n junctions. Although the band-gap of the pristine TiO_2 is 3.2 eV (387.5 nm), deep-level acceptors related to the Cr doping and other defects in the disordered TiO_2 shell layer can induce the absorption in the lower energy region as well as the slow response of the device (rising time in the sub-second order). Slightly higher relative absorbance in the high-energy portion of the VIS region than that of the pristine ZnO NWs can then be attributed to the TiO_2 shell layer.

4.2.3. Ideality factor of the Cr-doped TiO_2-ZnO core-shell p-n junction

The schematic illustration of the working device (at reverse bias) is shown in Fig. 4.10a. The p-n core-shell architecture is placed between an ITO glass and an Ag electrode, while the ITO glass acts as transparent front contact and Ag electrode as back contact and diffusive reflector in the UV region. The device in this work has an active area of 0.1 cm^2.

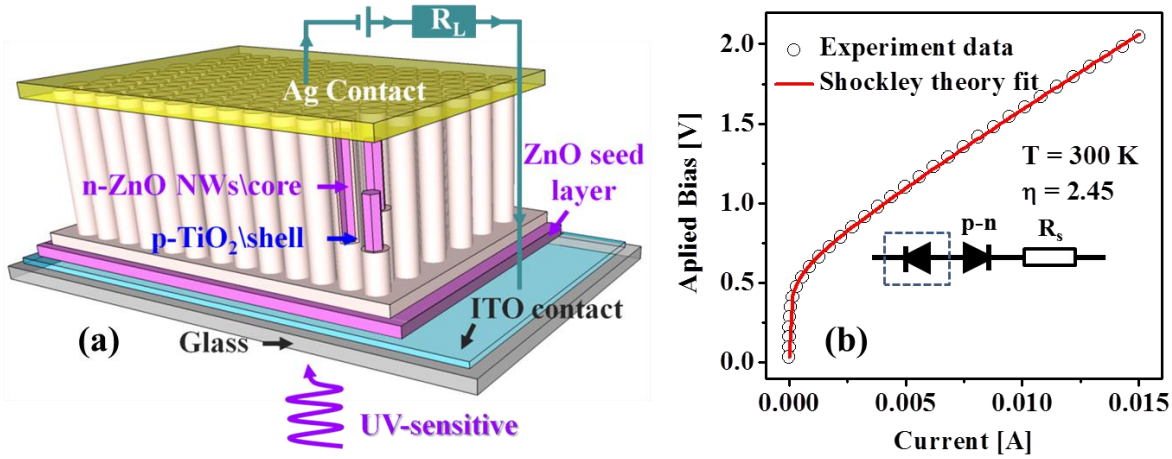

Figure 4.10. (a) Schematic illustration of the Cr-doped TiO_2-ZnO NWs p-n heterojunction device. (b) I-V response and ideality factor of p-n heterojunction device.

First, we investigated the ideality factor, which is related to the electrical performance of the p-n heterojucntion. A p-n junction diode can be represented by the equivalent circuit (the inset in Fig. 4.10b), including an ideal diode in series with a parasitic resistance. By use Shockley theory, the current (I) of p-n junction diode is expressed by a function of the applied-voltage V: [127] [128]

$$I = I_0\left(e^{q(V-IR_s)/\eta k_B T} - 1\right) \tag{4.1}$$

or in expression:

$$V(I) = \frac{\eta k_B T}{q}\left(\ln\frac{I}{I_0} + 1\right) + IR_s \tag{4.2}$$

where I_0 is reverse saturation current, η is the ideality factor, k_B is the Boltzmann constant, T is the measured diode absolute temperature and q is the elementary charge. The ideality factor η can be approximated by fitting of the experimental data using Eq. 4.2. This value is expected to be 1.0 – 2.0 in the single p-n junction diode as Shockley theory. The ideality factor η equals 1 when the diffusion current dominates and η equals 2 when the recombination current dominates. However, when the recombination current is much higher than expected,

which shows an ideal factor larger than 2 at low forward-biased, the reality cases are often encountered. It is contributed by some recombination processes such as multi-phonon recombination, radiative recombination or Auger recombination nother than the recombination at defect points of the device[127]. The abnormally diode ideality factor (lager than 2) also was elucidated by a series of junction diodes, including p-n junction diode and two Schottky diodes of the nonlinear metal-semiconductor contacts[31], [129] or multi-level recombination at extended defects[130]. In our case, by fitting the experimental data using Eq. 4.2, the value of ideality factor η of the device was approximated about 2.45 in range of 0 volt to 2 volt forward-biased. It is higher than the expected values from the theoretical and smaller than some previously reported values[31], [129], [130]. It should be proved that the metal-semiconductor contacts of the device are afforded ideal Ohmic contacts. However, with the nanowires array architecture of the p-n heterojunction, this device is not a single diode, it is a diodes array in parallel, and the total current can be writing:

$$I = \sum_i I_{0i}\left(e^{q(V-I_i R_{si})/\eta_i k_B T} - 1\right) \tag{4.3}$$

we assume that the nanowires array are homogeneous so that the total current of *m* diodes is given by:

$$I = mI_{0m}\left(e^{q\left(V-\frac{IR_m}{m}\right)\Big/\eta_m k_B T} - 1\right) = I_0\left(e^{q(V-IR_s)/\eta k_B T} - 1\right) \tag{4.4}$$

where $R_s = R_m/m$, $I_0 = mI_{0m}$ with I_{0m} is saturation current of each diode. Here, we can see that the ideality factor of individual diodes is closed to the ideality factor value of a parallel diodes array of 2.45. However, the nanowires array are not perfectly homogeneous and the recombination by defect points of p-n junction is much higher than expected values, which leads to the observed high ideality factor of 2.45.

4.2.4. Spectral response of Cr-doped TiO_2-ZnO NWs photodiode

As analysed above, this device works as a diodes array and the current of individual diodes is small, therefore, it is expected to work at high bias. In spite of the very small thickness of the TiO_2 shell layer and the rather complex nanowire morphology of the current device, the stability of this p-n heterojunction is remarkably high. It exhibits a very small leakage current (contributed by drift carries) as well as surprisingly high breakdown voltage (>15 V). For example, at the 5V bias and without light illumination, the rectification ratio (the ratio between forward current and reverse current at the same bias voltage) is 361, evidencing an ideal rectifying behavior of the device.

The wavelength-dependent spectral response of the device in UV, VIS and IR region was studied separately by illuminating the filtered light from the solar simulator. The incident light was illuminated from the front side (glass side) of the device. Figure 4.11a shows I-V curves of the device under UV, VIS and IR illumination at the same intergrated incident power of 104 μW. It is clearly seen that the present device is nonresponsive in the NIR region with wavelengths above 650 nm. In the VIS region also, it is almost nonresponsive, only giving little increase in the forward bias. This is likely due to the reduction of deep levels of the ZnO NWs[105] and a weak response of deep acceptor defect levels in the Cr-doped TiO_2 layer as discussed and shown in Fig. 4.7b and Fig. 4.9b. In clear contrast to the VIS and the IR irradiations, the I-V curves under the UV irradiation show pronounced response especially in the reverse bias. For example, at -5V reverse bias, the current increases from 150 μA (in the dark) to 21 mA thus the switch current ratio reads as high as 140, exhibiting a high signal to noise ratio. This value can be readily increased by increasing the TiO_2 shell thickness and reducing the dark current.

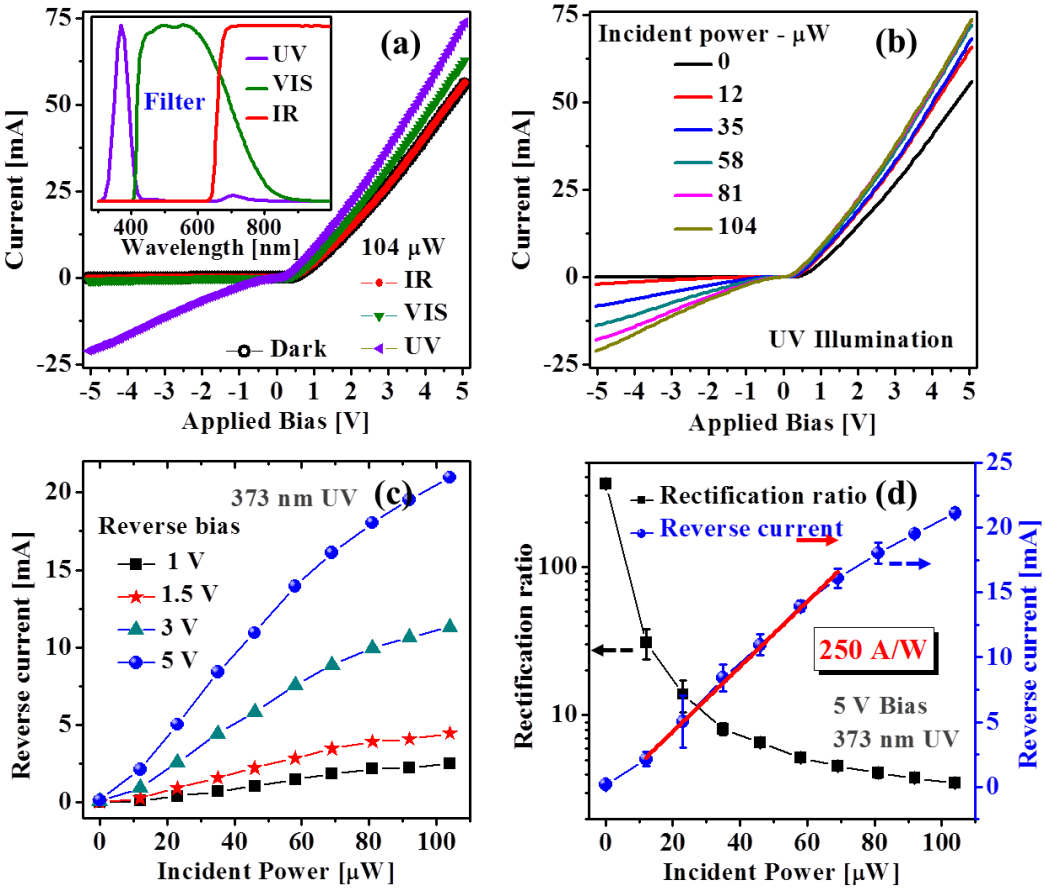

Figure 4.11. (a) Spectral response of the device taken under the UV, VIS, IR illumination with the same power (104 μW). The inset shows the transmission characteristics of the filters used in this measurement. (b) Power-dependent photocurrent of device. (c) Photocurrent response as function of incident power and reverse applied bias. (d) Dependence of rectification ratio and reverse current on incident power under 373 nm illumination and 5 V reverse applied bias.

I-V characteristics of this p-n heterojunction were investigated more systematically under UV irradiation with various incident powers ranging from 0 to 104 μW (Fig. 4.11b). Majority of the induced photocurrent originates from the electron-hole pairs generated in or near the depletion region, and then they are separated into free electrons and holes by the electrical field subsequently drifting to the electrodes. In this sense the small thickness of the TiO_2 shell works rather efficiently to transport the separated charges to the electrodes. Because of this ultrathin nature of both the ZnO and TiO_2 materials, the generated diffusion current can be minimized and the drift photocurrent reaches the electrodes swiftly, which results in the oper-

ating reverse bias as small as -0.5 V. At typical reverse bias of -5V and 58 μW of incident power, this device shows reverse current of 14 mA and switch current ratio as high as 93. This value is more than 3 times higher than the best data reported so far for the ZnO NW-based p-n junction device[120].

Figure 4.11c shows the reverse current of the p-n heterojunction on the UV light power under reverse bias varied from 1V to 5V. The response current is dramatically increased when the power and reverse bias increased. For more detailed characterization, Fig. 4.11d shows the dependence of rectification ratio and the relation with reverse current of the p-n heterojunction on the UV light power under an applied bias of 5 V. The rectification ratio (black filled squares) decreases rapidly up to around 20 μW, and then decreases slowly. This result evidences the efficient generation of the photocurrent in the depletion region under the UV illumination and shows good enough response of the photodiode by using this reverse bias. The I-P characteristic (blue filled cycle) of this device at the same reverse bias shows that the reverse current I increases almost linearly with the increase of the incident power P from 0 to 70 μW, which features a useful linear response as an ideal photodiode. By evaluating the slope of this I-P characteristic in this region, the responsivity of this device was found to be as high as 250 A/W. This value should be improved to 325 A/W if the UV light attenuation by the front glass window (30 %) is avoided by replacing to a UV-transparent window such as sapphire, and even larger value is possible if the device works at higher reverse bias.

4.2.5. High internal gain in Cr-doped TiO_2-ZnO UV photodiode

The mechanism for the high responsivity of the Cr-doped TiO_2-ZnO NWs p-n heterojunction can be explained by the high internal gain process where the carrier lifetime is much larger than transition time of carriers. As the measured result shown in Fig. 4.11a, the threshold for high responsivity or high internal gain is about 0.4 V, this value is far below the reverse bias

in which its potential energy can support a sufficient energy (> E_g) for the impact ionization process (or avalanche multi multiplication). However, a high internal gain in the Cr-doped TiO_2-ZnO p-n heterojunction can be achieved if the carrier lifetime is larger than carrier transit time of in the photoconductive device. It has been reported that the carriers trapping process by trap states or by oxygen adsorption and desorption process can induce a long life-time of the carrier in photoconductive device[131]–[134], [92], [135]. Under the reverse-applied bias, the TiO_2-ZnO heterojunction can work as a photoconductive device. Upon illumination at photon energy above E_g, electron-hole pairs are photogenerated; electrons move to ITO contact and holes migrate to Ag contact, resulting in a photocurrent through the device. Nevertheless, because of the large surface volume ratio in the TiO_2-ZnO core-shell structure, and with very thin p-TiO2 shell layer (~10nm), the electrons near TiO_2 surface could be captured by oxygen molecules [$O_2 + e^- \rightarrow O_2^-$].

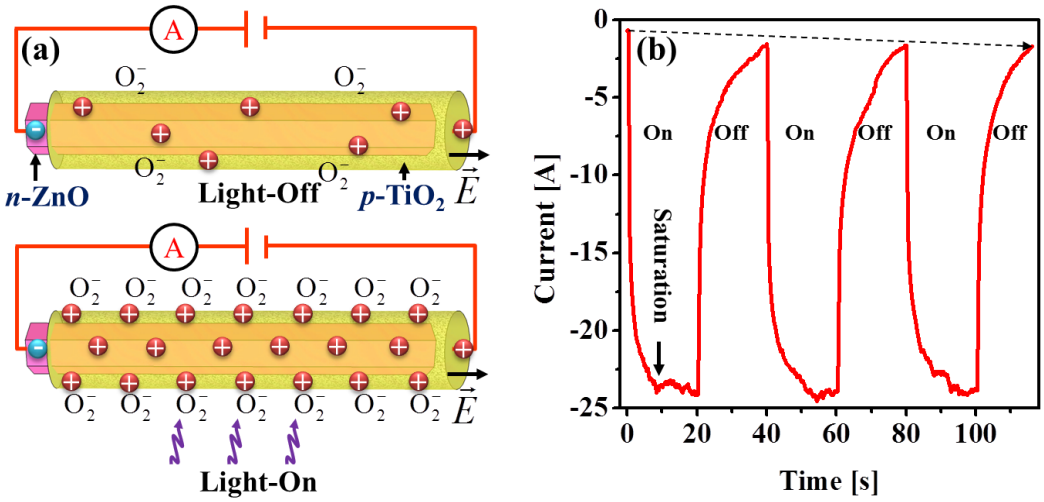

Figure 4.12. (a) Oxygen adsorbed on TiO_2 shell surface, in the dark (top) and in the light illumination (bottom). (b) Time dependence of the photocurrent with switching on/off the 373 nm UV illumination at 5 V reverse-biased.

This oxygen adsorption process is described as the schematic shown in Fig. 4.12a. In the dark, because of p-type conducting of TiO_2 shell layer, the electron is minor carrier then the number of adsorbed O_2 ions is small. In contrast, the number of adsorbed oxygen ions is increased

when the light is on since the electrons near TiO_2 surface are generated by photon absorption and then they are quickly captured by oxygen molecules, resulting in unpaired holes on TiO_2 shell layer with long lifetime. The unpaired holes concentration in TiO_2 shell layer as well as the conductivity of TiO_2-ZnO device is increased versus the illumination time, making device has slow response time but high responsivity as measured result of 250 A/W under 373 nm illumination at 5 V reverse applied bias. It should be noted that the adsorbed oxygen ions also can be desorbed by discharging process [$O_2^- + h^+ \rightarrow O_2$], it makes the unpaired holes concentration saturated. Figure 4.12b shows the time dependence of the current with switching on/off the 373 nm illumination at 5 V reverse bias. It was found that, the current is exponentially increased when the light is on, and saturated after about 10 second. It means that, the conductivity of the device is increased after turn on the light, which could be induced by the adsorption of oxygen molecules on the TiO_2 surface as discussed above. When the light is off, the unpaired concentration is decreased due to the oxygen desorption process. As seen in Fig. 4.12b, the conductivity of the device is slowly decreased after turn off the light, the dark current is therefore also increased versus illumination time.

The photoconductivity in the Cr-doped TiO_2-ZnO device also can be affected by other carrier trapping processes in ZnO nanowire as well as at semiconductor/contacts[131]. Thus, this enhancement of the conductivity induced by carrier trapping as well as oxygen adsorption processes can work as the internal gain, resulting in a high responsivity of the Cr-doped TiO_2-ZnO device. In addition, the TiO_2-ZnO heterojunction can work at high bias (breakdown > 15 V). Therefore, responsivity of the device can be improved at high applied bias where the "impact ionization" or avalanche multiplication process can be also taken into account.

4.2.6. Conclusion of Cr-doped TiO_2-ZnO p-n junction UV photodiode

By adopting a vacuum-free low-cost chemical fabrication route, we fabricated an infrared/visible-blind high-sensitivity UV photodetector composed of a p-n heterojunction core-shell nanowire architecture using n-type ZnO and p-type TiO_2 as two constituent TCO materials. The sol-gel fabrication process of Cr-doped TiO_2 shell layer yielded a high-quality conformal p-n heterojunction on a vertically grown ZnO nanowire array, which renders efficient charge separaton and carrier transfer. Surprisingly, in spite of its intricate 3D architecture with very small thickness of the TiO_2 shell, the device operates as a model p-n heterojunction with a linear response and sensitivity larger than 250 A/W (-5V reverse bias, UV illumination at 373 nm). The proposed combination of the current fabrication methods with the core-shell device architecture would greatly widen the application of the two commnly used meta oxide - ZnO and TiO_2 - for optoelectronics as well as for light harvesting nanomaterials for solar-hydrogen generation.

4.3. Plasmonic NPs-ZnO NWs hybrids for efficient solar-driven photocatalysis

In this section, we demonstrate on the measurements and simulations of visible active photo-catalyst composed of plasmonic metal nanoparticles and ZnO NWs array fabricated via all-wet-chemical route[136]. Owing to the coupling between the ZnO dielectric response and the Ag or Au nanoparticles excitation, efficient electronic excitation can be induced at the vicinity of the metal-ZnO interfaces since optically excited plasmonic particles not only can concentrate the electromagnetic field at the ZnO/particle interface, but also would act as efficient sources of plasmonic hot-electrons injected into the conduction band of the ZnO catalyst. Through the photodegradation and photoelectrochemical cell experiments, the obtained enhancement results using plasmonic metal-ZnO NWs here clarify the role of plasmon reso-

nance and provide us useful knowledge for the development of oxide-metal nano-hybrid material for solar energy conversion

4.3.1. Plasmon-enhanced photocatalysis

Artificial photosynthesis and photocatalysis have become central topics in energy and environmental research as one of the most promising clean processes for converting solar energy into chemical energy. Metal-oxide catalysts such as TiO_2-based self-cleaning house paint as well as window coating have been studied extensively. Although the remarkable success in the applications so far, most of the semiconductor catalyst have optical band gaps in the ultraviolet (UV) region, such as TiO_2 (3.2 eV)[97], ZnO (3.37 eV)[95], and $SrTiO_3$ (3.2 eV)[137] which are too large for enjoying efficient use of solar energy in the visible (VIS) and infrared (IR) region. Recent advances in the improvement of catalytic efficiency as well as development of the VIS-IR active catalyst have provoked numerous challenges in the field of photocatalysis and in nanophotonics.

Recently, plasmonic nanostructures have been demonstrated their great potentials for the applications in optics, photonics and opto-electronics, based on their extreme enhancement and nanoscale confinement of the electromagnetic field in the vicinity of their surfaces. Such features have also been realized to enhance the efficiency of catalytic materials by near-field enhancement and far-field scattering enhancements of the light while excited plasmons can also provide sufficient energies for injecting hot-electrons from metal nanostructures to semiconductor catalysts[138]–[141].

Among the various available photocatalysts, zinc oxide (ZnO) has been widely studied as a highly efficient material[142]–[151] because of its natural abundance, inexpensive fabrication processes, rendering, ZnO as a promising photocatalyst beside TiO_2 and $SrTiO_3$. In particular, ZnO nanowires (NWs) have been studied extensively as excellent catalysts because of their

high surface area and increased optical path-length mediated by light scattering and interference[146]–[151]. However, because of its wide bandgap, the photocatalytic activity of ZnO NWs is limited mainly under UV light, making the challenger for the use of ZnO in the solar-assisted photocatalysis application. To improve photocatalytic activity of ZnO NWs, beside the bandgap modification by doping of ZnO NWs with metal ions[148], [152]–[154], nanometals were also chosen as the co-catalysts materials for the enhancement of the charge separation[147], [155], [156] or as the plasmonic materials for the near field enhancement and hot-electron injection[150], [157], [158]. The catalytic activity of plasmonic nanometals-ZnO NWs heterostructures can be improved in both UV and VIS regions, however, the enhancement factor as well as the efficiency enhancement are dependent on the structure morphology and electric field direction. Deeper understanding for both UV and VIS catalytic enhancements of the AgNP-ZnO and AuNP-ZnO NWs hybrids based on measurement and electromagnetic field simulation are needed.

Here in this work, we aim for proposing an effective metal-oxide hybrid nano-architecture and its facile low-cost fabrication method together with the experimental demonstration of their visible photocatalytic activity. It is of high interest also to see how much extent the numerical analysis of the electromagnetic field in nanometer scale can contribute for explaining the improvement in chemical properties of the proposed nanostructures. The proposed nanomaterials here are the metal nanoparticles (NPs) loaded-ZnO nanowires (NWs) which exhibit highly improved catalytic activity in the visible region. The fabricated catalyst consist of a nearly-vertical ZnO nanowires array that are hydrothermally grown on the transparent conductive oxides (TCOs), such as on fluorine-doped tin oxide (FTO) or on ITO coated glass substrates. The plasmonic Ag and Au NPs were prepared separately and attached onto ZnO nanowires to form the AgNPs loaded-ZnO or AuNPs loaded-ZnO catalysts. The photodegradation of methylene blue (MB) molecules under solar light illumination was examined. Cata-

lytic activity of the metal-NPs loaded-ZnO surfaces was found to be 2-3 times higher than that of the pure-ZnO NWs. The photoelectrochemical (PEC) cell under photovoltaic configuration with NPs-loaded-ZnO NWs photoanodes showed clear photocatalitic activity in the VIS region while negligible activity was observed in the case of pure ZnO NWs photoanode. On the other hand, the numerical electromagnetic field simulations were used to investigate the optical properties of the materials as well as understanding the mechanism of the catalytic activity enhancement by the addition of plasmonic metal particles on ZnO NWs. The RCWA calculation was employed to clarify absorption characteristics of the catalysts in the visible region associated with the plasmonic extinction of AgNPs and AuNPs. The electric field calculations showed the strong electric field concentration at the interfaces between the metal NPs and ZnO in both UV (near the band gap of ZnO) and VIS (at resonance of localized surface plasmon) excitations. Especially, at plasmon resonance in the VIS region with AgNPs-ZnO case (c.a. 450nm) and with AuNPs-ZnO case (c.a. 560nm), the electric field enhancement were found to be 20 times, which provides high chances for internal photoemission to generate hot-electrons to overcome Schottky barrier and are injected into ZnO conduction band to make it functionalized as VIS active photocatalyst.

4.3.2. Preparation and characterization of metal NPs-ZnO NWs hybrid arrays

ZnO NWs arrays were synthesized on transparent conductive oxides (FTO or ITO) substrates (1x2 cm) by hydrothermal method[98] as present in the section 4.1. The fabricated ZnO NWs arrays were then washed in de-ionized water, in ethanol, and then annealed at 400 $^{\circ}$C in ambient air for 1 hour to enhance the crystallinity of ZnO crystals and the concentration of the shallow donors[105], [115]. The colloidal suspension of AgNPs (average diameter of 10 nm) was synthesized by adding sodium tetrahydroborate ($NaBH_4$ - Wako) to reduce the ionic silver ($AgNO_3$ - Wako) and stabilize the silver nanoparticles[159]. The aqueous solution of

AuNPs (average diameter of 13 nm) was synthesized by reducing ionic gold (hydrogen tetra-chloroaurate (III) tetrahydrate - $HAuCl_4$ - Wako) by using trisodium citrate anhydrous ($C_6H_5Na_3O_7$ - Wako)[160]. A drop casting of AgNPs or AuNPs suspensions onto ZnO NWs arrays were used to form the AgNPs-ZnO and AuNPs-ZnO hybrid nanowire arrays. The samples were then washed by de-ionized water to remove the excess amount of AgNPs and AuNPs and then dried and thermally treated at 150°C in air (at low oxygen content to avoid the oxidation process of the silver) for 1 hour to stabilize the metal-ZnO interfaces.

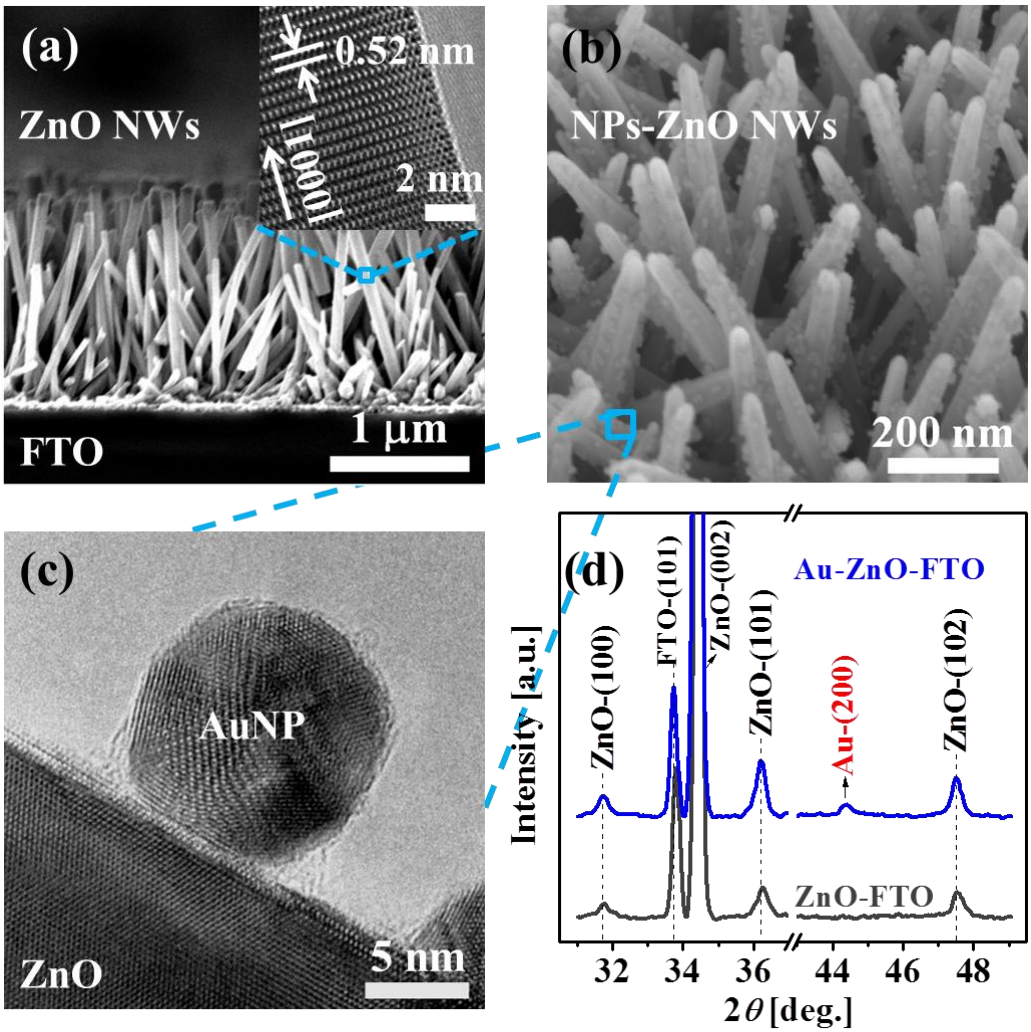

Figure 4.13. (a) Cross-sectional SEM image of a ZnO NWs array and a HR-TEM image (inset) of a single ZnO NW with [0001] growth orientation. (b) Tilted-view SEM image of a AuNPs-ZnO NWs array. (c) HR-TEM image of a AuNP on the ZnO NW surface. (d) XRD patterns of a AuNPs coated and a non-coated ZnO NWs array.

The investigation of the photodegradation of MB in water was carried out using NPs-ZnO NWs catalysts, in which, a 2 ml solution of MB molecule with concentration of 10^{-5} M in water was used. For photo-electric conversion (PEC) measurement, a simple PEC cell was used with photoanodes made of AgNPs-ZnO and AuNPs-ZnO hybrid nanowire arrays. These metal NPs-ZnO NWs arrays were grown on ITO substrates and were connected to high purity copper wire using silver paste and then an insulating epoxy was used to cover all the excess ITO surfaces on the edge of ITO glass to prevent the short-circuit current. The PEC cell measurements were carried out using photovoltaic configuration with the catalysts photoanodes and a Pt zigzag wire as counter electrode and the Na_2SO_4 solutions (0.5 M) as electrolyte. A standard AM 1.5G solar simulator (Jasco Otentosun - IV 5) with power density of 100 $mWcm^{-2}$ was used as sunlight source for both of PEC cell and photodegradation experiments. For the measurement with VIS irradiation, an additional optical filter was combined with solar simulator to eliminate UV light.

Figure 4.13a presents a cross-sectional SEM image of a ZnO NWs array grown on an FTO-glass substrate with an average wire length of 1 μm, the diameter of 50 nm, and the wire density of 2×10^{10} cm^{-2}. A high-resolution TEM image of a single ZnO NW (the inset in Fig. 4.13a) shows very high crystalline quality with [0001] growth orientation. A tilted-view SEM image of AuNPs-ZnO NWs array (Fig. 4.13b) shows that the particles are uniformly attached to the surface of ZnO NWs. In addition, a high-resolution TEM image of NP loaded NW (Fig. 4.13c) shows a good contact between metal-NPs and semiconductor-ZnO. Figure 4.13d shows the XRD patterns of the bare ZnO NWs on an FTO substrate (gray curve) and that of the AuNPs (blue curve), both are exhibiting ZnO diffraction peaks which are in good agreement with the JCPDS card No. 36-1451 of bulk ZnO with hexagonal wurtzite structure. In addition, a strong peak at 34.39° of ZnO (002) plane shows that the nanowires are well oriented and high crystalline quality. Besides, the XRD pattern of the AuNPs-ZnO NWs also

exhibits additional diffraction peak which is ascribed to the (200) plane of the AuNP. Regarding the AgNPs-ZnO NWs arrays, we also characterized them by the same TEM and XRD observations and confirmed that they exhibits similar morphology and the crystallinity as the AuNPs-loaded ZnO NWs array.

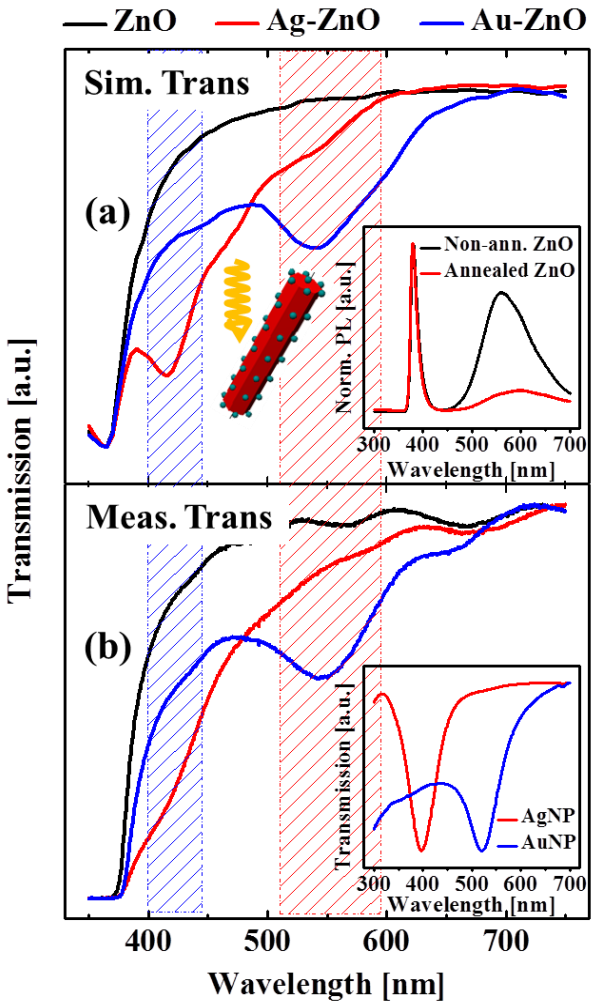

Figure 4.14. (a) Simulated and (b) Measured transmission spectra of bare ZnO NWs array (black curve), AgNPs-ZnO NWS hybrid (blue curve), and AuNPs- ZnO NWs hybrid (red curve). The insets in (a) shows simulation model for a unit cell, including NPs on ZnO surface with tilted angle of 30° with respect to the incident light direction. The photo luminescence spectra of the ZnO nanowires before and after annealing at 400 °C. Inset in (b) shows the experimental transmission spectra of the original AgNPs and AuNPs suspensions in water.

In order to elucidate the optical properties of metal NPs loaded-ZnO catalyst, firstly, the simulated transmission spectra were performed using RCWA method, and then compared with

UV-VIS spectra of the materials. Figure 4.14 presents the simulated (Fig. 4.14a) and measurd (Fig. 4.14b) spectra of the ZnO NWs arrays with and without plasmonic metals in the air surrounding medium. The geometry of the model is shown as an inset in Fig. 4.14a. For this simulation, the illuminating light has an incident angle of 30° with respect to the nanowire axis which will be discussed in more detail in the following. The inset in Fig. 4.14b shows the transmission spectra of the AgNPs and AuNPs suspended in water exhibiting the plasmon resonances at 390 nm and 523 nm, respectively. The simulated spectra are in good agreement with the measured spectra. The result indicates a high transparency for wavelength above 400 nm in case of bare ZnO NWs (black curve), while in the presence of plasmonic NPs, absorption feature around 415 nm for AgNPs-ZnO NWs hybrid (red curve) and wide absorption band from 450 nm to 630 nm for AuNPs-ZnO NWs hybrid (blue curve) are seen. Due to the dielectric screening from the ZnO, the plasmon resonances of NPs are slightly redshifted when NPs are attached on the ZnO NWs. With the presence of plasmonic metals, the optical densities of the NPs-loaded-ZnO NWs arrays were increased in visible (VIS) region, which is the requirement for the photocatalyst that operates under the solar light illumination.

The quality of ZnO NWs crystal was improved by annealing process and also evaluated by photoluminescence measurement as shown in the inset in Fig. 4.14a. As we can clearly see, broad VIS emission (c.a. 500-700 nm) was reduced by the annealing process, which is attributed to the increase in the shallow donor levels[105], resulting in a high donor concentration and improving the crystallinity and the conductivity of the ZnO catalyst.

4.3.3. Photodegradation of MB in water using metal NPs-NWs hybrid catalyst

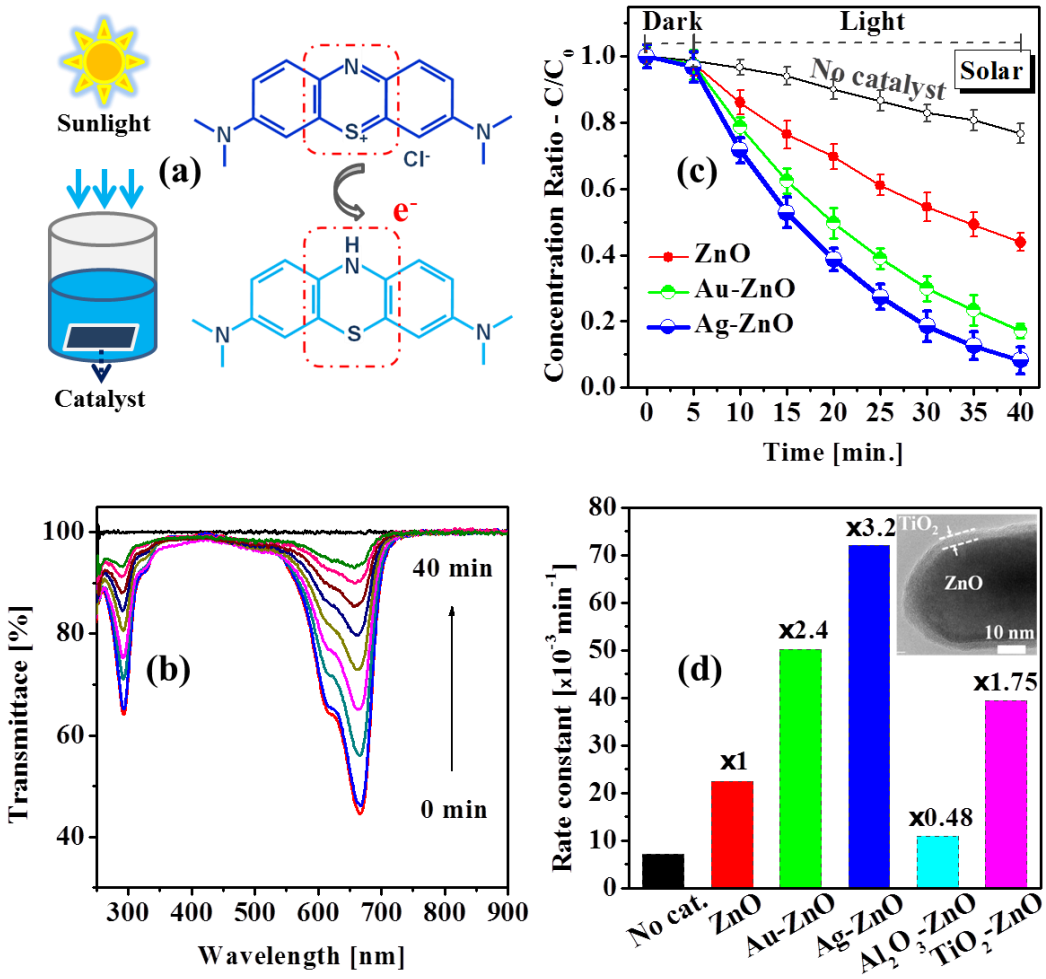

Figure 4.15. Photodegradation of methylene blue (MB) molecules in water under solar light illumination. (a) Experimental setup. (b) Photodegradation evolution as increasing the transparency of MB in presence of catalyst by the time irradiation. (c) Reductions of the concentration of MB are shown: without catalyst (gray curve), in the presence of bare ZnO NWs array (red curve), AuNPs-ZnO NWs array (green curve) and AgNPs-ZnO NWs array (blue curve). (d) The MB photodegradation rate constants in the presence of the different catalysts are shown. The inset shows a TEM image of a thin TiO_2 layer-coated ZnO NW catalyst.

One of the possible uses of the oxide photocatalyst is the decomposition of unwanted pollutant molecules and toxic molecules in water under sunlight illumination. The catalytic activity of the plasmonic metal loaded ZnO NWs catalysts was investigated by the photodegradation (reduction) of MB molecules under solar light illumination. The solution of MB (deep

blue) transforms into leucomethylene blue (transparent) as the reduction of MB takes place (Fig. 4.15a). Figure 4.15b shows the photodegradation evolution of MB molecules in water as increasing the transparency of solution by increasing the illumination time. Figure 4.15c show the photodegradation plot by monitoring the reduction of the MB concentration under solar light illumination[161]. Initially, the degradation of MB solution was evaluated without any light illumination to see the chemical process in dark and the instrument function of the measurement system that constitutes the background spectrum. After the light illumination, the concentration of MB is slowly reduced due to photoreaction without any catalyst. On the other hand, in the presence of catalysts, the molecules are drastically reduced by photocatalytic process. Especially, by loading plasmonic NPs onto ZnO, the catalytic activity of AuNPs-ZnO and AuNPs-ZnO becomes much higher than that of the pristine-ZnO NWs.

For further quantitative investigation, by using first-order Langmuir-Hinshelwood kinetics[162], we evaluated the apparent reduction rate of MB in the presence of catalysts as shown in Fig. 4.15d. Compared to the pritine-ZnO NWs case with the rate constant of 22.5 x $10^{-3}min^{-1}$, the photocatalytic activity of the NPs-ZnO hybired catalysts is remarkably enhanced by 2.4 to 3.2 times in cases of AuNPs-ZnO and AgNPs-ZnO, respectively. Because the plasmon resonance wavelength of AgNPs is shorter than that of AuNPs, the near-field enegy induced by AgNPs is closed to band gap of ZnO than Au case. Therefore, the enhancement in case of AgNPs-ZnO is higher than that of AuNPs-ZnO. For further investigation, the ZnO NW surfaces were also capped by ultra-thin oxide layers (thickness of 4 nm, the inset in Fig. 4.15d) of Al_2O_3 or anatase TiO_2 to determine the effects of the oxide surfaces. The oxide thin films were carried out using atomic layer deposition. As shown in Fig. 4.15d, Al_2O_3-coated ZnO NWs array show little catalytic activity, as expected from the bulk properties of the material and its wide band gap energy (8eV). On the other hand, the anatase TiO_2-coated ZnO NWs shows an improved catalytic activity in comparison with pure-ZnO

NWs (Fig. 4.15d), which is due to the improvement of the charges transport by removal of trap states[163] of ZnO during the forming of TiO_2 shell layer as well as the inherent catalytic activity of TiO_2. However, the catalytic activity of TiO_2 coated ZnO NWs is still far smaller than that of the NPs-loaded ZnO NWs, thus highlighting the dramatic enhancement of the catalytic activity induced by the plasmonic NPs. The above results can be summarized as follows. The catalytic activity is associated with the ZnO surface chemistry that is higher than Al_2O_3 and lower than the TiO_2, and the activity can be dramatically improved by a factor of two to three to the level that surpasses by far the activity of TiO_2 surface by the decoration of metal NPs. It should be noted that these plasmonic NPs-ZnO NWs catalysts are possible to be reused for many times with high stability. For example, after the catalysts were used they were rinsed by pure water for several times and dried in ambient air. This simple cleaning method allows us to use them for more than 10 times with stable catalytic activity.

To further understand the role of the metal NPs on the photocatalytic activity, we have measured the photocurrent using the photoelectrochemical cell (PEC) under irradiation from a solar simulator (Fig. 4.16). We investigated the photocatalytic activity of the plasmonic NPs-ZnO NWs hybrids by using them as the photoanodes in our PEC cell together with a cathode made of Pt zigzag wire. A 0.5 M of sodium nitrate solution (pH ~ 7) was used as the electrolyte. Photovoltaic configuration for PEC cell was used meaning that any bias voltage was not applied during the photocurrent measurements (Fig. 4.16c). Figure 4.16a-b present the photocurrent density of PEC with and without light illumination. Under standard solar light of $100mW/cm^{-2}$ as shown in Fig. 4.16a, the average photocurrents were 8.5 and 11 $\mu A/cm^{-2}$ for the two photoanodes made of AuNPs and AgNPs -ZnO NWs hybrids, respectively, while it is only 3.2 $\mu A/cm^{-2}$ in case of pure ZnO NWs photoanode. It is clearly seen that by using plasmonic NPs-ZnO NWs hybrids, their photocatalytic activities were enhanced from 2.5 - 3.5 times compared to bare ZnO NWs.

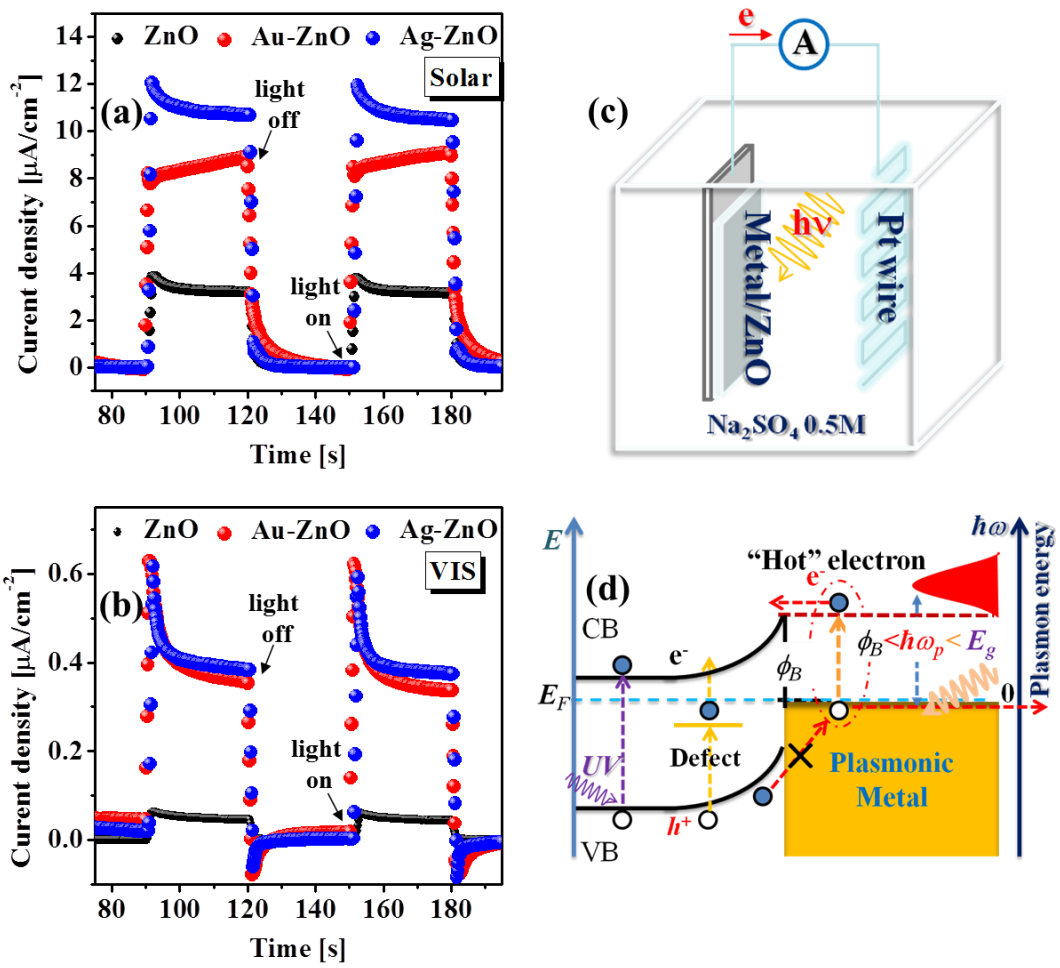

Figure 4.16. Photocurrent density of ZnO NWs and NPs-ZnO NWs hybrid photoanodes of the PEC cell under photovoltaic configuration. (a) Under solar light illumination with power density of 100 mWcm^{-2} (standard AM 1.5G filter) and (b) Under visible light illumination (wavelength in the range of 400 – 900 nm with power density of 33 mW-cm^{-2}). (c) Schematic of the photoelectrochemical cell under photovoltaic configuration. (d) Schematic illustration of the mechanism for VIS photocatalytic activity by plasmon-induced hot-electron of plasmonic NPs-ZnO NWs hybrid.

To investigate the mechanism of the activity enhancement, we measured photocurrent of PEC cell under pure VIS-IR irradiation (400 nm – 900 nm) by using optical filter to cut all UV light (Fig. 4.16b). With the VIS light illumination, little photocurrent is generated in case of pure ZnO NWs, while the photocurrents in cases of the AgNPs and AuNPs-loaded ZnO NWs are steeply rising over 0.6 μA/cm^{-2}. It should be emphasized that even under the VIS light irradiation, the photoelectric conversion is operative in the presence of plasmonic-metal NPs

loaded on the ZnO NWs catalyst. Figure 4.16d presents the possible mechanisms of the VIS photocatalysis of the plasmonic NPs-ZnO NWs hybrids, which are originated by plasmon-induced hot electrons or/and plasmon-enhanced defect absorptions of ZnO photocatalyst. The detailed mechanisms are discussed in the section bellow.

4.3.4. Electric field enhancement and discussion on the mechanism of plasmon-enhanced photocatalysis in plasmonic NPs-ZnO hybrid

To elucidate the optical properties as well as the enhancement mechanism of the plasmonic metal-loaded ZnO catalyst, the electric field (E-field) distribution around the nano-objects were carried out by using FDTD simulation as shown in Fig. 4.17. The simulations were performed including water as surrounding medium, which reproduces the experimental condition of the catalyst. Firstly, the localized surface plasmon resonance spectra of Ag-ZnO and Au-ZnO hybrids in water were simulated using RCWA to see the changes of resonance spectra of plasmonic hybrids when the surrounding medium changed from air to water. It was found that, the localized plasmon resonance spectra of Ag-ZnO and Au-ZnO hybrids are red-shifted from 415 nm (in air) to 450 nm (in water) for Ag-ZnO hybrid (Fig. 4.17a), and from 530 nm (in air) to 560 nm (in water) for Au-ZnO hybrid (Fig. 4.17d). The E-field distributions around plasmonic NPs-ZnO hybrids are shown in Fig. 4.17b-c (Ag-ZnO) and Fig. 4.17e-f (Au-ZnO). As seen, by using UV excitation at optical band-gap energy of 360 nm - ZnO NWs, the E-field enhancement near the Au-ZnO (Fig. 4.17b) and Ag-ZnO (Fig. 4.17e) interfaces were found to be 3 and 4 times larger, respectively, compared with E-field of the incident light. This enhancement in UV range, especially, corresponding to the optical band-gap of ZnO, can contribute remarkably to the efficiency of the photocatalysts. In addition, the excitation energy in UV range is larger than threshold of the interband transitions of Ag or Au, which can lead to the excitation of electrons far below the Fermi level, for example, the

interband transition from *d*-band to *sp*-band in gold. In this case, the photogenerated holes in *d*-band may act as the hot-holes and contribute to the injection current[139]. On the other hand, under VIS excitation at the frequency of plasmon resonances of 450 nm for Ag-ZnO (in water) and 560 nm for Au-ZnO (in water), the enhancement factors of E-field were found to be as high as 20 and 18 times in for Ag-ZnO (Fig. 4.17c) and Au-ZnO (Fig. 4.17f), respectively. These concentrated E-fields are mostly located at the interface between the metal NPs and the ZnO, also slightly penetrating into the subsurface of ZnO (Fig. 4.17c and Fig. 4.17f), indicating the concentration of photon energy into a tiny space at the NPs-ZnO interface.

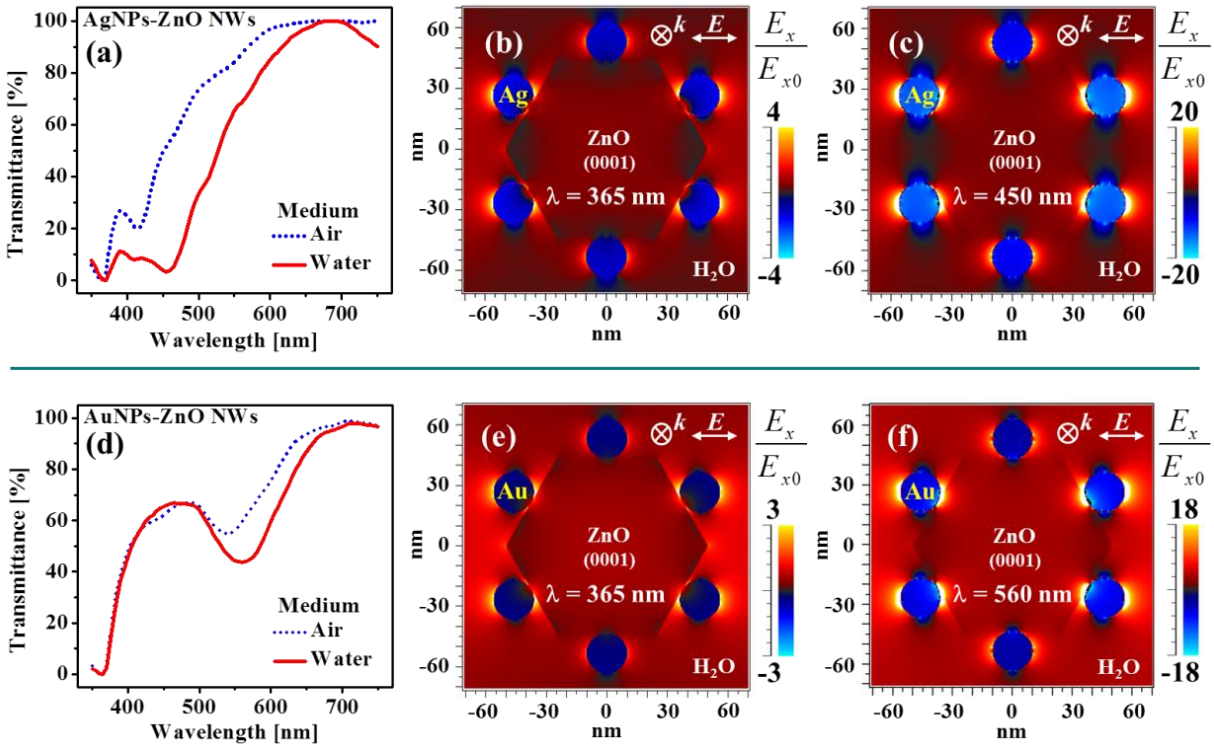

Figure 4.17. Simulated transmittance (red curves) of (a) AgNPs-ZnO NWs hybrid and (d) AuNPs-ZnO NWs hybrid in real working-condition medium of water. Simulated electric field distribution around plasmonic NPs-ZnO hybrids shows strong E-field enhancement and the hot-spots located at the interface of the metal and semiconductor would provide smart potential to hot-electrons: For AgNPs-ZnO NWs - (b) Under UV excitation of 365 nm with E-field enhancement of 4 and (c) under visible of plasmon resonance at 450 nm with strong E-field enhancement of 20. For AuNPs-ZnO NWs - (e) Under UV excitation of 365 nm with E-field enhancement of 3 and (f) Under visible of plasmon resonance at 560 nm with strong E-field enhancement of 18.

With a Schottky barrier at the hetero-junction between a metal with work function smaller or larger than the vacuum electron affinity of a p-type or a n-type semiconductor, respectively, the quantum transition probability of electrons with sufficient energy to overcome the barrier is given by:[138], [164]

$$\eta_i \approx C_F \frac{\left(h\nu - q\phi_B\right)^2}{h\nu} \tag{4.5}$$

where C_F is the device-specific Fowler emission coefficient, $q\phi_B$ is the Schottky barrier energy and $h\nu$ is the photon energy. Here, in the case of junctions between Ag with work function of 4.26–4.74 eV[165] or Au with work function of 5.1–5.47 eV[165] and native n-type ZnO NWs[126] with vacuum electron affinity of 4.19–4.5 eV[166], the Schottky barriers were estimated to be in the ranges from 0.1–0.5 eV for the Ag-ZnO junction and 0.5–1.3 eV for the Au-ZnO junction, which are far smaller than the plasmon energy of Ag-ZnO-water (at 450 nm, or 2.76 eV) and Au-ZnO-water (at 560 nm, or 2.21 eV). The concentrated plasmonic E-field at the metal-semiconductor interface assists the energy transfer of the plasmon energy through the metal interband transition (single particle excitation) that enables the excited electrons to readily overcome the Schottky barrier between the plasmonic metal and the catalyst semiconductor. This leads to the hot-electron injection from plasmonic metal into the conduction band of the ZnO catalyst via plasmon excitation and decay.

In this work, ZnO NWs were annealed to improve the donor concentration that can reduce Schottky barrier height of the ZnO-metal contacts, resulting in high hot-electron injection efficiency. The generated hot-electrons are then drifted into external circuit via ITO contact, resulting in the photocurrent generation under VIS light illumination as shown in Fig. 4.16b. It should be noted that the minute current seen in case of pure-ZnO NWs photoanode under VIS illumination (Fig. 16b) will be due possibly to the marginal defect absorption of ZnO

NWs by the deep donor level as reported[105], [167], which might be also combined with the VIS electric field enhancement that enhances the observed response.

The geometrical effects on the plasmon-induced hot-carrier injection from metal to semiconductor are necessary to be considered for realizing high quantum efficiency of the photoelectric transfer. Not only it depends on the Schotky barrier height and the plasmon energy, but it also depends on the momentum and energy distributions of the generated hot-carriers. One of the preferred geometry is that the hot-carriers's momentum must contain sufficiently large component in the direction perpendicular to the metal-semiconductor interfaceas well as the E-field component of the incident light[164], [139], [140], [168]. On the other hand, the quantum confinement is also expected to provide sufficient broad momentum distribution for electronic excitations making the hot-electron generation becomes remarkably efficient for nano-sized metal clusters[139]. For our plasmonic metals-loaded ZnO catalysts, the AgNPs and AuNPs with small size (~13 nm) can provide high quantum efficiency via plasmon-induced hot-carriers injection due to its broad momentum distribution associated with the light excitation. As shown in Fig. 4.17, with E-field excitation perpendicular to NPs-ZnO interface, the free electrons are excited to move in parallel to the E-field vector, resulting in the highest electron density at metal-semiconductor interfaces as well as highest E-field of the plasmon at the same position, which is an ideal condition to induce hot-electron injection. When the E-field is exactly parallel to the NPs-ZnO interface, the electrons are oscillated away from the ZnO surface and the induced E-field magnitude is weak (see e.g., the top and the bottom NPs in Fig. 4.17b-c and Fig. 4.17e-f) that can be resulted in weak electron injection probability in this condition.

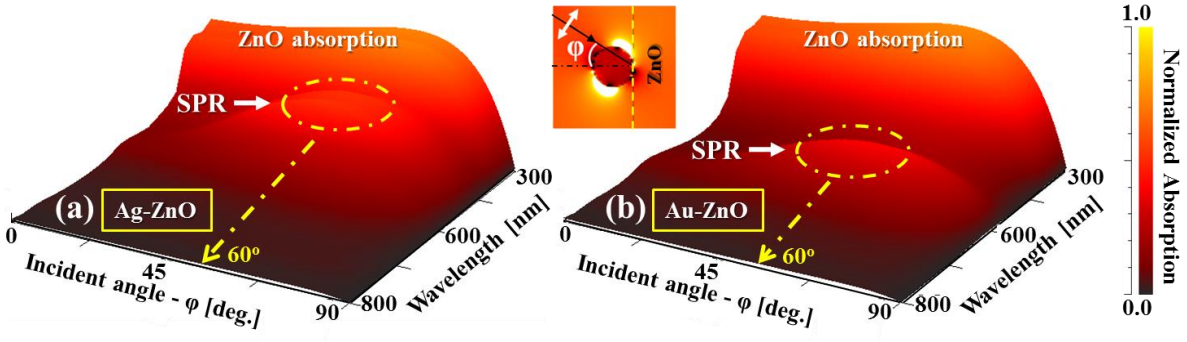

Figure 4.18. Electromagnetic simulations for the incident angle-dependent absorption of plasmonic NPs–ZnO NWs hybrids show the efficient absorption of the nanowire morphology with tiled-angle: (a) AgNP-ZnO NWs and (b) AuNP-ZnO NWs.

To understand the suitable geometrical condition for efficiently exciting the NP plasmons (and thus yielding higher photocurrent) we performed electromagnetic simulations with varying the light incident geometry and polarization. We did the RCWA simulation to simulate the absorption by varying the incident direction and polarization of the light with respect to the NPs-loaded ZnO NWs array. Examples of the simulations are shown in Fig. 4.18 which we can understand the optimal tilting angles of the-NWs array with respect to the substrate that provides the highest optical density. With metal NPs-loaded ZnO NWs, the plasmon absorption intensity strongly depends on the incident angle with the maximum at about 50 to 70^{o} (corresponds to the nanowire tilted-angle of about 20 - 30^{o} compared to incident light excitation). Additionally, the band-edge absorption of ZnO slightly depends on the incident angle exhibiting similar maximum at 50 - 70^{o}. As a whole, this structure shows an optimized absorption both for UV (ZnO band-edge absorption) and VIS (plasmon absorption) light at around 50 – 70^{o}. This angle nicely corresponds to the average tilted angle of our ZnO nanowires readily grown on the TCOs with the present wet chemical synthesis method.

4.3.5. Conclusion of plasmonic NPs-ZnO NW hybrids for efficient photocatalyst

We have fabricated ZnO nanowire array loaded with noble metal nanoparticles by all wet chemical synthesis. The fabricated materials exhibited improved photocatalytic activity 2.4 to

3.2 times higher than the pristine ZnO NWs array as we clarified by the degradation of methylene blue molecules under the solar light. They showed promising performance in photoanode application in the photoelectrochemical cell, and we confirmed that they exhibit substantial photocurrent not only in the ultraviolet region but also in the visible region. The electromagnetic field calculations elucidated the origin of the high optical density in VIS region and provide optimal geometrical condition suitable for high absorption for the light in the UV to VIS region. The strong near-field enhancement at the NPs-ZnO interface was also confirmed, elucidating in detail the microscopic mechanism for the efficient hot-carrier injection from metal to ZnO with the visible light illumination.

The combined plasmonic NPs-semiconductor NWs arrays such as studied here exhibit wide variety of application ranging from solar light photodegradation for environmental remediation to the solar water splitting for hydrogen generation. We expect that the activity of this class of materials can be further improved by appropriately designing the electromagnetic nearfield at the metal/oxide interface by the electromagnetic simulation as well as carefully choosing the constituent materials (oxides such as $SrTiO_3$, TiO_2, Fe_2O_3, WO_3, combined with metals such as Pt, Ru, Ni) via semiconductor band engineering. Together with nanophotonics designing, band engineering, and controlling the nano-architecture, e.g., by further adopting core-shell oxide heterojunction to efficiently promote carrier separation as well as to reduce the carrier diffusion length, we will be able to further improve the photocatalytic performance of the nanomaterials.

4.4. Summary of Chapter 4

We have presented the chemical synthesis and characterization of ZnO NWs for photoelectric conversion applications. By adopting another wet-synthesized p-type Cr-doped TiO_2 thin shell layer, the TiO_2-ZnO NWs core-shell structure showed good p-n heterojunction with an

ideality factor of 2.45. The p-n heterojunction was applied for visible blind - sensitive UV photodetector with high responsivity of 250 mA/W (-5V reverse bias, UV illumination at 373 nm). By combining with plasmonic nanoparticles, we have carried out an efficient solar-assisted photocatalyst. The optical properties of NPs-ZnO were investigated by both simultion and measurement. The strong near-field confined at NPs-ZnO interfaces could enhance light absorption in both UV and VIS regions, resulted in the photocatalytic enhancement as confirmed in both photodegradation and photoelectrochemical measurements. As the results, the fabricated plasmonic NPs-ZnO NWs hybrids exhibited improved photocatalytic activity 2 to 3 times higher than the pristine ZnO NWs array. In addition, the hot-spots located between plasmonic metal and ZnO could provide a sufficient energy for electrons to overcome Schottky barrier, inducing VIS catalytic activity of NPs-ZnO NWs hybrids. Out study on the development of cost-effective plasmonic-ZnO hybrids can be applied for other plasmonic metal-oxide nano-hybrids in order to improve the catalytic performance of the wide band-gap semiconductor materials

5. METAL-INSULATOR-METAL PLASMONIC PERFECT ABSORBER

In previous chapters, we have investigated the light confinement in small gaps between plasmonic objects and metal-oxide interfaces, and their applications in enhancing the light absorption in plasmonic hybrids for molecular sensing and photocatalysis. The absorption efficiency in photoactive devices can be achieved nearly unity with the well-designed plasmonic structure so called plasmonic perfect absorber. Perfect absorbers (PAs) based on plasmonic metamaterials have obtained increasing attentions in the recent years due to their subwavelength thicknesses, narrowband and near unity absorption. In this chapter, we demonstrate the design, fabrication and characterization of PAs with aluminum as the plasmonic material in a metal-insulator-metal (MIM) structure. Our newly developed fabrication approach combines scalable colloidal lithography and reactive ion etching, which enables easy large-area fabrication and offers wide-range tunability of the absorption wavelengths from visible (VIS) to mid-infrared (MIR) ranges. The fabricated Al-PAs showed narrowband absorption with high efficiency up to 98%. In the applications, we demonstrate the uses of Al-PAs as the selective thermal emitters with single-narrowband emissions, or in the selective surface-enhanced infrared absorption spectroscopy as shown a tentative result on the sensing of BSA molecules.

5.1. Plasmonic metamaterial perfect absorber

Metallic subwavelength structures, known as plasmonic metamaterials, have gained much attention due to their unique ability to display fascinating physical properties, thus providing many advanced applications. Among the family of plasmonic metamaterials perfect absorbers (PAs) show nearly 100 % narrow-band absorption at certain wavelengths which can be tuned arbitrarily by the metamaterial designs[169]–[176]. Perfect absorbers have already found a wide range of applications in photonics and opto-electronics such as selective thermal emitters[177]–[180], [26], [181] plasmonic refractive index sensors[182], surface-enhanced infra-

red absorption spectroscopy[183], [184], and CO_2 sensors[185].

In plasmon-enhanced light harvesting applications in infrared (IR) range such as thermophotovoltaics[186], [187], it is desirable to control the spectral emissions by selecting emitters in a narrowband matching to the absorption spectra of the thermophotovoltaic materials. According to Kirchhoff's law of thermal radiation, an absorber can emit thermal radiations at the same wavelength of the absorption spectrum. Several narrow-band thermal emitters have been demonstrated, such as devices based on photonic crystals[188], [189] made of quantum wells[190], SiC grating surface[191], plasmonic steel grating surface[192], plasmonic tungsten grating[193], holes arrays of Ag-SiO_2-Ag[194] and nanoamorphous carbon doped (CAN)/TiN-SiO_2-CAN/TiN[195]. Recently it is worth noting that patterned metal-insulator-metal (MIM) structures have attracted tremendous attention for selective thermal emitters due to their ease of controllability[179], [180], [26], [181], [185].

An MIM PA typically has a thick metallic film at the bottom as the back reflection plane and one or several pairs of insulator-metal structures. The patterning of MIM is commonly done by either photo-, electron- or nanoimprint- lithography, all of which require expensive instruments and cleanroom environment. A simple technique to fabricate large-scale structures with micron resolution is attractive to handily perform laboratory experiments for those who do not have nanofabrication facilities. Among the various nanofabrication techniques, colloidal lithography technique is a simple method to fabricate large-scale periodic structures without the lithography processes as mentioned above[196], [197]. In addition, colloidal spheres with size ranging from several hundred nanometers to several microns can be easily obtained facilitating the fabrication of IR plasmonic devices with great tunability.

With regard to plasmonic materials, gold (Au) and silver (Ag) are the two most widely used materials in a broad range from visible (VIS) to IR and even in terahertz (THz) regions.

Among the other materials, aluminum (Al) is another widely used plasmonic material. However, so far, the use of Al for plasmonic devices is only explored in the UV-VIS[61], [63], [65], [198] range because large losses of Al in NIR and MIR are considered to be disadvantage. In particular, because of its highly negative real part of permittivity in IR region[31], [76], Al could be considered as a promising candidate for IR plasmonic devices. Recently, Al has been used for dual-band absorption of mid-infrared metamaterial absorber using two pairs of circular-patterned metal–dielectric stacks[199], and for multispectral IR plasmonics device by exploiting native Al_2O_3 oxide layer as an insulator between two Al metallic layers to form MIM structure[200]. However, these Al IR plasmonic devices were limited to cost-effective due to employing the UV and electron beam lithography processes.

In this work, we show a facile method to fabricate large-scale perfect absorber based on plasmonic metamaterials in MIR region using aluminum. A MIM aluminum perfect absorber (Al-PA) structure on a silicon substrate consists of an Al film as a back reflection planar layer, an insulator of Al_2O_3 in the middle and the Al disks or Al holes array on the top. The parameters of the MIM Al-PA, including the periodicity, thicknesses of the transparent Al_2O_3 and the Al disk (holes) resonator layers, were optimized by rigorous coupled wave analysis (RCWA). The fabricated Al-PAs have nearly perfect absorption (c.a. 98%) with narrow band width (FWHM = 0.75 μm) and the resonance wavelength were tuned from 3 μm to 9 μm by adjusting the geometrical parameters. In the applications of the Al-PAs, we demonstrate the selective thermal emitters with single-narrow band emissions, and show a tentative result on SEIRA targeting the amide-II vibrational band of bovine serum albumin (BSA) molecules. In addition to that, with simple and inexpensive fabrication method, the IR PAs can be achieved on the flexible metallic substrates such as an example of Al-PAs on a 0.2 mm Cu plate, which was used as the bottom metallic layer. It is expected that the use of Al in IR and the fabrica-

tion technique developed in the present work can be extended in many other plasmonic applications in IR.

5.2. Design, simulation and fabrication of the metal disk-insulator-metal film perfect absorber ranging from VIS to IR

In this section, we show the design, simulation and fabrication of the Al-MIM PAs with top Al layer is a circular disks array.

5.2.1. Proposed structure and its optical properties

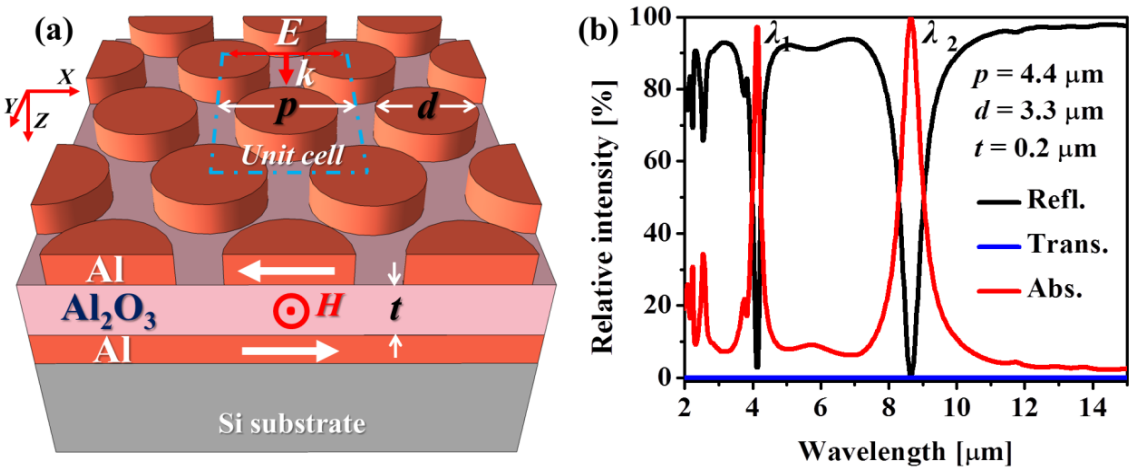

Figure 5.1. (a) Schematic design of the Al-PA with definition of a unit cell and parameters: periodicity (lattice constant) *p*, diameter of Al disk resonator *d* and insulator thickness *t*. The incident electromagnetic fields propagate along the z axis and the electric field is parallel to the x axis. (b) Simulated spectra of a typical Al-PA with p = 4.4 μm, d = 3.3 μm, and t = 0.2 μm, show the absorption efficiencies of the two resonance peaks at 4.16 μm and 8.65 μm with their absorption efficiencies were 97 % and 100 %, respectively.

The proposed MIM disks Al-PA structure is shown in Figure 5.1a: a hexagonal array of Al disks as resonators on the top and an Al film at the bottom, are separated by an Al_2O_3 insulator. The Al back plane film is chosen to have a thickness of about 100 nm to eliminate transmission of infrared radiation through the structure, and it also serve as a joule heater when current was applied to study thermal emissions from the samples. In the present Al-PA devic-

es, the thickness of Al disk resonator was fixed at 0.1 μm, and the resonance wavelength and absorptivity of the MIM structure are therefore mainly controlled by tuning the periodicity *p*, the diameter of resonator *d* and the thickness of the isolator *t*. For example, Figure 5.1b shows typical simulated spectra of an Al-PA structure with its parameters of p = 4.4 μm, d = 3 μm, and t = 0.2 μm. The RCWA method was used to calculate the simulated spectra of Al-PAs. The dielectric functions of Al, Au, Ag, W, and Si were taken from the literature[76], [31]. The dielectric function of Al_2O_3 was taken from literature[31]. The model of Al-PAs device was performed in a cad layout (RSoft CAD) with the unit cell as shown in Fig. 5.1a. The excitation electromagnetic field propagates along *Z* axis and the electric field oscillates along *X* axis (Fig. 5.1a). The index resolution was set to 10nm. The absorption at wavelength λ is given by: $A(\lambda)=1-R(\lambda)-T(\lambda)$, where $R(\lambda)$ and $T(\lambda)$ are the reflection and transmission of the structure, respectively. It was found that, the transmission of the Al-PA structure with a 100 nm Al back plane film is almost zero, therefore, the absorption of an Al-PA structure is simply given by $A(\lambda)=1-R(\lambda)$. We can see that the proposed structure has two narrow resonance bands, a short-wavelength λ_1 at 4.16 μm with an absorption efficiency of 97.2 %, and a main resonance long-wavelength λ_2 at 8.65 μm with absorption efficiency up to 100 %.

As mentioned, Al also has a good metallic property in the IR range with more negative real part of permittivity than Au, Ag and tungsten (W) which is often used for thermal emitter (Fig. 5.2a). For comparison, the simulations of the absorption efficiency of Au, Ag and W were also performed and shown in Fig. 5.2b. The results indicate perfect absorption can be achieved even with lossy metallic Al and W which are not common materials in plasmonics.

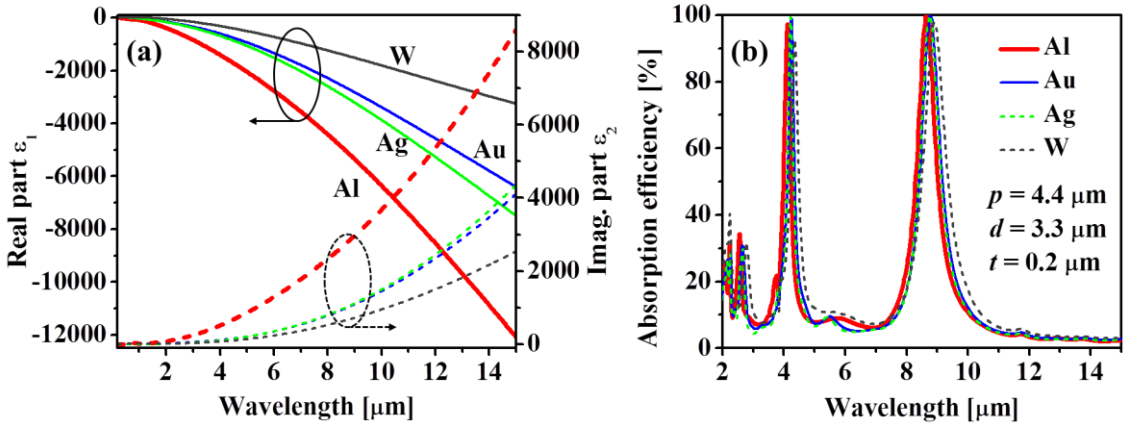

Figure 5.2. (a) Dielectric functions of common plasmonic materials (Au and Ag) and lossy metallic Al and W and (b) Their perfect absorption properties.

To elucidate the optical properties of the Al-PA, further simulations were performed as shown in Fig. 5.3. The resonance frequencies of the Al-PA are tuned by changing the diameter of the Al disk (Fig. 5.3a) or the periodicity (Fig. 5.3b). As we can see in Fig. 5.3a, with the periodicity and isolator thickness fixed, the long-wavelength resonance λ_2 is gradually increased by increasing the size of the Al disk, while the short-wavelength resonance λ_1 is hardly dependent on the size of Al disk *d* when *d* is small compared to the resonance wavelength - λ_1. In particular, when *d* is comparable to the resonance wavelength - λ_1, the short-wavelength resonance λ_1 is slightly dependent on the Al disk size *d*. In contrast, opposite behaviour is observed for the effect of the periodicity as shown in Fig. 5.3b. Long-wavelength resonance λ_2 has little dependence on the periodicity while the short-wavelength resonance λ_1 gradually shifts toward longer wavelength when the periodicity increases. For a periodic plasmonic structure, the coupling between surface plasmon (SP) and photonic mode could induce a shape resonance[201]–[203]. In Al-PA device, the short-wavelength resonance λ_1 is related to SP – photonic coupling (or delocalized plasmon)[174], [204] which strongly depends on the periodic property. The coupling between SP and photonic modes is stronger when the size of Al disk *d* is comparable to the resonance wavelength as indicated above. On

the other hand, the long-wavelength resonance λ_2 is related to the localized surface plasmon (LSP) resonance, which is strongly dependent on the size of the Al disk. Furthermore, the dipole oscillation of the free electron in the top Al disk resonator induces an anti-parallel dipole oscillated at the back plane layer, resulting in the formation of an electric current loop, which perform as a magnetic dipole. Thus, this type of resonance is often named as "magnetic mode" in MIM perfect absorber structures.

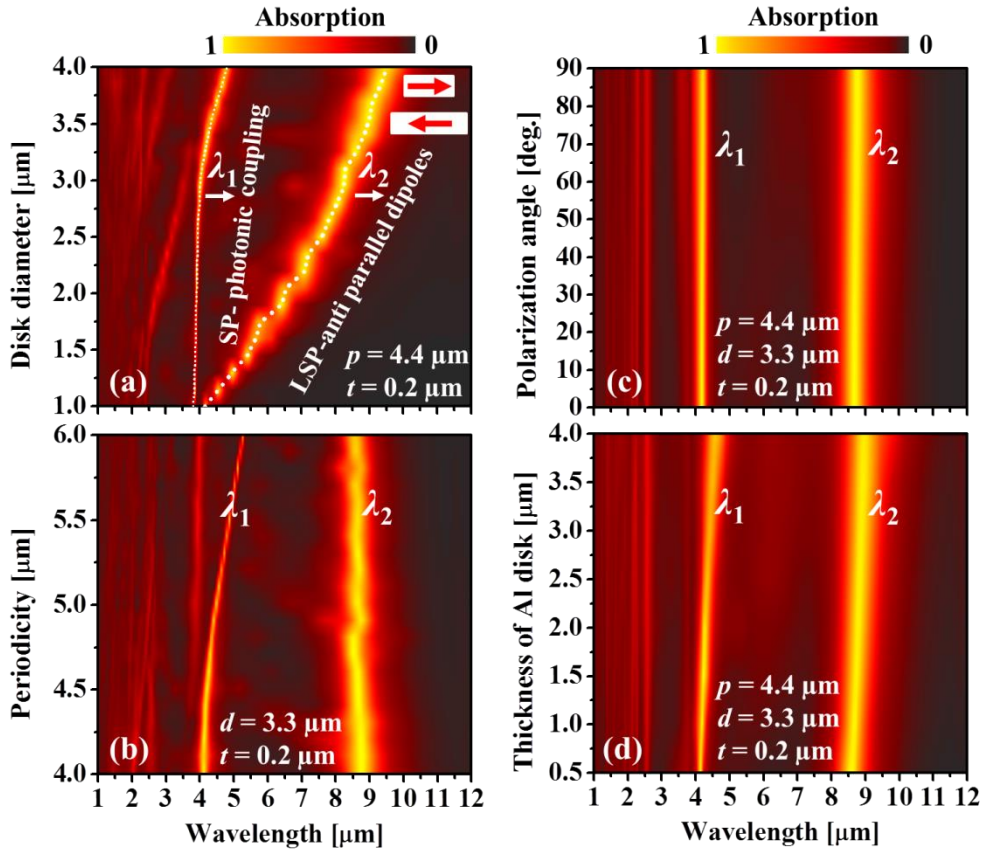

Figure 5.3. Simulated optical properties of the designed Al-PA. (a) The size-dependent resonance frequencies of resonator of the Al-PA. The periodicity of the Al-PA was fixed at 4.4 μm. (b) The periodicity-dependent resonance frequencies of the Al-PA. The resonator of Al-PA was fixed at 3.3 μm. (c) The polarization-independent resonance frequencies of the Al-PA. (d) Slightly red-shift of Al-PAs spectra by increasing the thickness of Al resonator. The periodicity, diameter and the thickness of insulator layer were 4.4 μm, 3.3 μm and 0.2 μm, respectively for the both (c) and (d).

An advantageous point of the hexagonal structure is its polarization independence. Figure 5.3c shows the simulated results of the polarization-independent resonance frequencies in Al-

PA device. It is clear to see that both resonance frequencies stay unchanged with changing polarization from 0 to 90°. It holds great advantage in many applications where non-polarized light source such sunlight is preferred to achieve high absorption efficiency since polarization-independent Al-PA structure is high azimuthal symmetry.

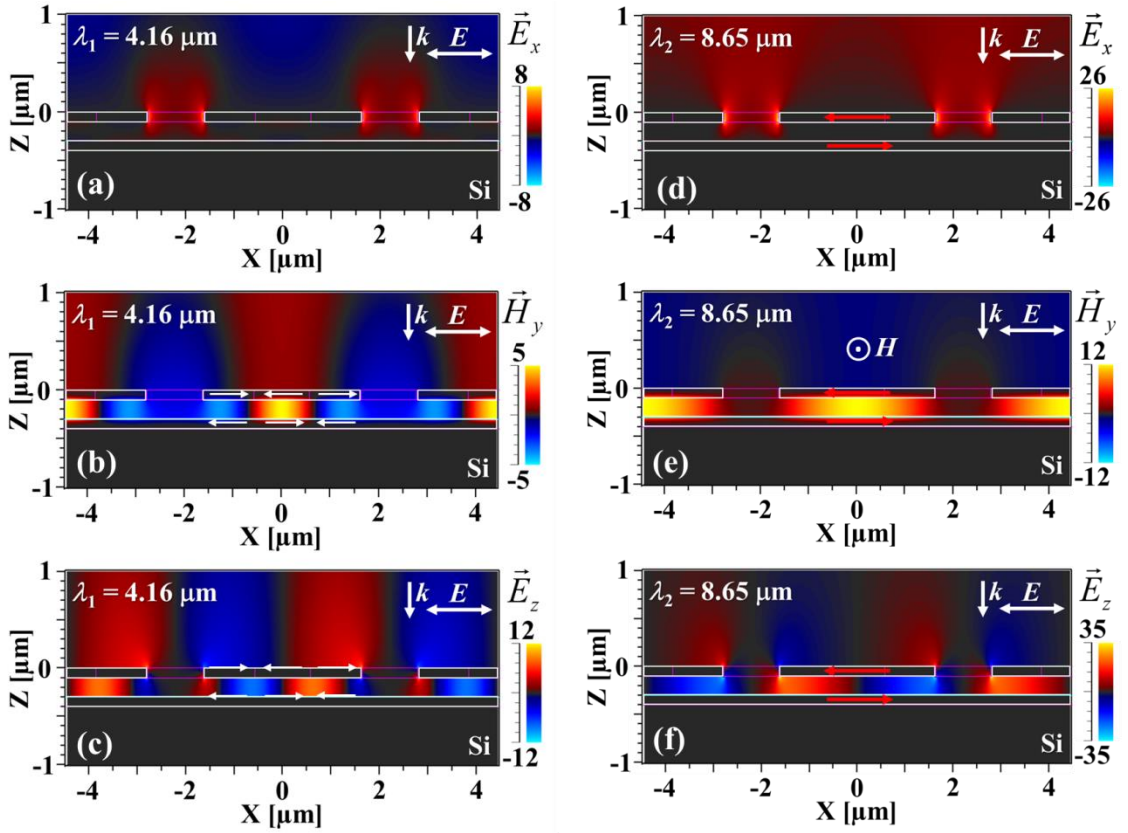

Figure 5.4. (a-c) and (d-f) Electromagnetic field distributions in Al-PA structure under polarized excitation at magnetic resonance at SP-photonic coupling mode (4.26 μm) and magnetic mode (8.65 μm), respectively. The electric fields propagate along Z axis and oscillate in X direction. The electromagnetic incident fields were normalized to 1.

To further clarify the original of these two modes in the Al-PAs structure, the electromagnetic field distributions were performed using FDTD method as shown in Fig. 5.4. The incident electromagnetic field amplitudes were normalized to 1. Figure 5.4a-c show simulated electromagnetic field distributions of the SP – photonic coupling at 4.16 μm. The enhanced electric field E_x in the incident wave plane is located at the edges of Al disk resonator with an enhancement factor of 8 (Fig. 5.4a), indicating the weak SP resonance. Three mag-

netic hot-pots in the insulating layer indicated the magnetic fields are oscillated in different phases, which are induced by the coupling between SP and photonic mode when the size of the Al disk (3.3 μm) is comparable with resonance wavelength - λ_1 (4.16 μm). The induced electric field E_z indicated SP – photonic coupling shows the hot-pots related to the charges motion in the three electric loop-likes (Fig. 5.4c). In contrast, the electromagnetic fields were strongly enhanced under magnetic mode excitation at 8.65 μm (Fig. 5.4d-f). The electric field E_x in the incident plane is enhanced by 26 folds and located at the edges of the Al disk (Fig. 5.4d), while magnetic field is enhanced by a single electric loop current in the isolating layer (Fig. 5.4e). The induced electric field E_z shows clearly the hot-spots are related to the charges motion in the electric loop-like (Fig. 5.4f).

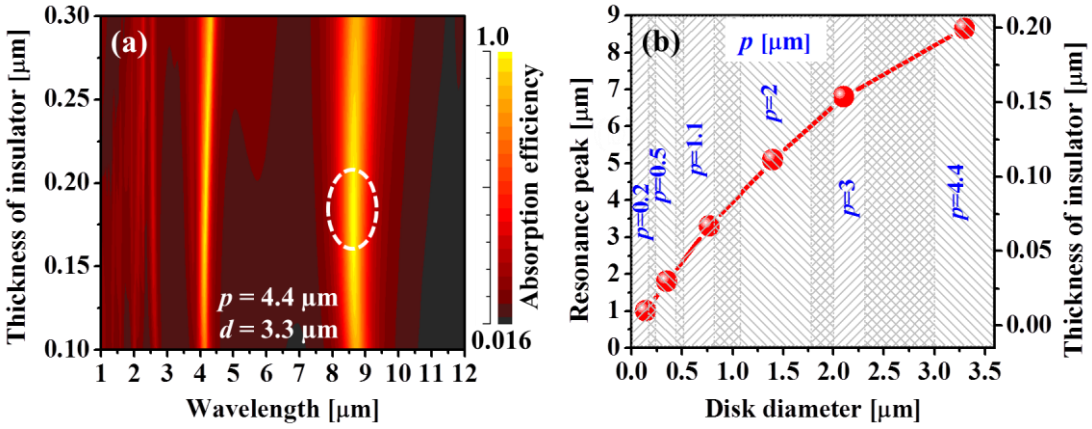

Figure 5.5. Wide-range tunability of the Al-PAs. (a) Simulated the dependence of the absorption efficiency on the isolator thickness in the case where p = 4.4 μm, r = 3.3 μm. The dashed oval shows highest absorption efficiency corresponding to the insulator thickness of about 200 nm. (b) Simulated the tunable resonance frequencies at magnetic mode ranging from 0.5 – 9 μm by tuning the size of Al disk with the suitable periodicity - p (or suitable PS spheres with variable diameters ranging from 0.2 μm to 4.4 μm,) and isolator thickness t.

As we described above, the resonance wavelength of the Al-PA is strongly depended on the size of the Al-disk resonator. Here, the detail analyses of the tenability of the Al-PA resonance frequencies are provided as shown in Fig. 5.5. Firstly, Fig. 5.5a shows the

optimization of absorption efficiency of Al-PAs by tuning the thickness of the insulator. Figure 5.5b shows the simulated evaluation for the tunable ability of resonance of the Al-PAs at magnetic resonances ranging from 0.5 - 9 μm. The thicknesses of Al back plane was 0.1 μm. The thickness of Al disk resonators were 0.1 μm for IR range and 0.04 μm for VIS range. It was found that, by choosing the suitable periodicity (available PS spheres) and tuning the Al disk resonator with the optimized isolator thickness, we can tune resonance wavelength of the Al-PA in a wide range from VIS to long-wavelength IR as shown in Fig. 5.5b. For example, a perfect absorber at 6.8 μm can be achieved by choosing the periodicity, Al disk resonator and insulator thickness to be 3.0 μm, 2.1 μm and 0.15 μm, respectively.

5.2.2. Fabrication of Al-PAs using conventional colloidal lithography

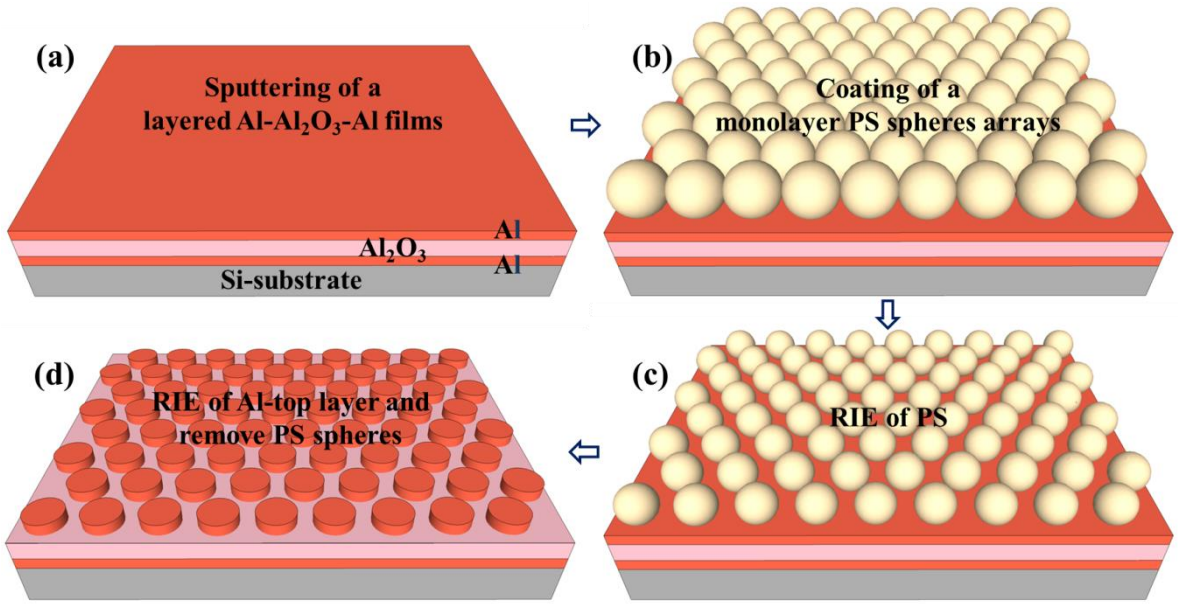

Figure 5.6. Illustration of the fabrication process. (a) Sputtered Al-Al_2O_3-Al film on a Si (100) substrate. (b) Self-assembled monolayer of PS spheres in close-packed hexagonal arrays. (c) Shrank PS mask after the RIE process with oxygen. (d) Final structure of the device after RIE of Al top layer and removal of the PS mask.

We realized large-scale IR plasmonic Al-PAs by combining colloidal lithography with RIE technique. The detailed step-by-step fabrication process is shown in Fig. 5.6. Firstly, a lay-

ered Al-Al_2O_3-Al films were deposited on top of Si (100) substrate using DC and RF sputtering methods (i-Miller CFS-4EP-LL, Shibaura) (Fig. 5.6a). The thicknesses of films from bottom to top were optimized as discussed in the previous subsection. The layered film was then coated with a monolayer of polystyrene spheres with suitable sizes (Polybead® Polystyrene Microspheres - Polysciences) to form a close-packed hexagonal array for a lithography mask (Fig. 5.6b). To form a monolayer of PS on Al-Al_2O_3-Al films, firstly, the sputtered films on Si substrates were aligned in a plastic box placed in a 10° tilled angle, then the plastic box was filled up with deionized water. A monolayer of PS spheres was created onto water surface by using a glass slide tilled at 30°, and then by using a micro-pump to drain the water in plastic box, this monolayer of PS spheres was finally formed on the sputtered Al-MIM films.

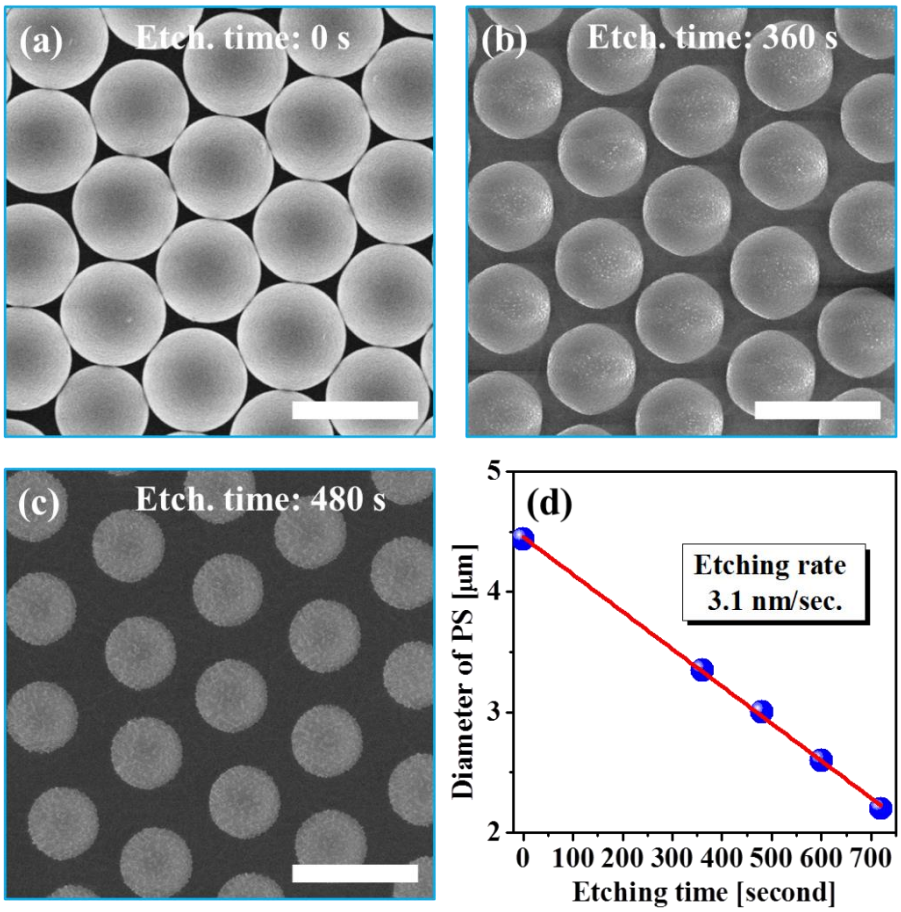

Figure 5.7. (a-c) SEM images of PS at different etching time. The scale bar is 5 μm for each image. (d) Size of PS mask as a function of etching time with the etching rate of about 3.1 nm/ second.

The size of the PS mask was shrunk by RIE process using oxygen gas (20sccm, APC pressure 1 Pa, antenna RF power 200 W, bias RF power 5 W, Ulvac CE-300I) (Figure 5.6c). The Al disk resonators were formed by etching the masked Al top layer at an etching rate of 0.82 nm/ second (dual-gases BCl_3/Cl_2, 3/3 sccm, APC pressure 0.15 Pa, antenna RF power 50 W, bias RF power 10 W, Ulvac CE-300I). The MIM Al-PAs were finally formed by removing the PS masks and carefully cleaned by toluene and methanol (Fig. 5.6d). The resonance of Al-PA can be readily tuned by changing the size of the PS mask with precise control of the etching time as SEM images shown in Fig. 5.7. The etching rate of PS mask was estimated to be 3.1 nm/ second (Fig. 5.7d).

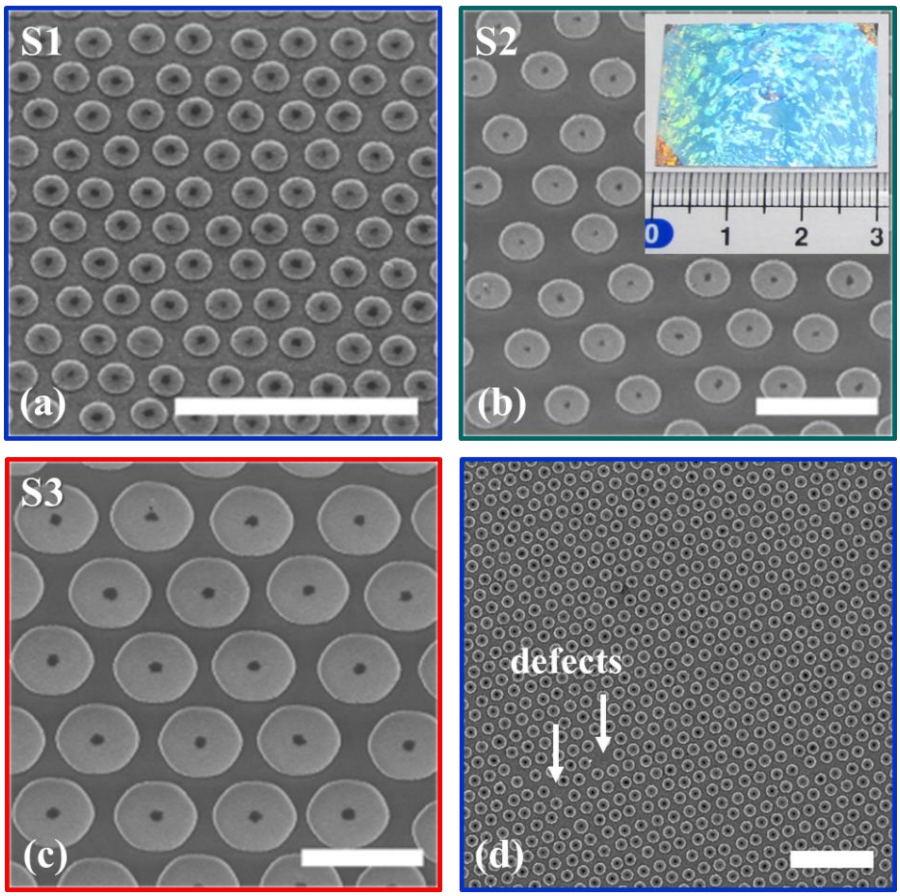

Figure 5.8. SEM images of three typical fabricated Al-PAs with their resonances as designed: (a) S1 (p = 1.1 μm, d = 0.7 μm, t = 0.05 μm) at 2.85 μm, (b) S2 (p = 3.0 μm, d = 1.7 μm, t = 0.15 μm) at 5.67 μm and (c) S3 (p = 4.4 μm, d = 3.3 μm, t = 0.2 μm) at 8.65 μm. The scale bar is 5 μm for each image. (d) Typical defects of the fabricated samples. The inset in (b) is a photograph of a fabricated Al-PA of 2×3 cm^2.

Following the rule of the tunable ability of resonance by tuning Al resonator size as shown in Figure 5b, we experimentally fabricated an array of Al-PAs with resonance spectra tuned in IR range using the fabrication method presented before. Figures 5.8a-c show SEM images of the three fabricated Al-PAs (samples S1, S2 and S3). Figure 5.8d shows some typical defects of the fabricated sample causing by colloidal lithography method. These samples were fabricated on 0.5x3 cm^2 area on Si (100) substrates. Inset of Fig. 5.8b shows a photograph of Al-PA sample fabricated on a 2x3 cm^2 substrate. The periodicity *p*, Al disk diameter *d* and thickness of Al_2O_3 insulator were chosen to realize narrowband resonances at 2.85 μm (sample S1 - p = 1.1 μm, d = 0.7 μm, t = 0.05 μm), at 5.67 μm (sample S2 - p = 3.0 μm, d = 1.7 μm, t = 0.15 μm) and at 8.65 μm (sample S3 - p = 4.4 μm, d = 3.3 μm, t = 0.2 μm).

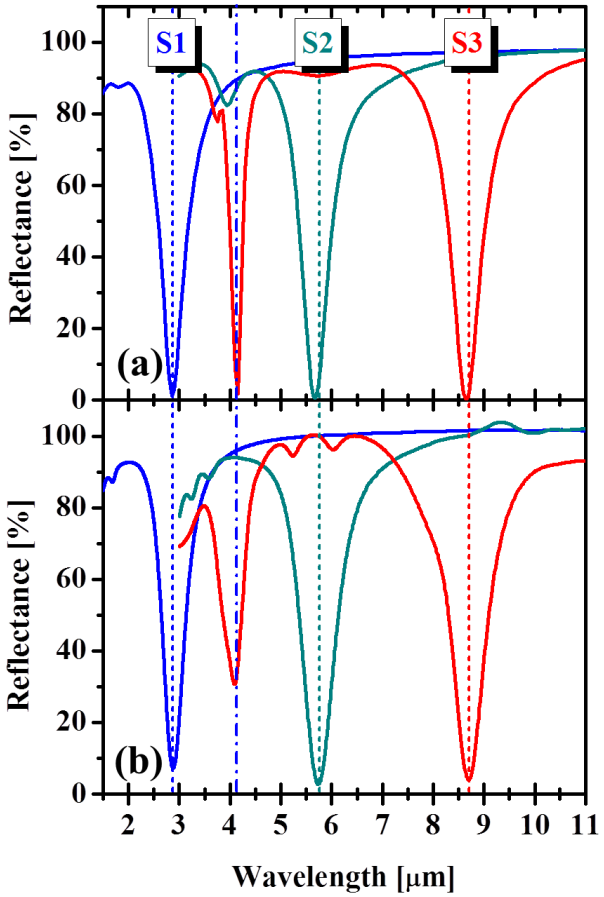

Figure 5.9. (a) Simulated and (b) Measured reflectance spectra of samples S1, S2 and S3 shown in Fig. 5.8.

Figures 5.9a-b show the simulated reflectance and measured spectra of the three samples, respectively. The reflectance spectra of the Al-PAs were taken using a Fourier transform infrared (FTIR) spectrometer (Nicolet iS50R FT-IR Thermo Scientific) with a liquid-nitrogen-cooled mercury cadmium telluride (MCT) detector and a KBr beam splitter. The experimental data were in good agreements with the simulation where the highest absorption efficiency as high as 97.5 % (reflectance 2.5 %) was observed for sample S2. It is noted that the SP-photonic coupling becomes weak when the periodicity is imperfect, which is often the case with colloidal lithography method. As we can see, while the simulated spectrum of sample S3 shows 97.2 % absorption efficiency at 4.16 μm, the fabricated sample shows a lower absorption efficiency of 68 %. The target of our work is to achieve narrow bandwidth and single mode thermal emission devices. Therefore, the nature of colloidal lithography is advantageous for our purpose.

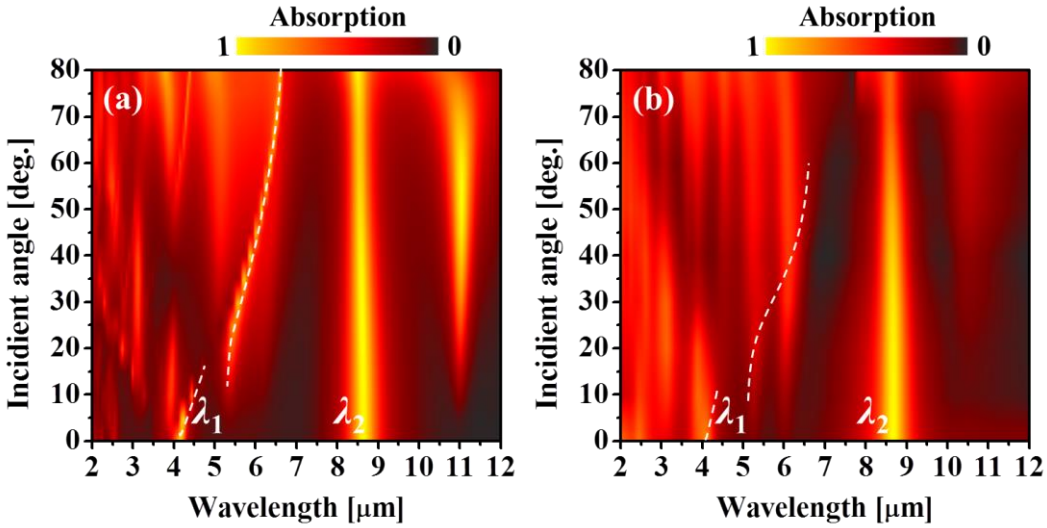

Figure 5.10. Incident angle-dependent resonance spectra of Al-PA. (a) Simulated and (b) Measured results for the case of S3 (p = 4.4 μm, d = 3.3 μm, t = 0.2 μm, magnetic resonance at 8.65 μm).

Furthermore, Al-PA is expected to be a wide-angle perfect absorber where it shows high absorption efficiency in a wide-range incident angle. Figure 5.10 show the simulated (Fig. 5.10a) and measured (Fig. 5.10b) results for the case of S3 (p = 4.4 μm, d = 3.3 μm, t = 0.2

μm, magnetic resonance at 8.65 μm). As we can see in both of the simulation and measurement, the peak position and absorption efficiency of the SP-photonic coupling mode (λ_1) is strongly dependent on the incident angle as expected, while the main magnetic mode (λ_2) shows the unchanged peak position and high absorption efficiency in a wide-range from 0° – 70°. In addition, at the tiled-incident excitation, the momentum projection on *Z* direction of the excited light can be tuned to matching with certain magnetic modes as shown in the simulation result with a longer-wavelength mode appeared at 10.5 - 11 μm, while it is slightly appeared in the measurement result.

5.3. Al-PAs based selective thermal emitters

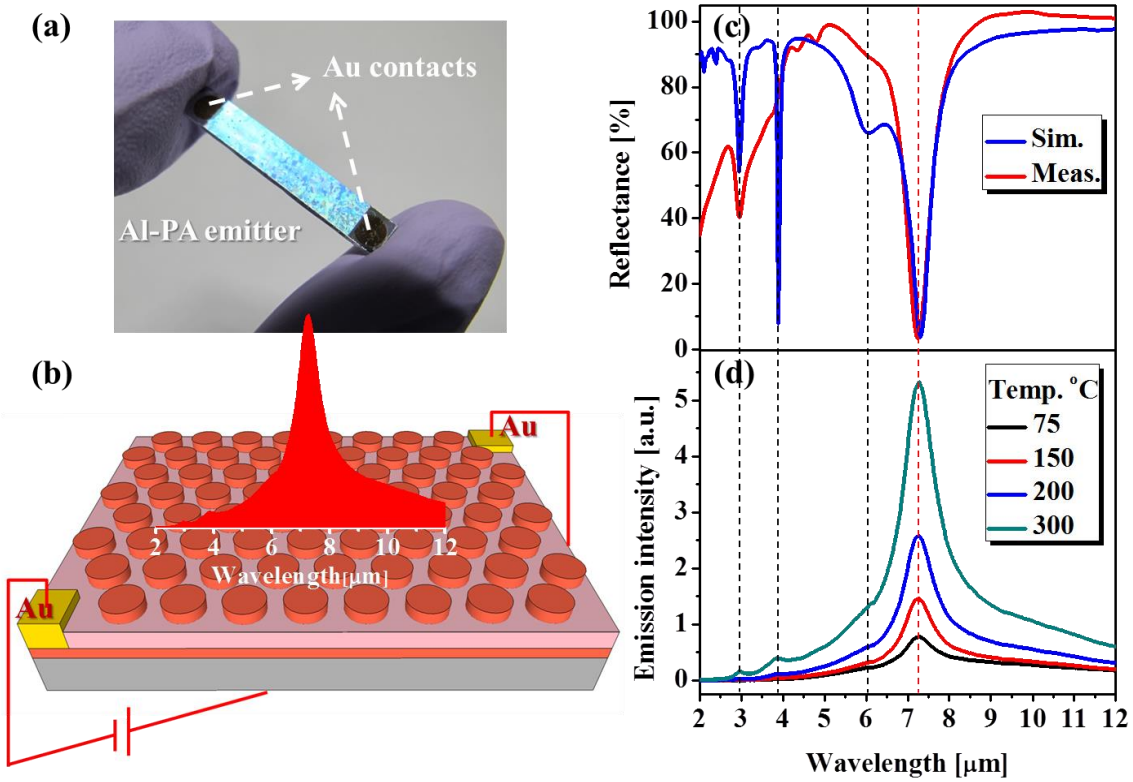

Figure 5.11. Al-PA based thermal emitter. (a) Photo and (b) Schematic of an Al-PAs thermal emitter device. (c) Simulated and measured reflectance spectra of an Al-PA designed at magnetic resonance of 7.26 μm (p = 4.4 μm, d = 2.3 μm, t = 0.2 μm). (d) Emission from Al-PA thermal emitter at different temperatures ranging from 75 – 300 °C.

In this section, we describe the thermal radiation from the Al-PAs, which are expected to be narrowband emissions. For a demonstration, we design an Al-PA thermal emitter with parameters of p = 4.4 μm, d = 2.3 μm, t = 0.2 μm, to have a resonance frequency of 7.26 μm at magnetic mode (Fig 5.11c). The Al-PA was fabricated on 0.5 x 3 cm^2 area on Si (100) substrates by the technique described before. Two 100-nm thick gold films were deposited onto the two Al contacts by thermal deposition. A photo and the schematic of the Al-PA thermal emitter device are shown in Fig 5.11a and Fig 5.11b, respectively.

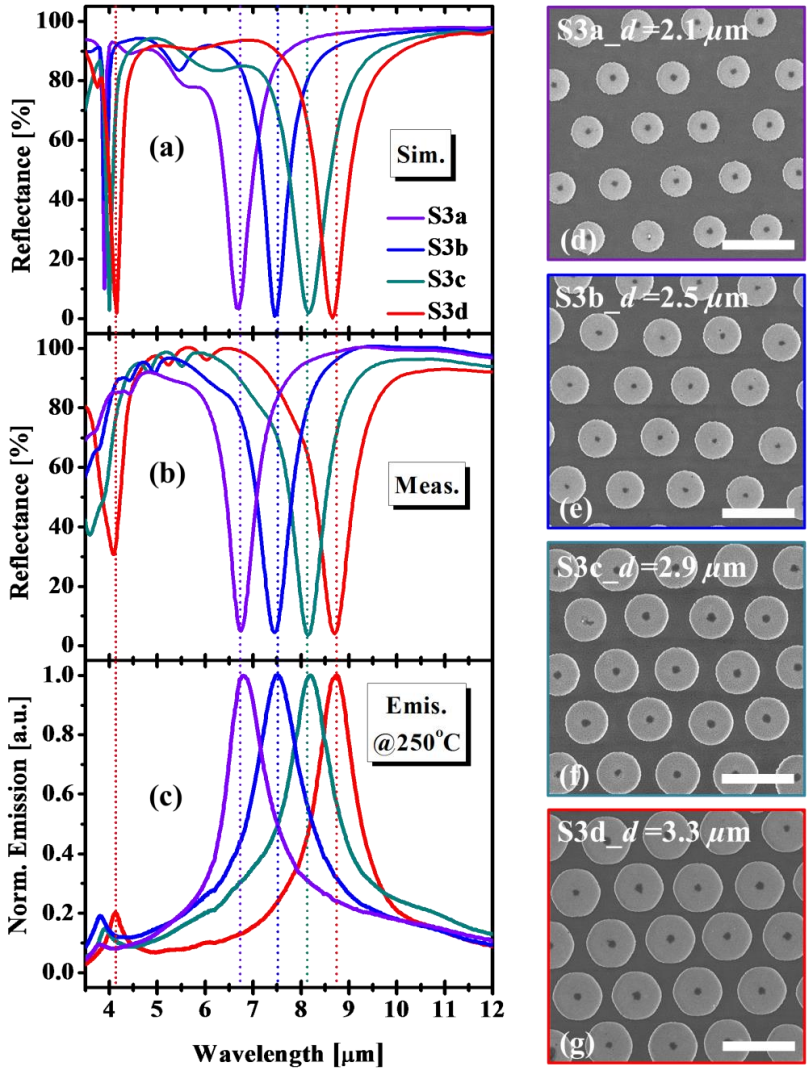

Figure 5.12. (a) Simulated and (b) Measured reflectance spectra of the samples S3a-d. (c) Emission spectra of samples S3a-d heated at 250^{o}C. The peak positions of the emissions match to the dips in reflectance spectra. (d-g) SEM images of the fabricated samples S3a-d, respectively. The scale bar is 5 μm for each SEM image.

To characterize the thermal radiation of Al-PAs, the fabricated Al-PA was heated by applying a sufficient current on the back plane Al through Au contacts. Then the thermal radiations from Al-PA emitter was collected by an FTIR spectrometer (Thermo Nicolet Nexus 670 FT-IR spectrometer, KBr beam splitter, MCT detector) equipped with two external concave Al mirrors to guide emission from Al-PA emitter to spectrometer. As we can see in Fig 5.11d, a single emission was achieved from Al-PA device at different temperatures ranging from 75 - 300 °C in ambient air. It could be noted that, the emission wavelength was identical to absorption wavelength, which clearly follows Kirchhoff's law of thermal radiation.

In order to demonstrate the selective thermal emission using Al-PAs, we designed four Al-PAs where the resonance wavelengths are at 6.73 μm (S3a with p = 4.4 μm, d = 2.1 μm, t = 0.2 μm), 7.46 μm (S3b with p = 4.4 μm, d = 2.5 μm, t = 0.2 μm), 8.15 μm (S3c with p = 4.4 μm, d = 2.9 μm, t = 0.2 μm) and 8.65 (S3d with p = 4.4 μm, d = 3.3μm, t = 0.2 μm), respectively. Figure 5.12a shows the simulated reflectance of the Al-PAs with the absorption efficiency higher than 96 %. Figure 5.12b shows the measured reflectance spectra of the fabricated devices. The measured spectra show high absorption efficiency at magnetic resonance modes, which match very well to the simulations. Figure 5.12c shows the normalized emission spectra of the Al-PAs at 250°C in ambient air. Our experimental results demonstrate the tenability of the narrow-band thermal emission by tuning the size of the Al disk resonators.

5.4. Al-PAs based surface-enhanced infrared spectroscopy

In this section, we demonstrate another application of Al-PAs as a plasmonic infrared antenna for SEIRA. A tentative result on sensing of BSA molecules adsorbed on Al_2O_3/Al surface expected that our Al-PAs can be used as an active SEIRA substrate for vibrational sensing.

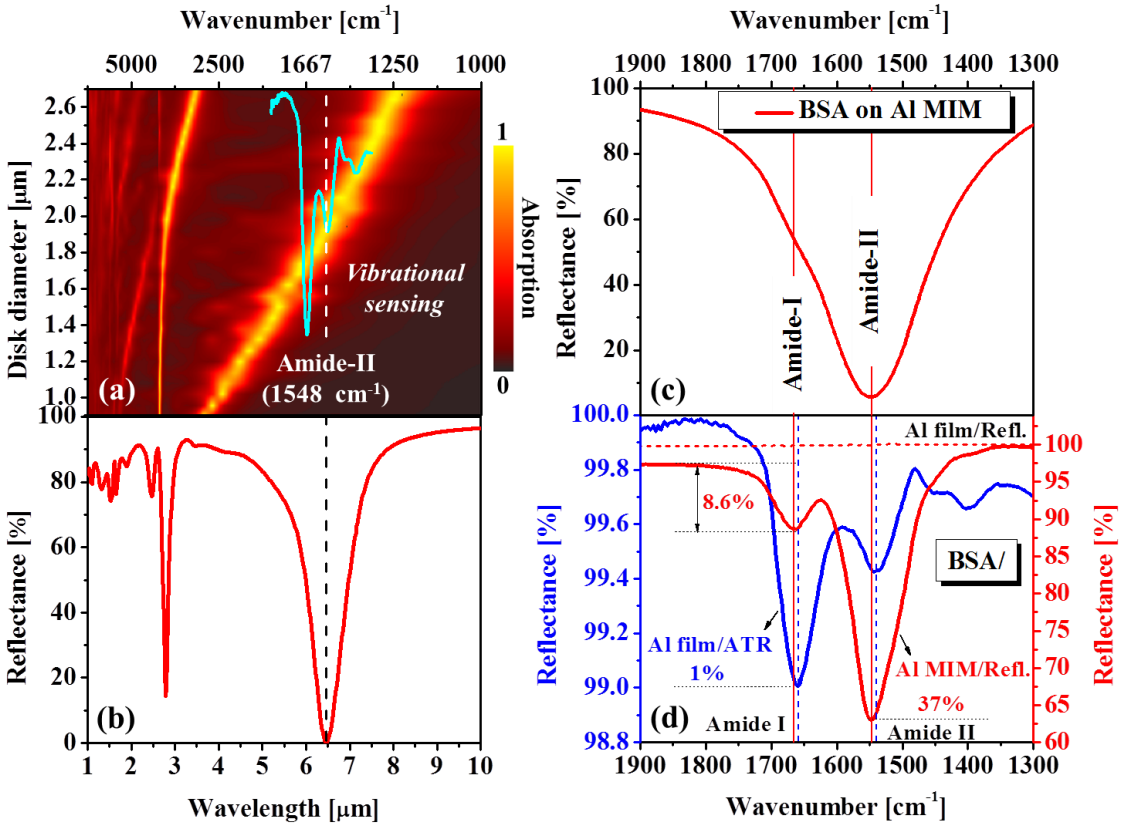

Figure 5.13. Vibrational sensing of BSA molecule adsorbed on Al surface using Al-PAs as a SEIRA substrate. (a) Simulated resonance spectra of Al-PAs with different resonator (p = 3 μm, t = 0.15 μm) in which Al-PAs resonance covered vibrations of molecules. (b) Simulated reflectance of an Al-PA (p = 3 μm, d = 1.9, t = 0.15 μm) with resonance of 6.46 μm for sensing amide-II band of BSA molecule. (c) Reflectance measurement of BSA-adsorbed Al-PA. (d) Vibrational signals of BSA molecules adsorbed on Al planar film with ATR (blue), or on Al planar film (dash red) and Al-PA (sloid red) with normal reflection configurations.

The matching between resonances frequencies (wavelengths) of Al-PAs with vibrational frequencies of the molecules allows Al-PAs can be used as the plasmonic active antenna for vibrational sensing. Figure 5.13a shows the simulated resonance spectra of Al-PAs with different Al resonators (p = 3 μm, t = 0.15 μm) covering a wide-range in MIR, which are overlapped on the vibrational of most common molecules. As we can see in this Fig. 5.13a, bovine serum albumin (BSA), a serum albumin protein, has two strongest vibrational bands located at 1662 cm^{-1} (amide-I) and 1548 cm^{-1} (amide-II). In this work, we describe a sensing of BSA molecules adsorbed on Al_2O_3/Al surface by SEIRA using Al-PA with resonance wave-

length of 6.46 μm (1548 cm^{-1}) (Fig. 5.13b) for targeting amide-II band. The parameters of fabricated sample were p = 3 μm, d = 1.9, t = 0.15 μm. For the comparisons, an Al planar film (100 nm thickness) was also fabricated at the same time of sputtering.

First, cleaned Al-PA and Al films were treated under oxygen plasma (100 W) for 30 second to remove any organic molecules contaminations, and to support a formation of Al_2O_3 layer on Al surface. This process is also needed to form positively charged Al-hydroxyl surface groups on Al_2O_3 oxide layer. Then, the treated Al surface samples were soaked in to BSA solution (Sigma Aldrich, 10^{-3} M in water, pH = 6.9) for 24 hour, and rinsed in distilled water and finally dried under a stream of nitrogen gas. The adsorption of BSA molecules on Al_2O_3 was formed via binding between the negative charges of the protein with the positively charged Al-hydroxyl surface groups[186]. As we can see in Fig. 5.14a showing an SEM image of BSA molecules adsorbed on Al-PA.

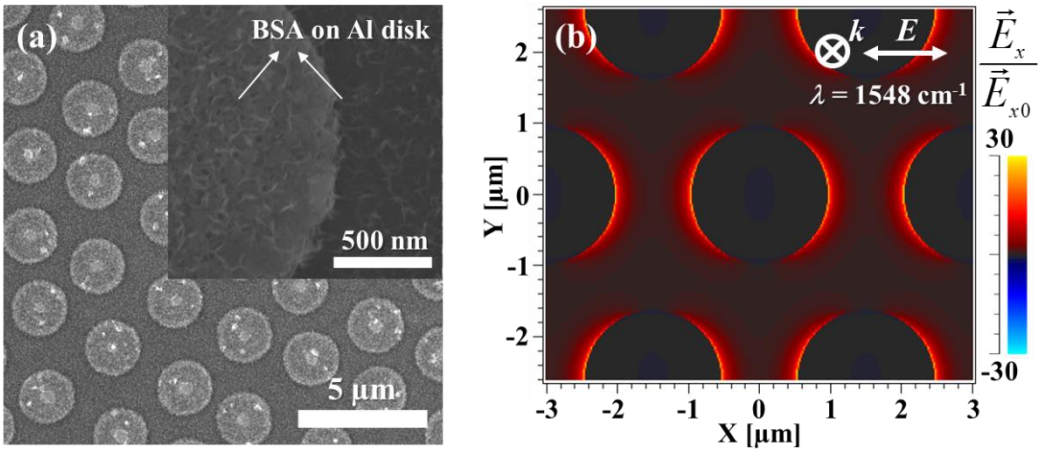

Figure 5.14. (a) SEM image of BSA adsorbed on Al-PA shows that BSA molecules are adsorbed on Al-PA surface. There is no molecule at the center of Al disk where Al-Al_2O_3 surface was modified during etching process. (b) Simulated electric field distribution on Al-PA under resonance excitation at magnetic mode -1548 cm^{-1}.

The FTIR spectra of BSA molecules adsorbed on an Al planar film was taken using ATR configuration (Nicolet IS50R FT-IR, DTGS-ATR detector and KBr beam splitter) in which its sensitivity is expected to be higher than that of normal transmission or reflection configu-

rations. The FTIR spectra of BSA molecules adsorbed on another Al planar film and Al-PA were taken using normal reflection configuration (Nicolet iS50R FT-IR, MCT detector, KBr beam splitter). Figure 5.13c presents reflectance spectra of BSA adsorbed Al-PA substrate with two amide bands and resonance spectra of Al-PA targeted to amide-II. Figure 5.13d shows relative reflectance vibrational signals of BSA molecules adsorbed on Al planar film under ATR configuration (blue), on Al planar film (dash red) and Al-PA (red) under conventional reflection geometries. It was found that, the relative reflectance of vibrational signals of BSA molecules adsorbed on Al film are below 0.1 % for both two amide bands in case ART configuration, and the signal intensity of amide-II is smaller than amide-I. In case of normal reflection configuration with low sensitivity, there was almost no signal from BSA adsorbed on Al planar film, but strongly vibrational signals were observed from BSA adsorbed on Al-PA. As we can see in Fig. 5.13d, the relative reflectance intensity of amide-I is 8.6 %, while with strong electric field enhancement at resonance of Al-PA by 30 folds under resonance excitation at 1548 cm^{-1} (Fig. 5.14d), the relative reflectance intensity of amide-II is as strong as 37%. It is noted that this value is far higher than that signal of amide-I. Thus, it is expected that, by using Al-PA as a SEIRA substrate, the vibrational signals from BSA molecule were strongly enhanced and the relative intensity between amide-I and amide-II can be controlled by using Al-PA with resonance targeted to certain vibrational frequency.

5.5. Al-PAs on Cu plate

It is desirable to have a large scale perfect absorber device on any cost-effective substrate for multiple applications. By using present colloidal lithography method and combining with other metallic plates like Al, Cu, stainless steel, we are able to carry out a large scale perfect absorber device. In this section, we demonstrate the design and fabrication of the aluminium perfect absorber consists of an Al disk resonator on top layer, an Al_2O_3 insulator and Cu plate

as a back-plane substrate. This structure also shows high performance perfect absorber, but it is simple and more inexpensive since it uses a cheap Cu plate and do not require Al back-plane layer.

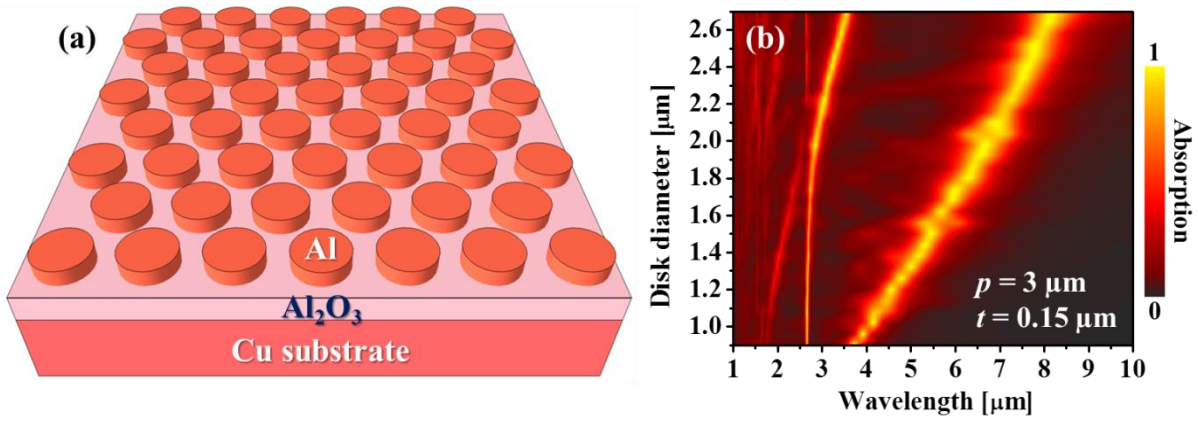

Figure 5.15. (a) Schematic of Al-PA using Cu plate. (b) Simulated absorption spectra of Al-PA on Cu plate with different Al resonator for the 3 μm periodicity and 0.15 μm thick Al_2O_3 insulator.

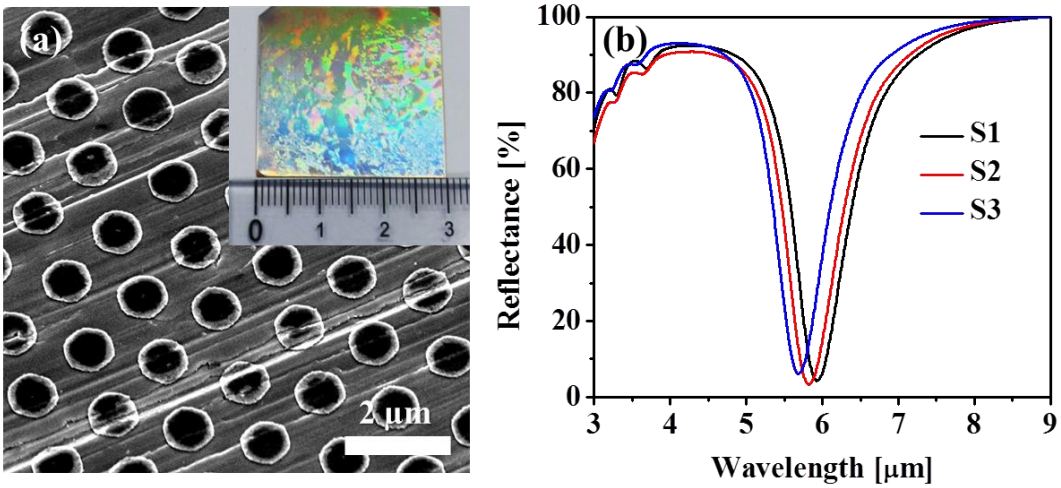

Figure 5.16. (a) SEM image of Al-PA on Cu plate, the inset shows a photo of fabricated sample. (b) Reflectance spectra of three fabricated Al-PAs on 0.2 μm Cu plate.

The schematic of Al-PA on Cu plate is shown in Fig. 5.15a. Figure 5.15b shows the simulated absorption spectra of Al-PA on Cu plate with different Al resonators for the case of 3 μm periodicity and 0.15 μm thick Al_2O_3 insulator. The dielectric functions of Al and Cu were taken from the literature[76]. The dielectric function of Al_2O_3 was taken from literature[31]. It was found that, this simple structure also gives high performance perfect absorption proper-

ty compared to previous Al-Al_2O_3-Al structure on Si substrate. For a demonstration, we fabricated Al-PAs on a 0.2 μm thick and 3x3 cm^2 size Cu plate. Figure 5.16a and the inset show an SEM image and a photo of the fabricated sample (S1). Figure 5.16b shows the reflectance spectra of three fabricated samples (S1, S2, and S3) with different Al resonators sizes. It is noted that, even the Cu plate has a roughness surface but it showed absorption efficiency as high as 95 % for the case of sample S1.

5.6. MIM holes Al-PAs based dual-band perfect absorber

To continuous employing the colloidal lithography method in order to develop other perfect absorber structures, we propose MIM holes Al-PAs using Al holes array on top metallic layer. This section presents our study on the design, simulation and fabrication of Al holes MIM dual-band infrared perfect absorber. This structure and present fabrication method also can be applied for VIS range by using suitable structure parameters.

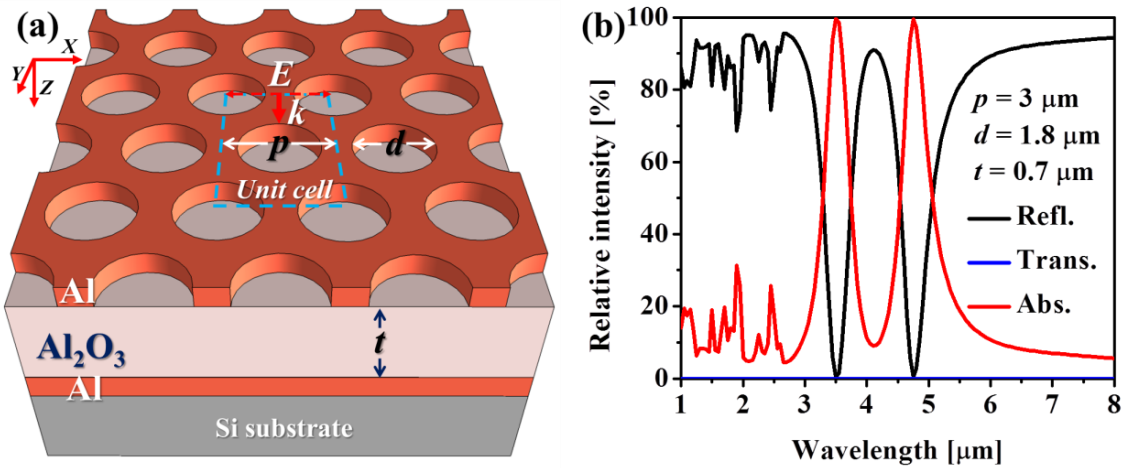

Figure 5.17. (a) Schematic of Al holes-Al_2O_3-Al MIM perfect absorber. (b) Simulated spectra of MIM holes Al-PAs with two perfect absorption bands at 3.5 μm and 4.7 μm in case 3 μm periodicity, 1.8 μm Al hole size, 0.7 μm thick insulator, and 0.1 μm thick top and bottom Al layers.

Figure 5.17a shows a schematic of the proposed MIM holes Al-PAs structure composed of an Al holes array on the top, an Al film at the bottom as the back-plane layer, and an Al_2O_3 insu-

lator between two metallic layers. Figure 5.17b shows the simulated spectra of MIM holes Al-PA with 3 μm periodicity, 1.8 μm Al hole size, 0.7 μm thick Al_2O_3 insulator, and 0.1 μm thick top and bottom Al layers. It was found that, the simulated spectra show dual perfect absorption band located at 3.5 μm and 4.7 μm, which could be related to SP-photonic coupling mode and magnetic resonance mode, respectively. By choosing different periodicity and controlling Al holes sizes as well as Al_2O_3 thickness, it is able to turn resonance of the MIM holes Al-PAs from VIS to MIR regions. Figure 5.18a shows the variable resonances in IR region of MIM holes Al-PAs with different periodicity and Al holes sizes. In this simulation, the hole size was fixed to 0.6*p*, the thicknesses of top and bottom layer were the same of 0.1 μm, and the thickness of insulator was 0.7 μm. Figure 5.18b shows the simulated spectra of three MIM holes Al-PAs (PA1 with p = 0.5 μm, d = 0.38 μm, t = 0.11 μm, PA2 with p = 1.1 μm, d = 0.77 μm, t = 0.3 μm, and PA3 with p = 3 μm, d = 1.8 μm, t = 0.7 μm) in which their resonances are ranging from VIS to MIR regions.

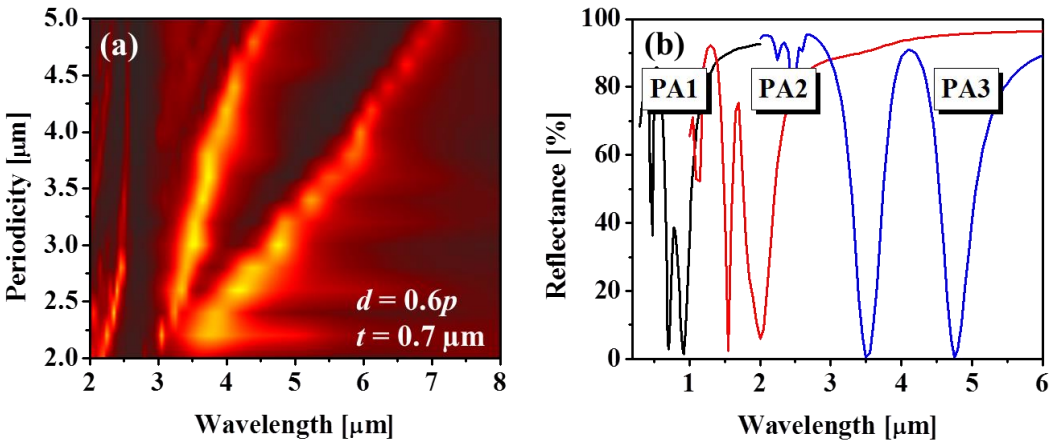

Figure 5.18. (a) Simulated absorption spectra of MIM holes Al-PAs with variable of periodicity p and Al holes sizes (d = 0.6p). Thicknesses of top and bottom Al layers were 0.1 μm, and thickness of insulator was 0.7 μm. (b) Simulated reflectance spectra of three MIM holes Al-PAs with resonances ranging from VIS to MIR regions. Parameters of these three Al-PAs are: PA1 p = 0.5 μm, d = 0.38 μm, t = 0.11 μm; PA2 p = 1.1 μm, d = 0.77 μm, t = 0.3 μm; and PA3 p = 3 μm, d = 1.8 μm, t = 0.7 μm.

We carried out MIM holes Al-PAs using colloidal lithography method. The detailed fabrication process of the MIM holes Al-PAs is shown in Fig. 5.19. First, we fabricated layered Al_2O_3-Al planar film on 1x1 cm^2 Si (100) substrate with optimized thicknesses using sputtering deposition. The sputtered Al2O3-Al film was then coated with a monolayer of PS spheres array as mask layer (Fig. 19a). The size of PS mask was shrunk using RIE process with the etching rate of 3.1 nm/ second (Fig. 19b). Then Al holes array was formed using electron beam or thermal deposition (Fig. 19c). The MIM holes Al-PAs was finally created by removing PS mask by using a sticky tape or sonication process, and then cleaned by toluene and methanol solutions.

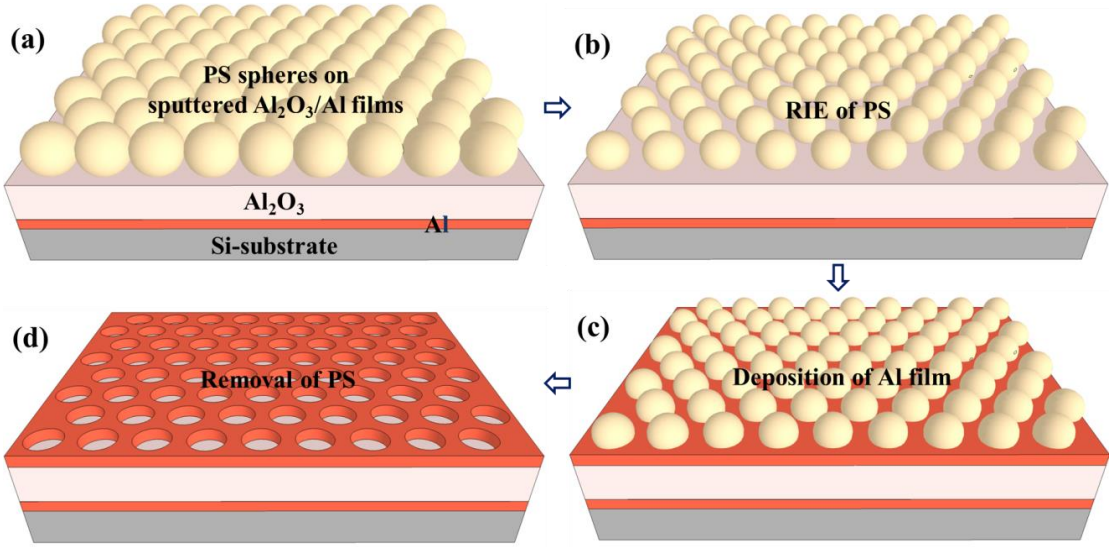

Figure 5.19. Illustration of fabrication process of MIM holes Al-PAs. (a) SAM of PS sphere on layered Al_2O_3-Al films. (b) RIE process to reduce PS mask size. (c) E-beam or thermal deposition of top Al layer. (d) Forming of MIM holes Al-PAs by removing PS mask.

The fabricated samples were characterized by SEM. Figures 5.20a-d show SEM images of four fabricated MIM holes Al-PAs with different Al holes sizes (S1: p = 3 µm, d = 2.5 µm, t = 0.7 µm, S2: p = 3 µm, d = 2.2 µm, t = 0.7 µm, S3: p = 3 µm, d = 1.9 µm, t = 0.7 µm, and S4: p = 3 µm, d = 1.65 µm, t = 0.7 µm). Figure 5.20e-f show typical defects of the fabricated samples. In these defects, the vacancy defects and stressing defects at boundaries between

domains are formed during SAM process of PS, while the roughness at the edges and the asymmetric of Al holes and periodicity (shifting) are formed during etching process of PS mask. These unwanted defects could reduce the quality of the fabricated MIM holes Al-PAs.

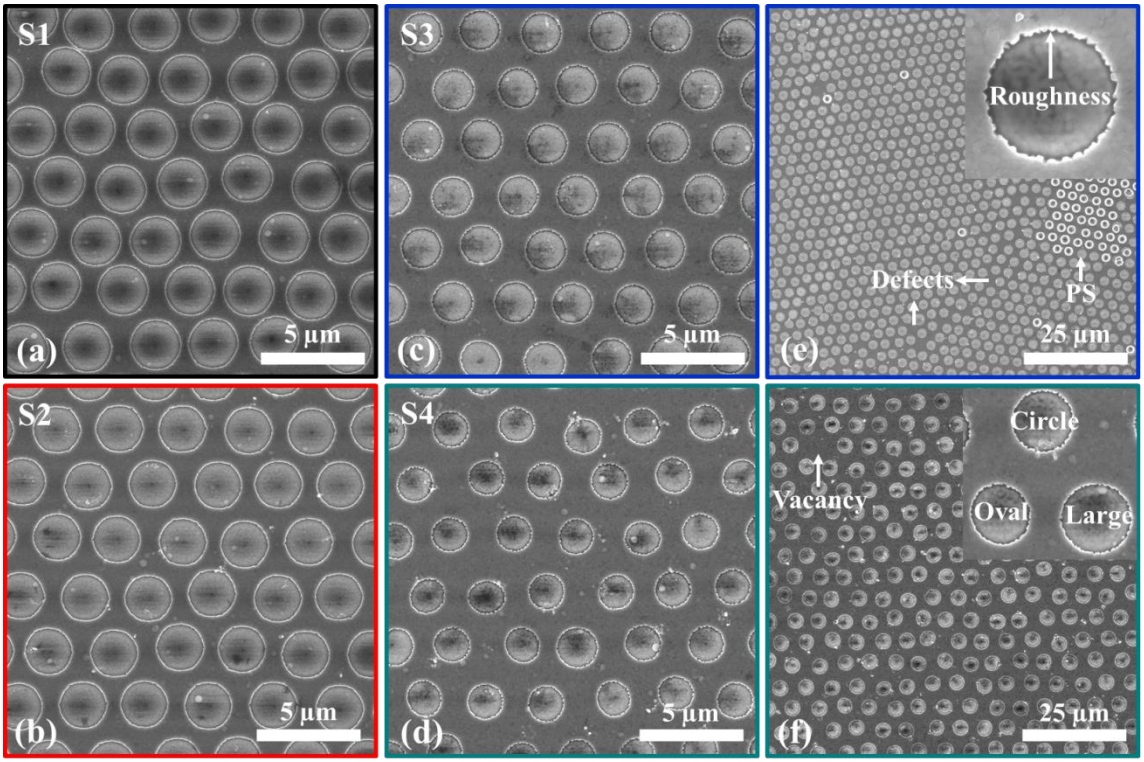

Figure 5.20. SEM images of four fabricated MIM holes Al-PAs. (a) S1: p = 3 μm, d = 2.5 μm, t = 0.7 μm. (b) S2: p = 3 μm, d = 2.2 μm, t = 0.7 μm. (c) S3: p = 3 μm, d = 1.9 μm, t = 0.7 μm. (d) S4: p = 3 μm, d = 1.65 μm, t = 0.7 μm. (e) and (f) Typical defects in fabricated MIM holes Al-PAs.

Figure 5.21 shows the simulated and measured reflectance spectra of four designed samples. It was found that, both simulation and measurement results are show dual-band perfect absorber, and these two bands are closed and degenerated into a broad band when the size of Al holes increased. There is a slightly difference at magnetic modes (around 4.5 μm) between simulation and measurement results. In addition, the absorption efficiencies of the fabricated samples are bellow 90%. These might cause by the defects as shown in SEM images (Fig. 5.20e-f). However, the result indicates that dual-band perfect absorber can be simply realized using MIM Al holes structure and colloidal lithography fabrication technique. This structure

and fabrication method can be applied to others metallic materials based MIM holes perfect absorber by simple replacing Al by those metals.

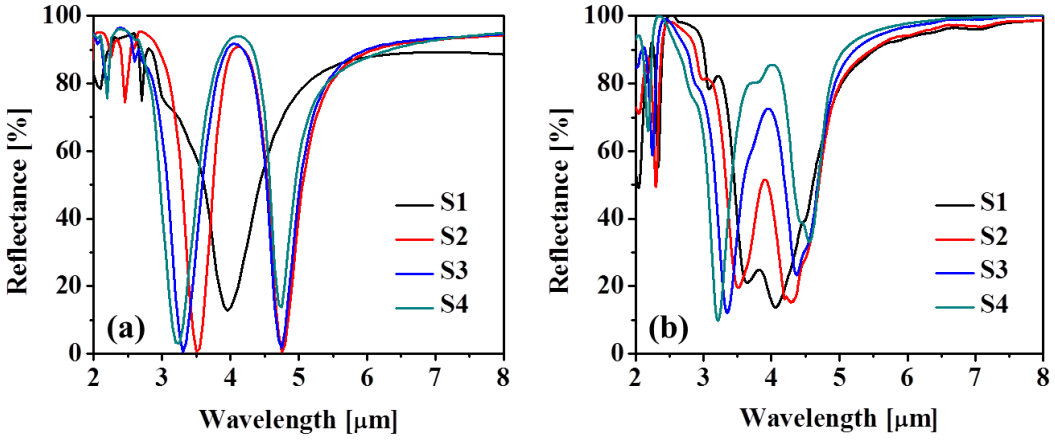

Figure 5.21. (a) Simulated and (b) Measured reflectance of four Al-PAs holes MIM devices. S1: p = 3 μm, d = 2.5 μm, t = 0.7 μm; S2: p = 3 μm, d = 2.2 μm, t = 0.7 μm; S3: p = 3 μm, d = 1.9 μm, t = 0.7 μm; S4: p = 3 μm, d = 1.65 μm, t = 0.7 μm.

We have proposed MIM Al holes based dual-band perfect absorber using simple fabrication process. This structure can also be used for applications in SEIRA, selective thermal emitters as well as MIM based photoconductive devices.

5.7. Broadband perfect absorber based on random gold nano-islands

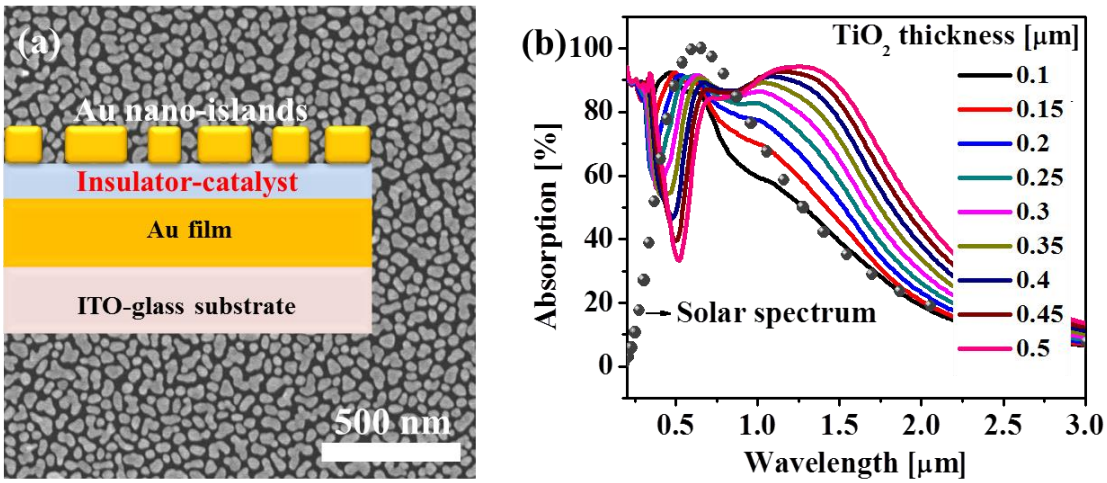

Figure 5.22. Proposed broadband perfect absorber for the efficient photocatalysis

In this section, we propose the design of the broadband MIM structure ranging from VIS to IR regions. The proposed structure composes of a random Au nano-islands on the top isolated to bottom Au film by a metal-oxide insulator film. Figure 5.22 shows the schematic design of the MIM structure with proposed top resonator layer of Au nano-islands as shown in SEM image. Because of its resonators have random size and shape distribution, the MIM can provide broad resonance ranging from VIS-NIR as the simulated results shown in Fig. 5.22b. In this simulation, we used TiO_2 as an insulator layer in order to propose this MIM structure for photocatalysis application. As seen that, by increasing the thickness of TiO_2 film, the resonance of MIM can be shifted to NIR region and its absorption accepts full spectrum of solar light. Therefore, the proposed broadband MIM structure can be applied for many applications related to solar energy conversion, such as photocatalysis, thin-film solar cells, thermoelectric and hearting devices.

5.8. Summary of Chapter 5

In conclusion, large-scale MIM disks and holes Al-PAs with flexible resonance-tunability in MIR region have been demonstrated by a facile fabrication method based on colloidal lithography combined with RIE processes. Simulations show that the hexagonal design of MIM disks and holes Al-PA has fascinating optical properties with two narrowband resonances with high absorption efficiency (up to 100 %). In these two resonance modes, the shot-wavelength resonance is related to SP-photonic coupling while the long-wavelength resonance is related to magnetic resonance.

In case of MIM disks AL-PAs, the short-wavelength mode is attributed to SP-photonic coupling (delocalized plasmon) and is strongly dependent on the periodicity. While the other mode, the long-wavelength mode related to LSP - electric dipoles coupling (magnetic mode) is strongly dependent on the diameter of the Al disk resonator and is almost not dependent on

periodic property. Furthermore, the SP-photonic mode was decline by a low-periodic structure fabricating by present colloidal lithography method, thus the fabricated Al-PAs showed single-narrowband resonance at LSP - electric dipoles coupling mode, and it can be well-controlled by RIE process. By controlling the size of Al disk resonator and choosing suitable periodicity, the simulation results showed a rule to tune resonance wavelength of the Al-PAs ranging from VIS to long-wavelength IR. Using this present colloidal lithography combined with RIE technique, we fabricated large-scale Al-PAs with narrowband resonance and wide-range resonance tenability from 3 – 9 μm. The fabricated Al-PAs device showed excellent optical properties with absorption efficiency up to 98%.

In the selective thermal emitting application of the MIM disks Al-PAs, the emissions showed highly selective thermal and single-narrowband emissions. Futhermore, this Al-PAs can act as IR active plasmonic antenna for SEIRA application as shown in a tentative result on the vibrational sensing of BSA molecules adsorbed on native Al_2O_3 surface.

With inexpensive fabrication method, the Al-PAs with large scale device can be formed on many different substrates even on Cu plate or other substrates depended on the application. We expected that our MIM disks and holes Al-PAs can be applied for many other applications in NIR and MIR such as wavelength–selective infrared photodetectors, surface-enhanced infrared absorption spectroscopy, IR plasmonic sensors, thermophotovoltaic as well as photon harvesting devices. We believe that Al is an excellent plasmonic material in IR and the fabrication method can be applied for the other class of devices.

6. SUMMARY

In this dissertation, a variety of different plasmonic hybrids made of metal and metal oxide ranging from VIS to IR were investigated using both numerical simulations and experimental studies. Depending on the resonances of the plasmonic hybrids, the suitable applications have been carried out.

In Chapter 2, the general introduction of plasmonics, including Drude model, the SPPs at interface of metal-dielectric, Kretschmann configuration for optical excitation of SPPs as well as the localized plasmon of metallic nanostructure were studied and numerically analysed using RCWA and FDTD methods. The RCWA and FDTD numerical simulations were introduced and applied to examine the optical properties of the plasmonic Au-dimer. The near-field enhancement in plasmonic nanogaps, and nonlinear electrons dynamic induced by intense THz pulse in Au percolated film were also discussed. In addition, two plasmonic hybrids composed metal and metal oxide, including AuNC-TiO_2 and Au MIM nano-sandwich, were introduced as the examples for demonstration of the plasmon-enhanced spectroscopy and plasmon-enhanced photocatalysis.

In Chapter 3, we introduced the plasmonic hybrids consisted of nanogaps in which their electric field hot-spots were extremely enhanced in a nanoscale volume for the applications in ultra-sensitive molecular sensing. We have carried out the floating aluminum bowtie antenna with strong hot-spot at the gap for the SERS application. Furthermore, we also demonstrated the *in situ* chemical synthesis of plasmonic hybrids of Au nano-islands and Au-patchy SiO_2 core-shell particles with multiple nanogaps as SEIRA substrates, which were then applied in the *in situ* FTIR molecular sensing. The experiment results on the *in situ* sensing of BSA and GSH molecules as well as the detection of trace amount of mercury ions in water using these plasmonic nanogaps hybrids showed nano-molar level sensing.

In Chapter 4, we have introduced the chemically-synthesized metal-oxide ZnO NWs and TiO_2 thin film for the photoelectric conversion applications. The p-n junction made of ZnO/TiO_2 core-shell nanowire hybrid showed high perfomance of the UV photodetector with a sensitivity of 250 A/W under UV illumination and 5 V bias. In the photocatalysis application, the plasmonic metal NPs-ZnO NWs hybrid showed catalytic activity higher than that of the pure ZnO catalyst by 2-3 folds. The mechanism of the plasmon-enhanced photocatalysis in this nano hybrid catalyst was carefully investigated using both electromagnetic field simulation and spectroscopic measurement. Here, metallic nanoparticles act as plasmonic antenna with strong electric field enhancement at metal-ZnO interface in both UV and VIS excitation, which plays as the near-field enhancement for the UV catalysis and the plasmon-induced hot carriers for the VIS catalysis.

In Chapter 5, we have introduced a class of aluminum plasmonic perfect absorbers fabricated by colloidal lithography method. The single-narrow band perfect absorber based on Al disks MIM structures or dual-band perfect absorber based on Al holes MIM structures were carefully design using RCWA and the fabricated devices showed high absorption efficiency with narrow bandwidth of 0.5 – 0.7 μm in a wide range covering IR region. These Al-PAs were applied for selective thermal emitters as well as SEIRA. In addition, the designs and the developed fabrication technique can be applied for VIS and NIR perfect absorbers as well as for multi-purpose applications such as selective detectors or in solar energy conversion.

Overall, we have showed that, by adopting suitable technique to release plasmonic hybrids in which their resonance ranging from VIS to IR ranges, we have carried out a variety of applications related sensing, photoelectric and thermal energy conversion. The design and fabricated structures showed cost-effective by using chemical fabrication method or using abundant plasmonic materials of aluminum.

PUBLICATIONS

Scientific papers

Chapter 2

[1] Y. Minami, J. Takeda, T. D. Dao, T. Nagao, M. Kitajima, and I. Katayama, "Nonlinear electron dynamics of gold ultrathin films induced by intense terahertz waves," Appl. Phys. Lett., vol. 105, no. 24, p. 241107, Dec. 2014.

[2] Z. Li, T. D. Dao, T. Nagao, and M. Yoshino, "Optical properties of ordered Dot-on-Plate nano-sandwich arrays," Microelectron. Eng., vol. 127, pp. 34–39, Sep. 2014.

[3] L. Liu, T. D. Dao, R. Kodiyath, Q. Kang, H. Abe, T. Nagao, and J. Ye, "Plasmonic Janus-Composite Photocatalyst Comprising Au and C-TiO 2 for Enhanced Aerobic Oxidation over a Broad Visible-Light Range," Adv. Funct. Mater., vol. 24, no. 48, pp. 7754–7762, Dec. 2014.

[4] R. Kodiyath, M. Manikandan, L. Liu, G. V. Ramesh, S. Koyasu, M. Miyauchi, Y. Sakuma, T. Tanabe, T. Gunji, T. Duy Dao, S. Ueda, T. Nagao, J. Ye, and H. Abe, "Visible-light photodecomposition of acetaldehyde by TiO 2 -coated gold nanocages: plasmon-mediated hot electron transport via defect states," Chem Commun, vol. 50, no. 98, pp. 15553–15556, Oct. 2014.

Chapter 3

[5] Chung V. Hoang, Thang D. Dao, Naoki Yamamoto, Masakazu Aono and Tadaaki Nagao, "Spectral Mapping of Plasmonic Resonance of Aluminum Bowtie Antennas for Surface Enhanced Raman Scattering." To be submitted

[6] Thi Ha Lien Nghiem*, Thang Duy Dao*, Kai Chen, and Tadaaki Nagao, "Ensesemble of gold-patchy nanoparticles with multiple hot-spots for dual SEIRA and SERS spectroscopy." To be submitted. (*These authors contributed equally to this work)

Chapter 4

[7] T. D. Dao, C. T. T. Dang, G. Han, C. V. Hoang, W. Yi, V. Narayanamurti, and T. Nagao, "Chemically synthesized nanowire TiO2/ZnO core-shell p-n junction array for

high sensitivity ultraviolet photodetector," Appl. Phys. Lett., vol. 103, no. 19, p. 193119, 2013.

[8] Thang Duy Dao, Gui Han , Nono Arai , Toshihide Nabatame , Yoshiki Wada, Chung Vu Hoang , Masakazu Aono, and Tadaaki Nagao, "Plasmon-mediated photocatalytic activity of wet-chemically prepared ZnO nanowire arrays." Phys. Chem. Chem. Phys., vol. 17, pp. 7395–7403, Feb. 2015.

[9] K. Chen, D. D. Thang, S. Ishii, R. P. Sugavaneshwa, and T. Nagao, "Selective patterned growth of ZnO nanowires/nanosheets and their photoluminescence properties," Opt. Mater. Express, vol. 5, no. 2, p. 353, Feb. 2015.

Chapter 5

[10] Thang Duy Dao, Kai Chen, Satoshi Ishii, Akihiko Ohi, Toshihide Nabatame, Masahiro Kitajima, and Tadaaki Nagao, "Aluminum Infrared Plasmonic Perfect Absorbers Based Selective Thermal Emitters Fabricated by Colloidal Lithography." To be submitted

[11] Thang Duy Dao, Kai Chen, Satoshi Ishii, Akihiko Ohi, Toshihide Nabatame, Masahiro Kitajima, and Tadaaki Nagao, "Aluminum Holes Array Based Dual-band Infrared Perfect Absorber Fabricated by Colloidal Lithography." To be submitted

[12] Kai Chen*, Thang Duy Dao*, Satoshi Ishii, and Tadaaki Nagao, "Infrared Al Metamaterial Perfect Absorbers for Plasmon-enhanced Infrared Spectroscopy." To be submitted. (*These authors contributed equally to this work)

Oral presentations

[1] Nov. 02-06, 2014: Thang D. Dao, K. Chen, S. Ishii, L. Gandham, A. Ohi, T. Nabatame, T. Nagao: "Large Area Aluminum Metamaterial Perfect Absorbers for Tunable Thermal Radiation", The 7th International Symposium on Surface Science 2014

[2] Sep.17-20, 2014: Thang D. Dao, K. Chen, S. Ishii, L. Gandham, A. Ohi, T. Nabatame, T. Nagao: "Large Area, Aluminum Metal-Insulator-Metal Infrared Perfect Absorber", The 75th JSAP Autumn meeting, OSA-JSAP joint symposia.

[3] Mar. 17-20, 2014: T. D. Dao, L. H. Nghiem, K. Chen and T. Nagao: "Ensemble of plasmonic gold-patchy nanoparticles with multiple hot-spots for dual SERS and SEIRA spectroscopy", The 61st JSAP Spring Meeting, 2014.

[4] Sep. 16-20, 2013: T. D. Dao, G. Han, N. Arai, C. Hoang, T. Nabatame, M. Aono, T. Nagao: "Plasmon-assisted photocatalitic activity of the metal-loaded oxide surfaces", The 2013 JSAP-MRS Joint Symposia.

[5] Sep. 11-14, 2012: T. D. Dao, T. Nagao, C. Hoang, G. Han, N. Arai, C. T. T. Dang: "Simple low-cost and high area p-n hetorojunction device based on ZnO nanowires: Combination with TiO2 and its application as a UV photodetector", The 73rd JSAP Autumn meeting OSA-JSAP joint symposia.

REFERENCES

[1] A. K. Geim and K. S. Novoselov, "The rise of graphene," *Nat. Mater.*, vol. 6, pp. 183–191, 2007.

[2] I. Sumio, "Helical microtubules of graphitic carbon," *Nature*, vol. 354, pp. 56–58, 1991.

[3] H. W. Kroto, J. R. Heath, S. C. O'Brien, R. F. Curl, and R. E. Smalley, "C60: Buckminsterfullerence," *Nature*, vol. 318, pp. 162–163, 1985.

[4] M. A. Reed, J. N. Randall, R. J. Aggarwal, R. J. Matyi, T. M. Moore, and A. E. Wetsel, "Observation of discrete electronic states in a zero-dimensional semiconductor nanostructure," *Phys. Rev. Lett.*, vol. 60, no. 6, p. 535, 1988.

[5] P. Yang, H. Yan, S. Mao, R. Russo, J. Johnson, R. Saykally, N. Morris, J. Pham, R. He, and H.-J. Choi, "Controlled growth of ZnO nanowires and their optical properties," *Adv. Funct. Mater.*, vol. 12, no. 5, p. 323, 2002.

[6] Z. L. Wang, "Piezoelectric Nanogenerators Based on Zinc Oxide Nanowire Arrays," *Science*, vol. 312, no. 5771, pp. 242–246, Apr. 2006.

[7] H. Hövel, S. Fritz, A. Hilger, U. Kreibig, and M. Vollmer, "Width of cluster plasmon resonances: bulk dielectric functions and chemical interface damping," *Phys. Rev. B*, vol. 48, no. 24, p. 18178, 1993.

[8] T. Klar, M. Perner, S. Grosse, G. Von Plessen, W. Spirkl, and J. Feldmann, "Surface-plasmon resonances in single metallic nanoparticles," *Phys. Rev. Lett.*, vol. 80, no. 19, p. 4249, 1998.

[9] S. Link and M. A. El-Sayed, "Size and Temperature Dependence of the Plasmon Absorption of Colloidal Gold Nanoparticles," *J. Phys. Chem. B*, vol. 103, no. 21, pp. 4212–4217, May 1999.

[10] C. Noguez, "Surface Plasmons on Metal Nanoparticles: The Influence of Shape and Physical Environment," *J. Phys. Chem. C*, vol. 111, no. 10, pp. 3806–3819, Mar. 2007.

[11] S. A. Maier, *Plasmonics fundamentals and applications*. New York: Springer, 2007.

[12] J. Homola, S. S. Yee, and G. Gauglitz, "Surface plasmon resonance sensors: review," *Sens. Actuators B Chem.*, vol. 54, no. 1, pp. 3–15, 1999.

[13] K. A. Willets and R. P. Van Duyne, "Localized Surface Plasmon Resonance Spectroscopy and Sensing," *Annu. Rev. Phys. Chem.*, vol. 58, no. 1, pp. 267–297, May 2007.

[14] J. R. Lakowicz, “Radiative decay engineering 5: metal-enhanced fluorescence and plasmon emission,” *Anal. Biochem.*, vol. 337, no. 2, pp. 171–194, Feb. 2005.

[15] L. J. David and P. V. D. Richard, “Surface Raman Electrochemistry Part I. Heterocyclic, Aromatic and Aliphatic Amines Adsorbed on the Anodized Silver Electrode,” *J. Electroanal. Chem.*, vol. 84, pp. 1–20, 1977.

[16] M. G. Albrecht and J. A. Creighton, “Anomalously intense Raman spectra of pyridine at a silver electrode,” *J. Am. Chem. Soc.*, vol. 99, no. 15, pp. 5215–5217, 1977.

[17] B. Sharma, R. R. Frontiera, A.-I. Henry, E. Ringe, and R. P. Van Duyne, “SERS: materials, applications, and the future,” *Mater. Today*, vol. 15, no. 1, pp. 16–25, 2012.

[18] K. R. Catchpole and A. Polman, “Design principles for particle plasmon enhanced solar cells,” *Appl. Phys. Lett.*, vol. 93, no. 19, p. 191113, 2008.

[19] Y. Tian and T. Tatsuma, “Mechanisms and Applications of Plasmon-Induced Charge Separation at TiO_2 Films Loaded with Gold Nanoparticles,” *J. Am. Chem. Soc.*, vol. 127, no. 20, pp. 7632–7637, May 2005.

[20] X. Zhang, Y. L. Chen, R.-S. Liu, and D. P. Tsai, “Plasmonic photocatalysis,” *Rep. Prog. Phys.*, vol. 76, no. 4, p. 046401, Apr. 2013.

[21] A. Hartstein, J. R. Kirtley, and J. C. Tsang, “Enhancement of the infrared absorption from molecular monolayers with thin metal overlayers,” *Phys. Rev. Lett.*, vol. 45, no. 3, p. 201, 1980.

[22] Y. Nishikawa, T. Nagasawa, K. Fujiwara, and M. Osawa, “Silver island films for surface-enhanced infrared absorption spectroscopy: effect of island morphology on the absorption enhancement,” *Vib. Spectrosc.*, vol. 6, no. 1, pp. 43–53, 1993.

[23] M. Osawa, “Surface-enhanced infrared absorption,” in *Near-Field Optics and Surface Plasmon Polaritons*, Springer, 2001, pp. 163–187.

[24] F. Neubrech, A. Pucci, T. Cornelius, S. Karim, A. García-Etxarri, and J. Aizpurua, “Resonant Plasmonic and Vibrational Coupling in a Tailored Nanoantenna for Infrared Detection,” *Phys. Rev. Lett.*, vol. 101, no. 15, Oct. 2008.

[25] D. Enders, T. Nagao, T. Nakayama, and M. Aono, “In situ Surface-Enhanced Infrared Absorption Spectroscopy for the Analysis of the Adsorption and Desorption Process of Au Nanoparticles on the SiO_2 /Si Surface,” *Langmuir*, vol. 23, no. 11, pp. 6119–6125, May 2007.

[26] X. Liu, T. Tyler, T. Starr, A. F. Starr, N. M. Jokerst, and W. J. Padilla, "Taming the Blackbody with Infrared Metamaterials as Selective Thermal Emitters," *Phys. Rev. Lett.*, vol. 107, no. 4, p. 045901, Jul. 2011.

[27] Y. Minami, J. Takeda, T. D. Dao, T. Nagao, M. Kitajima, and I. Katayama, "Nonlinear electron dynamics of gold ultrathin films induced by intense terahertz waves," *Appl. Phys. Lett.*, vol. 105, no. 24, p. 241107, Dec. 2014.

[28] Z. Li, T. D. Dao, T. Nagao, and M. Yoshino, "Optical properties of ordered Dot-on-Plate nanosandwich arrays," *Microelectron. Eng.*, vol. 127, pp. 34–39, Sep. 2014.

[29] L. Liu, T. D. Dao, R. Kodiyath, Q. Kang, H. Abe, T. Nagao, and J. Ye, "Plasmonic Janus-Composite Photocatalyst Comprising Au and C-TiO_2 for Enhanced Aerobic Oxidation over a Broad Visible-Light Range," *Adv. Funct. Mater.*, vol. 24, no. 48, pp. 7754–7762, Dec. 2014.

[30] R. Kodiyath, M. Manikandan, L. Liu, G. V. Ramesh, S. Koyasu, M. Miyauchi, Y. Sakuma, T. Tanabe, T. Gunji, T. Duy Dao, S. Ueda, T. Nagao, J. Ye, and H. Abe, "Visible-light photodecomposition of acetaldehyde by TiO_2-coated gold nanocages: plasmon-mediated hot electron transport via defect states," *Chem Commun*, vol. 50, no. 98, pp. 15553–15556, Oct. 2014.

[31] E. D. Palik, *Handbook of optical constants of solids*, 3rd ed. Academic press, 1998.

[32] B. R. Cooper, H. Ehrenreich, and H. R. Philipp, "Optical Properties of Noble Metals. II.," *Phys. Rev.*, vol. 138, no. 2A, p. A494, 1965.

[33] P. R. West, S. Ishii, G. V. Naik, N. K. Emani, V. M. Shalaev, and A. Boltasseva, "Searching for better plasmonic materials," *Laser Photonics Rev.*, vol. 4, no. 6, pp. 795–808, 2010.

[34] E. Kretschmann, "The ATR method with focused light—application to guided waves on a grating," *Opt. Commun.*, vol. 26, no. 1, pp. 41–44, 1978.

[35] J. M. Pitarke, V. M. Silkin, E. V. Chulkov, and P. M. Echenique, "Theory of surface plasmons and surface-plasmon polaritons," *Rep. Prog. Phys.*, vol. 70, no. 1, pp. 1–87, Jan. 2007.

[36] E. T. Arakawa, M. W. Williams, R. N. Hamm, and R. H. Ritchie, "Effect of damping on surface plasmon dispersion," *Phys. Rev. Lett.*, vol. 31, no. 18, p. 1127, 1973.

[37] J. Homola, "Surface Plasmon Resonance Sensors for Detection of Chemical and Biological Species," *Chem. Rev.*, vol. 108, no. 2, pp. 462–493, Feb. 2008.

[38] "http://optics.synopsys.com/rsoft/." .

[39] M. G. Moharam and T. K. Gaylord, “Rigorous coupled-wave analysis of planar-grating diffraction,” *JOSA*, vol. 71, no. 7, pp. 811–818, 1981.

[40] K. S. Yee, “Numerical Solution of Initial Value Problems of Maxwells Equations,” vol. 14, no. 3, pp. 302–307, 1966.

[41] V. Myroshnychenko, J. Rodríguez-Fernández, I. Pastoriza-Santos, A. M. Funston, C. Novo, P. Mulvaney, L. M. Liz-Marzán, and F. J. García de Abajo, “Modelling the optical response of gold nanoparticles,” *Chem. Soc. Rev.*, vol. 37, no. 9, p. 1792, 2008.

[42] M.-W. Chu, V. Myroshnychenko, C. H. Chen, J.-P. Deng, C.-Y. Mou, and F. J. García de Abajo, “Probing Bright and Dark Surface-Plasmon Modes in Individual and Coupled Noble Metal Nanoparticles Using an Electron Beam,” *Nano Lett.*, vol. 9, no. 1, pp. 399–404, Jan. 2009.

[43] J.-S. Huang, J. Kern, P. Geisler, P. Weinmann, M. Kamp, A. Forchel, P. Biagioni, and B. Hecht, “Mode Imaging and Selection in Strongly Coupled Nanoantennas,” *Nano Lett.*, vol. 10, no. 6, pp. 2105–2110, Jun. 2010.

[44] M. Liu, T.-W. Lee, S. Gray, P. Guyot-Sionnest, and M. Pelton, “Excitation of Dark Plasmons in Metal Nanoparticles by a Localized Emitter,” *Phys. Rev. Lett.*, vol. 102, no. 10, Mar. 2009.

[45] L. S. Slaughter, Y. Wu, B. A. Willingham, P. Nordlander, and S. Link, “Effects of Symmetry Breaking and Conductive Contact on the Plasmon Coupling in Gold Nanorod Dimers,” *ACS Nano*, vol. 4, no. 8, pp. 4657–4666, Aug. 2010.

[46] S.-C. Yang, H. Kobori, C.-L. He, M.-H. Lin, H.-Y. Chen, C. Li, M. Kanehara, T. Teranishi, and S. Gwo, “Plasmon Hybridization in Individual Gold Nanocrystal Dimers: Direct Observation of Bright and Dark Modes,” *Nano Lett.*, vol. 10, no. 2, pp. 632–637, Feb. 2010.

[47] S. J. Barrow, D. Rossouw, A. M. Funston, G. A. Botton, and P. Mulvaney, “Mapping Bright and Dark Modes in Gold Nanoparticle Chains using Electron Energy Loss Spectroscopy.,” *Nano Lett.*, vol. 14, no. 7, pp. 3799–3808, Jul. 2014.

[48] K. H. Fung, A. Kumar, and N. X. Fang, “Electron-photon scattering mediated by localized plasmons: A quantitative analysis by eigen-response theory,” *Phys. Rev. B*, vol. 89, no. 4, Jan. 2014.

[49] C. E. Talley, J. B. Jackson, C. Oubre, N. K. Grady, C. W. Hollars, S. M. Lane, T. R. Huser, P. Nordlander, and N. J. Halas, “Surface-Enhanced Raman Scattering from Individual Au Nanoparticles and Nanoparticle Dimer Substrates,” *Nano Lett.*, vol. 5, no. 8, pp. 1569–1574, Aug. 2005.

[50] D. C. Marinica, A. K. Kazansky, P. Nordlander, J. Aizpurua, and A. G. Borisov, "Quantum Plasmonics: Nonlinear Effects in the Field Enhancement of a Plasmonic Nanoparticle Dimer," *Nano Lett.*, vol. 12, no. 3, pp. 1333–1339, Mar. 2012.

[51] K. Yoshioka, Y. Minami, K. Shudo, T. D. Dao, T. Nagao, M. Kitajima, J. Takeda, and I. Katayama, "Terahertz-Field-Induced Nonlinear Electron Delocalization in Au Nanostructures," *Nano Lett.*, p. 150108084527006, Jan. 2015.

[52] T. Pakizeh, M. S. Abrishamian, N. Granpayeh, A. Dmitriev, and M. Käll, "Magnetic-field enhancement in gold nanosandwiches," *Opt. Express*, vol. 14, no. 18, pp. 8240–8246, 2006.

[53] Y. Ekinci, A. Christ, M. Agio, O. J. F. Martin, H. H. Solak, and J. F. Löffler, "Electric and magnetic resonances in arrays of coupled gold nanoparticle in-tandem pairs," *Opt. Express*, vol. 16, no. 17, pp. 13287–13295, 2008.

[54] C. V. Hoang, M. Oyama, O. Saito, M. Aono, and T. Nagao, "Monitoring the Presence of Ionic Mercury in Environmental Water by Plasmon-Enhanced Infrared Spectroscopy," *Sci. Rep.*, vol. 3, Feb. 2013.

[55] K. Kneipp, H. Kneipp, I. Itzkan, R. R. Dasari, and M. S. Feld, "Surface-enhanced Raman scattering and biophysics," *J. Phys. Condens. Matter*, vol. 14, no. 18, p. R597, 2002.

[56] P. L. Stiles, J. A. Dieringer, N. C. Shah, and R. P. Van Duyne, "Surface-Enhanced Raman Spectroscopy," *Annu. Rev. Anal. Chem.*, vol. 1, no. 1, pp. 601–626, Jul. 2008.

[57] D.-K. Lim, K.-S. Jeon, H. M. Kim, J.-M. Nam, and Y. D. Suh, "Nanogap-engineerable Raman-active nanodumbbells for single-molecule detection," *Nat. Mater.*, vol. 9, no. 1, pp. 60–67, Jan. 2010.

[58] N. A. Hatab, C.-H. Hsueh, A. L. Gaddis, S. T. Retterer, J.-H. Li, G. Eres, Z. Zhang, and B. Gu, "Free-Standing Optical Gold Bowtie Nanoantenna with Variable Gap Size for Enhanced Raman Spectroscopy," *Nano Lett.*, vol. 10, no. 12, pp. 4952–4955, Dec. 2010.

[59] P. J. Schuck, D. P. Fromm, A. Sundaramurthy, G. S. Kino, and W. E. Moerner, "Improving the Mismatch between Light and Nanoscale Objects with Gold Bowtie Nanoantennas," *Phys. Rev. Lett.*, vol. 94, no. 1, Jan. 2005.

[60] A. Kinkhabwala, Z. Yu, S. Fan, Y. Avlasevich, K. Müllen, and W. E. Moerner, "Large single-molecule fluorescence enhancements produced by a bowtie nanoantenna," *Nat. Photonics*, vol. 3, no. 11, pp. 654–657, Nov. 2009.

[61] G. H. Chan, J. Zhao, G. C. Schatz, and R. P. V. Duyne, "Localized Surface Plasmon Resonance Spectroscopy of Triangular Aluminum Nanoparticles," *J. Phys. Chem. C*, vol. 112, no. 36, pp. 13958–13963, Sep. 2008.

[62] C. Langhammer, M. Schwind, B. Kasemo, and I. Zorić, "Localized Surface Plasmon Resonances in Aluminum Nanodisks," *Nano Lett.*, vol. 8, no. 5, pp. 1461–1471, May 2008.

[63] M. W. Knight, L. Liu, Y. Wang, L. Brown, S. Mukherjee, N. S. King, H. O. Everitt, P. Nordlander, and N. J. Halas, "Aluminum Plasmonic Nanoantennas," *Nano Lett.*, vol. 12, no. 11, pp. 6000–6004, Nov. 2012.

[64] D. O. Sigle, E. Perkins, J. J. Baumberg, and S. Mahajan, "Reproducible Deep-UV SERRS on Aluminum Nanovoids," *J. Phys. Chem. Lett.*, vol. 4, no. 9, pp. 1449–1452, May 2013.

[65] M. W. Knight, N. S. King, L. Liu, H. O. Everitt, P. Nordlander, and N. J. Halas, "Aluminum for Plasmonics," *ACS Nano*, vol. 8, no. 1, pp. 834–840, Jan. 2014.

[66] S. K. Jha, Z. Ahmed, M. Agio, Y. Ekinci, and J. F. Löffler, "Deep-UV Surface-Enhanced Resonance Raman Scattering of Adenine on Aluminum Nanoparticle Arrays," *J. Am. Chem. Soc.*, vol. 134, no. 4, pp. 1966–1969, Feb. 2012.

[67] L. Li, S. Fang Lim, A. A. Puretzky, R. Riehn, and H. D. Hallen, "Near-field enhanced ultraviolet resonance Raman spectroscopy using aluminum bow-tie nano-antenna," *Appl. Phys. Lett.*, vol. 101, no. 11, p. 113116, Sep. 2012.

[68] H. Ehrenreich, H. R. Philipp, and B. Segall, "Optical Properties of Aluminum," *Phys. Rev.*, vol. 132, p. 1918, 1963.

[69] Keun-Ho Lee and K. J. Chang, "First-principles study of the optical properties and the dielectric response of Al," *Phys. Rev. B*, vol. 49, p. 2362, 1994.

[70] T. Andersson, C. Zhang, M. Tchaplyguine, S. Svensson, N. Mårtensson, and O. Björneholm, "The electronic structure of free aluminum clusters: Metallicity and plasmons," *J. Chem. Phys.*, vol. 136, no. 20, p. 204504, 2012.

[71] T. Stöckli, J.-M. Bonard, P.-A. Stadelmann, and A. Châtelain, "EELS investigation of plasmon excitations in aluminum nanospheres and carbon nanotubes," *Z. Für Phys. At. Mol. Clust.*, vol. 40, no. 1, pp. 425–428, 1997.

[72] D. Lehr, K. Dietrich, C. Helgert, T. Käsebier, H.-J. Fuchs, A. Tünnermann, and E.-B. Kley, "Plasmonic properties of aluminum nanorings generated by double patterning," *Opt. Lett.*, vol. 37, no. 2, pp. 157–159, 2012.

[73] A. Taguchi, Y. Saito, K. Watanabe, S. Yijian, and S. Kawata, “Tailoring plasmon resonances in the deep-ultraviolet by size-tunable fabrication of aluminum nanostructures,” *Appl. Phys. Lett.*, vol. 101, no. 8, p. 081110, 2012.

[74] M. Doherty, A. Murphy, R. Pollard, and P. Dawson, “Surface-Enhanced Raman Scattering from Metallic Nanostructures: Bridging the Gap between the Near-Field and Far-Field Responses,” *Phys. Rev. X*, vol. 3, no. 1, Jan. 2013.

[75] A. Reigue, B. Auguié, P. G. Etchegoin, and E. C. Le Ru, “CW measurements of resonance Raman profiles, line-widths, and cross-sections of fluorescent dyes: application to Nile Blue A in water and ethanol: Measuring resonance Raman spectra of fluorophores,” *J. Raman Spectrosc.*, vol. 44, no. 4, pp. 573–581, Apr. 2013.

[76] A. D. Rakic, A. B. Djurišic, J. M. Elazar, and M. L. Majewski, “Optical properties of metallic films for vertical-cavity optoelectronic devices,” *Appl. Opt.*, vol. 37, no. 22, pp. 5271–5283, 1998.

[77] D. Enders, T. Nagao, A. Pucci, T. Nakayama, and M. Aono, “Surface-enhanced ATR-IR spectroscopy with interface-grown plasmonic gold-island films near the percolation threshold,” *Phys. Chem. Chem. Phys.*, vol. 13, no. 11, p. 4935, 2011.

[78] S. J. Oldenburg, R. D. Averitt, S. L. Westcott, and N. J. Halas, “Nanoengineering of optical resonances,” *Chem. Phys. Lett.*, vol. 288, no. 2, pp. 243–247, 1998.

[79] H. Wang, J. Kundu, and N. J. Halas, “Plasmonic Nanoshell Arrays Combine Surface-Enhanced Vibrational Spectroscopies on a Single Substrate,” *Angew. Chem. Int. Ed.*, vol. 46, no. 47, pp. 9040–9044, Dec. 2007.

[80] R. Bardhan, N. K. Grady, and N. J. Halas, “Nanoscale Control of Near-Infrared Fluorescence Enhancement Using Au Nanoshells,” *Small*, vol. 4, no. 10, pp. 1716–1722, Oct. 2008.

[81] J. Kundu, F. Le, P. Nordlander, and N. J. Halas, “Surface enhanced infrared absorption (SEIRA) spectroscopy on nanoshell aggregate substrates,” *Chem. Phys. Lett.*, vol. 452, no. 1–3, pp. 115–119, Feb. 2008.

[82] T. H. L. Nghiem, T. N. Le, T. H. Do, T. T. D. Vu, Q. H. Do, and H. N. Tran, “Preparation and characterization of silica–gold core–shell nanoparticles,” *J. Nanoparticle Res.*, vol. 15, no. 11, Nov. 2013.

[83] Lyn Patrick ND, “Mercury toxicity and antioxidants-Part 1- role of glutathione and alpha-lipoic acid in the treatment of mercury toxicity,” *Altern. Med. Rev.*, vol. 7, p. 456, 2002.

[84] M. Bieri and T. Bürgi, "L -Glutathione Chemisorption on Gold and Acid/Base Induced Structural Changes: A PM-IRRAS and Time-Resolved in Situ ATR-IR Spectroscopic Study," *Langmuir*, vol. 21, no. 4, pp. 1354–1363, Feb. 2005.

[85] P. Kaur, M. Aschner, and T. Syversen, "Glutathione modulation influences methyl mercury induced neurotoxicity in primary cell cultures of neurons and astrocytes," *NeuroToxicology*, vol. 27, no. 4, pp. 492–500, Jul. 2006.

[86] Z. Guo, Z.-G. Liu, X.-Z. Yao, K.-S. Zhang, X. Chen, J.-H. Liu, and X.-J. Huang, "A molecular-gap device for specific determination of mercury ions," *Sci. Rep.*, vol. 3, Nov. 2013.

[87] Ü. Özgür, Y. I. Alivov, C. Liu, A. Teke, M. A. Reshchikov, S. Doğan, V. Avrutin, S.-J. Cho, and H. Morkoç, "A comprehensive review of ZnO materials and devices," *J. Appl. Phys.*, vol. 98, no. 4, p. 041301, 2005.

[88] L. Schmidt-Mende and J. L. MacManus-Driscoll, "ZnO–nanostructures, defects, and devices," *Mater. Today*, vol. 10, no. 5, pp. 40–48, 2007.

[89] A. Janotti and C. G. Van de Walle, "Fundamentals of zinc oxide as a semiconductor," *Rep. Prog. Phys.*, vol. 72, no. 12, p. 126501, Dec. 2009.

[90] M. Law, L. E. Greene, J. C. Johnson, R. Saykally, and P. Yang, "Nanowire dye-sensitized solar cells," *Nat. Mater.*, vol. 4, no. 6, pp. 455–459, Jun. 2005.

[91] H. Kind, H. Yan, B. Messer, M. Law, and P. Yang, "Nanowire ultraviolet photodetectors and optical switches," *Adv. Mater.*, vol. 14, no. 2, p. 158, 2002.

[92] C. Soci, A. Zhang, B. Xiang, S. A. Dayeh, D. P. R. Aplin, J. Park, X. Y. Bao, Y. H. Lo, and D. Wang, "ZnO Nanowire UV Photodetectors with High Internal Gain," *Nano Lett.*, vol. 7, no. 4, pp. 1003–1009, Apr. 2007.

[93] D. M. Bagnall, Y. F. Chen, Z. Zhu, T. Yao, S. Koyama, M. Y. Shen, and T. Goto, "Optically pumped lasing of ZnO at room temperature," *Appl. Phys. Lett.*, vol. 70, no. 17, p. 2230, 1997.

[94] M. H. Huang, "Room-Temperature Ultraviolet Nanowire Nanolasers," *Science*, vol. 292, no. 5523, pp. 1897–1899, Jun. 2001.

[95] S. R. Morrison, "Chemical Role of Holes and Electrons in ZnO Photocatalysis," *J. Chem. Phys.*, vol. 47, no. 4, p. 1543, 1967.

[96] Y. Wu, H. Yan, and P. Yang, "Semiconductor nanowire array: potential substrates for photocatalysis and photovoltaics," *Top. Catal.*, vol. 19, no. 2, pp. 197–202, 2002.

[97] K. Hashimoto, H. Irie, and A. Fujishima, "TiO_2 photocatalysis: a historical overview and future prospects," *Jpn. J. Appl. Phys.*, vol. 44, no. 12R, p. 8269, 2005.

[98] W. Wu, G. Hu, S. Cui, Y. Zhou, and H. Wu, "Epitaxy of Vertical ZnO Nanorod Arrays on Highly (001)-Oriented ZnO Seed Monolayer by a Hydrothermal Route," *Cryst. Growth Des.*, vol. 8, no. 11, pp. 4014–4020, Nov. 2008.

[99] J. M. Calleja and M. Cardona, "Resonant Raman scattering in ZnO," *Phys. Rev. B*, vol. 16, no. 8, p. 3753, 1977.

[100] R. Cuscó, E. Alarcón-Lladó, J. Ibáñez, L. Artús, J. Jiménez, B. Wang, and M. Callahan, "Temperature dependence of Raman scattering in ZnO," *Phys. Rev. B*, vol. 75, no. 16, Apr. 2007.

[101] I. Shalish, H. Temkin, and V. Narayanamurti, "Size-dependent surface luminescence in ZnO nanowires," *Phys. Rev. B*, vol. 69, no. 24, Jun. 2004.

[102] K. H. Tam, C. K. Cheung, Y. H. Leung, A. B. Djurišić, C. C. Ling, C. D. Beling, S. Fung, W. M. Kwok, W. K. Chan, D. L. Phillips, L. Ding, and W. K. Ge, "Defects in ZnO Nanorods Prepared by a Hydrothermal Method," *J. Phys. Chem. B*, vol. 110, no. 42, pp. 20865–20871, Oct. 2006.

[103] F. Selim, M. Weber, D. Solodovnikov, and K. Lynn, "Nature of Native Defects in ZnO," *Phys. Rev. Lett.*, vol. 99, no. 8, Aug. 2007.

[104] A. Janotti and C. G. Van de Walle, "Native point defects in ZnO," *Phys. Rev. B*, vol. 76, no. 16, Oct. 2007.

[105] S. Brochen, C. Granier, G. Feuillet, and J. Pernot, "Role of deep and shallow donor levels on n-type conductivity of hydrothermal ZnO," *Appl. Phys. Lett.*, vol. 100, no. 5, p. 052115, 2012.

[106] A. B. Djurišić and Y. H. Leung, "Optical Properties of ZnO Nanostructures," *Small*, vol. 2, no. 8–9, pp. 944–961, Aug. 2006.

[107] F. Fabbri, M. Villani, A. Catellani, A. Calzolari, G. Cicero, D. Calestani, G. Calestani, A. Zappettini, B. Dierre, T. Sekiguchi, and G. Salviati, "Zn vacancy induced green luminescence on non-polar surfaces in ZnO nanostructures," *Sci. Rep.*, vol. 4, Jun. 2014.

[108] H. Tang, H. Berger, P. E. Schmid, F. Levy, and G. Burri, "Photoluminescence in TiO_2 anatase single crystals," *Solid State Commun.*, vol. 87, no. 9, pp. 847–850, 1993.

[109] A. R. Bally, E. N. Korobeinikova, P. E. Schmid, F. Levy, and F. Bussy, "Structural and electrical properties of Fe-doped thin films," *J. Phys. Appl. Phys.*, vol. 31, no. 10, p. 1149, 1999.

[110] X. Li, S. Wu, P. Hu, X. Xing, Y. Liu, Y. Yu, M. Yang, J. Lu, S. Li, and W. Liu, "Structures and magnetic properties of p-type Mn:TiO_2 dilute magnetic semiconductor thin films," *J. Appl. Phys.*, vol. 106, no. 4, p. 043913, 2009.

[111] A. Ruiz, A. Cornet, G. Sakai, K. Shimanoe, J. R. Morante, and N. Yamazoe, "Preparation of Cr-Doped TiO_2 Thin Film of P-type Conduction for Gas Sensor Application.," *Chem. Lett.*, no. 9, pp. 892–893, 2002.

[112] R. Dholam, N. Patel, M. Adami, and A. Miotello, "Hydrogen production by photocatalytic water-splitting using Cr- or Fe-doped TiO_2 composite thin films photocatalyst," *Int. J. Hydrog. Energy*, vol. 34, no. 13, pp. 5337–5346, Jul. 2009.

[113] J. M. GallardoáAmores, V. SanchezáEscribano, and others, "FT Raman and FTIR studies of titanias and metatitanate powders," *J. Chem. Soc. Faraday Trans.*, vol. 90, no. 20, pp. 3181–3190, 1994.

[114] C. Pecharromán, F. Gracía, J. P. Holgado, M. Ocaña, A. R. González-Elipe, J. Bassas, J. Santiso, and A. Figueras, "Determination of texture by infrared spectroscopy in titanium oxide–anatase thin films," *J. Appl. Phys.*, vol. 93, no. 8, p. 4634, 2003.

[115] T. D. Dao, C. T. T. Dang, G. Han, C. V. Hoang, W. Yi, V. Narayanamurti, and T. Nagao, "Chemically synthesized nanowire TiO_2/ZnO core-shell p-n junction array for high sensitivity ultraviolet photodetector," *Appl. Phys. Lett.*, vol. 103, no. 19, p. 193119, 2013.

[116] H. Fabricius, T. Skettrup, and P. Bisgaard, "Ultraviolet detectors in thin sputtered ZnO films," *Appl. Opt.*, vol. 25, no. 16, pp. 2764–2767, 1986.

[117] J. B. K. Law and J. T. L. Thong, "Simple fabrication of a ZnO nanowire photodetector with a fast photoresponse time," *Appl. Phys. Lett.*, vol. 88, no. 13, p. 133114, 2006.

[118] G. Shen and D. Chen, "One-dimensional nanostructures for photodetectors," *Recent Pat. Nanotechnol.*, vol. 4, no. 1, pp. 20–31, 2010.

[119] X.-W. Fu, Z.-M. Liao, Y.-B. Zhou, H.-C. Wu, Y.-Q. Bie, J. Xu, and D.-P. Yu, "Graphene/ZnO nanowire/graphene vertical structure based fast-response ultraviolet photodetector," *Appl. Phys. Lett.*, vol. 100, no. 22, p. 223114, 2012.

[120] Y. H. Leung, Z. B. He, L. B. Luo, C. H. A. Tsang, N. B. Wong, W. J. Zhang, and S. T. Lee, "ZnO nanowires array p-n homojunction and its application as a visible-blind ultraviolet photodetector," *Appl. Phys. Lett.*, vol. 96, no. 5, p. 053102, 2010.

[121] Q. Tang, L. Lin, X. Zhao, K. Huang, and J. Wu, "p–n Heterojunction on Ordered ZnO Nanowires/Polyaniline Microrods Double Array," *Langmuir*, vol. 28, no. 8, pp. 3972–3978, Feb. 2012.

[122] R. Ghosh and D. Basak, "Electrical and ultraviolet photoresponse properties of quasialigned ZnO nanowires/p-Si heterojunction," *Appl. Phys. Lett.*, vol. 90, no. 24, p. 243106, 2007.

[123] C. Periasamy and P. Chakrabarti, "Large-area and nanoscale n-ZnO/p-Si heterojunction photodetectors," *J. Vac. Sci. Technol. B Microelectron. Nanometer Struct.*, vol. 29, no. 5, p. 051206, 2011.

[124] H.-D. Um, S. A. Moiz, K.-T. Park, J.-Y. Jung, S.-W. Jee, C. H. Ahn, D. C. Kim, H. K. Cho, D.-W. Kim, and J.-H. Lee, "Highly selective spectral response with enhanced responsivity of n-ZnO/p-Si radial heterojunction nanowire photodiodes," *Appl. Phys. Lett.*, vol. 98, no. 3, p. 033102, 2011.

[125] D. Hofmann, A. Hofstaetter, F. Leiter, H. Zhou, F. Henecker, B. Meyer, S. Orlinskii, J. Schmidt, and P. Baranov, "Hydrogen: A Relevant Shallow Donor in Zinc Oxide," *Phys. Rev. Lett.*, vol. 88, no. 4, Jan. 2002.

[126] D. Look, G. Farlow, P. Reunchan, S. Limpijumnong, S. Zhang, and K. Nordlund, "Evidence for Native-Defect Donors in n-Type ZnO," *Phys. Rev. Lett.*, vol. 95, no. 22, p. 225502, Nov. 2005.

[127] C. T. Sah, R. N. Noyce, and W. Shockley, "Carrier generation and recombination in pn junctions and pn junction characteristics," *Proc. IRE*, vol. 45, no. 9, pp. 1228–1243, 1957.

[128] Dieter K. Schroder, *Semiconductor material and device characterization*. Wiley, 2006.

[129] J. M. Shah, Y.-L. Li, T. Gessmann, and E. F. Schubert, "Experimental analysis and theoretical model for anomalously high ideality factors (n≫2.0) in AlGaN/GaN p-n junction diodes," *J. Appl. Phys.*, vol. 94, no. 4, p. 2627, 2003.

[130] O. Breitenstein, P. Altermatt, K. Ramspeck, and A. Schenk, "The origin of ideality factors n> 2 of shunts and surfaces in the dark IV curves of Si solar cells," in *Proceedings of the 21st European Photovoltaic Solar Energy Conference*, 2006, pp. 625–628.

[131] R. R. Mehta, "Photoconductive gain greater than unity in CdSe films with Schottky barriers at the contacts," *J. Appl. Phys.*, vol. 44, no. 1, p. 325, 1973.

[132] M. Razeghi and A. Rogalski, "Semiconductor ultraviolet detectors," *J. Appl. Phys.*, vol. 79, no. 10, p. 7433, 1996.

[133] Y. Liu, C. R. Gorla, S. Liang, N. Emanetoglu, Y. Lu, H. Shen, and M. Wraback, "Ultraviolet detectors based on epitaxial ZnO films grown by MOCVD," *J. Electron. Mater.*, vol. 29, no. 1, pp. 69–74, 2000.

[134] E. Monroy, F. Omnès, and F. Calle, "Wide-bandgap semiconductor ultraviolet photodetectors," *Semicond. Sci. Technol.*, vol. 18, no. 4, p. R33, 2003.

[135] L. T. Singh, R. P. Sugavaneshwar, and K. K. Nanda, "Carbon nanotube-ZnO nanowire hybrid architectures as multifunctional devices," *AIP Adv.*, vol. 3, p. 082106, 2013.

[136] Thang Duy Dao, Gui Han , Nono Arai , Toshihide Nabatame , Yoshiki Wada, Chung Vu Hoang , Masakazu Aono, and Tadaaki Nagao, "Plasmon-mediated photocatalytic activity of wet-chemically prepared ZnO nanowire arrays," *Phys. Chem. Chem. Phys.*, vol. 17, pp. 7395–7403, Feb. 2015.

[137] T. K. Townsend, N. D. Browning, and F. E. Osterloh, "Nanoscale Strontium Titanate Photocatalysts for Overall Water Splitting," *ACS Nano*, vol. 6, no. 8, pp. 7420–7426, Aug. 2012.

[138] M. W. Knight, H. Sobhani, P. Nordlander, and N. J. Halas, "Photodetection with Active Optical Antennas," *Science*, vol. 332, no. 6030, pp. 702–704, May 2011.

[139] A. O. Govorov, H. Zhang, and Y. K. Gun'ko, "Theory of Photoinjection of Hot Plasmonic Carriers from Metal Nanostructures into Semiconductors and Surface Molecules," *J. Phys. Chem. C*, vol. 117, no. 32, pp. 16616–16631, Aug. 2013.

[140] R. Sundararaman, P. Narang, A. S. Jermyn, W. A. Goddard III, and H. A. Atwater, "Theoretical predictions for hot-carrier generation from surface plasmon decay," *Nat. Commun.*, vol. 5, p. 5788, Dec. 2014.

[141] C. Clavero, "Plasmon-induced hot-electron generation at nanoparticle/metal-oxide interfaces for photovoltaic and photocatalytic devices," *Nat. Photonics*, vol. 8, no. 2, pp. 95–103, Jan. 2014.

[142] Y. Zheng, C. Chen, Y. Zhan, X. Lin, Q. Zheng, K. Wei, and J. Zhu, "Photocatalytic Activity of Ag/ZnO Heterostructure Nanocatalyst: Correlation between Structure and Property," *J. Phys. Chem. C*, vol. 112, no. 29, pp. 10773–10777, Jul. 2008.

[143] R. Y. Hong, J. H. Li, L. L. Chen, D. Q. Liu, H. Z. Li, Y. Zheng, and J. Ding, "Synthesis, surface modification and photocatalytic property of ZnO nanoparticles," *Powder Technol.*, vol. 189, no. 3, pp. 426–432, Feb. 2009.

[144] S. Gao, X. Jia, S. Yang, Z. Li, and K. Jiang, “Hierarchical Ag/ZnO micro/nanostructure: Green synthesis and enhanced photocatalytic performance,” *J. Solid State Chem.*, vol. 184, no. 4, pp. 764–769, Apr. 2011.

[145] P. Fageria, S. Gangopadhyay, and S. Pande, “Synthesis of ZnO/Au and ZnO/Ag nanoparticles and their photocatalytic application using UV and visible light,” *RSC Adv.*, vol. 4, no. 48, p. 24962, 2014.

[146] F. Xu, Z.-Y. Yuan, G.-H. Du, T.-Z. Ren, C. Bouvy, M. Halasa, and B.-L. Su, “Simple approach to highly oriented ZnO nanowire arrays: large-scale growth, photoluminescence and photocatalytic properties,” *Nanotechnology*, vol. 17, no. 2, pp. 588–594, Jan. 2006.

[147] Q. Wang, B. Geng, and S. Wang, “ZnO/Au Hybrid Nanoarchitectures: Wet-Chemical Synthesis and Structurally Enhanced Photocatalytic Performance,” *Environ. Sci. Technol.*, vol. 43, no. 23, pp. 8968–8973, Dec. 2009.

[148] T. Jia, W. Wang, F. Long, Z. Fu, H. Wang, and Q. Zhang, “Fabrication, characterization and photocatalytic activity of La-doped ZnO nanowires,” *J. Alloys Compd.*, vol. 484, no. 1–2, pp. 410–415, Sep. 2009.

[149] D. Jian, P.-X. Gao, W. Cai, B. S. Allimi, S. Pamir Alpay, Y. Ding, Z. L. Wang, and C. Brooks, “Synthesis, characterization, and photocatalytic properties of ZnO/(La,Sr)CoO_3 composite nanorod arrays,” *J. Mater. Chem.*, vol. 19, no. 7, p. 970, 2009.

[150] H. M. Chen, C. K. Chen, C.-J. Chen, L.-C. Cheng, P. C. Wu, B. H. Cheng, Y. Z. Ho, M. L. Tseng, Y.-Y. Hsu, T.-S. Chan, J.-F. Lee, R.-S. Liu, and D. P. Tsai, “Plasmon Inducing Effects for Enhanced Photoelectrochemical Water Splitting: X-ray Absorption Approach to Electronic Structures,” *ACS Nano*, vol. 6, no. 8, pp. 7362–7372, Aug. 2012.

[151] Y. L. Chen, L.-C. Kuo, M. L. Tseng, H. M. Chen, C.-K. Chen, H. J. Huang, R.-S. Liu, and D. P. Tsai, “ZnO nanorod optical disk photocatalytic reactor for photodegradation of methyl orange,” *Opt. Express*, vol. 21, no. 6, pp. 7240–7249, 2013.

[152] C. Wu, L. Shen, Y.-C. Zhang, and Q. Huang, “Solvothermal synthesis of Cr-doped ZnO nanowires with visible light-driven photocatalytic activity,” *Mater. Lett.*, vol. 65, no. 12, pp. 1794–1796, Jun. 2011.

[153] Y. Zhang, M. K. Ram, E. K. Stefanakos, and D. Y. Goswami, “Enhanced photocatalytic activity of iron doped zinc oxide nanowires for water decontamination,” *Surf. Coat. Technol.*, vol. 217, pp. 119–123, Feb. 2013.

[154] J. M. Wu and W. T. Kao, "Heterojunction Nanowires of $Ag_xZn_{1-x}O$–ZnO Photocatalytic and Antibacterial Activities under Visible-Light and Dark Conditions," *J. Phys. Chem. C*, vol. 119, pp. 1433–1441, 2015.

[155] C. Ren, B. Yang, M. Wu, J. Xu, Z. Fu, Y. lv, T. Guo, Y. Zhao, and C. Zhu, "Synthesis of Ag/ZnO nanorods array with enhanced photocatalytic performance," *J. Hazard. Mater.*, vol. 182, no. 1–3, pp. 123–129, Oct. 2010.

[156] T. Wang, Z. Jiao, T. Chen, Y. Li, W. Ren, S. Lin, G. Lu, J. Ye, and Y. Bi, "Vertically aligned ZnO nanowire arrays tip-grafted with silver nanoparticles for photoelectrochemical applications," *Nanoscale*, vol. 5, no. 16, p. 7552, 2013.

[157] H. M. Chen, C. K. Chen, M. L. Tseng, P. C. Wu, C. M. Chang, L.-C. Cheng, H. W. Huang, T. S. Chan, D.-W. Huang, R.-S. Liu, and D. P. Tsai, "Plasmonic ZnO/Ag Embedded Structures as Collecting Layers for Photogenerating Electrons in Solar Hydrogen Generation Photoelectrodes," *Small*, vol. 9, no. 17, pp. 2926–2936, Sep. 2013.

[158] X. Zhang, Y. Liu, and Z. Kang, "3D Branched ZnO Nanowire Arrays Decorated with Plasmonic Au Nanoparticles for High-Performance Photoelectrochemical Water Splitting," *ACS Appl. Mater. Interfaces*, vol. 6, no. 6, pp. 4480–4489, Mar. 2014.

[159] L. Mulfinger, S. D. Solomon, M. Bahadory, A. V. Jeyarajasingam, S. A. Rutkowsky, and C. Boritz, "Synthesis and study of silver nanoparticles," *J. Chem. Educ.*, vol. 84, no. 2, p. 322, 2007.

[160] J. Kimling, M. Maier, B. Okenve, V. Kotaidis, H. Ballot, and A. Plech, "Turkevich Method for Gold Nanoparticle Synthesis Revisited," *J. Phys. Chem. B*, vol. 110, no. 32, pp. 15700–15707, Aug. 2006.

[161] A. Houas, H. Lachheb, M. Ksibi, E. Elaloui, C. Guillard, and J.-M. Herrmann, "Photocatalytic degradation pathway of methylene blue in water," *Appl. Catal. B Environ.*, vol. 31, no. 2, pp. 145–157, 2001.

[162] M. R. Hoffmann, S. T. Martin, W. Choi, and D. W. Bahnemann, "Environmental applications of semiconductor photocatalysis," *Chem. Rev.*, vol. 95, no. 1, pp. 69–96, 1995.

[163] M. Liu, C.-Y. Nam, C. T. Black, J. Kamcev, and L. Zhang, "Enhancing Water Splitting Activity and Chemical Stability of Zinc Oxide Nanowire Photoanodes with Ultrathin Titania Shells," *J. Phys. Chem. C*, vol. 117, no. 26, pp. 13396–13402, Jul. 2013.

[164] R. H. Fowler, “The analysis of photoelectric sensitivity curves for clean metals at various temperatures,” *Phys. Rev.*, vol. 38, no. 1, p. 45, 1931.

[165] H. B. Michaelson, “The work function of the elements and its periodicity,” *J. Appl. Phys.*, vol. 48, no. 11, p. 4729, 1977.

[166] K. Jacobi, G. Zwicker, and A. Gutmann, “Work function, electron affinity and band bending of zinc oxide surfaces,” *Surf. Sci.*, vol. 141, pp. 109–125, 1984.

[167] R. M. Sheetz, E. Richter, A. N. Andriotis, and M. Menon, “Defect-induced optical absorption in the visible range in ZnO nanowires,” *Phys. Rev. B*, vol. 80, no. 19, p. 195314, Nov. 2009.

[168] P. J. Schuck, “Nanoimaging: Hot electrons go through the barrier,” *Nat. Nanotechnol.*, vol. 8, pp. 799–800, 2013.

[169] N. Landy, S. Sajuyigbe, J. Mock, D. Smith, and W. Padilla, “Perfect Metamaterial Absorber,” *Phys. Rev. Lett.*, vol. 100, no. 20, May 2008.

[170] Y. Avitzour, Y. Urzhumov, and G. Shvets, “Wide-angle infrared absorber based on a negative-index plasmonic metamaterial,” *Phys. Rev. B*, vol. 79, no. 4, Jan. 2009.

[171] J. Hao, J. Wang, X. Liu, W. J. Padilla, L. Zhou, and M. Qiu, “High performance optical absorber based on a plasmonic metamaterial,” *Appl. Phys. Lett.*, vol. 96, no. 25, p. 251104, 2010.

[172] K. Aydin, V. E. Ferry, R. M. Briggs, and H. A. Atwater, “Broadband polarization-independent resonant light absorption using ultrathin plasmonic super absorbers,” *Nat. Commun.*, vol. 2, p. 517, Nov. 2011.

[173] C. Wu, B. Neuner, G. Shvets, J. John, A. Milder, B. Zollars, and S. Savoy, “Large-area wide-angle spectrally selective plasmonic absorber,” *Phys. Rev. B*, vol. 84, no. 7, Aug. 2011.

[174] M. Pu, C. Hu, M. Wang, C. Huang, Z. Zhao, C. Wang, Q. Feng, and X. Luo, “Design principles for infrared wide-angle perfect absorber based on plasmonic structure,” *Opt. Express*, vol. 19, no. 18, pp. 17413–17420, 2011.

[175] Z. Fang, Y.-R. Zhen, L. Fan, X. Zhu, and P. Nordlander, “Tunable wide-angle plasmonic perfect absorber at visible frequencies,” *Phys. Rev. B*, vol. 85, no. 24, Jun. 2012.

[176] R. Feng, W. Ding, L. Liu, L. Chen, J. Qiu, and G. Chen, “Dual-band infrared perfect absorber based on asymmetric T-shaped plasmonic array,” *Opt. Express*, vol. 22, no. S2, p. A335, Mar. 2014.

[177] K. Ikeda, H. T. Miyazaki, T. Kasaya, K. Yamamoto, Y. Inoue, K. Fujimura, T. Kanakugi, M. Okada, K. Hatade, and S. Kitagawa, "Controlled thermal emission of polarized infrared waves from arrayed plasmon nanocavities," *Appl. Phys. Lett.*, vol. 92, no. 2, p. 021117, 2008.

[178] H. T. Miyazaki, K. Ikeda, T. Kasaya, K. Yamamoto, Y. Inoue, K. Fujimura, T. Kanakugi, M. Okada, K. Hatade, and S. Kitagawa, "Thermal emission of two-color polarized infrared waves from integrated plasmon cavities," *Appl. Phys. Lett.*, vol. 92, no. 14, p. 141114, 2008.

[179] Y.-H. Ye, Y.-W. Jiang, M.-W. Tsai, Y.-T. Chang, C.-Y. Chen, D.-C. Tzuang, Y.-T. Wu, and S.-C. Lee, "Localized surface plasmon polaritons in Ag/SiO_2/Ag plasmonic thermal emitter," *Appl. Phys. Lett.*, vol. 93, no. 3, p. 033113, 2008.

[180] M. Diem, T. Koschny, and C. Soukoulis, "Wide-angle perfect absorber/thermal emitter in the terahertz regime," *Phys. Rev. B*, vol. 79, no. 3, p. 033101, Jan. 2009.

[181] H.-H. Chen, H.-H. Hsiao, H.-C. Chang, W.-L. Huang, and S.-C. Lee, "Double wavelength infrared emission by localized surface plasmonic thermal emitter," *Appl. Phys. Lett.*, vol. 104, no. 8, p. 083114, Feb. 2014.

[182] N. Liu, M. Mesch, T. Weiss, M. Hentschel, and H. Giessen, "Infrared Perfect Absorber and Its Application As Plasmonic Sensor," *Nano Lett.*, vol. 10, no. 7, pp. 2342–2348, Jul. 2010.

[183] K. Chen, R. Adato, and H. Altug, "Dual-Band Perfect Absorber for Multispectral Plasmon-Enhanced Infrared Spectroscopy," *ACS Nano*, vol. 6, no. 9, pp. 7998–8006, Sep. 2012.

[184] Y. Li, L. Su, C. Shou, C. Yu, J. Deng, and Y. Fang, "Surface-enhanced molecular spectroscopy (SEMS) based on perfect-absorber metamaterials in the mid-infrared," *Sci. Rep.*, vol. 3, Oct. 2013.

[185] H. T. Miyazaki, T. Kasaya, M. Iwanaga, B. Choi, Y. Sugimoto, and K. Sakoda, "Dual-band infrared metasurface thermal emitter for CO2 sensing," *Appl. Phys. Lett.*, vol. 105, no. 12, p. 121107, Sep. 2014.

[186] J. S. G and T. Eric S, "Complex Thermoelectric Materials." nature materials, 2008.

[187] A. Lenert, D. M. Bierman, Y. Nam, W. R. Chan, I. Celanović, M. Soljačić, and E. N. Wang, "A nanophotonic solar thermophotovoltaic device," *Nat. Nanotechnol.*, vol. 9, no. 2, pp. 126–130, Jan. 2014.

[188] M. U. Pralle, N. Moelders, M. P. McNeal, I. Puscasu, A. C. Greenwald, J. T. Daly, E. A. Johnson, T. George, D. S. Choi, I. El-Kady, and R. Biswas, "Photonic crystal enhanced narrow-band infrared emitters," *Appl. Phys. Lett.*, vol. 81, no. 25, p. 4685, 2002.

[189] M. Laroche, R. Carminati, and J.-J. Greffet, "Coherent Thermal Antenna Using a Photonic Crystal Slab," *Phys. Rev. Lett.*, vol. 96, no. 12, Mar. 2006.

[190] T. Inoue, M. De Zoysa, T. Asano, and S. Noda, "Single-peak narrow-bandwidth mid-infrared thermal emitters based on quantum wells and photonic crystals," *Appl. Phys. Lett.*, vol. 102, no. 19, p. 191110, 2013.

[191] J. Le Gall, M. Olivier, and J.-J. Greffet, "Experimental and theoretical study of reflection and coherent thermal emissionby a SiC grating supporting a surface-phonon polariton," *Phys. Rev. B*, vol. 55, no. 15, p. 10105, 1997.

[192] J. A. Mason, D. C. Adams, Z. Johnson, S. Smith, A. W. Davis, and D. Wasserman, "Selective thermal emission from patterned steel," *Opt. Express*, vol. 18, no. 24, pp. 25192–25198, 2010.

[193] J. T. K. Wan, "Tunable thermal emission at infrared frequencies via tungsten gratings," *Opt. Commun.*, vol. 282, no. 8, pp. 1671–1675, Apr. 2009.

[194] M.-W. Tsai, T.-H. Chuang, C.-Y. Meng, Y.-T. Chang, and S.-C. Lee, "High performance mid-infrared narrow-band plasmonic thermal emitter," *Appl. Phys. Lett.*, vol. 89, no. 17, p. 173116, 2006.

[195] S. Tay, A. Kropachev, I. E. Araci, T. Skotheim, R. A. Norwood, and N. Peyghambarian, "Plasmonic thermal IR emitters based on nanoamorphous carbon," *Appl. Phys. Lett.*, vol. 94, no. 7, p. 071113, 2009.

[196] J. C. Hulteen and R. P. Van Duyne, "Nanosphere lithography: a materials general fabrication process for periodic particle array surfaces," *J. Vac. Sci. Technol. A*, vol. 13, no. 3, pp. 1553–1558, 1995.

[197] Y.-C. Chang, S.-C. Lu, H.-C. Chung, S.-M. Wang, T.-D. Tsai, and T.-F. Guo, "High-Throughput Nanofabrication of Infra-red and Chiral Metamaterials using Nanospherical-Lens Lithography," *Sci. Rep.*, vol. 3, Nov. 2013.

[198] L. Zhou, Q. Gan, F. J. Bartoli, and V. Dierolf, "Direct near-field optical imaging of UV bowtie nanoantennas," *Opt. Express*, vol. 17, no. 22, pp. 20301–20306, 2009.

[199] N. Zhang, P. Zhou, D. Cheng, X. Weng, J. Xie, and L. Deng, "Dual-band absorption of mid-infrared metamaterial absorber based on distinct dielectric spacing layers," *Opt. Lett.*, vol. 38, no. 7, pp. 1125–1127, 2013.

[200] Sencer Ayas, Ahmet Emin Topal, Andi Cupallari, Hasan Guner, Gokhan Bakan, and Aykutlu Dana, "Exploiting Native Al2O3 for Multispectral Aluminum Plasmonics," *ACS Photonics*, vol. 1, pp. 1313–1321, 2014.

[201] Y. J. Chen, E. S. Koteles, R. J. Seymour, G. J. Sonek, and J. M. Ballantyne, "Surface plasmons on gratings: coupling in the minigap regions," *Solid State Commun.*, vol. 46, no. 2, pp. 95–99, 1983.

[202] U. Schröter and D. Heitmann, "Grating couplers for surface plasmons excited on thin metal films in the Kretschmann-Raether configuration," *Phys. Rev. B*, vol. 60, no. 7, p. 4992, 1999.

[203] A. Sobhani, M. W. Knight, Y. Wang, B. Zheng, N. S. King, L. V. Brown, Z. Fang, P. Nordlander, and N. J. Halas, "Narrowband photodetection in the near-infrared with a plasmon-induced hot electron device," *Nat. Commun.*, vol. 4, p. 1643, Mar. 2013.

[204] T. Kelf, Y. Sugawara, R. Cole, J. Baumberg, M. Abdelsalam, S. Cintra, S. Mahajan, A. Russell, and P. Bartlett, "Localized and delocalized plasmons in metallic nanovoids," *Phys. Rev. B*, vol. 74, no. 24, Dec. 2006.

[205] Kurosch Rezwan, Lorenz P. Meier, Mandana Rezwan, Janos Vo¨ro¨s, Marcus Textor, and Ludwig J. Gauckler, "Bovine Serum Albumin Adsorption onto Colloidal Al_2O_3 Particles A New Model Based on Zeta Potential and UV−Vis Measurements," *Langmuir*, vol. 20, pp. 10055–10061, 2004.